Chapter 3

Wave Propagation with Finite Exciting Sources

3.1 DIFFRACTION AND NONUNIFORM EXCITATION

3.1.1 Introduction

In Chapter 1 we described the one-dimensional theory of the piston transducer, on the assumption that the stress and strain fields within it are uniform. In practice, when the diameter of the transducer is finite, the stress fields may have several nodes and antinodes across the diameter, as would any waveguide or electromagnetic (EM) resonator. When the diameter of the transducer is larger than the wavelength and the Q of the system is not too high, these resonant effects tend to be washed out and the stress fields can be assumed to remain essentially uniform between the exciting electrodes.

Even if the excitation is perfectly uniform, however, the stress fields at some distance from the transducer may not be. Because of diffraction, the acoustic beam emitted from the transducer will increase its diameter with distance and the field components in the beam will exhibit fine structure variations, both along its length and across its diameter. Just as in optics, there are two distinct regions of interest, the near-field region, or the *Fresnel zone*, and the far-field region, or the *Fraunhofer zone*. Within the Fresnel zone, the outside diameter of the beam remains essentially uniform; the beam then spreads beyond this region. Within the Fresnel zone there are rapid variations of the stress fields within the beam, both along its axis and radially.

Throughout this chapter the analysis will be based, for simplicity, on the excitation of longitudinal waves in a liquid medium. In Sec. 3.1.2 we consider

excitation of spherical waves in a liquid. In Sec. 3.1.3 we develop a Green's function and, from it, derive the Rayleigh Sommerfeld integral, which we will use extensively in our analyses throughout the rest of the chapter. Our results for excitation by a piston transducer in a liquid medium will be essentially the same as those we would expect for longitudinal or shear wave excitation in a solid medium [1].

In Sec. 3.2 we employ the Rayleigh–Sommerfeld integral to derive the essential features of diffraction from a plane piston transducer. Then we will use Hankel and Fourier transform methods to derive more extensive results for diffraction from a piston transducer and from its surface wave equivalent, the one-dimensional rectangular transducer.

In Sec. 3.3 we use the same techniques to analyze diffraction from a concave spherical focused transducer or lens focused system, and we will discuss excitation of and propagation of Gaussian beams. We will pay considerable attention to the concepts of transverse definition and range definition of a focused beam, to sidelobes, and to the problem of speckle, which occurs with coherent wave excitation. The example of a scanned acoustic microscope will be discussed in some detail.

In Sec. 3.4 we consider the effect of diffraction when short pulses are used to excite a transducer. In this case, much of the "ringing" phenomenon in the Fresnel zone tends to disappear.

In Sec. 3.5 we discuss concepts of acoustic imaging without the use of physical lenses. In Sec. 3.5.1 we first define the A-scan, B-scan, and C-scan with examples drawn from medical imaging and nondestructive testing; we also discuss the concepts of time-delay and phase-delay focusing.

In Sec. 3.5.2 we derive basic imaging theories for transducer arrays, using matched filter concepts. By employing the paraxial approximation, we determine sidelobe levels for various types of continuous array systems, and then show how grating lobes occur in a system with a finite number of periodically spaced transducer elements, and how sidelobe levels are affected by missing elements.

In Sec. 3.5.3 we consider the concept of the Fresnel lens and show how subsidiary foci occur. We show that the errors due to a finite number of phase samples in digitally sampled systems are very similar to those of Fresnel lenses: in both cases there are subsidiary foci, and the sidelobe levels are increased by the sampling errors.

In Sec. 3.5.4 we discuss chirp focused systems. We then consider examples of various types of transmission, imaging, reflection imaging, and two-dimensional array systems.

In Sec. 3.5.5 we discuss time-delay focused systems. We consider the use of lumped delay lines, charge-coupled-device (CCD) delay lines, and synthetic aperture digitally processed systems, and give a brief description of tomography, comparing this concept to synthetic aperture focusing.

In Sec. 3.5.6 we discuss the concepts of holographic imaging, giving examples of various types of holographic image reconstruction schemes. In addition, we describe the scanning laser acoustic microscope (SLAM), which uses the same type of technology. We also describe how the holographic methods can be very powerful for measuring the vibration amplitude of vibrating objects.

Finally, in Sec. 3.6 we use the analytical methods developed in Sec. 3.1 to analyze scattering from small and large objects. We deal with the scattering theory for objects whose size is much larger than the wavelength, as well as for objects at the opposite Rayleigh limit, whose size is much less than a wavelength. We also describe the use of quasistatic analysis and other approximate techniques based on ray-tracing concepts.

3.1.2 Spherical Waves in a Liquid or Solid

First we consider the excitation of waves by a small vibrating sphere. This derivation will show that for good excitation efficiency, the size of the sphere must be comparable to the wavelength. Furthermore, we need the basic results to derive the waves excited by various forms of transducers and to obtain a simple understanding of the scattering of waves from a small object, such as a flaw in a solid or a dust particle in water.

The displacement $\mathbf{u}$ associated with longitudinal waves in an isotropic medium can be derived from a potential ϕ, where $\mathbf{u} = \nabla\phi$ and ϕ obeys the wave equation

$$\nabla^2\phi - \frac{1}{V^2}\frac{\partial^2\phi}{\partial t^2} = 0 \tag{3.1.1}$$

where $V = \sqrt{(\lambda + 2\mu)/\rho_{m0}}$ is the longitudinal wave velocity and λ and μ are the Lamé constants for an isotropic solid.

In spherical coordinates for a wave whose components vary as $\exp(j\omega t)$, this equation can be written as

$$\frac{1}{R^2}\frac{\partial}{\partial R}\left(R^2\frac{\partial\phi}{\partial R}\right) + k^2\phi = 0 \tag{3.1.2}$$

where $k = \omega/V$ and we have assumed no variation of the potential with angle. The solutions of this equation are

$$\phi = \frac{Ae^{\mp jkR}}{R} \tag{3.1.3}$$

The $-$ sign corresponds to a spherical wave propagating outward from the origin and the $+$ sign corresponds to one propagating in toward it. More generally, the solution of Eq. (3.1.2) has the form

$$\phi = \frac{f(t \mp R/V)}{R} \tag{3.1.4}$$

Vibrating sphere. Before dealing with the plane piston transducer, let us first consider the wave excited by a small spherical transducer of radius a. In this case, we use the relation $\mathbf{u} = \nabla\phi$ in Eq. (3.1.3) for a wave propagating radially outward to write

$$u_R = \frac{\partial\phi}{\partial R} = -\frac{Ae^{-jkR}}{R^2}(1 + jkR) \tag{3.1.5}$$

Thus if $u_R = u_R(a)$ at the spherical surface, then

$$\phi = -\frac{u_R(a)a^2}{R(1 + jka)} e^{-jk(R-a)} \tag{3.1.6}$$

Liquid medium. In a liquid medium, the pressure p is isotropic. Thus we can write $p = -T_1 = -T_2 = -T_3$ or $p = -T_R$. It follows that

$$-\nabla \cdot \mathbf{T} = \nabla p = \omega^2 \rho_{m0} \mathbf{u} = \omega^2 \rho_{m0} \nabla \phi \tag{3.1.7}$$

On integration, we see that, generally, for a liquid,

$$p = \omega^2 \rho_{m0} \phi \tag{3.1.8}$$

with

$$p = -\kappa \Delta = -c_{11} S_1 \tag{3.1.9}$$

where $\kappa = (\lambda + \frac{2}{3}\mu)$. As discussed in Sec. 2.1, the parameter κ is called the bulk elastic modulus and the dilation is $\Delta = S_1 + S_2 + S_3$. We note that

$$k^2 = \frac{\omega^2 \rho_{m0}}{c_{11}} \tag{3.1.10}$$

For a liquid, it follows that

$$k^2 = \frac{\omega^2 \rho_{m0}}{\kappa} \tag{3.1.11}$$

If $v_R = j\omega u_R$ is the radial velocity, the effective wave impedance Z for a spherical wave traveling outward in an anisotropic solid or a liquid is

$$\begin{aligned} Z &= -\frac{T_R}{v_R} = \frac{p}{v_R} = \frac{j\omega \rho_{m0} R}{1 + jkR} \\ &= \frac{k^2R^2 + jkR}{1 + k^2R^2} Z_0 \end{aligned} \tag{3.1.12}$$

where $Z_0 = \rho_{m0}\omega/k$ is the plane wave impedance of the medium.

We note that far from the origin, where $kR >> 1$, the wave impedance approaches Z_0. However, for a small source near the origin ($kR << 1$), the wave impedance becomes imaginary, and there is very little real power flow. Because there is very little real power flow near the source, it is difficult to excite acoustic waves from a source much smaller than a wavelength in diameter.

To put it another way, suppose that the surface of a sphere of radius a is pulsating so that its surface acceleration is $\partial^2 u_R/\partial t^2$ or $-\omega^2 u_R(a)$. It follows from Eq. (3.1.5) that the radial displacement $u_R(R)$ is

$$u_R(R) = \frac{a^2 u_R(a) e^{-jk(R-a)}}{R^2} \frac{1 + jkR}{1 + jka} \tag{3.1.13}$$

The real power Re (P) radiated is therefore

$$\text{Re}\,(P) = 2\pi R^2\, \text{Re}\,(Z) v_R v_R^* = 2\pi R^2\, \text{Re}\,(Z) \omega^2 |u_R^2(R)| \tag{3.1.14}$$

It follows, by substituting Eqs. (3.1.12) and (3.1.13) in (3.1.14), that the complex power P, defined as $P = 2\pi R^2 Z v_R v_R$, is

$$P = 2\pi a^2 Z_0 \frac{k^2a^2 + jka^2/R}{1 + k^2a^2} |v_R^2(a)| \tag{3.1.15}$$

This is the final formula required for determining radiation from a sphere. We conclude that:

1. When $kR >> 1$, then $u_R \approx -jk\phi$, so that $|u_R| \alpha |\phi|$ at distances more than a few wavelengths from the transducer.
2. Real power is conserved and does not change with radius. The real power emitted is

$$\text{Re } (P) = \frac{k^2a^2}{1 + k^2a^2} 2\pi a^2 Z_0 |v_R^2(a)| \tag{3.1.16}$$

   and the power intensity $I(R) = \text{Re } (P)/4\pi R^2$ falls off as $1/R^2$.
3. The real power emitted for a given $v_R(a)$ does not vary with R even if $ka >> 1$. However, if $ka <<$ [illegible] power intensity at the transducer for a given $v_R(a)$ varies as k^2a^2. [illegible] becomes very small as $ka \rightarrow 0$.
4. As R changes, react[illegible] is not conserved and becomes dominant at the spherical transducer [illegible] < 1. When $ka << 1$, the pressure at the transducer is essentially $\pi/2$ out of phase with the velocity and very small, and the effective impedance is inductive of value $jkRZ_0$. Thus, in this case, there is no real load on the transducer.

These conclusions also hold for the plane transducer and other transducer shapes. The transducer size (in this case its diameter) must be of the order of half a wavelength or more to obtain efficient excitation of acoustic waves.

3.1.3 Green's Function

Here we show how to derive a Green's function, which we use in the analysis of diffraction of the waves excited by transducers. We derive this function by adding spherical wave solutions to give the potential at any point due to waves excited by, for instance, a piston transducer. The boundary conditions we will apply are most conveniently stated for pressure waves in a liquid, but the results we obtain are a good approximation to the truth for waves in isotropic solids, provided that the transducer is several wavelengths in diameter [1,2]. For very small transducers or for excitation of waves in a solid, other techniques are needed. The angular spectrum methods described in Secs. 3.2.2 and 3.2.3 are more rigorous, while still convenient to employ. In practice they yield essentially the same results as the Green's function approach given here.

The spherically symmetric solution of the wave equation of Sec. 3.1.2 implies that the potential at the point x', y', z' of a longitudinal wave due to a source at

a point x, y, z can be written in the form

$$G = \frac{Ae^{-jkR}}{R} \tag{3.1.17}$$

where

$$R = [(x - x')^2 + (y - y')^2 + (z - z')^2]^{1/2} \tag{3.1.18}$$

It is easy to show by differentiation that this solution obeys the relation $\nabla^2\phi + k^2\phi = 0$ ($G = \phi$), except where $R = 0$ when $\nabla^2\phi \to \infty$. More generally, Eq. (3.1.17) is a solution of the wave equation for a source point at x, y, z, with

$$\nabla^2 G + k^2 G = \delta(x' - x, y' - y, z' - z) \tag{3.1.19}$$

where x', y', and z' are now the independent variables, so all differentiations are with respect to the variables x', y', and z'. The function $\delta(x' - x, y' - y, z' - z)$ is the three-dimensional Dirac delta function, which satisfies the equation

$$\int_{-\infty}^{\infty}\int_{-\infty}^{\infty}\int_{-\infty}^{\infty} \delta(x' - x, y' - y, z' - z)\, dx'\, dy'\, dz' = 1 \tag{3.1.20}$$

with $\delta(x' - x, y' - y, z' - z) \to \infty$ as $R \to 0$.

Equation (3.1.17) satisfies the boundary conditions at infinity and corresponds to a wave propagating outward from the point x, y, z. The function G is called the *free-space Green's function.* To find the constant A, we integrate Eq. (3.1.19) over a small sphere of radius a, enclosing the point x, y, z. Thus

$$\int_{a\to 0} (\nabla^2 G + k^2 G)\, dV = 1 \tag{3.1.21}$$

Using Gauss's theorem, it follows that the first term in the integrand becomes

$$\int_{s_a} \nabla G \cdot \mathbf{n}\, ds = -4\pi A \tag{3.1.22}$$

where s_a is the surface of the sphere. The second term in the integrand becomes

$$k^2 \int_{a\to 0} G\, dV = 4\pi k^2 A \int_{a\to 0} \frac{1}{R} R^2\, dR = 0 \tag{3.1.23}$$

It is apparent, therefore, that as $a \to 0$, $A \to -1/4\pi$. Thus the free-space Green's function is

$$G = \frac{-e^{-jkR}}{4\pi R} \tag{3.1.24}$$

Helmholtz's theorem. We want to find a solution for the potential at a point due to excitation by a transducer. We shall show that this is mathematically equivalent to finding the general solution for ϕ at any point, given ϕ and $\nabla\phi$ on a surface surrounding the point x, y, z. To do this, we consider the solutions of

the wave equation

$$\nabla^2\phi + k^2\phi = 0 \tag{3.1.25}$$

We now use Green's theorem: We multiply Eq. (3.1.25) by G and subtract the result from the product of Eq. (3.1.19) with ϕ. We integrate the resulting expression over an arbitrary volume V, using the relation $\int \phi(x', y', z')\delta(x' - x, y' - y, z' - z)\, dV' = \phi(x, y, z)$, to obtain the formula

$$\begin{aligned}\phi(x, y, z) &= \int_{V'} (\phi\nabla'^2 G - G\nabla'^2\phi)\, dV' \\ &= \int_{V'} \nabla' \cdot (\phi\nabla' G - G\nabla'\phi)\, dV'\end{aligned} \tag{3.1.26}$$

where now we have used the $'$ superscript to make it clear that we are differentiating with respect to the variables x', y', and z'. By applying Gauss's theorem to the integral of Eq. (3.1.26), we see that

$$\phi(x, y, z) = \int_{s'} (\phi\nabla' G - G\nabla'\phi) \cdot \mathbf{n}\, ds' \tag{3.1.27}$$

where s' is any surface enclosing the point x, y, z and $\mathbf{n}$ is the outward normal from the volume V. Substituting the solution we have already found for G [Eq. (3.1.24)] in Eq. (3.1.27), we see that we can determine ϕ at any point if we know ϕ and $\nabla\phi$ on the surrounding surface. This result is known as *Helmholtz's integral theorem*.

Sommerfeld radiation condition. Now consider a piston transducer of area S_1 in a baffle of area S_2, as illustrated in Fig. 3.1.1. Let the rest of the enclosing surface of the volume considered be called Σ and let $R \to \infty$ as $z \to \infty$.

When $R \to \infty$, then $\phi \to (\exp -jkR)/R$, as does G. In this case, the contribution to the integral of Eq. (3.1.27) becomes zero on Σ, because the two terms in the integrand cancel out. Therefore, we can ignore contributions to the integral from the surface at infinity; this assumption is known as the *Sommerfeld radiation condition*.

Kirchhoff formula. We assume that both ϕ and $\nabla\phi \cdot \mathbf{n}$ are zero on the baffle. This is equivalent to assuming that in a liquid, both the pressure and normal displacement are zero on the baffle. Under these conditions, we can write Eq. (3.1.27) in the form

$$\phi(x, y, z) = \int_{S_1} (\phi\nabla' G - G\nabla'\phi) \cdot \mathbf{n}\, ds' \tag{3.1.28}$$

where $\mathbf{n}$ is the normal pointing *into* the transducer and S_1 is the area of the transducer. Therefore, if both ϕ and $\nabla\phi \cdot \mathbf{n}$ are specified at the transducer, then $\phi(x, y, z)$ can be found by using the value of G given in Eq. (3.1.24).

The Kirchhoff formula of Eq. (3.1.28) is useful and often employed in prac-

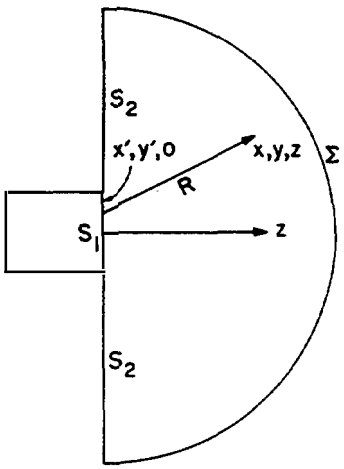

Figure 3.1.1 Piston transducer enclosed in a baffle.

tice; it is not rigorously correct, however, because it cannot be self-consistent, since ϕ and $\nabla\phi \cdot \mathbf{n}$ cannot be specified independently everywhere on the enclosing surface. For example, if $\phi = 0$ on a flat baffle at $z = 0$, and ϕ is finite on the transducer, then $\nabla\phi \cdot \mathbf{n}$ must be large near the edge of the transducer (i.e., there must be a fringing field). Mathematically, ϕ and $\nabla\phi \cdot \mathbf{n}$ cannot both be specified on all enclosing surfaces; this is an overspecification.

It is not even rigorously correct to specify ϕ and $\nabla\phi \cdot \mathbf{n}$ on the transducer. However, for transducers whose cross-sectional dimensions are several wavelengths, it is usually reasonable to employ the simple plane wave condition

$$\frac{\partial\phi}{\partial z} = -\frac{\partial\phi}{\partial z'} \approx -jk\phi \tag{3.1.29}$$

at the transducer, and take $\phi = \partial\phi/\partial z' = 0$ on S_2. We can then specify both ϕ and $\nabla\phi \cdot \mathbf{n}$ on S_1.

We expect these approximations to be valid if the cross-sectional dimensions of the transducer are more than several wavelengths; then the boundary conditions at the baffle are not very important and the use of Eq. (3.1.29) gives results close to the truth. The boundary conditions at the baffle become important only when the transducer is relatively narrow (e.g., less than a wavelength in extent). This happens, for instance, with the small elements of a transducer array used in acoustic imaging devices (see Sec. 3.5).

Rayleigh–Sommerfeld formula. Because we cannot specify both ϕ and $\partial\phi/\partial z'$, we observe that there are certain internal inconsistencies in the direct use of the Kirchhoff formula of Eq. (3.1.28). It is better, if we can, to use a formula in which only the potential or its gradient is specified on the boundary. To do this, we choose a different Green's function in Eq. (3.1.27), such that $G = 0$ or $\partial G/\partial z = 0$ on the transducer and its baffle. Then we need specify only $\partial\phi/\partial n$ or ϕ at the transducer.

Possible Green's functions for the fields at $z \leq 0$, which satisfy one of the required boundary conditions at the plane $z = 0$, are those due to a source

$\delta(x' - x, y' - y, z' - z)$ and its image $\delta(x' - x, y' - y, z' + z)$ in the plane $z = 0$. These Green's functions must have one of the following forms:

$$G = -\frac{1}{4\pi}\left(\frac{e^{-jkR_1}}{R_1} \pm \frac{e^{-jkR_2}}{R_2}\right) \tag{3.1.30}$$

where

$$R_1 = \sqrt{(z - z')^2 + (x - x')^2 + (y - y')^2} \tag{3.1.31}$$

and

$$R_2 = \sqrt{(z + z')^2 + (x - x')^2 + (y - y')^2} \tag{3.1.32}$$

We observe that the Green's function with the positive sign in Eq. (3.1.30) obeys the boundary condition $\partial G/\partial z' = 0$ at $z' = 0$, while that with the negative sign obeys the boundary condition $G = 0$ at $z' = 0$.

Rigid baffle. The first choice of Green's function, with a positive sign, in Eq. (3.1.30) yields a solution for the potential at any point ($z \geq 0$) in the form

$$\phi(x, y, z) = -\frac{1}{2\pi}\int_s u_z(x', y', 0)\frac{e^{-jkR}}{R}\,ds' \tag{3.1.33}$$

where the integral is taken over the area of the transducer and it is assumed that $u_z = 0$ outside the transducer (i.e., on the baffle). Thus this choice of Green's function is rigorously correct for a flat piston transducer surrounded by a rigid baffle.

Pressure release baffle. The second choice of Green's function, with a negative sign, in Eq. (3.1.30) yields a solution for the potential at any point ($z \geq 0$) in the form

$$\phi(x, y, z) = \frac{jk}{2\pi}\int_s \phi(x', y', 0)\frac{e^{-jkR}(1 + 1/jkR)\cos\theta}{R}\,ds' \tag{3.1.34}$$

where θ is the angle between the radius vector $\mathbf{R}$ and the z axis.

Normally, we are interested in regions several wavelengths from the transducer. In this case we can assume that $kR >> 1$ and write Eq. (3.1.34) in the Huygens–Fresnel form:

$$\phi(x, y, z) = \frac{jk}{2\pi}\int_s \phi(x', y', 0)\frac{e^{-jkR}}{R}\cos\theta\,ds' \tag{3.1.35}$$

Note that the choice of Green's function used in Eqs. (3.1.34) and (3.1.35) implies that it is convenient to assume that $\phi(x', y') = 0$ on the baffle. Thus for waves excited in a liquid, Eq. (3.1.34) or (3.1.35) apply to a transducer for which the pressure is zero on the $z = 0$ plane outside the transducer (i.e., the *pressure release baffle*). The results of Eq. (3.1.34) or (3.1.35) are not exact for waves in a solid unless it is assumed that $\phi = 0$ on the plane outside the transducer. This zero

potential assumption is equivalent to assuming, for a liquid, that normal stress is zero on the plane $z = 0$ outside the transducer. But zero longitudinal wave potential does not imply zero stress in a solid, although this is probably a fairly reasonable approximation at the baffle for most practical cases.

Transient source. The similar expressions for a source $u_z(x', y', 0)$ or $\phi(x', y', 0)$, which vary arbitrarily with time, can be found by taking the Fourier or Laplace transform of either Eq. (3.1.33) or Eq. (3.1.35). The result for a transducer in a rigid baffle is

$$\phi(t, x, y, z) = -\frac{1}{2\pi} \int_s \frac{1}{R} u_z \left(t - \frac{R}{V} \right) ds' \tag{3.1.36}$$

where u_z is given at the point $x', y', 0$.

It follows that if $u_z(x', y', 0)$ or $\phi(x', y', 0)$ is known at a transducer surface and, correspondingly, $u_z(x', y', 0)$ or $\phi(x', y', 0)$ is zero on the surrounding baffle, it is possible to find the potential at any point x, y, z.

PROBLEM SET 3.1

1. Writing the impedance Z for a spherical wave in the form $Z = R + jX$, plot R/Z_0 and X/Z_0 as a function of kR from $kR = 0$ to 10. At what values of R/λ is $|Z|$ within 10% and 1% of Z_0? You will see from your results that reactive impedance effects are important only for very small transducers or very near the edge of large transducers.
2. Use Eq. (3.1.33) to work out general integral formulas for the values of u_z, u_x, and u_y excited by a planar transducer that is surrounded by a rigid baffle.
3. Assuming that a transducer is infinite in extent in the y direction and that the fields are uniform with y, work out from Eq. (3.1.33) a general formula for the potential at x, z when $u_z(x', 0)$ is known. You will find it convenient to write $R = [r^2 + (y - y')^2]^{1/2}$ with $r = [z^2 + (x' - x)^2]^{1/2}$ and $t = (y' - y)/r$. You will need the relation

$$H_0^{(2)}(\alpha) = \frac{2j}{\pi} \int_0^\infty \frac{e^{-j\alpha(1+t^2)^{1/2}}}{(1 + t^2)^{1/2}} dt$$

where $H_0^{(2)}(\alpha)$ is a zeroth-order Hankel function of the second kind. The asymptotic form of this Bessel function ($\alpha >> 1$) is

$$H_0^{(2)}(\alpha) \sim j \frac{1 - j}{\sqrt{\pi\alpha}} e^{-j\alpha}$$

Find the form of $\phi(x, z)$ for arbitrary values of kr and for the case, normally of most practical interest, when $kr >> 1$.

Answer:

$$\phi(r) = \frac{j - 1}{2\sqrt{\pi}} \int u_z(x', 0) \frac{e^{-jkr}}{\sqrt{kr}} dx'$$

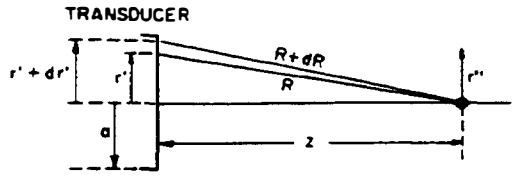

Figure 3.2.1 Notation used in the diffraction theory for the plane piston transducer.

3.2 PLANE PISTON TRANSDUCERS

3.2.1 Fields on the Axis

We will use the results of Sec. 3.1.2 to derive the field on the axis of a cylindrical plane piston transducer. We assume that the displacement at the face of the transducer $u_z(r, 0) = u_0$ to be uniform over its radius and zero outside it. We consider the piston transducer of radius a to be radiating into a liquid. Our results will also be valid for radiation into an isotropic solid if we use the same boundary conditions at $z = 0$ on the potential gradient $\partial\phi/\partial z$. The excitation at a distance R from a ring of radius r' to $r' + dr'$ on the transducer, as illustrated in Fig. 3.2.1, is given by Eq. (3.1.33). Thus the amplitude of a wave at point z on the axis is

$$\phi(0, z) = -u_0 \int_{r'=0}^{a} \frac{e^{-jkR}}{R} r'\, dr' \tag{3.2.1}$$

The assumption that $u_z = 0$ outside the radius a of the transducer is equivalent to assuming that the transducer is placed in a rigid baffle.

Using the relations $R^2 = r'^2 + z^2$ and $R\, dR = r'\, dr'$, we find that

$$\begin{aligned} \phi(0, z) &= -u_0 \int_{r'=0}^{a} e^{-jkR}\, dR \\ &= \frac{u_0 e^{-jkR}}{jk}\Bigg|_{r'=0}^{a} \end{aligned} \tag{3.2.2}$$

Thus

$$\begin{aligned} \phi(0, z) &= \frac{u_0}{jk}\left[e^{-jk(a^2+z^2)^{1/2}} - e^{-jkz}\right] \\ &= -\frac{2}{k} u_0 \sin k\left(\frac{\sqrt{a^2+z^2} - z}{2}\right) e^{-jk[(a^2+z^2)^{1/2}+z]/2} \end{aligned} \tag{3.2.3}$$

By differentiating this equation with respect to z, we can show that

$$u_z(0, z) = u_0\left[e^{-jkz} - \frac{z}{(a^2 + z^2)^{1/2}} e^{-jk(a^2+z^2)^{1/2}}\right] \tag{3.2.4}$$

This formula reduces to $u_z = u_0$ at $z = 0$, while the magnitude of $\phi(0, z)$ on the axis is $(2/k)u_z(0)\,|\sin(ka/2)|$. As we shall see later, $u_z(r, z)$ and $\phi(r, z)$ vary rapidly with radius near the transducer.

Fresnel or paraxial approximation. If $z^2 >> a^2$, we can use the *Fresnel approximation* or *paraxial approximation* and expand the square roots in the phase-varying terms of Eq. (3.2.4) to first order in a^2/z^2, while keeping only the zeroth-order terms in a^2/z^2 in the amplitude. In this case, we use Eq. (3.1.8) to write Eq. (3.2.4) in the approximate form.†

$$\begin{aligned} \frac{-T_3(0, z)}{Z_0} \approx v_z(0, z) &\approx -v_0 e^{-jk[z + (a^2/2z)]} - e^{-jkz} \\ &= 2jv_0 e^{-jkz} \sin \frac{\pi a^2}{2z\lambda} e^{-j\pi a^2/2z\lambda} \end{aligned} \tag{3.2.5}$$

where $k = 2\pi/\lambda$, $T_3(0, z) \approx c_{11}\partial u_z(0, z)/\partial z$, $v_0 = j\omega u_0$, $v_z = j\omega u_z$ is the particle velocity, $T_3(0, z)$ is the stress on axis in the z direction, and Z_0 is the impedance per unit area of the medium.

We assume that the average power intensity is $I(0)$ at the surface of the transducer and that $I(0) \approx Z_0|v_0^2|/2$. The power intensity at the axis, $I(z) = Z_0|V_z^2|/2$, can then be written in the form

$$\begin{aligned} I(z) &= 4I(0) \sin^2 \frac{\pi a^2}{2\lambda z} \\ &= 4I(0) \sin^2 \frac{\pi}{2S} \end{aligned} \tag{3.2.6}$$

where we define a normalized parameter, *the Fresnel parameter*, by the relation

$$S = \frac{z\lambda}{a^2} \tag{3.2.7}$$

Fraunhofer and Fresnel zone. The region for which $z >> a^2/\lambda$ or $S >> 1$ is called the far-field region or the *Fraunhofer zone*. When $S >> 1$, it follows from Eq. (3.2.6) that the power intensity at the axis, $I(z)$, is

$$I(z) \approx \left(\frac{\pi a^2}{\lambda z}\right)^2 I(0) = \left(\frac{\pi}{S}\right)^2 I(0) \tag{3.2.8}$$

In the Fraunhofer zone, where $S >> 1$, $I(z)$ decreases as $1/z^2$.

The region for which $z < a^2/\lambda$ or $S < 1$ is called the *Fresnel zone*. In this case, the signal potential ϕ is maximum on the axis where the argument of the sine term in Eq. (3.2.6) or, more exactly, the argument of the sine term in Eq. (3.2.3), is $(2m + 1)\pi/2$. From Eq. (3.2.3), it follows that the value of z at the point where the potential is maximum is

$$\begin{aligned} z = z_{max} &= \frac{a^2}{(2m + 1)\lambda} - \frac{(2m + 1)\lambda}{4} \\ &\approx \frac{a^2}{(2m + 1)\lambda} \qquad [ka >> (2m + 1)\pi] \end{aligned} \tag{3.2.9}$$

† Note that this approximation is valid only for $ka >> 1$. An example illustrating this point is given in Eq. (3.2.9) and the discussion following it.

The approximate form of the second line of Eq. (3.2.9) is equivalent to using Eq. (3.2.5) or Eq. (3.2.6). So the Fresnel approximation tends to be valid for very large values of ka (i.e., when the transducer diameter is many wavelengths).

The Fresnel approximation form of Eq. (3.2.9) can be written in terms of the Fresnel parameter S, as follows:

$$S = S_{max} = \frac{1}{2m + 1} \tag{3.2.10}$$

At the point where $z = z_{max}$, the amplitude $|v_z(z)/v_z(0)| = 2$ (i.e., v_z is double its average value at the transducer). The velocity v_z is zero at z_{min}, where

$$z = z_{min} = \frac{a^2}{2m\lambda} \qquad (ka >> 2m\pi) \tag{3.2.11}$$

or

$$S = S_{min} = \frac{1}{2m} \tag{3.2.12}$$

Note that the axial fields vary rapidly with distance for small z. This is because $kR = k(r^2 + z^2)^{1/2}$ varies rapidly with radius when z is small, for the contributions from each ring element of the transducer alternately add and subtract. For large R, however, where

$$R = z\left(\frac{1 + r^2}{z^2}\right)^{1/2} \approx z + \frac{r^2}{2z} \tag{3.2.13}$$

there is only a small variation of kR with r, so that all the contributions from the disk add. This occurs when $a^2/2z < \lambda/2$ (i.e., there is less than a half-wavelength difference in length between the rays) or $S > 1$.

The condition $z = a^2/\lambda$ or $S = 1$ corresponds exactly to the condition $m = 0$ (the last maximum) in Eq. (3.2.10). We call this point, $S = 1$, the crossover point between the Fresnel and Fraunhofer zones, or the *Fresnel limit*. Within the Fresnel zone, we expect to see the displacement vary rapidly with radius. Outside the radius a, however, the fields fall rapidly to zero (i.e., most of the energy is contained within the radius a). Thus if $z < a^2/\lambda$ or $S < 1$, the beam is essentially confined within its original diameter. Now suppose that we use another transducer of the same size to detect the transmitted signal. In this case the rapid variations of the field over the diameter of the receiving transducer wash out and the signal received by the receiving transducer varies very little within the Fresnel zone (see Fig. 3.2.7). This is equally true when one transducer is used as a receiver and transmitter of a perfectly reflected signal, provided that the total path length of the beam is less than a^2/λ.

Beyond the region $z = a^2/\lambda$ or $S = 1$, Eq. (3.2.8) shows that the intensity falls off monotonically as $1/z^2$ and, on axis, drops to the value at the transducer only when $z = \pi a^2/\lambda$ or $S = \pi$. A plot of $|u_z(0, z)|$ is given as a function of $S = z\lambda/a^2$ in Fig. 3.2.2 for a value of $ka = 100$, which is equivalent to $a/\lambda \approx 16$ or $z/\lambda \approx 16$ at $S = 1$. This plot is obtained from the exact solution of Eq. (3.2.2)

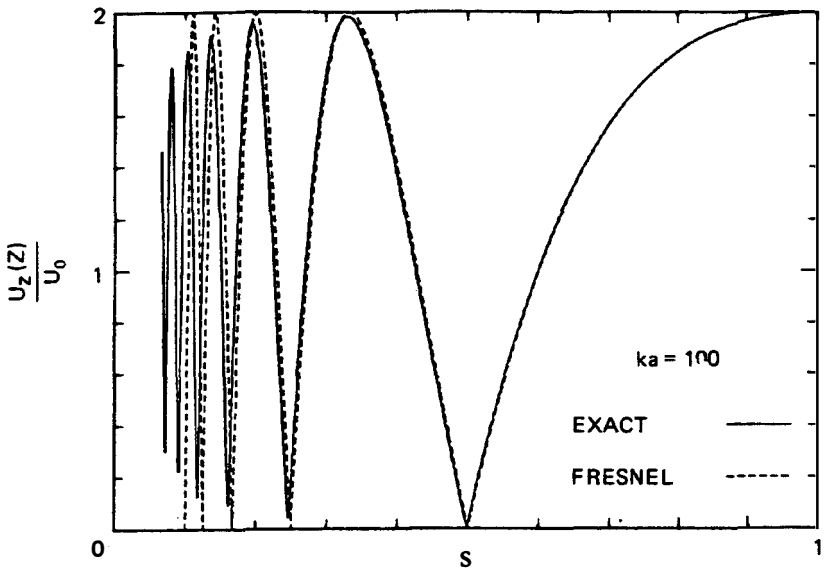

Figure 3.2.2 Plot of the variation of the normalized axial displacement field $|u_z(0, z)/u_0|$ as a function of normalized distance $S = z\lambda/a^2$.

while the dashed line in Fig. 3.2.2 is a plot for the approximate solution of Eq. (3.2.5) (the Fresnel approximation). Thus the maximum values of $|(u_z(0, z)|$ for small values of S are less than 2 and the minimum values are greater than zero but approach the appropriate paraxial or Fresnel solution as S is increased. It is convenient, and often accurate enough, to use the Fresnel approximation, because the results can be expressed in terms of only one parameter S. It is a universal solution that is valid for the values of ka used in many practical transducers employed in isotropic media, and it is easier to compute the solutions for points off-axis than to use the exact form for the solution. Further plots of the field variation on- and off-axis are given in Figs. 3.2.3 and 3.2.4. These plots are derived by the methods given in Sec. 3.2.2.

Fraunhofer approximation. In the Fraunhofer region, we assume from the start that $z >> a$, and we can use a simple analysis appropriate to the Fraunhofer zone to find the fields off-axis [2]. As illustrated in Fig. 3.2.5, we write the coordinates of a point in spherical coordinates, as r, θ, ψ, where $r = 0$ at the center of the transducer and $\theta = 0$ on the z axis. Initially, it is convenient to work in cylindrical coordinates, with the cylindrical coordinates of a point at r'', z, ψ corresponding to a point at r, θ, ψ in spherical coordinates, and with r', 0, ψ' the cylindrical coordinates of a point at the transducer surface. At a plane z, an element of area on the transducer at the point r', 0, ψ' is a distance R from the point r'', z, ψ, where

$$R_1^2 = r'^2 + r''^2 - 2r'r'' \cos(\psi - \psi') \tag{3.2.14}$$

and

$$R = \sqrt{R_1^2 + z^2} = \sqrt{z^2 + r'^2 + r''^2 - 2r'r'' \cos(\psi - \psi')} \tag{3.2.15}$$

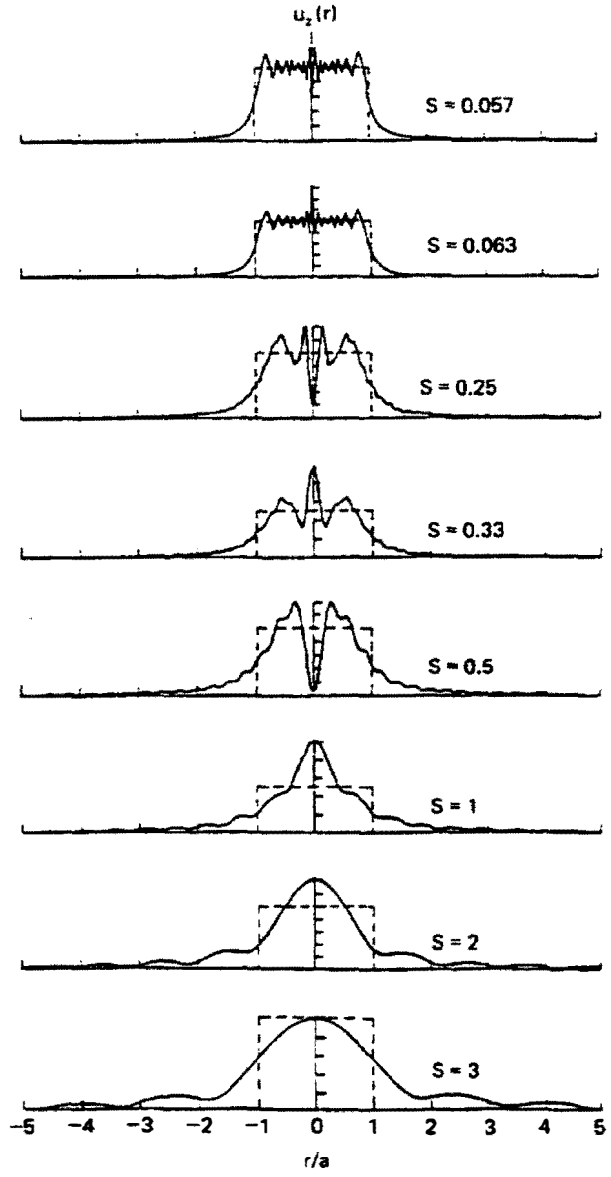

Figure 3.2.3 Radial variation of displacement $u_z(r, z)$ for $ka = 100$, plotted for different values of $S = z\lambda/a^2$ [dashed lines, value of $u_z(r, 0)$ at the transducer].

If we write $z^2 + r'^2 = r^2$ and $r' = r \sin \theta$, Eq. (3.2.15) becomes

$$R = \sqrt{r^2 + r'^2 - 2rr' \sin \theta \cos (\psi - \psi')} \tag{3.2.16}$$

In the Fraunhofer approximation, we assume that $r' << r$ and that only first order terms in r' are kept in the Taylor expansion. This yields the result

$$R \approx r - r' \sin \theta \cos (\psi - \psi') \tag{3.2.17}$$

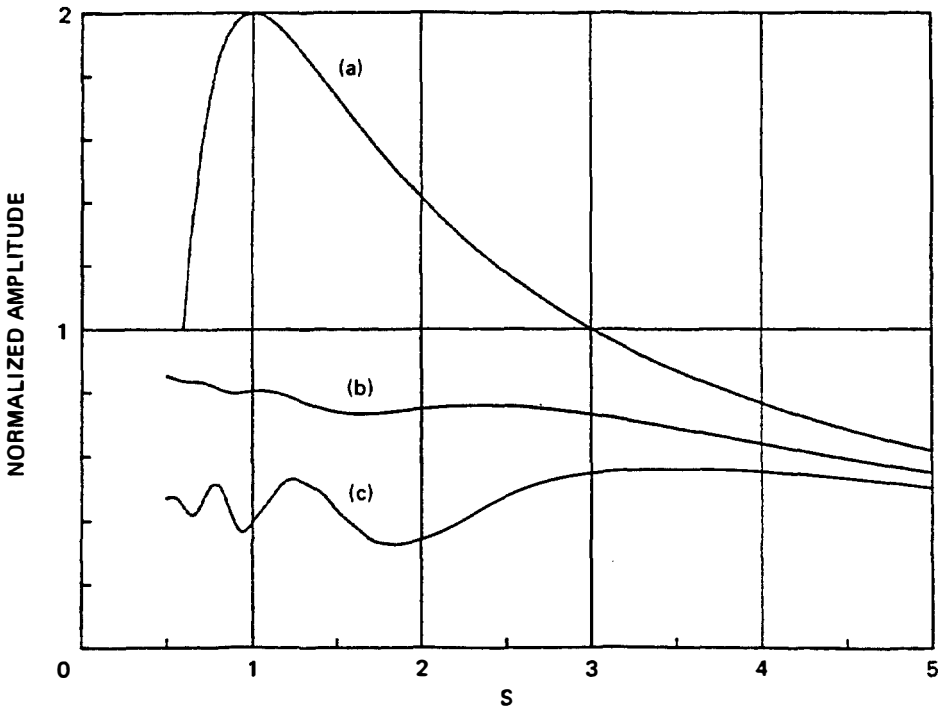

Figure 3.2.4 Plots of amplitude of the signal emitted by a transducer of radius a as a function of $S = z\lambda/a^2$: (a) ratio of the amplitude on axis $u_z(0, z)/u_z(0)$ to the average amplitude at the transducer; (b) ratio of the average amplitude at a receiving transducer, of the parameter $\bar{u}_z\ (r,z)/u_z(0)$ to the amplitude at the transmitter (averaged over the face of a receiving transducer of radius a); (c) ratio of the amplitude at $r = a$ to the average amplitude at the transmitter $u_z(a, z)/u_z(0)$.

From Eq. (3.1.33), the contribution to the field at r, θ, 0 is

$$\phi(r, \theta) = -\frac{u_0}{2\pi}\int_{\psi=0}^{2\pi}\int_{r'=0}^{a}\frac{e^{-jkR}}{R}\,r'\,d\psi'\,dr' \tag{3.2.18}$$

If we take account only of the effect of the change in r on the phase term, and put $R = r$ in the denominator of Eq. (3.2.18), then

$$\phi(r, \theta) = -\frac{e^{-jkr}u_0}{2\pi r}\int_{\psi=0}^{2\pi}\int_{r'=0}^{a}e^{jkr'\sin\theta\cos(\psi-\psi')}\,r'\,dr'\,d\psi' \tag{3.2.19}$$

We use the Bessel function identity

$$J_0(z) = \frac{1}{2\pi}\int_0^{2\pi}e^{jz\cos\psi}d\psi \tag{3.2.20}$$

where $J_0(z)$ is a Bessel function of the first kind of zeroth order. Then it follows that

$$\phi(r, \theta) = -\frac{u_0}{r}e^{-jkr}\int_0^a r'J_0(kr'\sin\theta)\,dr' \tag{3.2.21}$$

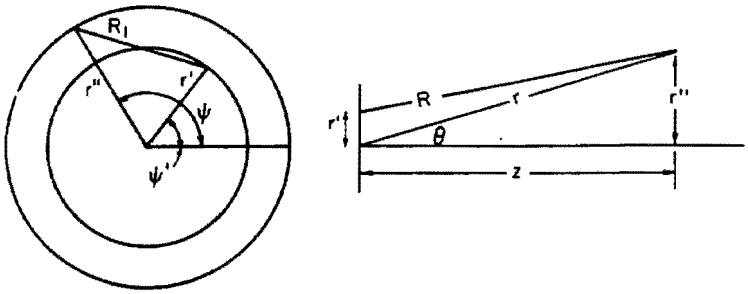

Figure 3.2.5 Notation used for Fraunhofer diffraction theory.

Using the relation $\int z J_0(z)\, dz = zJ_1(z)$, where $J_1(z)$ is a first-order Bessel function, we obtain the result

$$\phi(\quad \theta) = -\frac{a^2}{r}\frac{J_1(ka \sin \theta)}{ka \sin \theta} e^{-jkr} u_0 \tag{3.2.22}$$

It follows that the power intensity $I(r, \theta)$ at r, θ, with a power intensity $I(0)$ at the transducer, is

$$I(r, \theta) \approx \left(\frac{\pi a^2}{\lambda r}\right)^2 \text{jinc}^2 \left(\frac{a \sin \theta}{\lambda}\right) I(0) \tag{3.2.23}$$

where jinc $X = J_1(2\pi X)/\pi X$. The functions jinc X and jinc^2 X are plotted in Fig. 3.2.6.†

If $\theta = 0$, then $I(r, 0) \approx (\pi a^2/\lambda z^2) I(0)$, which agrees with Eq. (3.2.8). Where $J_1(ka \sin \theta) = 0$, $I(r, \theta) = 0$. The first zero is where $ka \sin \theta = 3.83$. When $ka >> 1$ or $a >> \lambda$, then $\theta = \theta(\text{zero})$ is small and

$$\theta(\text{zero}) = \frac{0.61\lambda}{a} \tag{3.2.24}$$

On the same basis, the amplitude of the signal drops by 3 dB at the point

$$\theta(3 \text{ dB}) \approx \frac{0.25\ \lambda}{a} \tag{3.2.25}$$

This is the extent of the first lobe of the beam, which is called the *main lobe*. There are also minor sidelobes for larger values of θ.

Note that at the plane $z = a^2/\lambda$ ($S = 1$), Eq. (3.2.25) predicts that at a radius $r'' = 0.25a$, the field will be reduced in amplitude by 3 dB from the axial field. Thus, on this approximate basis at $z = a^2/\lambda$, a cylindrical beam is confined to an area smaller than its original size. More exact calculations, given in the next section and plotted in Fig. 3.2.3, indicate that at $z = a^2/\lambda$, the 3-dB point is at $r'' \approx 0.35a$.

We conclude that for $z < a^2/\lambda$, the acoustic beam tends to remain confined to its original radius. Beyond this point, its intensity varies with θ and several lobes appear in the radiation pattern. In the Fraunhofer region, the intensity $I(r)$ falls off as I/r^2.

† Note that there is no established convention for the normalization of jinc X. Here we have chosen a normalization that makes its value 1 at $X = 0$.

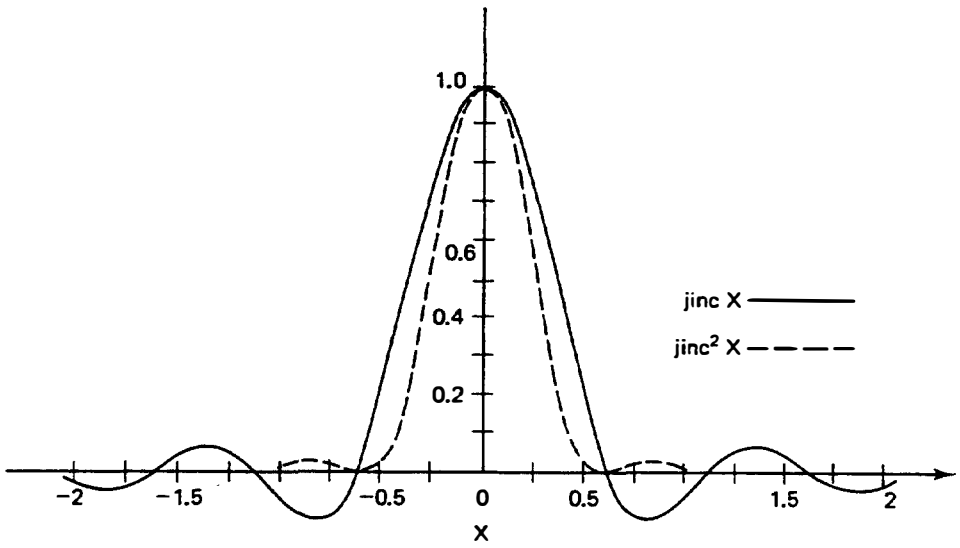

Figure 3.2.6 Plot of jinc X and jinc^2 X where jinc $X = J_1(2\pi X)/\pi X$.

If the transducer is surrounded by a pressure release baffle (zero impedance), we can find a result equivalent to Eq. (3.2.23) by using Eq. (3.1.35) to obtain

$$I(r, \theta) \approx I(0)\left[\frac{\pi a^2}{\lambda r} \text{ jinc } \left(\frac{a}{\lambda} \sin \theta\right) \cos \theta\right]^2 \tag{3.2.26}$$

Thus even an infinitesimal radius transducer, with jinc $(a \sin \theta/\lambda) = 1$, in a pressure release baffle has an angular response with its 3-dB points at $\theta = 45°$.

We have now discussed the differences between the behavior of a transducer in a rigid baffle and that of one in a pressure baffle. An example of a transducer in a rigid baffle would be a transducer in water, surrounded by a metal disk whose impedance is much higher than that of water. An example of a transducer in a pressure release baffle would be a small transducer, or one element of an array of identical transducers, spaced by a distance of a wavelength or more from each other, separated from a water bath by a Mylar film, so that there is water on one side of the film and air on the other. In practice, the behavior of a transducer array depends on the spacing between the array elements. Thus the angular response of a transducer array element may lie between the response of a transducer in a pressure release baffle and that of a transducer in a rigid baffle [3].

3.2.2 Radial Variation of the Field Using a Hankel Transform and Spatial Frequency Concepts

The theory we have given so far can be extended to deal with the radial variation of the fields. However, it is often more convenient to derive the necessary results by using Fourier transform or Hankel transform methods [2].

The basic idea, stated in terms of a rectangular coordinate system, is to carry out a spatial Fourier transform in x, y coordinates of the fields at the transducer.

This determines the excitation of the plane wave components with transverse propagation constants k_x and k_y, in the x and y directions, respectively. By analogy to Fourier transformation in the time domain, k_x and k_y are called the *transverse spatial frequencies*. The contributions of the propagating plane waves are summed at the plane z and an inverse transform is carried out to determine the fields at that plane. The process is entirely equivalent in cyclindrical coordinates, except that here we call the transverse propagation constant α where $k_r = \alpha$, make use of cylindrical symmetry, and employ Hankel transforms.

A spherically symmetric solution of the longitudinal wave equation in cylindrical coordinates (r, θ, z), for waves that vary as exp $(j\omega t)$, is

$$\phi(\alpha r, \beta z) = A(\alpha) J_0(\alpha r) e^{-j\beta z} \tag{3.2.27}$$

By analogy to Fourier transformation in the time domain, the parameters α and β are called the *radial* and *axial spatial frequencies*, respectively. By differentiating Eq. (3.2.27) with respect to z, for waves in a liquid, we can write

$$u_z(\alpha r, \beta z) = -j\beta A(\alpha) J_0(\alpha r) e^{-j\beta z} \tag{3.2.28}$$

where $J_0(x)$ is a Bessel function of zeroth order of the first kind and

$$\beta^2 + \alpha^2 = k^2 \tag{3.2.29}$$

In general, β may be real or imaginary. We can also use this formulation for solid materials by neglecting contributions from the shear wave potential term ψ_θ; this assumption will be discussed more fully in Sec. 3.2.3. We write the complete spatial solutions for $u_z(r, z)$ in the form

$$u_z(r, z) = -\int_0^\infty j\beta A(\alpha) e^{-j\beta z} J_0(\alpha r)\, d\alpha \tag{3.2.30}$$

The definition of the Hankel transform of a function $g(r)$ is

$$G(\alpha) = \int_0^\infty g(r) J_0(\alpha r) r\, dr \tag{3.2.31}$$

where

$$g(r) = \int_0^\infty G(\alpha) J_0(\alpha r) \alpha\, d\alpha \tag{3.2.32}$$

Therefore, at $z = 0$, it follows from Eqs. (3.2.30)–(3.2.32) that

$$\text{———} \qquad \int_0^a u_z(r, 0) J_0(\alpha r) r\, dr \tag{3.2.33}$$

where $A(\alpha)$ is the amplitude of the term with a radial spatial frequency α, and $u_z(r, 0)$ is only finite from 0 to a. For a cylindrical piston transducer, $u_z(r, 0) = u_0$ and is uniform. Integrating Eq. (3.2.33) and using the identity $xJ_1(x) = \int xJ_0(x)\, dx$ yields the result

$$-j\beta A(\alpha) = u_0 a J_1(\alpha a) \tag{3.2.34}$$

where $J_1(x)$ is a Bessel function of the first order of the first kind. Hence, at any plane z, it follows from Eqs. (3.2.30) and (3.2.34) that

$$u_z(r, z) = au_0 \int_0^\infty J_1(\alpha a)J_0(\alpha r)e^{-j\beta z}\, d\alpha \tag{3.2.35}$$

We can find $u_z(r, z)$ at any point r, z from this relation. We can also find the average value of $u_z(r, z)$ over a radius a, which is proportional to the signal detected by another transducer of radius a. If we call this quantity $\overline{u_z(r, z)} = (2/a^2) \int_0^a u_z(r, z)r\, dr$, the signal detected by a second identical and ideal transducer, which is perfectly matched to the propagating medium, is

$$\overline{u_z(r, z)} = 2u_0 \int_0^\infty \frac{J_1^2(\alpha a)}{\alpha} e^{-j\beta z}\, d\alpha \tag{3.2.36}$$

It follows, by using the relation

$$\int_0^\infty \frac{J_1^2(\alpha x)}{\alpha}\, d\alpha = \frac{1}{2} \tag{3.2.37}$$

that $\overline{u_z(r, 0)} = u_0$, as it should. Note that we can also find the longitudinal wave contribution to the pressure, as well as any other parameter of interest, by extending this formulation.

It is often convenient to normalize these formulas in terms of the Fresnel parameter $S = z\lambda/a^2$, and, in addition, to use the equivalent of the Fresnel or paraxial approximation. This makes it possible to express the results in terms of only one variable, S. We put $\alpha a = Y$ and write

$$\beta = \sqrt{k^2 - \alpha^2} \approx k - \frac{\alpha^2}{2k} \tag{3.2.38}$$

This approximation, which is discussed more fully in Sec. 3.2.3, implies that only waves propagating at small angles to the axis contribute to the total field.

Equations (3.2.35) and (3.3.36) reduce, respectively, to the following normalized forms:

$$u_z(r, z) = u_0 e^{-jkz} \int_0^\infty J_1(Y)J_0\frac{rY}{a} e^{jY^2S/4\pi}\, dY \tag{3.2.39}$$

The average value of $u_z(r, z)$ in a radius a is

$$\frac{\overline{u_z(r, z)}}{u_0} = 2e^{-jkz} \int_0^\infty \frac{J_1^2(Y)}{Y} e^{jY^2S/4\pi}\, dY \tag{3.2.40}$$

It is not necessary, in principle, to use the assumption of Eq. (3.2.38) to obtain analogous results in Eqs. (3.2.39) and (3.2.40) (see Prob. 6), but the advantage of this procedure is that the results can be normalized and then expressed in terms of one curve. Otherwise, we must use the two parameters ka and S to specify the problem. The radial variation of $u_z(r, z)$ has been plotted in Fig. 3.2.3 from the exact solution for various values of the parameter $S = z\lambda/a^2$ and a value

of $ka = 100$, which corresponds to $z/a = a/\lambda \approx 16$ when $S = 1$. This value of ka is comparable to that for a typical transducer used in medical applications (19 mm diameter for use at 2.25 MHz, giving $a/\lambda \approx 14$).

The radial variation of $u_z(r, z)$ exhibits sharp maxima and minima near the axis, as we would expect from the theory given in Sec. 3.2.1. Near the transducer, the Fresnel ripples (i.e., the radial variations) are relatively rapid and the beam is well confined to its original diameter. At $S = 1$, the effective beam diameter at the 3-dB points is reduced to approximately 0.35 of its original diameter. The beam expands beyond this point until its effective diameter reaches the original diameter, although a considerable portion of the energy remains outside the main beam near $S = 3$. The Fraunhofer theory predicts the positions of the lower-order maxima and minima in the beam even for $S = 1$, but they are not as well defined as in the simple theory.

In Figs. 3.2.4 and 3.2.7, we give plots alculated from Eqs. (3.2.39) and (3.2.40) of $u_z(0, z)/u_0$, $u_z(a, z)/u_0$, and $|u_z(r, z)|/u_0$ as a function of S. The latter parameter gives the diffraction loss between two identical transducers, spaced a distance z apart, that is often required for calibration [4]. If the beam is reflected from a perfect plane reflector at a plane z and received by the original transmitting transducer, the diffraction loss may be determined for these curves by replacing z with $2z$. In Fig. 3.2.7, we also give the correction ϕ_R, due to diffraction, to the phase of , is always

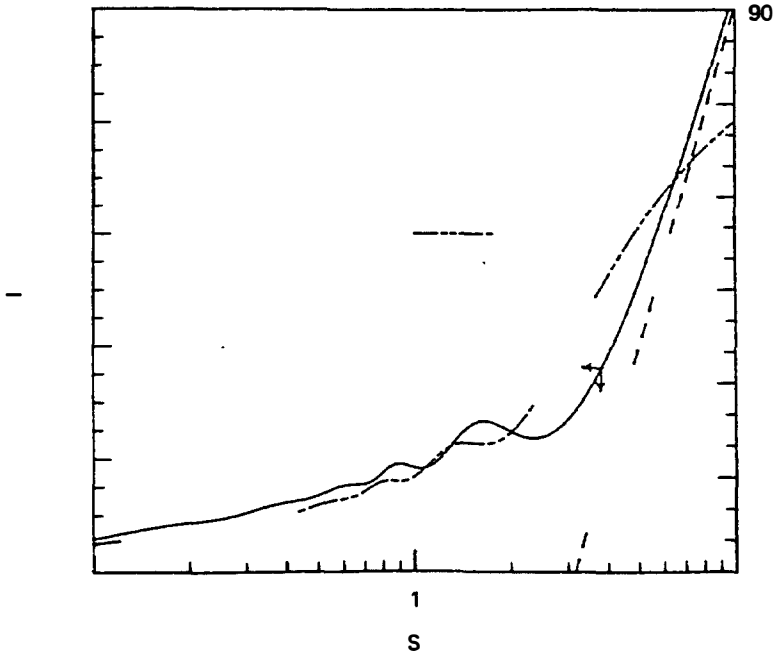

Figure 3.2.7 Diffraction loss and phase retardation between two equal-sized transducers of radius a spaced by a distance z ($S = z\lambda/a^2$). The phase retardation is $\phi_R = kz - \phi(\text{total})$, where $\phi(\text{total})$ is the total phase change between the two transducers. A comparison of the calculated loss with the simple Fraunhofer approximation (the dashed-line plot) is also given. For $S > 10$, this approximation is adequate for estimating the loss between transducers.

less than kz; ϕ_R must be known to make absolute velocity measurements based on measurement of phase.

Note that Figs. 3.2.4 and 3.2.7 are plotted using the paraxial or Fresnel approximation $\alpha^2 << k^2$. The use of this approximation makes it easy to calculate the result when the beam passes through several different media; the total value of S is determined by adding the values of S determined for each region, using the appropriate values of z and λ in these regions. The situation is somewhat more complicated when the interfaces occur in regions where the paraxial approximation does not hold. In this case, however, as the diffraction losses for $S < 1$ are normally small, the breakdown of the paraxial approximation in these regions may not matter too much.

Example: Piston Transducer for Probing the Human Body

Consider a transducer to be used for examining the human body by placing it in contact with the patient. The maximum depth required for examination is approximately 20 cm. As the attenuation in the body varies approximately linearly with frequency and is of the order of 1 dB/cm/MHz, the total attenuation of a reflected wave at a depth of 20 cm will be 40 dB/MHz. This tends to limit the maximum frequency employed. Typically, operating frequencies of 2 to 5 MHz are used in the diagnostic examination of adults; the higher frequencies in this range are employed for children, with frequencies as high as 20 MHz used for examination of the eye or near-surface features such as the carotid artery.

Suppose that we consider a 2.25-MHz transducer for which the acoustic wavelength is 0.67 mm ($V = 1.5 \times 10^5$ cm/s). If we choose the end of the operating range to be at $z = 3a^2/\lambda$, where the 3-dB beam diameter is comparable to that of the transducer, we find that the radius of the transducer is 0.67 cm, or that its diameter is 1.3 cm, approximately $\frac{1}{2}$ in. Thus, in medical practice, transducers of this diameter can provide a beam with a maximum excess loss, due to diffraction, of approximately 6 dB, after reflection from a flat plane and traveling a path $6a^2/\lambda$ long. The one-way diffraction loss in traveling a distance $3a^2/\lambda$ ($S = 3$) to the point of interest is, from Fig. 3.2.7, only 2.5 dB. The transverse definition of such a beam will also be better than 1.3 cm.

Note that small reflectors in the Fresnel region of the beam may not always be characterized correctly because the beam intensity is not uniform either over its cross section or along its length. For this reason, it is often advisable to sacrifice the advantage of greater beam intensity or definition obtained by operating in the Fresnel region, and to work in the Fraunhofer region instead. One or more transducers can be employed to observe specific regions, each designed with a radius such that $1 < S < 3$ where the beam has not spread too much, so that its intensity is relatively strong. This procedure is normally employed in quantitative nondestructive evaluation (NDE) of solid materials, where accurate calibrations are needed to determine the size and nature of a flaw.

3.2.3 Diffraction from Rectangular Transducers

The diffraction theory derived in the preceding section can also be adapted to rectangular systems. This is most conveniently accomplished by using a Fourier transform approach or a spatial frequency analysis that is analogous to the Hankel

transform theory already given for the cylindrical transducer. In this case, there is no simple analytical solution for the field variation along the central axis of a rectangular transducer, so the more general solution is employed.

The two-dimensional solutions we shall give here are applicable to: (1) rectangular transducers of finite width in the x direction, which are assumed to be infinitely long in the y direction; and (2) surface wave transducers of finite width, whose width is much larger than the Rayleigh wave wavelength. In the latter case, we assume that the surface wave field variation in the y direction remains invariant and that the ϕ and ψ_x potential variations in the x and z directions obey the wave equation

$$\frac{\partial^2 \phi}{\partial x^2} + \frac{\partial^2 \phi}{\partial z^2} + k_r^2 \phi = 0 \tag{3.2.41}$$

where k_r is the Rayleigh wave propagation constant. Thus we use the same formalism for surface waves as for the simple rectangular transducer, only replacing k by k_r and taking the propagation constant in the z direction to be β.

For any potential function $\phi(x, z)$, we can write

$$\phi(x, z) = \int_{-\infty}^{\infty} A(\alpha) e^{-j\beta z} e^{-j\alpha x} \, d\alpha \tag{3.2.42}$$

where $A(\alpha)$ is the amplitude of the spatial frequency component α. The parameters α and $A(\alpha)$ obey the relations

$$\beta^2 + \alpha^2 = k^2 \tag{3.2.43}$$

and

$$A(\alpha) = \frac{1}{2\pi} \int_{-\infty}^{\infty} \phi(x, 0) e^{j\alpha x} \, dx \tag{3.2.44}$$

respectively. For a transducer of width w, if ϕ is a longitudinal wave potential, then

$$u_z(\alpha, x, z) = -j\beta A(\alpha) e^{-j\beta z} e^{j\alpha x} \tag{3.2.45}$$

More generally, the surface wave displacement component $u_z(x, y, z)$ depends on both ϕ and ψ_x. At any plane y below the surface we can write

$$u_z(\alpha, x, y, z) = B(\alpha, y) e^{-j\beta z} e^{-j\alpha x} \tag{3.2.46}$$

We assume that $B(\alpha, y)$ does not change with z; thus a straight crested component of the surface wave (the equivalent of a plane wave component of a bulk wave), expressed by Eq. (3.2.46), exists. On this basis, we sum the components of different α to form the total field. We assume that ϕ, ψ_x, u_x, u_y, and the other field components can be treated in the same way.

Ideally, for a rectangular bulk wave transducer on a solid material, we should take account of the contributions of the longitudinal and shear wave potential to the displacement and stress at any point. This difficulty does not occur when the propagating medium is a liquid. Even with a solid, the effect of the shear wave

potential term is small for excitation from a longitudinal wave transducer. Similarly, the effect of the longitudinal wave potential term is small for excitation by a shear wave transducer. Thus we treat the longitudinal wave transducer by neglecting the shear wave potential term.

We assume that the transducer is uniformly excited by a potential ϕ_0 over its width w. From Eq. (3.2.44), the spatial frequency component $A(\alpha)$ has an amplitude

$$A(\alpha) = \frac{w}{2\pi}\phi_0 \frac{\sin(\alpha w/2)}{\alpha w/2} \tag{3.2.47}$$

Thus

$$\phi(x, z) = \frac{w}{2\pi}\phi_0 \int_{-\infty}^{\infty} e^{-jz(k^2-\alpha^2)^{1/2}} e^{-j\alpha x} \frac{\sin(\alpha w/2)}{\alpha w/2}\, d\alpha \tag{3.2.48}$$

We assume that the function $\sin(\alpha w/2)/(\alpha w/2)$ is large only for small α. This is equivalent to using the paraxial ray assumption and assuming that only rays at a small angle to the axis are important, or that $\alpha^2 << k^2$. We can then write Eq. (3.2.48) in the form

$$\phi(x, z) = \frac{w}{2\pi}\phi_0 e^{-jkz} \int_{-\infty}^{\infty} e^{j\alpha^2 z/2k} e^{-j\alpha x} \frac{\sin(\alpha w/2)}{\alpha w/2}\, d\alpha \tag{3.2.49}$$

It is convenient to define a normalized diffraction parameter

$$S = \frac{4z\lambda}{w^2} \tag{3.2.50}$$

with $Y = \alpha w/2$. Equation (3.2.49) can now be written in the form

$$\phi(x, z) = \frac{\phi_0}{\pi} e^{-jkz} \int_{-\infty}^{\infty} e^{-2jYx/w} e^{jY^2 S/4\pi} \frac{\sin Y}{Y}\, dY \tag{3.2.51}$$

We can also find the average value of $\phi(x, z)$ over a transducer of width w to determine the diffraction loss between two transducers spaced by a distance z. The result is

$$\frac{\overline{\phi(x, z)}}{\phi_0} = \frac{e^{-jkz}}{\pi} \int_{-\infty}^{\infty} \left(\frac{\sin Y}{Y}\right)^2 e^{jk^2 S/4\pi}\, dY \tag{3.2.52}$$

Figure 3.2.8 shows plots of $|\phi(0, z)/\phi_0|$ and $|\overline{\phi(x, z)}/\phi_0|$ as a function of S.

Note that now there are no deep nulls in the axial field variation with z. Complete cancellation occurs in a cylindrical system only because the contribution to the axial field by a ring of radius r and thickness dr on the transducer is proportional to the term $[\exp(-jkR)/R]r\, dr = [\exp(-jkR)]\, dR$. Thus elements of incremental length dR contribute equal amplitudes to the axial fields and can cancel each other out. This same relation does not hold for a rectangular transducer.

Note also that the last amplitude maximum of $\phi(0, z)$ is near $S = 1.2$, which is only 2.5 dB higher than the value at the transducer, rather than the 6 dB higher

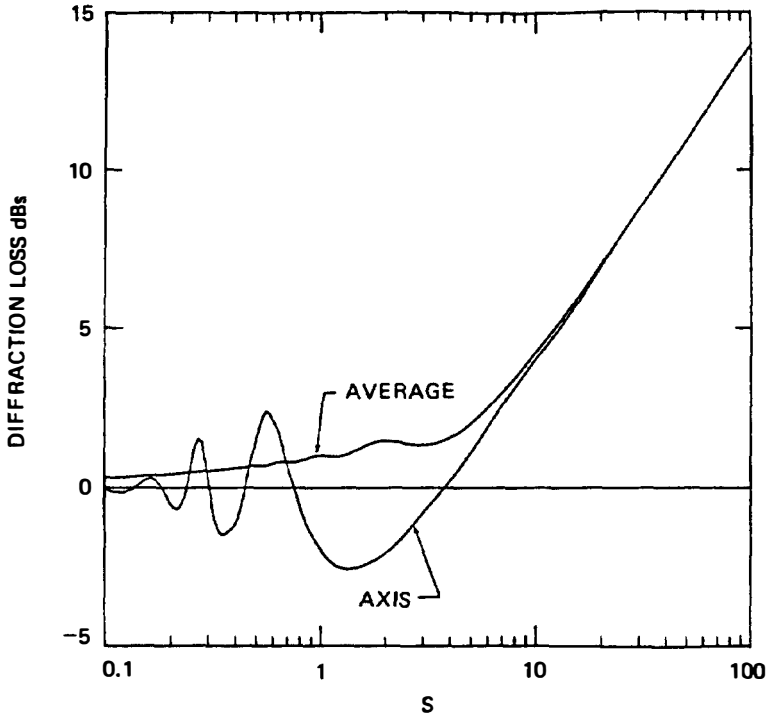

Figure 3.2.8 Plot of the average potential $|\phi(x, z)/\phi_0|$ and the potential on the axis $|\phi(0, z)/\phi_0|$ of a rectangular transducer.

obtained with a cylindrical transducer. The Fresnel length is therefore near $S \approx 1$ or $\lambda z/(w/2)^2 \approx 1$. The actual value of $S = 1.2$, the Fresnel length of a rectangular transducer, clearly corresponds to the value of $S = z\lambda/a^2 = 1$ for the Fresnel length of a cylindrical transducer.

Fraunhofer diffraction field by the method of stationary phase. Finally, we consider diffraction in the far field. First we write

$$\alpha = k \sin \theta' \tag{3.2.53}$$

or

$$Y = \frac{kw}{2} \sin \theta' \tag{3.2.54}$$

with

$$d\alpha = k \cos \theta' \, d\theta' \tag{3.2.55}$$

From Eq. (3.2.47), the amplitude $A(\theta') \, d\theta'$ of the plane wave excited in the element of angle $d\theta'$ can be written in the form

$$A(\theta') \, d\theta' = kw \frac{\phi_0}{2\pi} \frac{\sin [(kw \sin \theta')/2]}{(kw \sin \theta')/2} \cos \theta' \, d\theta' \tag{3.2.56}$$

Thus we expect the amplitude of the waves emitted from the transducer into an angular range $d\theta'$ to vary as $[\text{sinc } (w \sin \theta')/\lambda] \cos \theta'$.

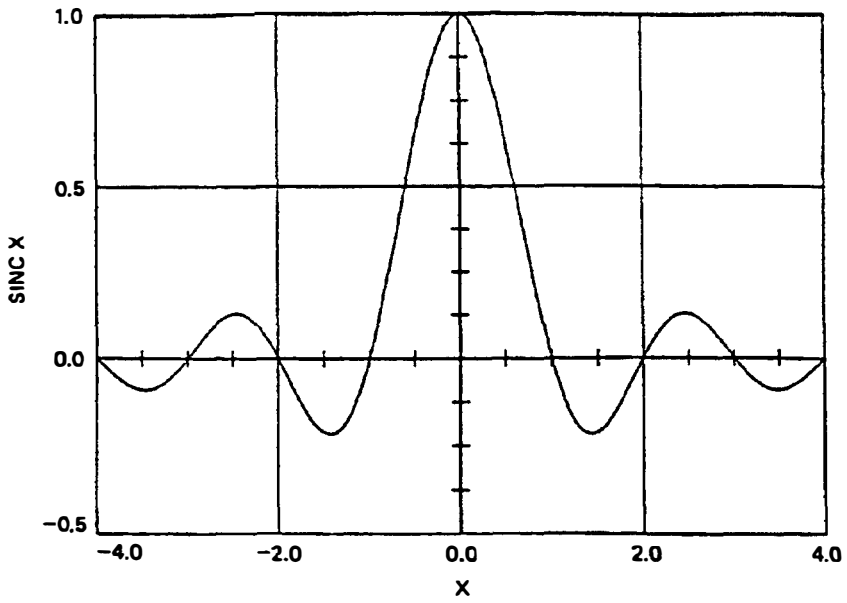

Figure 3.2.9 Plot of sinc $X = (\sin \pi X)/\pi X$.

It is convenient to write Eq. (3.2.48) in terms of θ' to obtain the result

$$\phi(x, z) = \frac{kw}{2\pi} \phi_0 \int_{-\infty}^{\infty} e^{-jkr\cos(\theta' - \theta)} \frac{\sin [(kw \sin \theta')/2]}{(kw \sin \theta')/2} \cos \theta' \, d\theta' \tag{3.2.57}$$

where

$$\begin{aligned} z &= r \cos \theta \\ x &= r \sin \theta \end{aligned} \tag{3.2.58}$$

We assume that kr is large in the Fraunhofer region. In this case we can use the *method of stationary phase*, as given in Appendix G, to evaluate the integral. This technique is based on the idea that as the phase of the exponential term in the integrand varies rapidly as θ' is varied, the main contribution to the integral must come from near the region where the rate of phase change is zero (stationary phase). This is where $\sin(\theta' - \theta) = 0$ or $\theta' = \theta$ (i.e., where the plane wave component excited by the transducer is aimed toward the observer at x, z). Then, writing $\cos(\theta' - \theta) \approx 1 - (\theta' - \theta)^2/2$ in the argument of the exponential, and putting $\sin \theta' \approx \sin \theta$ and $\cos \theta' \approx \cos \theta$, as discussed in Appendix G, we obtain the result

$$\frac{\phi(x, z)}{\phi_0} \doteq \frac{w}{\sqrt{r\lambda}} \operatorname{sinc}\left(\frac{w}{\lambda} \sin \theta\right) \cos \theta e^{-j(kr - \pi/4)} \tag{3.2.59}$$

where $\operatorname{sinc} X = \sin(\pi X)/\pi X$. The sinc X function is plotted in Fig. 3.2.9. Thus Eq. (3.2.59) leads us to conclude that $\phi(x, z)$ and u_r vary as $\cos \theta \operatorname{sinc}[(w \sin \theta)/\lambda]$.

This relation should be compared to that for a cylindrical transducer in a pressure release baffle [(Eq. (3.1.35)]. The same cos θ term appears when the potential is specified at the plane of the transducer (see Prob. 2). Here, if we had specified $u_z = \partial\phi/\partial z = u_0$ at the plane of the transducer, with $u_z = 0$ for $|x| > w/2$, there would be no cos θ term in the far field. An infinitely long rectangular transducer immersed in a liquid would give the same type of far-field pressure variation as a Rayleigh wave transducer.

Note that the amplitude falls off as $1/\sqrt{r}$, because the power intensity in a cylindrical spreading beam must fall off as $1/\sqrt{r}$, due to conservation of power. Therefore, at the same distance from the transducer, diffraction losses in a cylindrical beam are less severe than in a spherical beam. In practice, the diffraction loss of a rectangular transducer, of finite length h in the y direction, will tend to a $1/\sqrt{r}$ variation in the far field when $r >> h^2/\lambda$.

3-dB points. The argument of the sinc function is 0.455 $\pi/2$ at the 3-dB points, provided that $w/\lambda >> 1$ (i.e., provided we can ignore the cos θ term). The spacing between 3-dB points is therefore, to this approximation,

$$\Delta x(3\text{ dB}) = \frac{0.89r\lambda}{w} \tag{3.2.60}$$

where $x = r \sin\theta$. The zero points of the response are at

$$x(\text{zero}) = \frac{\pm r\lambda}{w} \tag{3.2.61}$$

The first sidelobe of the response occurs where $x = \pm 3r\lambda/2w$ and is reduced 13 dB in amplitude from the main lobe.

PROBLEM SET 3.2

1. Consider a cylindrical piston transducer in the form of a ring of outer radius a and inner radius b.
   (a) Find the variation of displacement and the potential field along its axis, and show that as the ring becomes infinitesimal ($b \to a$), there are no longer sharp dips in the z-directed field on the axis.
   (b) Find the radial field variation in the Fraunhofer region.
2. A rectangular piston transducer in a pressure release baffle (zero impedance baffle) is infinitely long in the y direction and finite in the x direction.
   (a) Assuming that $\phi(x', 0)$ on the transducer varies only in the x direction, use Eq. (3.1.35) to find $\phi(x, z)$ at any point by putting $t = (y' - y)/r$, where $r = [z^2 + (x - x')^2]^{1/2}$ and integrating from $t = -\infty$ to $t = \infty$. Apply the method of stationary phase given in Appendix G to the integral, to find a simple form of the integral for $kr >> 1$. Keep the term cos θ in Eq. (3.1.35) in that form and do not substitute for it until you have used the method of stationary phase.
   (b) Using your result for (a), find the Fraunhofer solution for the potential at a point x,

z that is due to the excitation of a rectangular transducer of width w by a uniform potential ϕ_0.

Answer:

$$\frac{\phi(x, z)}{\phi_0} = \frac{w}{\sqrt{r\lambda}} \operatorname{sinc} \frac{w \sin \theta}{\lambda} e^{-j(kr - \pi/4)} \cos \theta$$

where $x = r \sin \theta$ and $r = \sqrt{x^2 + z^2}$. The result shows that the fields fall off as $1/\sqrt{r}$ in a cylindrical system.

3. Repeat Prob. 2 for an infinitely long rectangular piston transducer in a rigid baffle, excited by a displacement field $u_z(x', 0) = u_0$ on the transducer.
4. Repeat Prob. 3, using the Fourier transform method for a rectangular transducer.
5. Using the results of Prob. 3, and assuming that $u_z(x')$ has the form $u_z(x') = u_0 \exp(-\alpha x'^2)$ and that the transducer is infinitely wide, find an analytic expression for the fields at any point x, z. It is reasonable to employ the paraxial approximation ($x'^2 \ll z^2$); this is a valid assumption when α is so large that only regions for which x' is small contribute to the field. Find an analytic expression for the fields at any point x, z by completing the square in x' in the argument of the exponentials. You may need the result

$$\sqrt{\frac{\pi}{\beta}} = \int_{-\infty}^{\infty} e^{-\beta x^2} \, dx$$

6. **(a)** Consider the errors in the derivation of the paraxial forms of Eqs. (3.2.39) and (3.2.40). Use the exact form of Eq. (3.2.36) and expand up to fourth order in α. Write the new normalized forms of Eqs. (3.2.39) and (3.2.40) in terms of S and ka.
   (b) Suppose that the main contribution to Eq. (3.2.40) comes from the region $Y < 10$. In this case, write the condition for the maximum phase error in the exponential term (i.e., the fourth-order term) as less than $\pi/4$. Find the minimum value of S to satisfy this condition as a function of ka. What is $S(\text{min})$ for $ka = 100$? The result will be by no means a good estimate of the error, but this derivation should give you a feel for how the error in the paraxial theory depends on the parameters.
7. Consider the use of a rectangular transducer as a receiver. Supposes that a plane longitudinal wave of amplitude $u_0[\exp(-jkr)]$, with the direction of propagation in the r direction at an angle θ to the z axis, is incident on a transducer of width w with its plane perpendicular to the z direction. Assume that the output of the receiving transducer is proportional to the average value of u_z over the width of the transducer, defined as

$$\bar{u}_z = \frac{1}{w} \int_{-w/2}^{w/2} u_z \, dx$$

where u_z is the displacement in the z direction due to the incident longitudinal wave. Determine how the received signal varies with θ and show that your result has the same variation with θ as Eq. (3.2.59).

8. **(a)** A plane wave is incident in the z direction on a thin penny-shaped crack of radius a, and is scattered by it. Determine the amplitude of the scattered wave in the forward direction (i.e., at an angle θ from the axis where $\theta < \pi/2$). Assume that just beyond the crack, $u_z = 0$ in the region $r < a$. This implies that if the incident

wave is u_z^i and the scattered wave is u_z^s, then

$$u_z = u_z^i + u_z^s$$

and

$$u_z^s = -u_z^i \qquad (r < a)$$

Thus you may assume that the scattered field is due to a piston transducer with a field u_z^s at a plane $z = 0$ [just beyond the crack ($z < 0$)].

(b) Find the total field on the axis and show that in the Fresnel approximation, there is always a bright spot on the axis whose amplitude does not vary with z.

(c) Find an expression for the magnitude of the total field at a point r, θ in the Fraunhofer region of the scatterer.

3.3 FOCUSED TRANSDUCERS

3.3.1 Field of a Focused Spherical Transducer

As we discussed in Sec. 3.2, the beam emitted from a piston transducer spreads radially due to diffraction. Thus, at some distance from the transducer, the power intensity may be too low, while the beam diameter is too large to obtain good transverse definition when probing an object. Therefore, we often employ a focused acoustic beam, as in optics, to obtain good transverse definition and high acoustic beam intensity at a point of interest.

As in optics, we can use lenses to focus the acoustic beam. But often the simplest way to obtain a focused acoustic beam is to use a spherically shaped transducer. Such a transducer will produce a focused beam near its center of curvature. We normally focus the beam to a spot smaller than the transducer diameter, thus obtaining a beam intensity much higher than that at the transducer itself. So in this section we shall use the methods employed in Sec. 3.2.1 to determine the intensity of the beam near its focus in terms of the beam intensity at the transducer surface.

We consider a spherical transducer with a diameter $2a$ and a radius of curvature z_0, as illustrated in Fig. 3.3.1. We shall use a paraxial theory, or *Fresnel approximation*, in which we assume that $a^2 \ll z^2$ to treat the properties of the beam emitted from the transducer. Equations (3.1.33) and (3.2.1) for the potential of a transducer in a rigid baffle are strictly true only for a flat piston transducer in a flat baffle. To avoid the difficulty this presents, we can assume that the acoustic beam, initially, follows geometrical ray paths normal to the surface of the transducer, and that the acoustic source is at the plane of the baffle $z = z_1$. Suppose that the distance from a point on the transducer, along a ray path normal to its face, to the point of interception with the plane of the baffle, r', z_1, ψ', is R_1. We

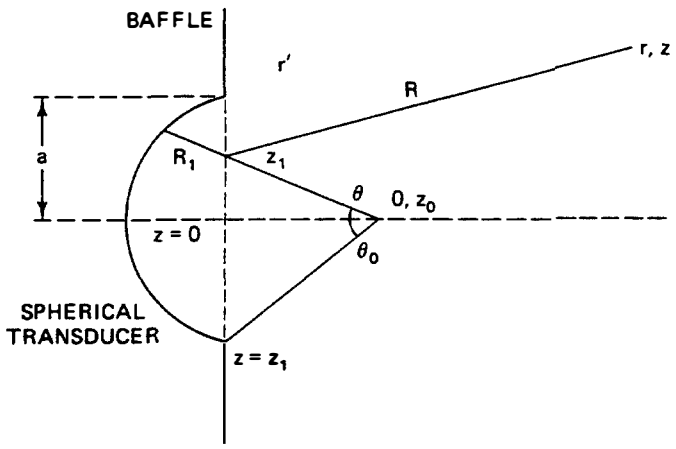

Figure 3.3.1 Notation used in the analysis of a spherical transducer.

can then take the phase of the beam emitted from this point to be exp $(-jkR_1)$. The displacement at the plane of the baffle can be found by ray optics. We assume that the radial displacement at the transducer is $u_0(\theta)$. The displacement in the z direction at the plane of the baffle is

$$u_z(\theta) = u_0(\theta) \cos\theta \frac{z_0}{z_0 - R_1} \tag{3.3.1}$$

But $z_0 - R_1 = (z_0 - z_1)/\cos\theta$. Since $z_0 - z_1 = z_0 \cos\theta_0$, where θ_0 is the aperture angle of the transducer, it follows that

$$u_z(\theta) = u_0(\theta) \frac{\cos^2\theta}{\cos\theta_0} \tag{3.3.2}$$

On this basis, we can use the Rayleigh–Sommerfeld theory, in the form of Eq. (3.2.1) or (3.2.33), and treat the plane of the baffle as the source, for all we have done is to alter the phase of the source at the plane of the baffle and multiply $u_0(\theta)$ by $\cos^2\theta/\cos\theta_0$.

We now suppose that the transducer is excited by a uniform displacement u_0. The total potential at a point r, z, 0 from all contributions at a distance R from points r', 0, and ψ' on the baffle is

$$\phi(r, z, 0) \approx -\frac{u_0}{2\pi} \iint \frac{e^{-jk(R+R_1)} \cos^2\theta}{R \cos\theta_0} r'\, dr'\, d\psi' \tag{3.3.3}$$

Referring to Fig. 3.3.1, we see that

$$R = \sqrt{r'^2 + r^2 - 2rr' \cos\psi' + (z - z_1)^2} \tag{3.3.4}$$

By simple geometry, it is easy to show, to the paraxial approximation, that

$R_1 \approx z_1 - r'^2/2z_0$. Thus, keeping only second-order terms in r and r', we find that

$$R_1 + R \approx z + \frac{r'^2 + r^2 - 2rr' \cos \psi'}{2z} - \frac{r'^2}{2z_0} \tag{3.3.5}$$

Here we have neglected z_1 in the denominator of the first term on the right-hand side of Eq. (3.3.5), since it is of second order in r' and would contribute only fourth-order terms in r and r' to the result. Thus if $z = z_0$, the second-order terms in r' cancel out. We will assume that as far as the amplitude variation is concerned, the R term in the denominator of Eq. (3.3.3) is equal to z, and to the paraxial or Fresnel approximation $\cos^2 \theta \approx 1$ and $\cos \theta_0 \approx 1$. Then Eq. (3.3.3) can be written in the form

$$\phi(r, z) = -e^{-jk(z + r^2/2z)} \frac{u_0}{2\pi z} \int_0^a \int_0^{2\pi} e^{-(jkr'^2/2)(1/z - 1/z_0)} e^{(jkrr'/z)\cos\psi'} r' \, dr' \, d\psi' \tag{3.3.6}$$

Integrating with respect to ψ', we find that

$$\phi(r, z) = -e^{-jk(z + r^2/2z)} \frac{u_0}{z} \int_0^a J_0\left(\frac{krr'}{z}\right) e^{-(jkr'^2/2)(1/z - 1/z_0)} r' \, dr' \tag{3.3.7}$$

where $J_0(x)$ is a Bessel function of the first kind and of zeroth order.

We now consider the form of the potential at the plane $z = z_0$. Ray optics indicate that this is the focal plane; thus we shall call it the *geometrical focus*. As we shall see, diffraction effects tend to bring the point of maximum axial beam intensity nearer to the lens (i.e., to a plane $z < z_0$). Hence the *true focus* is at a plane $z < z_0$.

At the geometrical focal plane, the potential on axis is

$$\phi(0, z_0) = -\frac{a^2 e^{-jkz_0}}{2z_0} u_0 \tag{3.3.8}$$

By differentiating with respect to z, we can find $u_z(z)$ and show that

$$u_z(0, z_0) \approx \frac{j\pi a^2}{\lambda z_0} e^{-jkz_0} u_0 \qquad (kz_0 >> 1) \tag{3.3.9}$$

It follows that the ratio of the beam intensity $I(0, z_0)$ on axis at $z = z_0$ to the beam intensity $I(0)$ at the transducer is

$$\frac{I(0, z_0)}{I(0)} = \left(\frac{\pi a^2}{z_0 \lambda}\right)^2 = \left(\frac{\pi}{S}\right)^2 \tag{3.3.10}$$

where, as before, $S = z_0\lambda/a^2$. Thus if the beam is focused at z_0, and if $z_0 < \pi a^2/\lambda$, the beam intensity at the geometrical focus will be larger than that at the transducer. Note that this implies that the focused transducer will normally be operated with its focal point in a region where the parameter $S = \lambda z_0/a^2$ is such that $S < \pi$.

Transverse definition. Now consider the fields at the optical focal plane $z = z_0$ for finite r. It follows from Eq. (3.3.7) that

$$u_z(r, z_0) = \frac{j\pi a^2 e^{-jkz_0} e^{-jkr^2/2z_0}}{\lambda z_0} \frac{2J_1(kra/z_0)}{kra/z_0} u_0 \tag{3.3.11}$$

Thus the beam intensity at the plane $z = z_0$ varies as

$$\frac{I(r, z_0)}{I(0)} = \left(\frac{\pi a^2}{z_0 \lambda}\right)^2 \left(\text{jinc } \frac{ra}{\lambda z_0}\right)^2 \tag{3.3.12}$$

where

$$\text{jinc } X = \frac{J_1(2\pi X)}{\pi X} \tag{3.3.13}$$

This function is plotted in Fig. 3.2.6.

The variation of the beam intensity at the focal plane is exactly the same in form as that in the Fraunhofer region of a plane piston transducer at $z = z_0$. However, the beam intensity can now be chosen at will and can also be much larger than at the transducer itself, which changes the scales of both the axial and radial variations of the field.

3-dB definitions, *F* number, and lens aperture. The radius at which the beam intensity becomes zero is

$$r_0(\text{zero}) = \frac{0.61 z_0 \lambda}{a} = \frac{0.61\lambda}{\sin \theta_0} = \frac{0.61\lambda}{\text{aperture}} \tag{3.3.14}$$

where θ is the half-angle subtended at the geometric focus by the transducer lens, and the *aperture of the lens* is defined as $\sin \theta_0$. The diameter of the beam at the 3-dB points, which we take as a measure of its definition, is

$$d_r(3 \text{ dB}) \approx \frac{0.51 z_0 \lambda}{a} = \frac{0.51\lambda}{\sin \theta_0} = 1.02\lambda F \tag{3.3.15}$$

where we call $F = z_0/2a = z_0/D$ the *F number of a lens or transducer*, and D its diameter. Thus

$$\frac{d_r(3 \text{ dB})}{D} = \frac{0.25 z_0 \lambda}{a^2} = 0.25S \tag{3.3.16}$$

So, by focusing, the effective beam diameter can be made smaller at its geometric focus than at the transducer, provided that $z_0 << 4a^2/\lambda$ (i.e., $S << 4$).

Sidelobes. Note that the beam intensity falls off radially as $(\text{jinc } X)^2$ where $X = ra/\lambda z_0$. A plot of this function is given in Fig. 3.2.6. The first sidelobe is at $kra/z_0 = 5.136$ or $r = 0.82 z_0 \lambda/a$, and is 17.6 dB lower in amplitude than the main lobe.

The sidelobe level is important because it dictates how well the transducer

can respond to a wanted signal rather than to an interfering one. Suppose that a focused transducer is used to search for two point sources, A and B, and that point source B emits power at a level 30 dB higher than does A. If the transducer is focused on A, and B happens to be located at a distance $r = 0.82z_0\lambda/a$ from A, we see B on the first sidelobe of the transducer and are unable to detect the presence of A; therefore, we cannot be certain where the true source is located. If B is only 10 dB higher in magnitude than A, however, the resulting sidelobes do not present a major problem, because the signal received from sidelobe B is 7.6 dB less than that received by A, and we can locate both sources.

Coherent and incoherent imaging. The sidelobe problem becomes even more severe if we wish to observe a large illuminated area in which dark spots are present, or a small absorber in a bright background. In the worst cases, the sum of the signals from the higher-order sidelobes may be much larger than the signal from the main lobe.

As an example, the signal amplitude variation across a one-dimensional object with a spatial step function insonification was calculated for the one-dimensional sinc X response by Lemons and Quate [5]; it is illustrated in Fig. 3.3.2. We assume that the receiving transducer is being moved past the object. As we observe from Fig. 3.3.2(a), there is quite severe "ringing" near a sharp edge when the step object function is insonified with a coherent plane wave. This problem is often severe in coherent imaging systems. By contrast, as shown in Fig. 3.3.2(b), when we employ an incoherent imaging system (i.e., one in which a noise source or a source with a broad range of frequencies present is used), there are no phase additions of the signals. Thus only the intensities (the square of the amplitudes), rather

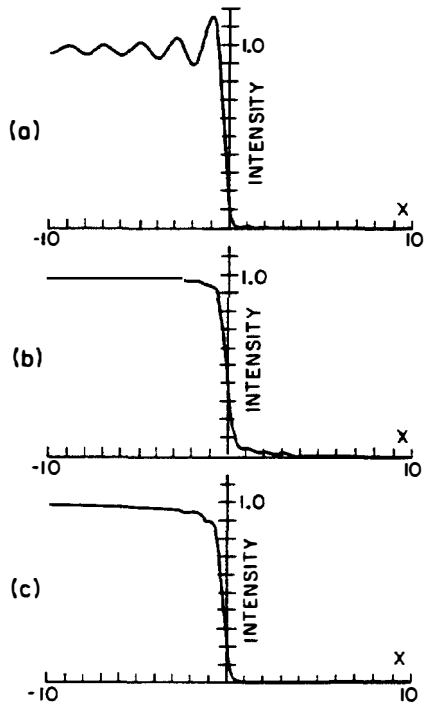

Figure 3.3.2 Calculated one-dimensional images of a step function object: (a) conventional coherent image; (b) conventional incoherent image; (c) image produced by a confocal scanning system using coherent radiation. (From Lemons and Quate [5].)

than the amplitudes of the sidelobes, add and the ringing effect virtually disappears. When two confocal lens are used, one for insonification and the other as a receiver, with a knife-edged object between them, the spatial response is squared. Hence the sidelobe level amplitudes now vary as (sinc X)^2 in the one-dimensional case [(jinc X)^2 in a cylindrically-symmetric system]; this squaring results in a clean image of a sharp edge, as shown in Fig. 3.3.2(c). It can be shown that the amplitude response of a confocal system to a step function object is identical to the intensity response of an incoherent single lens system to a step function object. Hence the confocal system gives a sharper edge response than an incoherent single lens system.

Rayleigh two-point definition. Obviously, the use of the simple 3-dB definition is not necessarily adequate. Consequently, it is more common to use the *Rayleigh definition*, which is based on the *two-point definition*. This definition uses the idea that two neighboring point sources can be distinguished from each other if the maximum response to one is located at the first zero of response to the second point. On this basis, the two points are spaced by a distance d_{cr} (Rayleigh), which is defined as

$$d_{cr}(\text{Rayleigh}) = 1.22\lambda F = \frac{0.61\lambda}{\sin \theta_0} \tag{3.3.17}$$

where the subscript c denotes coherent sources and the subscript r denotes definition in the radial direction.

The two-point response observed in practice depends on the type of insonification used. With coherent insonification, the result will depend on the relative phases of the two point sources. If the phase difference between the insonification of the two points is ϕ, the total intensity, defined as the square of the magnitude of the response to the two coherent sources, $I_c(X)$, is of the form

$$I_c(X) = |\text{jinc}\,(X - 0.30) + e^{j\phi}\,\text{jinc}\,(X + 0.30)|^2 \tag{3.3.18}$$

This function is plotted in Fig. 3.3.3 for different phases ϕ.

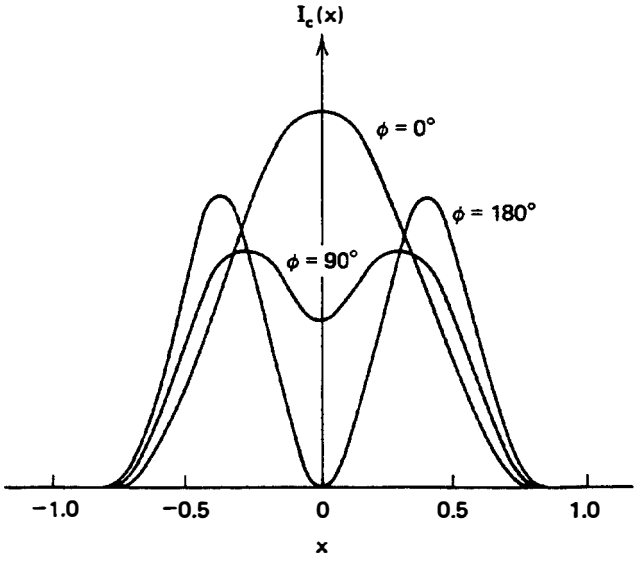

Figure 3.3.3 Image intensity for two mutually coherent point sources separated by the Rayleigh distance.

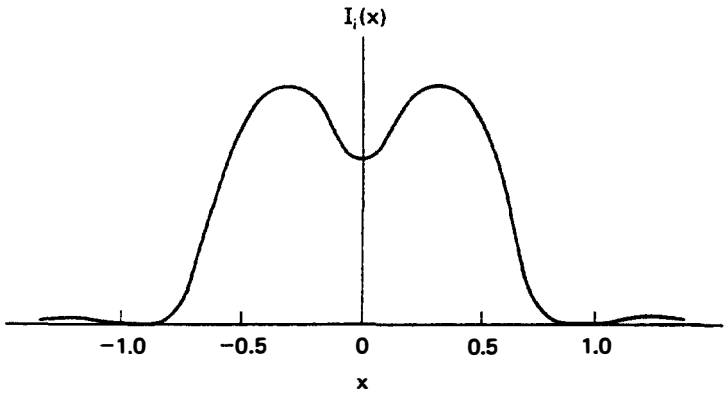

Figure 3.3.4 Image intensity for two incoherent point sources separated by the Rayleigh distance.

When the two coherent sources are 180° out of phase, there is a deep null at the point midway between them, as we might expect. However, if the two coherent sources are in phase, there is no minimum and thus the two points cannot be distinguished. When the sources are 90° out of phase, there is a minimum of intensity at the center point, which is 26.5% below the maximum value of the intensity.

On the other hand, if the sources are insonified completely incoherently, as is possible in optical systems and only possible to a limited extent, using very short pulses in acoustic systems, there is no correlation between the two sources and hence the product terms between them do not contribute to the total intensity. Thus the intensity for incoherent sources $I_i(X)$ is just the sum of the squares of the two individual intensities, or

$$I_i(X) = \text{jinc}^2\,(X - 0.30) + \text{jinc}^2\,(X + 0.30) \tag{3.3.19}$$

where the subscript i denotes incoherent sources. This function is plotted in Fig. 3.3.4. Because there is now a 26.5% dip at the center point, the two sources can be distinguished from each other.

Therefore, the Rayleigh criterion of definition for incoherent imaging is often stated in this form: *Two points can be distinguished if there is a 26.5% dip in intensity at the midpoint between them.* This definition corresponds to a separation between the two points by a distance d_{ir}(Rayleigh), defined as

$$d_{ir}(\text{Rayleigh}) = 1.22\lambda F = \frac{0.61\lambda}{\sin\theta_0} \tag{3.3.20}$$

Note that with coherent, in-phase sources, the two points must be separated by a distance d_{cr}(Rayleigh), defined as

$$d_{cr}(\text{Rayleigh}) = 1.64\lambda F = \frac{0.82\lambda}{\sin\theta_0} \tag{3.3.21}$$

to obtain the same 26.5% dip in level between them. Thus the use of incoherent sources improves the Rayleigh definition by a factor of 1.34 over the worst case for coherent sources.

Sparrow two-point definition. For two-point definition, we must be able to distinguish the dip in level between the images of the two points. This criterion is far more general in application than simply placing one point where the zero response to the other point occurs. It can apply equally well to coherent imaging or, for example, a Gaussian beam, where there is no sharp spatial zero in response to a point source. Detection of the minimum level in the two-point response must, in practice, depend on the noise level of the system and the properties of the display system, which means that the 26.5% dip in the Rayleigh definition is an arbitrary requirement. It is therefore worthwhile to consider yet another two-point definition, the *Sparrow criterion* [6]: *The intensity halfway between the two points is just equal to the total intensity at one point.*

Calculations define the Sparrow criterion for incoherent imaging, d_{ir}(Sparrow), as

$$d_{ir}(\text{Sparrow}) = 1.02\lambda F = \frac{0.51\lambda}{\sin \theta_0} \tag{3.3.22}$$

while for two coherent in-phase sources, it is d_{cr}(Sparrow), defined as

$$d_{cr}(\text{Sparrow}) = 1.42\lambda F = \frac{0.76\lambda}{\sin \theta_0} \tag{3.3.23}$$

We shall use this criterion in Sec. 3.3.3, as well as the Rayleigh criterion, to consider the scanning microscope. Note that for incoherent imaging, the Sparrow criterion is almost identical to the single-point 3-dB criterion, while for coherent imaging, it leads to a definition approximately 1.5 times worse than that for incoherent imaging.

Speckle. The *speckle* phenomenon occurs only in coherent imaging systems and often leads to images of poor quality. When an optical image is illuminated under coherent laser light rather than room light, for instance, speckle is what gives its appearance a granular character. One reason for this phenomenon is that on a rough surface (rough in the scale of wavelengths of light), light will be reflected by many points into a focused receiver lens or transducer. The transducer response to these random sources depends on the sidelobe level at the random source. When the receiver is focused on a point A, which is illuminated by a broad beam, as illustrated in Fig. 3.3.5, the contributions from all the random scatterers may add to the contribution from the main lobe, thus giving rise to a bright spot at A. On the other hand, when the receiver is focused on another point B, the reflections from the random scatterers outside the main lobe may tend to cancel it out, hence creating a dark spot at the point B in the image. As the transducer is moved from point to point, some points will be darker, and others brighter, than the average beam intensity, thus displaying the speckle phenomenon. Similar phenomena can occur in images of semitransparent media such as body tissue, where the random additions from points in front of and behind the focal point give rise to speckle. The spots observed in the image will tend to have a size of the order of the focal spot size d_r, and the image will have a granular appearance.

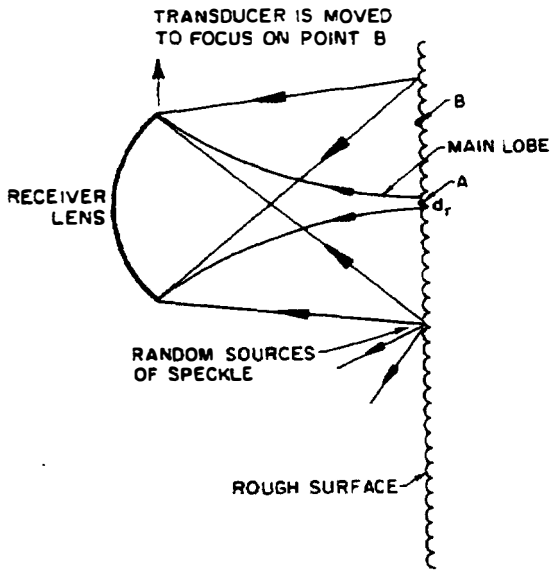

Figure 3.3.5 Speckle phenomenon. The broad insonifying beam, which is presumed to give uniform illumination over the whole area, is not shown.

Speckle is usually present in acoustic imaging systems because of the coherent sources normally used, the coherent detectors employed, and the fact that the typical media (e.g., body tissue and polycrystalline materials) are granular in nature and semitransparent. As we will discuss further in Sec. 3.5.3, the phenomenon can be minimized by using a mechanically scanned confocal imaging system where the transmitter insonifies only a small area, corresponding to the focal diameter of the receiver lens. When this is used, the point response is a (jinc X)^2 function, which is always positive; the sidelobe and speckle levels are very low and the mechanical scan gives signal averaging. Using short pulses for insonification can also minimize speckle by making the system behave as if it were partially incoherent.

Depth of focus. We now determine the variation of the acoustic potential, and hence the pressure and displacement along the axis of the lens. Just as with the plane cylindrical piston transducer, we will find that the fields along the axis of the focused transducer vary rapidly. In the limit $z_0 << a^2/\lambda$ or $S << 1$ (i.e., deep in the Fresnel zone), we can use the results to define a depth of focus d_z(3 dB) as the distance between the points where the field on axis is 3 dB less than that at the focal point.

We return to Eq. (3.3.7) and put $r = 0$ with $z \neq z_0$. The equation can then be integrated directly to yield

$$\begin{aligned}\phi(0,z) &= \phi(0,z_0)Z(z)e^{-jk(z-z_0)}e^{-j(\pi/2S)(z_0/z-1)} \\ &= (jS)\phi(0,0)Z(z)e^{-jkz}e^{-j(\pi/2S)(z_0/z-1)}\end{aligned} \tag{3.3.24}$$

where

$$Z(z) = (z_0/z)\,\mathrm{sinc}[1/2S)(z_0/z-1) \tag{3.3.25}$$

and sinc $X = (\sin \pi X)/\pi X$ and $S = z_0\lambda/a^2$.

It follows from Eq. (3.3.24) that the phase change from the source to the focal point is $\pi/2$ less than kz. For small changes in z near the focus, we can write $y = (z - z_0)/z_0$, and $z_0/z - 1 \approx -y$. It follows that near the focus there is an additional linear decrease in phase with z to the points $y = \pm S$. There is then an additional change in phase by π at each point $y = nS$. The phase is plotted in Fig. 3.3.5a as a function of y.

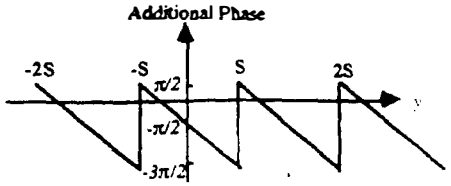

Fig. 3.3.5a Phase shift through focus.

Thus, in addition to the phase change kz, there is a π phase change through the focal point. This is due to the term $\exp[-j(\pi/2S)(z_0/z-1)]$ where $z_0/z-1=\pm S$, i.e., at the 3 dB points.

We shall assume that the beam intensity is proportional to $|\phi(z)^2|$. We may find the 3-dB range definition, deep in the Fresnel zone where $a^2/\lambda z_0 >> 1$ (i.e., $S << 1$), by determining where the argument of the sinc function becomes $1/\sqrt{2}$; in this case, we can ignore the variation of z_0/z. Thus, with this approximation, the 3-dB points occur where

$$z - z_0 = \pm 0.89 \frac{z_0^2}{a^2}\lambda = \pm\frac{0.89\lambda}{\sin^2\theta_0} \tag{3.3.26}$$

where θ is the half-angle subtended by the lens at the optical focal point 0, z_0. Thus a simple approximation for the depth of focus is

$$d_z(3\text{ dB}) = \frac{1.8\lambda}{\sin^2\theta_0} = \frac{1.8z_0^2}{a^2}\lambda = 7.1\lambda F^2 = 3.5\frac{z_0}{a}d_r(3\text{ dB}) \tag{3.3.27}$$

Another useful way to write this relation is in the form

$$\frac{d_z\ (3\text{ dB})}{z_0} = 1.8S \tag{3.3.28}$$

We see that the depth of focus is directly related to the Fresnel parameter of the lens. When the depth of focus is very small, we can write $z \approx z_0$ and use only first-order terms in $z - z_0$. In the region where the beam size is small, Eq. (3.3.25) takes the simple form

$$Z(z) = \text{sinc}\frac{z - z_0}{2Sz_0} \tag{3.3.29}$$

This expression is very convenient for estimating the beam intensity along the axis of the lens, at least near the focal plane. The sinc function is plotted as the dashed line in Fig. 3.3.6(a), and also in Fig. 3.2.9.

Geometrical concepts for depth of focus. These relations for the depth of focus can be illustrated geometrically, as shown in Fig. 3.3.7. The beam initially converges along its geometrical optics path (a cone) but diverges from this path near the focus. From Eq. (3.3.14), the radius of the beam to its zero amplitude point at the focal plane is $r_0 = 0.61\lambda z_0/a$. A cylinder of this radius intersects the edge of the geometrical beam where

$$\frac{z - z_0}{z_0} = \pm\frac{r_0}{a} = \pm 0.61\frac{z_0\lambda}{a^2} \tag{3.3.30}$$

Thus the depth of focus estimated by this approach is

$$d_z = 1.22\lambda\left(\frac{z_0}{a}\right)^2 \tag{3.3.31}$$

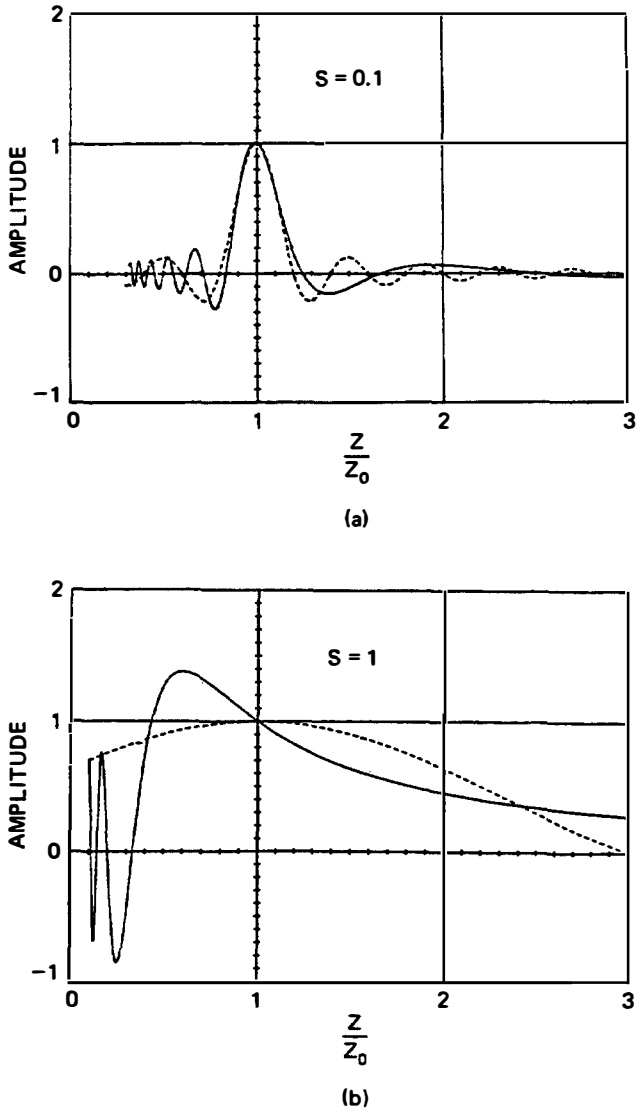

Figure 3.3.6 Normalized pressure or potential variation along the axis of a spherical lens: (a) $S = 0.1$; (b) $S = 1$. We take the amplitude to be unity at $z = z_0$. Solid line, plot of Eq. (3.3.25); dashed line, plot of Eq. (3.3.29).

This geometrical picture is a satisfying concept, but it is unreliable, for its estimate of beam intensity is, to say the least, crude.

Equations (3.3.25) and (3.3.29) show that the wave amplitude along the axis passes through several subsidiary maxima and minima. Thus simple geometrical considerations do not provide a complete picture of the behavior of the beam. In particular, if we wish to use the beam to probe for small reflectors, we may obtain inaccurate and misleading results when the reflector is outside the region of the depth of focus. This problem is illustrated in Fig. 3.3.6, which shows the multiple maxima and minima along the axis of the beam; the solid line plots are calculated from Eq. (3.3.25) and the dashed line plots, from Eq. (3.3.29). The situation illustrated in Fig. 3.3.6(a) corresponds to a value of $S = 0.1$, or a ratio of focal spot diameter d_r(3 dB) to a transducer radius of $d_r/2a = z_0\lambda/4a^2 = 0.025$.

For a weaker lens with $S = 1$ (i.e., $d_r/2a = 0.25$), as illustrated in Fig. 3.3.6(b), the formulas of Eq. (3.3.27) are not as accurate. In this case, the fields

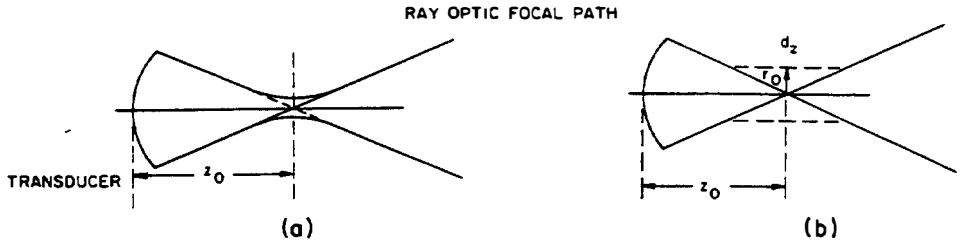

Figure 3.3.7 Focused beam from a spherical transducer. (a) The beam initially converges, as we expect from geometrical optics, but diverges from the geometrical optics path when it nears the focus. (b) Demonstration that the depth of focus can be estimated geometrically. A cylinder of radius r_0 passes through the zero amplitude points at the focal plane. The depth of focus is taken to be the length of this cylinder where it intersects the cone formed by the outside of the geometrical optic beam.

actually increase as z decreases from z_0; this is due to the variation of the z_0/z term in Eq. (3.3.25). Thus, although Eq. (3.3.25) is accurate for a wide range of the parameter S, the approximate formula of Eq. (3.3.27) for the depth of focus is completely reliable only for highly convergent lenses.

A convenient set of lens design curves is given in Fig. 3.3.8. We call the true focal length of the lens f, so that $\phi(z)$ or $u_z(z)$ is maximum on the axis at $z = f$. The parameter f/z_0 is plotted in Fig. 3.3.8; it decreases as S increases. Thus the effective focal length of a weak lens is less than its geometrical optics focal length. As we can see from Fig. 3.3.8, the true value of the depth of focus, d_z(true), is also less than its approximate value, d_z(approx.), which is given by Eq. (3.3.28). Because the focal point is nearer to the lens, the amplitude of $Z(f)$ is larger than the value of $Z(z_0)$.

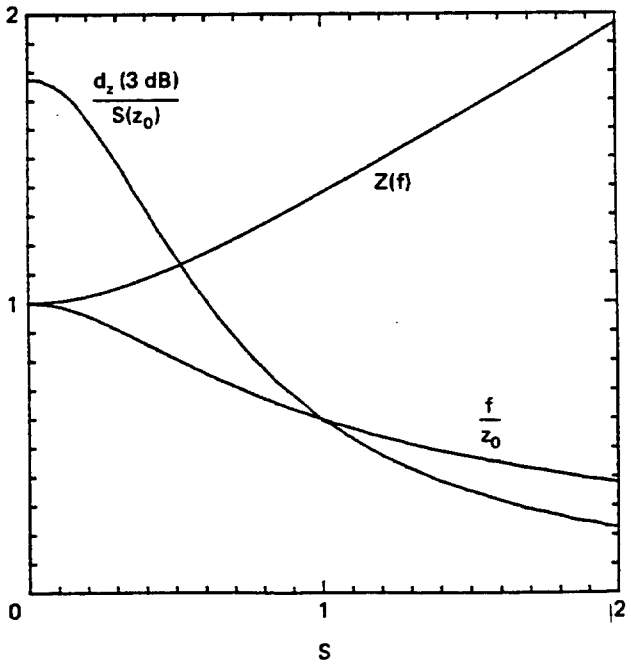

Figure 3.3.8 Plot of the effective parameters of weakly focused lenses as a function of $S = z_0\lambda/a^2$.

Example: Focused Transducer for Medical Applications

We now consider a medical example. Suppose that we require a beam diameter d_r(3 dB) = 1.5 mm, at a distance of 10 cm from the body surface, at a frequency of 2.25 MHz (λ = 0.67 mm). From Eq. (3.3.15), a = (0.5 × 10 × 0.067)/0.15 (i.e., a = 2.2 cm). In this case, S = 0.14 and Eq. (3.3.27) shows that the depth of focus is 2.5 cm. Figure 3.3.8 shows that f has, in fact, decreased to 9.6 cm and that with these parameters, d_z(true) = 2.4 cm.

Now suppose that we try to obtain a much larger depth of focus, d_z(3 dB) = 10 cm, with z_0 = 10 cm. In this case, Eq. (3.3.27) yields the result a = 1.1 cm; hence, from Eq. (3.3.15), the beam diameter at the optical focal point is d_r(3 dB) = 3 mm, with S = 0.56. But Fig. 3.3.8 shows that the focal point is actually at 8 cm and that d_z(true) = 6.8 cm. One or more iterations would, of course, let us design for the correct d_z. Even in this case, however, we can obtain a fairly good estimate of the beam parameters by using Eq. (3.3.27).

Reflection from a plane reflector. Another important criterion for judging the behavior of an imaging system is based on the reflection of a focused beam from a perfect plane reflector. We shall determine, here, how the reflected signal $V(z)$, measured with the input transducer used as the receiver, varies with the position z of a planar reflector. We will assume that the surface of the planar reflector is perpendicular to the axis of the lens.

When a perfect plane reflector is located at the geometrical focus of the lens, we expect the reflected signal to attain its maximum value. Here we define a perfect reflector as one for which the reflection coefficient $R(\theta)$ of a plane wave incident on the plane at an angle θ to the normal is such that $R(\theta) = 1$. More generally, as we have seen in Sec. 2.5, a plane wave incident on a solid may excite Rayleigh waves, or bulk shear and longitudinal waves, in the solid. Consequently, $R(\theta)$ may, in general, have an amplitude and phase that vary with θ, and $|R(\theta)| \leq 1$.

For a perfect reflector, we will take the normalized return signal $V(z)$ to be†

$$V(z) = \frac{\iint \phi^2(x, y, z)\, dx\, dy}{\iint |\phi^2(x, y, z_0)|\, dx\, dy} \tag{3.3.32}$$

where $\phi^2(x, y, z)$ is the point spread function at the plane z of this confocal lens system used in a reflection mode. We define a two-dimensional Fourier transform of $\phi(x, y, z)$ by writing

$$\phi(k_x, k_y, z) = \iint \phi(x, y, z) e^{-j(k_x x + k_y y)}\, dx\, dy \tag{3.3.33}$$

with

$$\phi(x, y, z) = \frac{1}{4\pi^2} \iint \phi(k_x, k_y, z) e^{j(k_x x + k_y y)}\, dk_x\, dk_y \tag{3.3.34}$$

†Equation (3.3.32) is adequate for use with the paraxial approximation. Liang et al. [7] have shown that a more accurate formula is

$$V(z) = \frac{\int \phi(x, y, z) u_z(x, y, z)\, dx\, dy}{\int \phi(x, y, z_0)\, u_z(x, y, z_0)\, dx\, dy}$$

where k_x and k_y are the transverse spatial frequencies, as discussed in Secs. 3.2.2 and 3.2.3.

It follows from Parseval's theorem that for a perfect reflector, Eq. (3.3.32) can be written in the following form [8]:

$$V(z) = \frac{\iint \phi(k_x, k_y, z)\phi(-k_x, -k_y, z)\, dk_x\, dk_y}{\iint \phi(k_x, k_y, z_0)\phi(-k_x, -k_y, z_0)\, dk_x\, dk_y} \tag{3.3.35}$$

Referring to Fig. 3.3.1, we may take the displacement $u_z(x', y', z_1)$ in the z direction at the baffle to be of the form

$$u_z(x', y', z_1) = P(x', y')e^{-jkR_1(x', y')} \tag{3.3.36}$$

where we call $P(x', y')$ the *pupil function* of the lens.

Writing Eqs. (3.3.4)–(3.3.5) in rectangular coordinates, we find that

$$R = \sqrt{(x' - x)^2 + (y' - y)^2 + (z - z_1)^2} \approx z - z_1 + \frac{(x - x')^2 + (y' - y)^2}{2z} \tag{3.3.37}$$

and

$$R_1 = z_1 - \frac{x'^2 + y'^2}{2z_0} \tag{3.3.38}$$

At $z = z_0$, with the use of the paraxial approximation, we find that

$$\phi(x, y, z_0) = -\frac{1}{2\pi}\frac{e^{-jkz_0}}{z_0} e^{-jk(x^2+y^2)/2z_0} \iint P(x', y')e^{jk(xx'+yy')/z_0}\, dx'\, dy' \tag{3.3.39}$$

We assume that the focused acoustic beam at the geometrical focal plane has a relatively small cross section, so that $k(x^2 + y^2)/2z_0 \ll 1$. In this case, Eq. (3.3.39) becomes

$$\phi(x, y, z_0) = -\frac{e^{-jkz_0}}{2\pi z_0} \iint P(x', y')e^{jk(xx'+yy')/z_0}\, dx'\, dy' \tag{3.3.40}$$

From this result, we see that the potential at the geometrical focal plane is the Fourier transform of the pupil function.

Comparing Eqs. (3.3.34) and (3.3.40), we see that

$$\phi(k_x, k_y, z_0) = -\frac{z_0 e^{-jkz_0}}{2\pi k^2} P(x', y') \tag{3.3.41}$$

where

$$\begin{aligned} k_x &= \frac{kx'}{z_0} \\ k_y &= \frac{ky'}{z_0} \end{aligned} \tag{3.3.42}$$

Thus we can regard the plane wave component k_x, k_y as being associated with the ray leaving the plane $z = z_1$ from the point x', y'.

The form of the plane wave k_x, k_y at the plane z is

$$\phi(k_x, k_y, z) = \phi(k_x, k_y, z_0)e^{-jk_z(z-z_0)} \tag{3.3.43}$$

where, from the wave equation for plane waves,

$$k_x^2 + k_y^2 + k_z^2 = k^2 \tag{3.3.44}$$

We substitute Eqs. (3.3.41), (3.3.43), and (3.3.44) in Eq. (3.3.35), to show that

$$V(z) = \frac{}{\iint P(x', y')P(-x', -y')\,dx'\,dy'} \tag{3.3.45}$$

In cylindrical coordinates, this expression becomes, for a symmetric lens,

$$V(z) = \frac{e^{-2jkz_0}\int P^2(r')e^{-2jk(z-z_0)\sqrt{1-r'^2/z_0^2}}\,r'\,dr'}{\int P^2(r')r'\,dr'} \tag{3.3.46}$$

Let us now consider the result for a lens in which $P^2(r') = 1$ from $r' = 0$ to $r' = a$. It is convenient to write $r' = z_0 \sin\theta$ with $a = z_0 \sin\theta_0$. In this case,

$$V(z) = \frac{}{\int_{\theta}^{\theta_0} \sin\theta\cos\theta\,d\theta} \tag{3.3.47}$$

For a paraxial system, we can put $\cos\theta = 1$ in the amplitude terms, to find that

$$V(z) = \frac{e^{-2jk(z-z_0)\cos\theta_0} - e^{-2jk(z-z_0)}}{} e^{-2jkz_0} \tag{3.3.48}$$

or

$$V(z) = \frac{\sin[k(z-z_0)(1-\cos\theta_0)]}{k(z-z_0)(1-\cos\theta_0)} e^{-jk(z-z_0)(1+\cos\theta_0)}e^{-2jkz_0} \tag{3.3.49}$$

This is the response $V(z)$ of a lens to a perfect plane reflector.

3-dB resolution for $V(z)$. It follows from Eq. (3.3.48) that the 3-dB points for $V(z)$ from a plane reflector are spaced by a distance d_{ps}(3 dB), where

$$d_{ps}(3\text{ dB}) = \frac{0.45\lambda}{1-\cos\theta_0} \tag{3.3.50}$$

For θ_0 small, Eq. (3.3.50) can be written in the form

$$d_{ps}(3\text{ dB}) = \frac{0.9\lambda}{\theta_0^2} \tag{3.3.51}$$

Thus this result is similar to that obtained from the depth of focus (i.e., the response

on the axis) of a single lens. The depth of focus for a two-way or confocal reflecting system, or the response for reflection from a point reflector, is less than this value (i.e., it is where the sinc^2 function drops by 3 dB). We call the confocal depth of focus d_{zs}(3 dB); its value is

$$d_{zs}(3 \text{ dB}) = \frac{1.28\lambda}{\sin^2 \theta_0} \tag{3.3.52}$$

Thus the 3-dB response points for a plane reflector are closer together than the 3-dB depth of focus for a point reflector.

The analysis we have carried out here is similar to that given by Atalar [9]. The reader is referred to his work and to that of Liang et al. [7] for more complete derivations. Liang et al. derived a more rigorous nonparaxial formulation based on the reciprocity theorem; both sets of authors derived formulas for an imperfect reflecting plane. The results they obtained for this latter case are similar to Eq. (3.3.46) and can be written, in our terms, in the form

$$V(z) = \frac{e^{-2jkz_0} \int P^2(r') R(r') e^{-2jk(z-z_0)\sqrt{1-r'^2/z_0^2}}\, r'\, dr'}{\int P^2(r') r'\, dr'} \tag{3.3.53}$$

where $R(r')$ is the plane wave reflectivity function for a wave incident on the plane reflector at an angle θ, and $r' = z_0 \tan \theta$.

This result has been of great help in understanding the behavior of the acoustic microscope and its contrast mechanisms, which we discuss in the following section.

3.3.2 Scanned Acoustic Microscope

The acoustic microscope is an acoustic equivalent of the optical microscope [5, 7, 9–19]. It has been employed in both transmission and reflection modes, with water, liquid argon, liquid nitrogen, high-pressure gases, or liquid helium used as the operating medium. The acoustic wavelength in water is approximately 5000 Å at 3 GHz, which is comparable to wavelengths normally employed in the optical microscope. In practice, the device has been used over a wide range of frequencies, ranging, at the time of writing, from 2 MHz to 8 GHz, with definitions in water of better than 4000 Å at an operating frequency of 3 GHz, and in liquid helium of 300 Å at an operating frequency of 8 GHz. The upper-frequency limit, at normal temperatures, is determined by the attenuation in the operating medium; in most materials, this increases as the square of the frequency. In liquid helium, at temperatures of the order of 0.1°K, the attenuation is very low, so the upper-frequency limit is determined basically by problems of exciting and receiving acoustic waves.

Water has the dual advantages of convenience and having the lowest attenuation at room temperature (191 dB/cm at 1 GHz) of the possible operating media [5, 10]. At 60°C, its attenuation drops to 95 dB/cm, so high-frequency microscopes are often operated at this temperature using a water path in the range 30 to 100 μm.

Other operating media provide interesting alternatives to water. Liquid nitrogen and liquid argon have been used because they have low attenuations, and

lower acoustic velocities than water [5]. Liquid helium, which can be used at temperatures as low as 0.1°K, has extremely low acoustic velocities and attenuation, and hence a very small wavelength and fine definition [10]. A high-pressure gas can provide yet another low-velocity operating medium with relatively low attenuation [11]. Typically, with many of these media, the acoustic matching problem is severe due to their very low acoustic impedances.

The acoustic microscope responds to different properties in the object under examination from those responded to by the optical microscope. Because acoustic waves measure mechanical properties, the contrast of the microscope is determined by variations in elasticity, density, and acoustic attenuation in the medium. Therefore, acoustic wave devices are particularly suited to observing soft tissue or biological cell structure, which tend to be transparent to light. And because acoustic waves can penetrate optically opaque materials, the acoustic microscope is also very useful for observing features in integrated-circuit structures under metal films and other such optically opaque structures. It can also be used to measure the surface structure of metals. Because the individual grains of a polycrystalline material are anisotropic, their acoustic reflectivity varies from grain to grain, according to their orientations; thus the surface structures of metals show up well acoustically.

The optical microscope has been undergoing a long period of development since it was invented 300 years ago. Extremely sophisticated compound lens designs with very little chromatic or spherical aberration are now used routinely. But it is extremely difficult to contrive such low-aberration designs for acoustic lenses, because severe off-axis aberrations result from the large changes in refractive indices between the media employed. Another difference between the two types of devices is that conventional optical microscopes are designed to use incoherent illumination with phase-insensitive detectors (the eye, a photographic film, or a photodetector), while acoustic insonification tends to be coherent and acoustic receiving transducers are phase-sensitive.

As discussed in Sec. 3.3.1, a single-lens system with a coherent source will tend to give images containing a large amount of speckle. A different approach using *confocal scanned microscopy*, has been taken in the design of the acoustic microscope. A high-quality focus is obtained only on the axis of a lens; in a transmission system, both the transmitting and receiving lenses are focused on the same point, with either the object or the lenses moved mechanically. This produces a scanned image, in much the same manner as a TV raster scan that has very little speckle, (see the discussion of speckle in Sec. 3.3.1). The output of the scanning microscope is used to modulate the intensity of the spot on a cathode ray tube which is itself moved synchronously over the face of the tube with the mechanical movement of the object under the microscope.

An early reflection mode version of the acoustic microscope lens system is shown in Figs. 3.3.9 and 3.3.10. A plane wave is excited by a thin film zinc oxide transducer on sapphire, which has a high longitudinal acoustic wave velocity of 11.1 km/s. A spherical depression is cut in the opposite surface of the sapphire to form a lens. A drop of water or some other fluid is placed between the lens and the flat object to be observed; the surface of the object is located close to the

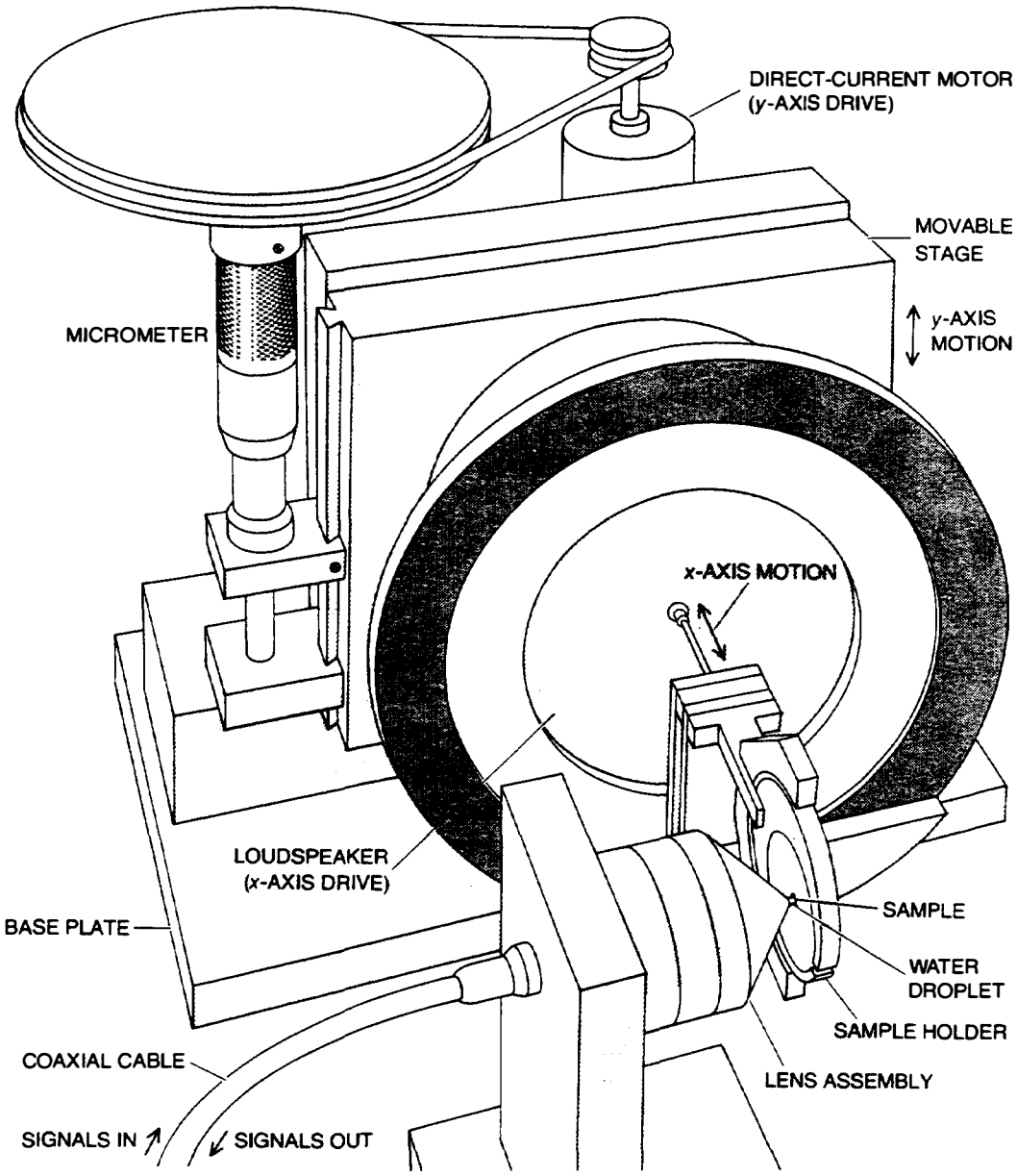

Figure 3.3.9 Scanned acoustic microscope. (After Quate [16].)

focal point of the lens. The transducer lens system is used as both transmitter and receiver for short RF tone bursts. After amplification and detection, the output from the receiving transducer is used to modulate the intensity of a cathode ray tube. At points where the effective reflectivity of the object is small, the electrical signal output is small; conversely, at points where the effective reflectivity of the object is large, the output is strong.

In the early version of the device, a picture was formed by scanning the object mechanically with a loudspeaker movement, as shown in Fig. 3.3.9; this produced the line scan. The lens system was scanned at right angles to the line scan, but much more slowly, by a piezoelectric or hydraulic movement; this formed the frame

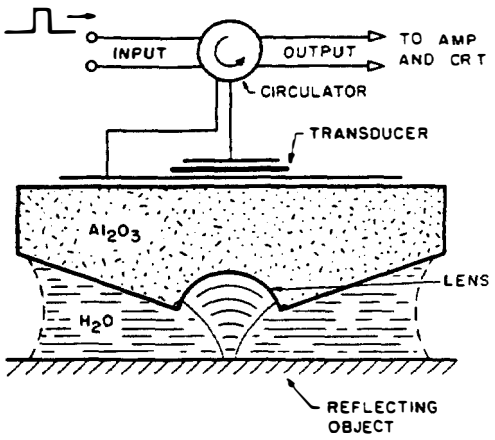

Figure 3.3.10 Lens of the acoustic microscope. (After Lemons and Quate [5].)

scan. More recent versions of the device use more sophisticated mechanical scans, with the lens scanned in both directions so that the object under observation can remain stationary. Great care is taken to ensure that the scan is repeatable.

We expect this type of lens to have a focal point on its axis but possibly to suffer from severe spherical aberrations (i.e., aberrations resulting from the inaccuracy of the paraxial approximation). Consider the ray geometry shown in Fig. 3.3.11. Ideally, if the velocity ratio between the two media were infinity, then, from Snell's law, all rays would be refracted to the center of curvature of the lens; thus there would be no spherical aberration, which would imply, in Fig. 3.3.11, that $\theta' = 0$. For a typical optical lens material in which the velocity ratio between the two media is of the order of 1.5, the aberrations are extremely severe, as illustrated in Fig. 3.3.12. In the case of sapphire and water, the ratio of the acoustic velocities is 7.4:1, which is large enough to cause very little aberration.

Figure 3.3.12 also shows calculations for materials with low and high velocity ratios, using a high ratio of acoustic velocities in the two media; in the acoustic case, the deviation from the paraxial focus is essentially undetectable. In practice, this implies that the aberrations are so weak that the diffraction limit of the lens is not affected. Thus a lens with almost perfect on-axis performance can be made for the acoustic microscope in a relatively simple manner.

The microscope illustrated in Figs. 3.3.9 and 3.3.10 has the additional ad-

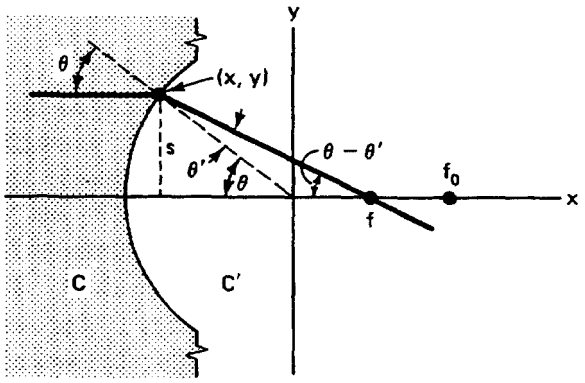

Figure 3.3.11 Geometry for the ray-tracing analysis of spherical aberrations. (After Lemons, as noted in Lemons and Quate [5, 17].)

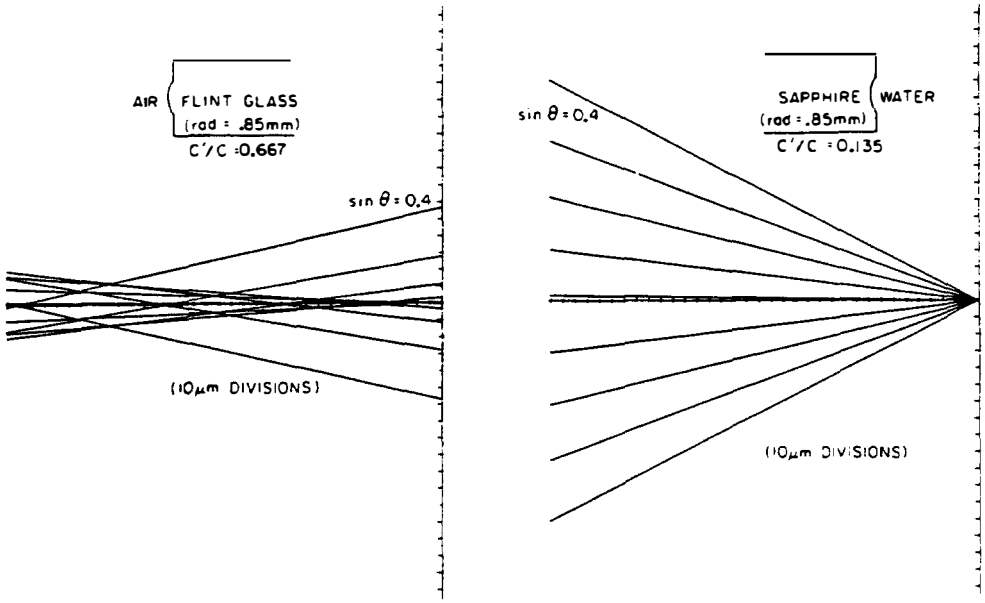

Figure 3.3.12 Ray-tracing comparison of the performance of a single-surface lens, with C' the wave velocity in the solid and C the wave velocity in the air or water medium: (a) light optical system; (b) Acoustic system. (After Lemons and Quate, as noted in Lemons and Quate [5, 18].) The paraxial focus lies at the ordinate.

vantage that the lens is used twice. Thus its amplitude response or point spread function (PSF) is the product of the response of the transmitting and receiving lenses, and the PSF is therefore (jinc $X)^2$ where $X = ra/\lambda z_0 = r/\lambda \sin \theta_0$.

Note that this function is always positive and that the amplitude away from the point $X = 0$ ($r = 0$) decreases much more rapidly than it does for the simple single lens. Consequently, the single-point 3-dB definition d_{rs}(3 dB) is better for a confocal microscope than for a single lens, becoming, in this case,

$$d_{rs}(3 \text{ dB}) = \frac{0.37\lambda}{\sin \theta_0} \tag{3.3.54}$$

For a single lens, the 3-dB definition [see Eq. (3.3.15)] is

$$d_r(3 \text{ dB}) = \frac{0.51\lambda}{\sin \theta_0} \tag{3.3.55}$$

Here the subscript s denotes a confocal scanned system.

For the same reasons, the sidelobe levels for this double-lens configuration are a factor of 2 in dB lower than for a single lens. For a single lens, the first sidelobe is 17.6 dB below the main lobe amplitude, whereas for the scanning microscope double-lens system, the first sidelobe level is 35 dB below the main lobe, a radical improvement. Similarly, the total power outside the main lobe is considerably reduced from the simple lens result. This implies that when objects of finite area are insonified from a coherent focused source, there is relatively little illumination outside the main lobe, so the addition of the sidelobe amplitudes from

this region does not give rise to severe spurious responses. As we have already seen in discussing Fig. 3.3.2, with incoherent insonification of a knife edge, the sidelobe intensities, rather than amplitudes, are added, so the problem is no longer serious. In the scanning microscope, the amplitudes of the sidelobes can add, but are equal in magnitude to the sidelobe intensities obtained with incoherent insonification. Thus its sidelobe problems are normally unimportant, and the ringing, speckle, and granularity of the images we normally expect with coherent imaging systems do not occur. This fact has already been illustrated from another viewpoint in our discussion of Fig. 3.3.2(c).

As we have seen throughout this section, the 3-dB definition is not always an adequate criterion for performance of an imaging system. Instead, it is better to use either the Rayleigh or Sparrow criterion for the two-point response, as described in Sec. 3.3.2. The Rayleigh definitions for the three cases of interest, incoherent imaging, coherent imaging, and confocal scanned coherent imaging, are

$$\begin{aligned} d_{ri}(\text{Rayleigh}) &= \frac{0.61\lambda}{\sin\theta_0} \\ d_{rc}(\text{Rayleigh}) &= \frac{0.82\lambda}{\sin\theta_0} \\ d_{rs}(\text{Rayleigh}) &= \frac{0.56\lambda}{\sin\theta_0} \end{aligned} \tag{3.3.56}$$

respectively. Thus there is a slight improvement in the Rayleigh definition for the scanning microscopes, compared to an incoherently insonified system with a single lens of the same aperture. Similarly, we find that the Sparrow definitions for the same cases are

$$\begin{aligned} d_{ri}\ (\text{Sparrow}) &= \frac{0.51\lambda}{\sin\theta_0} \\ d_{rc}(\text{Sparrow}) &= \frac{0.76\lambda}{\sin\theta_0} \\ d_{rs}(\text{Sparrow}) &= \frac{0.51\lambda}{\sin\theta_0} \end{aligned} \tag{3.3.57}$$

respectively.

As an example, the acoustic microscope of Lemmons and Quate typically has an acceptance angle θ_0 of 50° (i.e., an aperture of 0.77). Thus, at a frequency of 3 GHz in water, the Rayleigh two-point definition is 0.73λ or 3650 Å and the 3-dB and Sparrow definitions are 0.66λ or 3300 Å.†

The acoustic microscope has been used in transmission, for looking at thin biological samples. In the reflection mode, where the same lens and transducer

†With an aperture this wide, the paraxial formulation is not completely accurate. Here we have based our estimates on the value of sin θ_0. But it could equally be argued that using the F number z_0/D would be better; in this case, the estimated definitions would be slightly worse.

are used as both transmitter and receiver, the thickness of the sample is not necessarily limited, as it is in transmission microscopy, although the best definition is obtained only for objects near its surface. A reflection microscope, of course, is ideal for looking at integrated circuits.

We do not have space here to deal with the many possible applications and complexities of the acoustic microscope. It is important to realize, however, that the use of acoustics will produce images quite different from those obtained with optics. Acoustic waves respond to the elastic, rather than the optical, properties of the object under examination and these properties can often be of interest in medical applications. In addition, the contrast mechanisms of the acoustic microscope are not necessarily the same as those of the optical microscope. Attenuation plays its part, of course, but there are also phase-contrast mechanisms that occur due to the relatively large velocity changes between the media involved, and the fact that solids support more than one type of wave motion.

As an example of the contrast mechanisms which occur, we suppose, first, that the microscope is focused on the surface of a solid material under examination. As the impedance of many solids such as silicon, aluminum, and glass is very high compared to that of water, the reflection coefficient of the wave will be large and the image of the surface will be bright.

Now suppose that the lens is moved toward the solid so that the focal point is below its surface, as shown in Fig. 3.3.13. As discussed in Sec. 2.5.2, a Rayleigh wave can now be excited on the surface of the solid by rays leaving a point A on the lens at an angle of incidence θ_r, which satisfies the relation.

$$\sin \theta_r = \frac{V_w}{V_R} \tag{3.3.58}$$

where V_w is the acoustic velocity in the water medium of the miscroscope and V_R is the Rayleigh wave velocity [12–14]. The Rayleigh wave reradiates bulk waves into the water at an angle θ_r to the axis, which excite the lens at a point B, at the same distance from the axis as the point A [12].

A second near-axis ray incident on the surface of the solid, when reflected, can also reexcite the lens. The two resulting sets of reflected rays can be in or out of phase with each other; so the surface image may be dark or light depending

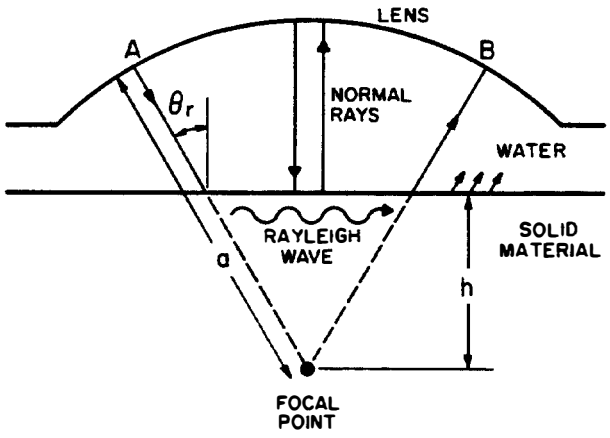

Figure 3.3.13 Rayleigh wave excitation by an acoustic microscope lens.

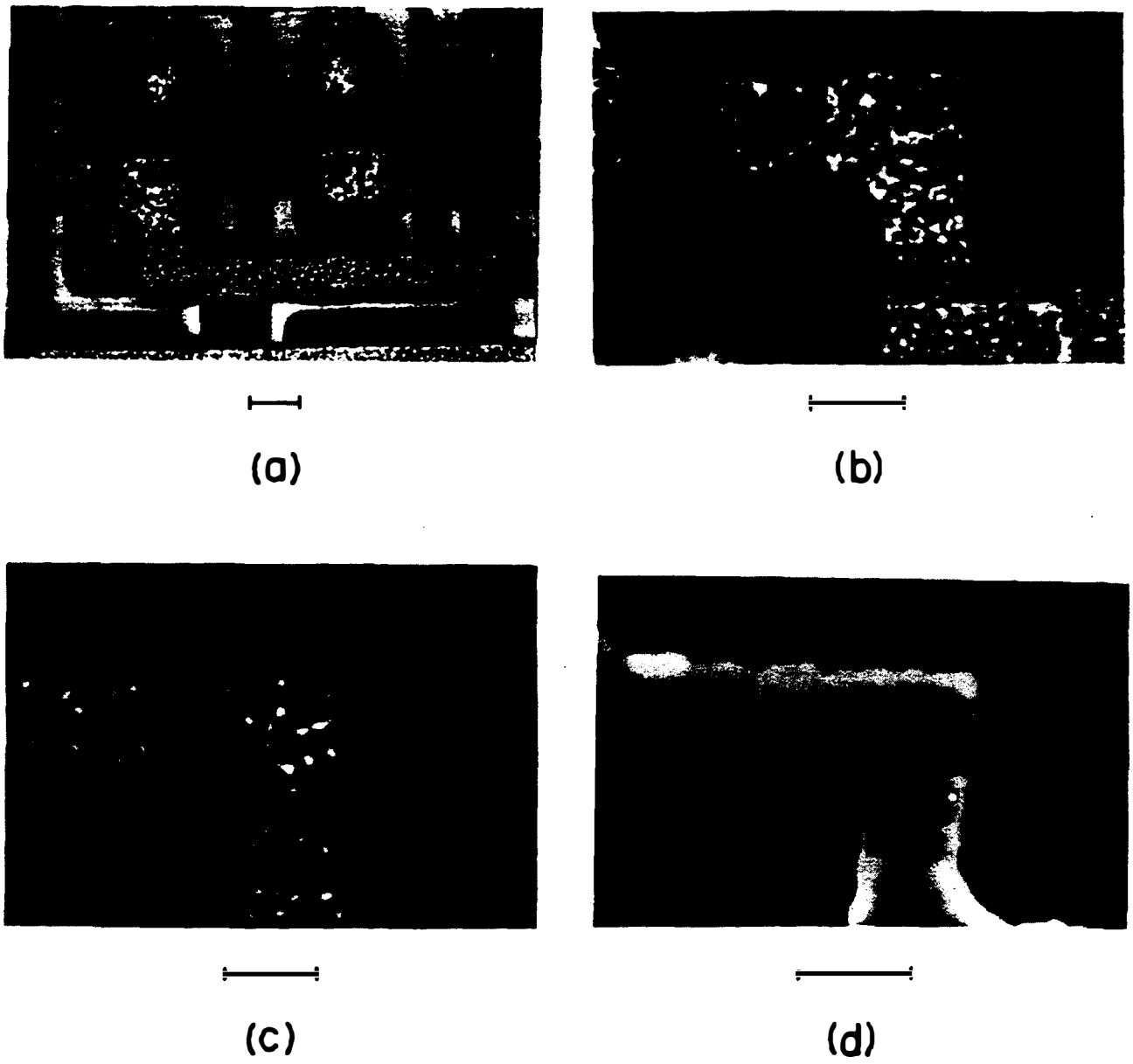

Figure 3.3.14 (a) Acoustic image of bipolar transistors on a silicon integrated circuit; (b) high-magnification acoustic image of the base contact of a transistor; (c) optical micrograph of the same area as in part (b); (d) SEM micrograph of the same area as in part (b). Scale bars are 3 μm. (After Hadimioglu and Quate [19].)

on the position $h = z_0 - z$ of the focus below the surface of the substrate. Therefore, a reversal of contrast can occur as a result of this mechanism (see Prob. 9).

By analyzing such contrast mechanisms, we can obtain a great deal of information about internal structure of solids [13–16, 19] (Problem 9). A particularly good example of this is the observation of layers underneath metal films; results of such experiments are shown in Figs. 3.3.14 and 3.3.15. In contrast to the optical situation, acoustic waves can propagate through a metal film and the amplitudes

of the reflected waves will depend critically on its thickness. If there is also an oxide layer beneath the metal film, as there is in the gate structure of many integrated circuits, the reflected waves will change in amplitude and phase, and the image will be different. Thus it is often quite easy to determine the presence of an oxide layer beneath a gate, or whether there is good adhesion between a metal layer and a substrate.

The contrast mechanisms in the acoustic microscope are still being investigated and their regions of applicability determined. The importance of this device is that it can measure an entirely new range of parameters with definitions comparable to those of the best optical microscopes.

The basic principles of scanned acoustic microscopy have also led to the development of a new type of scanned coherent optical microscope with excellent definition. The scanning technique is also being employed for photoacoustic microscopy, where an optically focused scanned modulated laser beam is used to

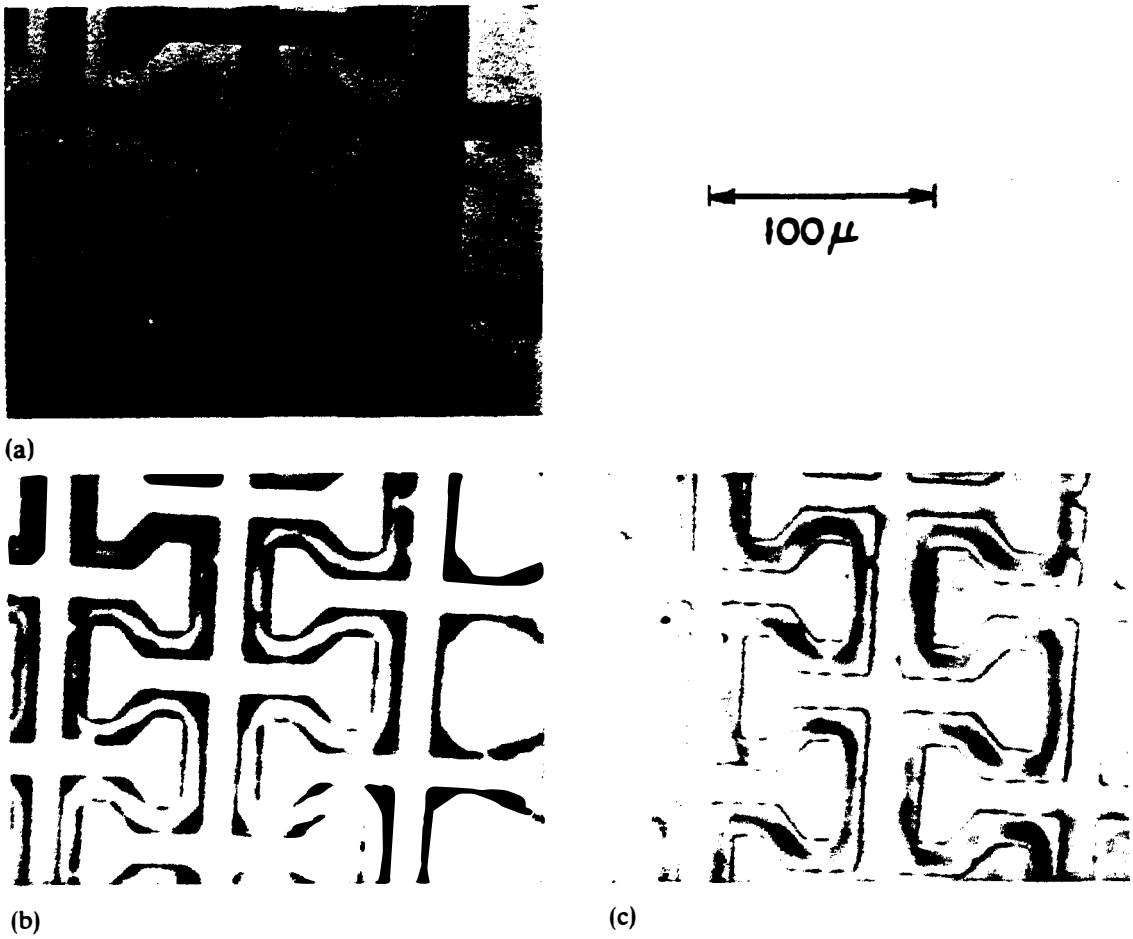

Figure 3.3.15 Optical (a) and acoustic (b) and (c) comparison of a 1000-Å layer of chrome on glass. The acoustic pictures are taken at a frequency of 2.6 GHz. In part (b), the focal spot has been moved 0.5 μm below the surface; in part (c), it has been moved −1 μm below the surface. The effects of poor adhesion can be seen clearly. (After Bray et al. [14].)

modulate the surface temperature of a solid. The consequent expansion and contraction of the solid excites acoustic waves, which can be detected by a relatively coarse acoustic transducer placed against the lower surface of the substrate. Acoustic waves can also be detected in the air or liquid medium above the substrate [20]. The images obtained are comparable in definition to those obtained with the optical beam. Similar ideas are also being applied to design a scanned x-ray microscope. The reader is referred to the proceedings of a conference on scanned image microscopy for further information on this subject [15].

3.3.3 Gaussian Beams and the Paraxial Equation

In Sec. 3.3.2 we showed that a spherical transducer produces a focused beam whose diameter at the focal plane is determined by the initial angle of convergence of the beam, and whose focal length is approximately equal to the radius of curvature of the transducer, which determines the shape of the initial phase front of the wave. The signal amplitude can vary rapidly along the axis and over radial cross sections. As we have seen, this is because of the rapidly varying phase differences between the rays emitted from neighboring points on the transducer; the more rapid the phase variation with radius, the more closely spaced are the maxima and minima. Thus at points near the transducer where the phase varies rapidly, both the axial and radial variations of the field are rapid and large.

One way to overcome this difficulty is to taper the amplitude of excitation of the transducer over its radius. It is clear that if the amplitude of the excitation falls off monotonically away from the central axis, the outer rays will not be able to cancel out the contributions from those near the axis; thus the field variation along the axis and over a radial cross section will be much less. In fact, as we shall show, a Gaussian taper gives the ideal amplitude variation, producing a beam with a Gaussian profile whose fields vary smoothly in all directions.

Wave equation for paraxial beams. Gaussian beams have been extensively studied in laser applications and are well understood [21–23]. For a longitudinal acoustic wave, we write the wave equation in the form

$$\nabla_T^2\phi + \frac{\partial^2\phi}{\partial z^2} + k^2\phi = 0 \tag{3.3.59}$$

where $\nabla_T^2 \equiv \partial^2/\partial x^2 + \partial^2/\partial y^2$. We define ϕ as

$$\phi = f(r, z)e^{-jkz} \tag{3.3.60}$$

Then we make the approximation that $f(r, z)$ varies slowly enough that $|\partial f/\partial z| \ll |kf|$ and $|\partial^2 f/\partial z^2| \ll |k\partial f/\partial z|$. In this case, Eq. (3.3.59) can be written in the approximate form

$$\nabla_T^2 f - 2jk\frac{\partial f}{\partial z} = 0 \tag{3.3.61}$$

The usual treatment of laser optics is to obtain an exact solution of Eq. (3.3.59); this solution has the profile of a Gaussian beam [21–23]. Here we shall

adopt a different approach, which gives the same solution. We do this to better understand the paraxial approximation and correlate the results with our earlier derivation for spherical lenses. We use Eq. (3.1.35) and write the potential at any point in the form

$$\phi(x, y, z) = -\frac{1}{2\pi}\iint u_z(x', y', 0)\frac{e^{-jkR}}{R}\,dx'\,dy' \tag{3.3.62}$$

We now make the paraxial approximation, writing $R \approx z + [(x - x')^2 + (y - y')^2]/2z$, that is, we approximate the solution of the spherical wave equation $\phi = \exp(-jkR)/R$ by writing

$$\frac{e^{-jkR}}{R} \approx \frac{e^{-jkz}e^{-jk[(x-x')^2+(y-y')^2]/2z}}{z} \tag{3.3.63}$$

Note that *this approximate result is an exact solution of Eq. (3.3.61).* We can therefore use the paraxial approximation as the solution of Eq. (3.3.59), provided that the beam profiles with which we are concerned have only relatively slow variations in amplitude along the axis. In this case we can write Eq. (3.3.62) in the form

$$\phi(x, y, z) = -\frac{e^{-jkz}}{2\pi z}\iint u_z(x', y', 0)e^{-jk[(x-x')^2+(y-y')^2]/2z}\,dx'\,dy' \tag{3.3.64}$$

Gaussian beam. We now consider a beam with a Gaussian profile at the plane $z = 0$. We shall show that the profile of this beam is Gaussian everywhere. We take the initial displacement amplitude of the beam at $z = 0$ to be

$$u_z = u_0 e^{-(r'/w_0)^2} \tag{3.3.65}$$

where w_0 is the effective radius at the $1/e$ point of the Gaussian profile.

We substitute Eq. (3.3.65) into Eq. (3.3.64) and write

$$\phi(x, y, z) = \frac{u_0 e^{-jkz}}{2\pi z}\int_{-\infty}^{\infty}\int_{-\infty}^{\infty}[e^{-(x'^2+y'^2)/w_0^2}] \times \{e^{-jk[(x-x')^2+(y-y')^2]/2z}\}\,dx'\,dy' \tag{3.3.66}$$

or

$$\phi(x, y, z) = -\frac{u_0 e^{-jk(z+r^2/2z)}}{2\pi z}\int_{-\infty}^{\infty}\int_{-\infty}^{\infty}[e^{-(jk/2z+1/w_0^2)(x'^2+y'^2)}] \times [e^{-jk(xx'+yy')/z}\,dx'\,dy'] \tag{3.3.67}$$

We complete the square in x' and y' in the argument of the exponential and carry out the infinite integrals using the relation

$$\int_{-\infty}^{\infty} e^{-\alpha x^2}\,dx = \sqrt{\pi/\alpha} \tag{3.3.68}$$

We then find, after considerable algebra, that $\phi(x, y, z)$ is symmetric about the z

axis and can be written in the form

$$\phi(r, z) = \phi_0 \frac{w_0}{w(z)} e^{-j[kz - \eta(z)]} e^{-r^2[1/w^2 + jk/2R]} \tag{3.3.69}$$

This result is stated in terms of the following set of parameters:

$$z_0 = \frac{\pi w_0^2}{\lambda} \tag{3.3.70}$$

$$w^2(z) = w_0^2\left(1 + \frac{z^2}{z_0^2}\right) \tag{3.3.71}$$

$$\eta(z) = \tan^{-1}\frac{z}{z_0} \tag{3.3.72}$$

$$R(z) = z + \frac{z_0^2}{z} \tag{3.3.73}$$

and

$$-jk\phi_0 = u_0 \tag{3.3.74}$$

The parameters $w(z)$, w_0, z, and $R(z)$ are illustrated in Fig. 3.3.16.

The potential varies smoothly along the axis and has a Gaussian amplitude variation with radius at all values of z. The radius of the beam at the $1/e$ point is $w(z)$. For $z >> z_0$, the surfaces of constant phase are where

$$z + \frac{r^2}{2z} = \text{constant} \tag{3.3.75}$$

but the equation of a circle of radius $R >> z_0$, centered on the origin in the region where $R >> r$, is

$$R = \sqrt{z^2 + r^2} \approx z + \frac{r^2}{2z} \tag{3.3.76}$$

A comparison of Eq. (3.3.75) with Eq. (3.3.76) shows them to be identical in form. Therefore, the surfaces of constant phase are spherical and of radius R when $z >> z_0$. Furthermore, Eq. (3.3.71) shows that the profile of the $1/e$ points of the beam

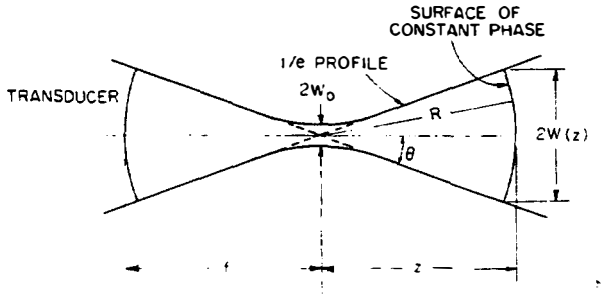

Figure 3.3.16 Profile of a Gaussian beam emitted from a transducer at $z = -f$.

$r = w$ is hyperbolic in shape, becoming a straight line in the regions where $z >> z_0$. Thus the half-angle θ of the beam at the $1/e$ points is

$$\theta = \tan^{-1} \frac{w_0}{z_0} \approx \frac{\lambda}{\pi w_0} \tag{3.3.77}$$

We conclude that a Gaussian beam with an input half-angle θ will have a $1/e$ width at the focus (i.e., minimum beam diameter) of

$$d_r\left(\frac{1}{e}\right) = 2w_0 \approx \frac{2\lambda}{\pi\theta} \tag{3.3.78}$$

If the exciting transducer intercepts the axis at $z = -f$, the relation between f and $w(f)$ is

$$f = z_0 \left(\frac{w^2}{w_0^2} - 1\right)^{1/2} = \frac{\lambda}{\pi\theta^2} \left(\frac{w^2}{w_0^2} - 1\right)^{1/2} \tag{3.3.79}$$

Thus we can regard f as the focal length of a Gaussian transducer whose coordinates are defined by Eq. (3.3.79). The axial field drops by 3 dB from the maximum where $w = w_0\sqrt{2}$ or at $z = \pm z_0$, that is, the depth of focus is

$$d_z(3 \text{ dB}) = 2z_0 = \frac{2\lambda}{\pi\theta^2} \tag{3.3.80}$$

Apodization. A Gaussian beam would be very suitable for probing complicated structures because of its relatively simple form; the problem is how to produce it. In practice, the transducer cannot have an infinite width and a Gaussian taper to infinity; its width must be finite. In optical systems, this finite width is many wavelengths in extent, so the Gaussian taper is a very good approximation to the truth. In acoustic systems, however, where the wavelength is larger, this is not always the case.

We can use Eq. (3.3.64) to show that if the phase variation at a spherical acoustic transducer located at $z = -f$ is taken to be of the form $\exp [jk(x'^2 + y'^2)]/2z$, there will be no phase variation at the focal plane $z = 0$. Furthermore, the amplitude variation at this focal plane [see Prob. 5 and Eq. (3.3.40)] is the two-dimensional Fourier transform of the amplitude variation at the plane $z = -f$. This argument leads to the conclusion that a Gaussian amplitude profile at the transducer yields a Gaussian beam.

More generally, there are various types of aperture weightings that can form a beam at the focal plane that is very much like a Gaussian beam. The excitation obtained tends to be very close to that required for a Gaussian beam, but with a finite step in $u_z(x', y', 0)$ or $\phi(x', y', 0)$ to zero at the edges of the transducer. One example of a commonly used taper in signal processing that is appropriate for focusing, as discussed in Sec. 4.5, is *Hamming* weighting; this is also the one-dimensional form $u_z(x')$, which would have an amplitude at a cylindrical transducer of the form

$$A(x') = 0.08 + 0.92 \cos^2 \frac{\pi X'}{D} \tag{3.3.81}$$

A detailed study of the Fourier transform of $A(x)$, which is also given in Sec. 4.5, leads to the conclusion that the Hamming taper is similar to the Gaussian taper, but not as extreme. It yields a focal width 1.3 times the focal width for a uniform amplitude excitation at the transducer, with a maximum first sidelobe level of -4 dB, as compared to -13 dB for the sinc X response obtained with a focused, uniformly excited strip beam.

It is not easy to construct a Gaussian beam because it is not easy to taper the amplitude of the beam. It is far simpler to make such transducers when an array of separately excited elements is employed, for this allows us to excite each element with the correct amplitude (see Sec. 3.5.2) [21]. Thus the technique for making single transducers involves depositing electrodes on the piezoelectric substrate to simulate such an array, and either exciting the electrodes with suitable amplitude weighting or varying the area of the electrodes to simulate this weighting.

PROBLEM SET 3.3

1. In this problem we use some simple ways to estimate the 3-dB focal diameter and depth of focus.

(a) Consider a spherical lens of radius a. Estimate the depth of focus for a point on the axis by assuming that the 3-dB point is where the ray lengths R from a point on the axis to the edge and from the same point on the axis to the center of the lens differ by $\lambda/2$. Compare your result with Eq. (3.3.27).

(b) Estimate the diameter of the beam at the 3-dB points d_r(3 dB) by finding the condition at the focal plane for which $R(\max) - R(\min) = \lambda/2$. In both cases you will find it convenient to use Eq. (3.3.5).

(c) Consider a hollow beam from an annular ring focused transducer that extends from $r = a$ to $r = b$. Using the methods of parts (a) and (b), estimate the depth of focus and the 3-dB width of the beam when $b - a \ll a$. Compare your estimate of the 3-dB width of the beam with the exact solution for $(b - a) \to 0$.

2. **(a)** Consider an annular ring focused transducer (i.e., part of a sphere of radius z_0 extending from $r = a$ to $r = b$). Discuss, physically, why the depth of focus becomes infinite as $b \to a$. To do this, consider the fields at any point on the axis due to rays arriving from the transducer. By tracing these rays to the focal plane $z = z_0$, show, physically, that there will be considerable energy on the sidelobes at the plane $z = z_0$.

(b) If $b - a \ll a$, use Eq. (3.3.7) to work out the total power in the main lobe of the beam at its focal plane, where the main lobe is defined as being the region between the first zero-amplitude points. Compare this with the total power P(total) supplied to the beam at $z = 0$ (assume that the acoustic impedance is the plane wave impedance). Find

$$S = \frac{P(\text{total}) - P(\text{main lobe})}{P(\text{main lobe})} = \frac{P(\text{sidelobe})}{P(\text{main lobe})}$$

and show that the parameter $S \to \infty$ as $(b - a)/a \to 0$. You will need the relation

$$\int_0^{X_m} XJ_0^2(\alpha X) = \frac{X_m^2}{2} J_1^2(\alpha X_m)$$

where $J_0(\alpha X_m) = 0$, $\alpha X_1 = 2.405$, and $J_1(\alpha X_1) = 0.520$.

3. (a) Generalize Eq. (3.3.6) to determine the signal received at r, z, ψ due to the excitation $u_z(r', \psi')$ [exp $(-jkR_1]$ at r', ψ', z_1.
   (b) Use the method of stationary phase, as described in Appendix G, to show that the main contribution of the signal arriving at r, ψ comes from r_0', ψ_0', where the phase Φ is such that $(\partial\Phi/\partial r') = 0$ and $(\partial\Phi/\partial\psi') = 0$. Show that r, ψ lies on the optical ray path from r_0', ψ_0'. This result is, in fact, the mathematical justification for ray tracing.
   (c) Following through with the method of stationary phase, carry out a Taylor expansion in terms up to $(\psi' - \psi_0')^2$ and $(r' - r_0')^2$ to find the amplitude of the beam at r, ψ, and compare your result with what you would expect from geometrical optics. This result gives a complete justification of ray tracing theory.
   (d) Discuss why this type of theory breaks down near the focus or when ka is small.
4. Prove Eq. (3.3.69) from Eq. (3.3.67) by carrying through the algebra.
5. An acoustic beam is excited at $z = 0$ with an amplitude

$$u_z(r', 0) = A(r')e^{jkr'^2/2z_0}$$

   (a) Find the focal point of this beam using the paraxial theory of Sec. 3.3.3.
   (b) Assuming that the beam is excited with a Gaussian amplitude profile $A(r') = \exp[-(r'/w)^2]$, find the profile of the beam at the focal plane. You will find it convenient to write

$$r' \cos\psi' = x'$$

$$r' \sin\psi' = y'$$

$$r \cos\psi = x$$

$$r \sin\psi = y$$

   and to work out your results in Cartesian coordinates using Eq. (3.3.64).
6. Suppose that we construct a reflection acoustic microscope with a sapphire lens, using a liquid indium–gallium mixture as the operating medium, to observe internal cracks in Pyrex glass. The incident wave in the liquid excites a shear wave in the glass. For an operating frequency of 500 MHz, a spherical lens with an acceptance angle of $\theta_0 = 45°$ is employed. Estimate the Sparrow definition of the microscope and the 3-dB depth of focus of the scanning system.
   Note: For the depth of focus, you will need to modify the usual depth of focus formula to account for the fact that the lenses are used twice [see Eq. (3.3.52)].

Indium–gallium:	$V_l = 2.8$ km/s
Pyrex glass:	$V_s = 3.28$ km/s
Sapphire:	$V_l = 11$ km/s

7. Consider the solution of Eq. (3.3.61) for the beam from a flat piston transducer. Use the paraxial forms for the expression of Eq. (3.2.62) [see Eq. (3.2.5)] for the potential on axis for a flat piston transducer to find the potential at a point r, z by writing

$$f(r, z) = f_0(z) + r^2 f_2(z) + r^4 f_4(z) + \cdots$$

   and equating terms of equal power in r in Eq. (3.3.61). You will find it convenient to write Eq. (3.3.61) in the form

$$\frac{1}{r}\frac{\partial}{\partial r}\left(r\frac{\partial f}{\partial r}\right) - 2jk\frac{\partial f}{\partial z} = 0$$

(a) By expanding $f(r, z)$ to fourth order in r, find the value of r for the 3-dB point at $z = a^2/\lambda$. How does this compare with the exact result ($r = 0.35a$) and with the result of an expansion to second order?

(b) By writing f_4 in terms of f_0, show that the potential initially increases with r at the planes where $\partial f_0/\partial(z) = 0$ and $\partial^2 f_0/\partial z^2$ is positive (i.e., where there is a minimum potential on the axis).

8. Use the method of Prob. 7 to calculate the potential in the neighborhood of the focus of a spherical lens. It is convenient to employ Eq. (3.3.25) in the approximate form of Eq. (3.3.29). Keep only second-order terms in r and z by using the approximation that near the focus, $\text{sinc } X \approx 1 - \pi^2 X^2/6$. Show that to this degree of approximation, the contours of constant amplitude are ellipsoids.

(a) Find the ratio of the major to minor axes of the ellipsoids when the amplitude of the potential on the surface of each ellipsoid is reduced to κ times its maximum value at the focus.

(b) Find the phase variation of the potential along the surface of an ellipsoid of constant κ.

9. Consider the situation shown in Fig. 3.3.13, where rays normal to the surface of the substrate and at the Rayleigh angle to the substrate excite return echoes.

(a) Assuming that the wave velocity in the lens material is infinite, work out, by ray tracing, the time-delay difference T between the two sets of echoes. Give your result in terms of the Rayleigh wave velocity V_R, the velocity in water V_w, and the radius a of the lens. Take the focal point to be at a depth h below the surface of the substrate.

Answer:

$$T = \frac{2h}{V_w}(1 - \cos\theta_R)$$

(b) Assuming that a CW signal of frequency $\omega/2\pi$ is being used to excite the lens, work out expressions for the values of h at the points where the output signal is maximum or minimum. Suggest how this information could be used to determine V_R.

10. (a) By expanding $\text{sinc } X$ to second order in X, use Eq. (3.3.25) to find the form of the potential on the axis of a spherical lens near the geometrical focus $z = z_0$. Writing $z/z_0 = p$, differentiate with respect to p and find where the potential on axis is maximum. This is the true geometrical focus $z = f$ for the lens.

(b) Find an approximate expression for $Z(f)$ from your result.

(c) Compare your results with the exact solution of Fig. 3.3.8 for $S = 0.2$, $S = 0.5$, and $S = 1$.

3.4 PULSED EXCITATION OF TRANSDUCERS

In Sec. 3.2.1 we showed that there are relatively rapid variations of the fields in the Fresnel region and slower variations, with distance and angle, in the Fraunhofer region. These field variations are associated with phase differences of the rays that reach a given point from the transducer. When a transducer is excited with a short pulse that is only one or two RF cycles long, some of these phase cancellations and additions disappear and the response becomes smoother. For instance,

the nulls found on the axis in the CW case disappear, to be replaced by minima in the pressure profile, and the variation of the fields across the beam are smoother.

In this section we carry out the analysis for pulsed excitation in a liquid. For simplicity and for consistency with the literature, we shall derive our results in terms of the initial velocity excitation of the transducer face, and determine the pressure at a point z, r, θ in space. We shall show that when a transducer is excited uniformly across its face, the signal received at the point z, r, θ is strictly dependent on the distance of this point from the nearest and farthest points on the transducer. The length of the signal received at z, r, θ depends on the time difference between the rays from these two points.

The particle velocity can be written in the form

$$\mathbf{v} = -\nabla\psi \tag{3.4.1}$$

with $\psi = -\partial\phi/\partial t$ defined as the *Rayleigh velocity potential.*† Then, from the Green's function theory [Eq. (3.1.36)], it follows that

$$\psi = \frac{1}{2\pi}\int_s \frac{v(t - R/V)}{R} ds \tag{3.4.2}$$

where s is defined as the area of the transducer and $v(t - R/V)$ is the velocity of the transducer face at a time $t - R/V$.

The equation of motion for a liquid can be written in the form

$$\nabla p = -\rho_{m0}\frac{\partial v}{\partial t} \tag{3.4.3}$$

where $p = -T_1 = -T_2 = -T_3$ is the pressure. It follows from Eqs. (3.4.1) and (3.4.3) that

$$p = \rho_{m0}\frac{\partial\psi}{\partial t} \tag{3.4.4}$$

where p is the pressure in the liquid.

Transient response on- and off-axis of a piston resonator. We now consider the transient response on the axis of a cylindrical piston transducer. We assume that the velocity $V(t)$ at the transducer is symmetric about the axis. Equation (3.4.2) is written in the form

$$\psi = \int_{r'=0}^{a} \frac{v(t - R/V)}{R} r'\, dr' \tag{3.4.5}$$

Putting $R^2 = r'^2 + z^2$ and $R\, dR = r'\, dr'$, it follows that

$$\psi = \int_z^{\sqrt{z^2+a^2}} v\left(t - \frac{R}{V}\right) dR \tag{3.4.6}$$

†Note that the use of a minus sign with $v = -\nabla\psi$ agrees with the definition for the velocity potential used by Lord Rayleigh.

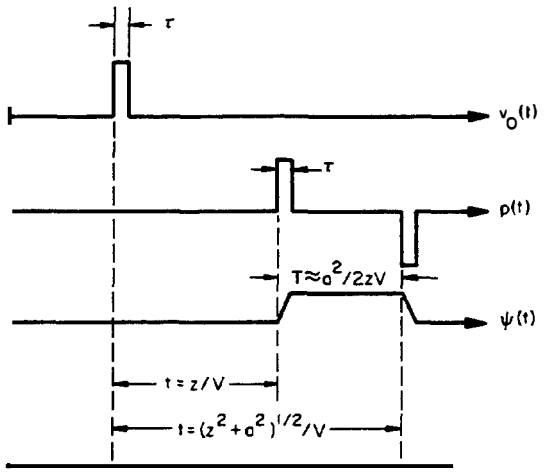

Figure 3.4.1 Exciting and received signals on-axis in the Fresnel region when a transducer is excited with a short pulse of length τ.

If the transducer is excited by an extremely short velocity pulse of amplitude v_0 and length τ, then Eq. (3.4.6) implies that at the plane z, the potential on-axis $\psi(0, z)$ will be of constant amplitude $\tau v_0 V$ and finite in the time range $z/V < t < (z^2 + a^2)^{1/2}/V$, that is, from the time the initial ray along the axis reaches point 0, z to the time the last ray from the edge of the transducer reaches the same point.

The pressure p at the point 0, z is the differential with respect to time of the velocity potential. Thus we can write

$$p = \rho_{m0} \int_z^{\sqrt{z^2+a^2}} \frac{\partial}{\partial t}\left[v\left(t - \frac{R}{V}\right)\right] dR \tag{3.4.7}$$

or differentiate ψ directly to find p. Writing $\partial v/\partial t = -V(\partial v/\partial R)$, it follows that

$$p = \rho_{m0} V\left\{v\left(t - \frac{z}{V}\right) - v\left[t - \frac{(a^2 + z^2)^{1/2}}{V}\right]\right\} \tag{3.4.8}$$

Fresnel region. Equation (3.4.8) shows that the pressure at the point z due to an initial short velocity pulse v_0 of length τ consists of a positive pulse followed by a negative pulse, with the pulses delayed from each other by a time T, where

$$T \approx \frac{(z^2 + a^2)^{1/2} - z}{V} \approx \frac{a^2}{2zV} \tag{3.4.9}$$

We have assumed in this derivation that $T >> \tau$ or $a^2/2z >> V\tau$, which corresponds to the observer being in the Fresnel, or near-field, region. These results are illustrated in Fig. 3.4.1. In this case, it follows from Eq. (3.4.8) that the pressure pulses have equal and opposite amplitudes of value

$$|p| = \rho_{m0} v_0 V \tag{3.4.10}$$

where v_0 is the initial pulse amplitude. Hence, on-axis, *the pressure in the Fresnel region does not vary with z.*

Another way of looking at this result, which gives a great deal of physical insight into the behavior of pulsed transducers, has been given by Weight and

Hayman [24]. They suggest that there are two contributions to the signal, a plane wave and an edge wave. Consider a point r, z, which is off-axis with $r < a$. When the transducer is excited by a short pulse, there is a contribution to p from the nearest point to the receiver delayed by a time $T = z/v$. There will be contributions of opposite sign from points on the edge of the transducer, as we have described. Thus it is as though two types of waves are excited: (1) a quasi-plane wave, excited by the main surface of the transducer, whose amplitude is independent of r when $r < a$; and (2) following signals from the edge of the transducer, known as *edge waves*, which are of opposite sign from the quasi-plane wave pulse and delayed by a time $t = R/v$, where R is the distance between the receiving point and a point on the edge of the transducer. We observe that the quasi-plane wave contribution does not exist at points r, z where $r > a$.

This concept has been generalized to deal with waves excited by a transducer in contact with the surface of a solid. In this case, a longitudinal wave transducer, for example, can excite longitudinal and shear edge waves, as well as surface waves. When a finite-length pulse is used, the output can be calculated by taking the convolution of the exciting signal with the calculated response to a very short pulse.

Fraunhofer region. In the Fraunhofer region, where $a^2/2z \ll V\tau$, the pulses overlap and tend to cancel each other out. These results are illustrated in Fig. 3.4.2. From Eq. (3.4.8) it follows that with $a^2 \ll z^2$ and $a^2/2z \ll V\tau$, the pressure consists of two short pulses of opposite sign of length $a^2/2zV$ and amplitude $\rho_{m0}Vv_0$, separated by a time τ, as illustrated in Fig. 3.4.2. The velocity potential is the negative integral of the pressure pulse, and corresponds to a positive pulse of length τ and amplitude ψ, defined as

$$\psi = \frac{v_0 a^2}{2z} \tag{3.4.11}$$

We see that the potential falls off as $1/z$, as we might expect.

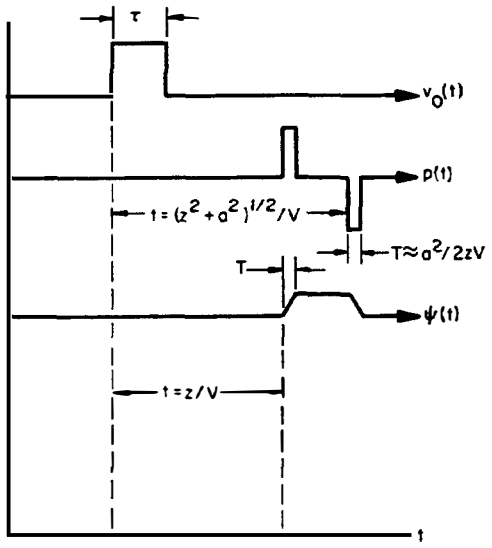

Figure 3.4.2 Exciting and received signals on-axis in the Fraunhofer region when a transducer is excited with a short pulse of length τ.

Excitation with a tone burst. The picture becomes clearer when the transducer is excited by an RF tone burst of constant amplitude, perhaps several RF cycles long. On the axis in the Fresnel, or near-field, region (defined at the frequency of the tone burst), the arriving signal corresponds to two tone bursts of opposite sign, delayed from each other by the time difference $T = a^2/2zV$. In the Fresnel zone, at a point where the pressure is normally at a maximum, these two tone bursts catch up to each other and add where they overlap, thus doubling the amplitude of the signal. At a CW pressure minimum, the overlapping tone bursts tend to cancel each other out. In the Fraunhofer, or far-field, region, the overlapping tone bursts are out of phase, and the signal amplitude is reduced.

Numerical calculations of this type have been made by Robinson et al. [25], Beaver [26], and Tancrell et al. [27]. Beaver has carried out the calculations for an exciting waveform one RF cycle long, as shown in Fig. 3.4.3. He assumed in his calculations a piston of radius 5λ.

Beaver has also carried out the calculations at different axial distances to account for the pressure variation over the radial cross section. As we might expect, the plane wave signals arriving from the transducer surface are essentially undistorted, while those from its edge add out of phase because of their different

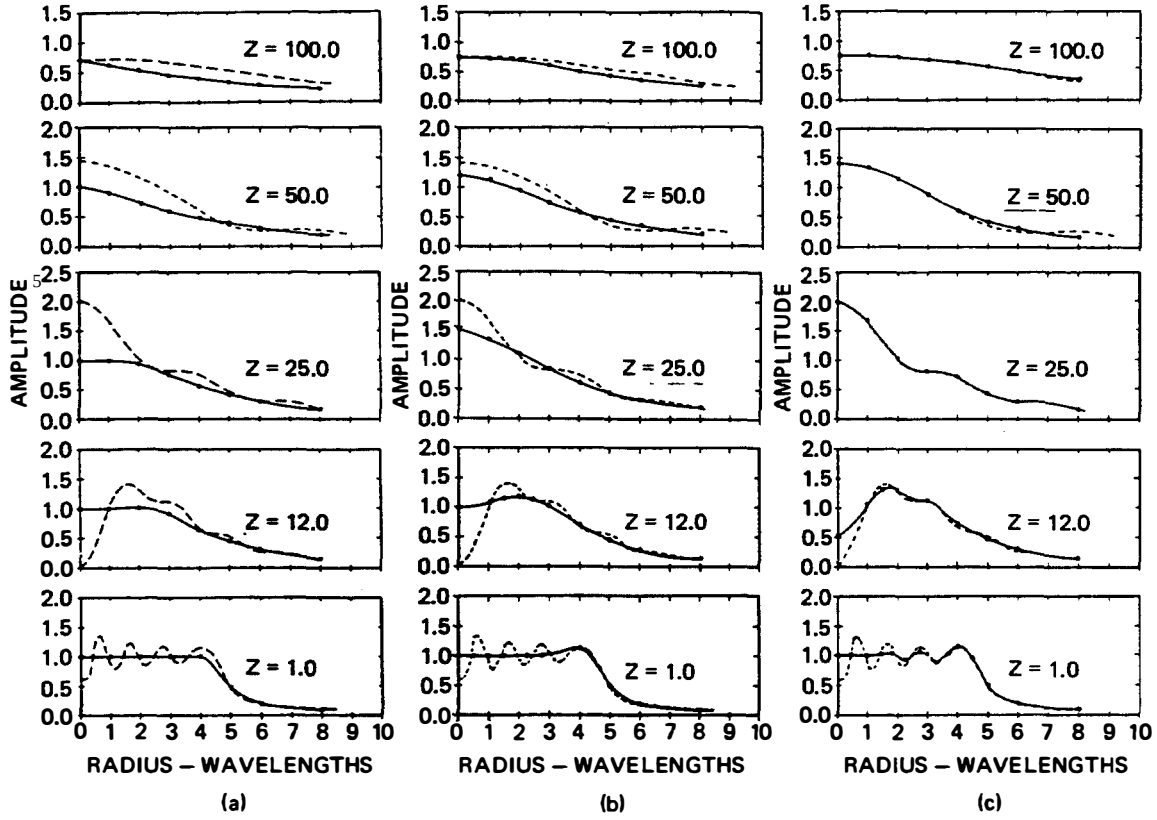

Figure 3.4.3 Sonic-field amplitude verus radius for various normalized axial positions Z expressed in wavelengths. $Z = 25$ corresponds to the Fresnel length $S = 1$. The CW field profile is shown by the dashed-line plots. (a) A 5.0λ radius piston, type I pulse (half an RF cycle); (b) a 5.0λ radius piston, type II (one full RF cycle); (c) a 5.0λ radius piston, type III pulse (four RF cycles). (After Beaver [26].)

time delays. At points off-axis, there is always a strong signal from the plane wave component, with a relatively weak signal arriving from the edge of the transducer.

Beaver calculated how the pressure varies with axial position for signals, or tone bursts, that he calls types I, II, and III, which correspond to half an RF cycle, one full RF cycle, and four RF cycles long, respectively. These are compared to the CW results in Fig. 3.4.3. As we might expect, the pressure variation with radius tends to be smoothed out by the use of short pulses. This is because there is very little interference between the RF signals that arrive from different parts of the transducer when short exciting pulses are used. As a result, when short-pulse excitation is employed, the field variations are smoother and the pronounced maxima and minima observed in the CW case tend to disappear. Thus experiments carried out with short RF pulses are in some ways not as difficult to interpret as those that employ long RF pulses.

Tancrell et al. obtained a very similar set of results for a rectangular transducer

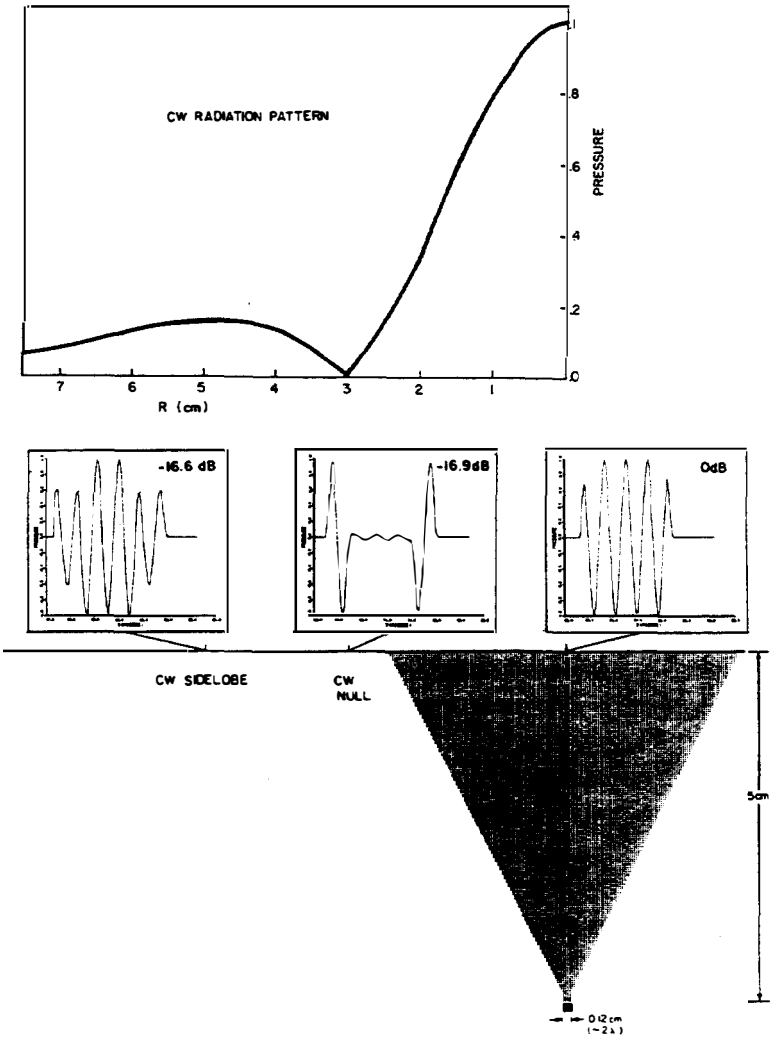

Figure 3.4.4 Far-field pattern for CW radiation and for a four-cycle exciting pulse, showing the time waveform at locations corresponding to the CW null and the CW sidelobe. (After Tancrell et al. [27].)

[27]. In Fig. 3.4.4, the pulse shapes obtained confirm the general picture given by Figs. 3.4.1 and 3.4.2. For several cycle-exciting pulses, the signals on axis in the far field tend to add, thus making the center three cycles larger than the ends of the pulse. At a CW null in the far field, however, the signals tend to cancel, except where they fail to overlap. Once more at a sidelobe maximum, they tend to add where they overlap, but are smaller where they do not. The maximum time-delay differences of the signals arriving at a particular point are determined by the distances of the nearest and farthest rays to the transducer from that point. The extremal rays arriving at a point on axis correspond to a ray from the center and another from the edge, but for a point far off the axis, the extremal rays correspond to those from each edge of the transducer.

PROBLEM SET 3.4

1. Consider a spherical transducer excited by a short unipolar positive velocity pulse. Work out the form of the pulses to be expected on axis, both in front of the optical focal point, at the optical focal point, and beyond the focal point. Show that the sign of the pulse changes from one side of the focal plane to the other. You will need to generalize the results of Eq. (3.4.8) using Eqs. (3.3.7) and (3.3.24).

3.5 LENSLESS ACOUSTIC IMAGING

3.5.1 Introduction

A. Applications of Acoustic Imaging

In Sec. 3.3.2 we described the scanned acoustic microscope, which employs a physical lens and mechanical scanning to produce high-quality acoustic images. Here we will emphasize an alternative approach to the problem, by reviewing other methods of acoustic imaging that use acoustic waves to probe a material and produce a visual image of its internal structure. We will describe how electronically scanned arrays and other synthetic imaging techniques, such as acoustic holography, can replace the physical lenses normally employed in optics. Such techniques give far more flexibility and speed, and tend to eliminate some of the difficulties due to internal reflections that are associated with physical lenses, but with the penalty of considerable complexity. They are used to detect flaws in materials and probing the human body in medical diagnostics; they are also employed in sonar systems for visualizing objects in the sea.

Because of their complexity, most of the work on electronically scanned imaging has been limited to two-dimensional systems. These systems typically have good definition in one transverse dimension, the x direction, and good range resolution in the z direction, but definition in the other transverse dimension, the

y direction, is relatively poor. For this reason, much of our analysis will be limited to one-dimensional array systems.

In the nondestructive testing (NDT) field, the standard techniques employed for inspection of solid parts have included x-rays, radiographics, and acoustics, eddy current testing in metals, and dye penetrants. Noninvasive techniques currently employed in clinical testing include radiographic and acoustic methods and, to a more limited extent, infrared detection. Radiological techniques have, of course, been used in both medical and NDT applications for many years, with the major advantage that the resultant pictures are in a familar form. However, they also have several disadvantages. The most serious, of course, is the potential danger to human beings associated with ionizing radiation: for example, X-rays cannot safely be used to examine the fetus of a pregnant woman. In addition, radiological techniques are difficult to apply to moving objects, such as the valves in the heart. Neither are they suited to large metallic structures because of the highly penetrating radiation they require, which, as well as being dangerous, is also difficult to use, because it takes very large apparatus and requires the area where the structure is examined to be cleared of all personnel.

Acoustic waves can penetrate both the body and large metal structures without difficulty. They measure mechanical or elastic properties, which, in the NDT case, are directly associated with the strength and life of the structure. In the medical case, these properties are related to the elastic and mechanical properties of the body, which are of direct clinical interest.

We can gain important insights into the nature of the images obtained with acoustic waves from an understanding of acoustic wave propagation. An acoustic image will not have the familiar form of an optical image, which is a serious problem. As an example, we expect the optically displayed acoustic image of a sphere to look more complicated and less familiar than the optical image, for several reasons. First, most materials are at least partially transparent to acoustic waves, whereas an optical image normally corresponds to the visualization of the surface of an object. Visually, we can see only the surface of the body. An acoustic wave, however, sees its entire interior, including all the regions through which it passes, as though the object were semitransparent. This phenomenon complicates the nature of the image, as well as giving more information than is optically observable.

A second problem associated with acoustic wave imaging is that acoustic waves are usually excited by signals with a relatively narrow bandwidth. Thus, as discussed in Sec. 3.3.1, the same problems that occur when observing objects with laser illumination—namely, interference rings and speckle—also are observed in acoustic images. This again makes an acoustic image more difficult to recognize than the optical image we are used to.

A third important phenomenon in NDT is that both longitudinal and shear waves can propagate in the same medium. When, for instance, a longitudinal acoustic wave is reflected from an arbitrary object, it can give rise to both longitudinal and shear reflected waves. Suppose, for instance, that we want to obtain an image of a simple object such as a spherical defect in a solid. As discussed in Sec. 3.6, we expect to see signals reflected from its front face, as well as both shear

and longitudinal waves, which pass through its interior, reflected from its back face. Thus the images obtained from even as simple an object as a sphere may be considerably more complicated than the equivalent optical images, and less easy to recognize.

One advantage of acoustical techniques is the ease with which extremely short acoustic pulses, one or two RF cycles long, can be employed. Consequently, good range definition can be obtained relatively easily with acoustics, whereas the range definition in optics is dictated essentially by the depth of focus of a lens. Thus an important advantage of acoustic imaging is that we can differentiate image planes at different distances from the transmitter by using short pulses. In Sec. 3.4 we reexamined some of the concepts of acoustic wave propagation to take account of transient phenomena that are not normally of importance in optics.

Because this new acoustic technology produces images that are not always easily recognizable to an untrained observer, it has taken time to be adopted in practice. As an example, a large background of clinical experience has long existed for the use of x-ray techniques in medicine; a similar body of experience with acoustic imaging had to be developed before acoustic methods could be put into widespread use in medical diagnosis.

B. A-Scan, B-Scan, and C-Scan Imaging

Before discussing imaging systems, it is worth reviewing the standard acoustic techniques employed in NDT and medical diagnosis. In the simplest and most common NDT applications, a simple, single piezoelectric transducer is used to excite an acoustic wave in the object being examined. Commonly, the transducer is placed in a water bath and the acoustic wave excited by the transducer propagates through the water and into the object. The advantage of this technique is that the transducer is readily movable. However, because there is a large impedance mismatch between the water and the metal, the system may also be relatively inefficient in NDT applications.

A-scan. A second technique, illustrated schematically in Fig. 3.5.1, is to place the transducer directly against the solid material to be examined, making contact between the transducer and the sample with grease or a thin layer of rubber. This technique is particularly convenient in medical diagnostic applications because of the flexibility of the human body and the consequent ease with which such contact can be made with it.

Now suppose that the acoustic transducer is excited by a short electrical pulse. If the transducer is correctly designed, it will emit an acoustic pulse of length $\tau_p \approx 1/\Delta f$ determined by the bandwidth Δf of the transducer. The generated acoustic pulse passes into the object and is reflected by the acoustic impedance discontinuities caused by the presence of flaws or internal structures of the body. The return echo signal is received at the transducer and is amplified and displayed as a function of time on an oscilloscope. The time delay of the echo is $T = 2z/V$, where z is the distance of the flaw from the surface and V is the acoustic wave velocity in the material being examined. Thus the distance of the flaw from the

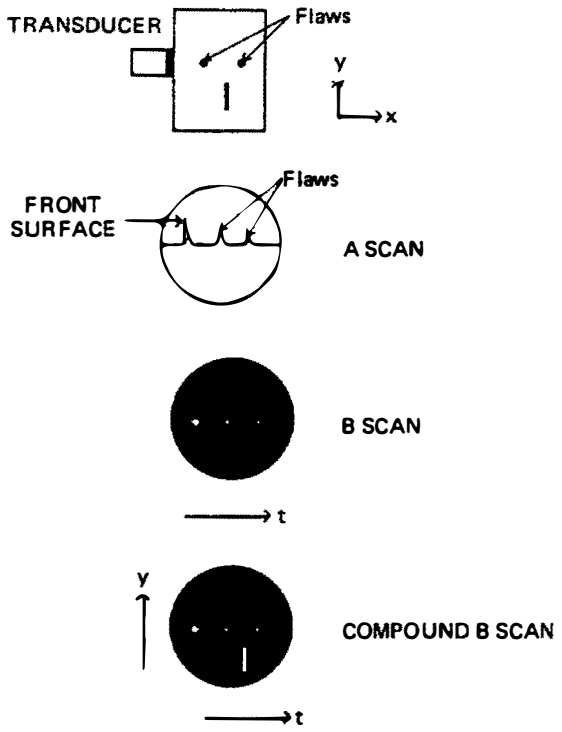

Figure 3.5.1 A-scan and B-scan operations. (After Kino [28].)

surface or its range can be determined from the time delay of the pulse observed on the oscillocope. The accuracy of the measurement of the range definition is determined by the pulse length τ_p and is $\Delta z_p \approx V\tau_p/2$. Furthermore, the amplitude of the return echo depends on the size and shape of the flaw, so that a rough estimate of the size of the flaw can be obtained by measuring the amplitude of the return echo. This technique is known as the amplitude scan, or the *A-scan*, technique.

By moving the transducer along the surface of the object being examined, various flaws can be detected while the A-scan information is being obtained, as shown in Fig. 3.5.1. Thus we can detect the transverse position of flaws, although the definition of the system in the transverse direction will be dictated basically by the size of the transducer. If the distance z of the flaw from the transducer is such that $z >> a^2/\lambda$, where a is the radius of the transducer and λ is the wavelength of the center frequency of the pulse, then, because of diffraction, the transducer behaves almost like a point source, with the beam diameter at the flaw tending to be much larger than that of the transducer. If, on the other hand, the flaw is in the near field of the transducer ($z << a^2/\lambda$), the transverse definition is comparable to the radius of the transducer. Thus we obtain the best definition when the transducer diameter is chosen so that the flaw is located roughly at the boundary between the near and far fields of the transducer. This typically means that the definition in the transverse direction will be relatively crude, of the order of 1 cm at operating frequencies of a few megahertz. The definition can be improved by using a focused transducer; however, this will give good definition over only a limited range, the extent of which is determined by the depth of focus of the lens, as discussed in Sec. 3.2.

Although the transverse definition is limited, the range definition of such an A-scan system can be relatively accurate, as we have seen, because it is dictated by the length of the pulse. Such a device is normally used with a baseband pulse only two or three cycles long, with a transducer whose bandwidth is comparable to its center frequency; this is different from the conventional radar systems, which use a relatively long tone burst. At low frequencies, the definition is poor. As the frequency is increased to improve the definition, however, the attenuation of the signal in most solids typically increases as the square of the frequency, so that there is a limit to the upper frequency that can be used. Thus the larger the structures, the lower the frequency and hence the poorer the definition that can be obtained.

For nondestructive testing of materials such as nuclear reactor steel, where the walls of the reactor may be as much as 25 cm thick, the operating frequencies employed are of the order of 2.25 MHz. As the acoustic velocity of longitudinal waves in such materials is approximately 6 km/s, the best range definition that can be obtained is of the order of 3 to 5 mm, and the transverse definition will be several times worse. In aircraft materials, such as titanium or aluminum, frequencies as high as 20 MHz may be used, with a correspondingly better definition. Frequencies as high as 400 MHz have been employed for examining structural ceramics, yielding a definition of the order of 25 μm ($V = 10^6$ cm/s). Still higher frequencies, in the range 2 to 3 GHz, have been used to image integrated circuits with the acoustic microscope.

Similarly, in medical diagnostics, the maximum usable frequency for acoustic waves to penetrate as much as 20 cm into the human body is of the order of 2 to 5 MHz, because the attenuation in body tissue is approximately 0.8 dB/cm MHz and varies linearly with frequency. Higher frequencies are used to observe shallower objects, such as the internal organs of children, for instance, or the carotid artery near the body surface. Similarly, for observations of the human eye, which is less than 3 cm in extent, relatively high frequencies, in the range 10 to 20 MHz, can be employed. The scale is reduced still further for observing body cells and thin layers of tissue, where, as we have discussed in Sec. 3.3.2, very high frequencies, in the range 1 to 8 GHz, can be employed.

B-scan. A disadvantage of the A-scan method is that it is slow and tedious to use. Only one line of amplitude information can be observed at a time, and although mechanical means can be used to move a transducer relatively rapidly, this results in large amounts of information that must still be interpreted by a human operator.

An alternative technique is the brightness scan, or the *B-scan*, method, in which the return echo signal is used to modulate the intensity of the spot on an oscilloscope, while the time delay is represented by the horizontal position of the shot and the mechanical position along the surface of the object is represented by the vertical position of the spot on the oscilloscope. By this means, a crude picture of the structure within the material can be presented, as illustrated in Fig. 3.5.1.

The problem here is that few structures are completely flat, and it is difficult to make contact over very large regions with those that are not flat. Thus B-scan

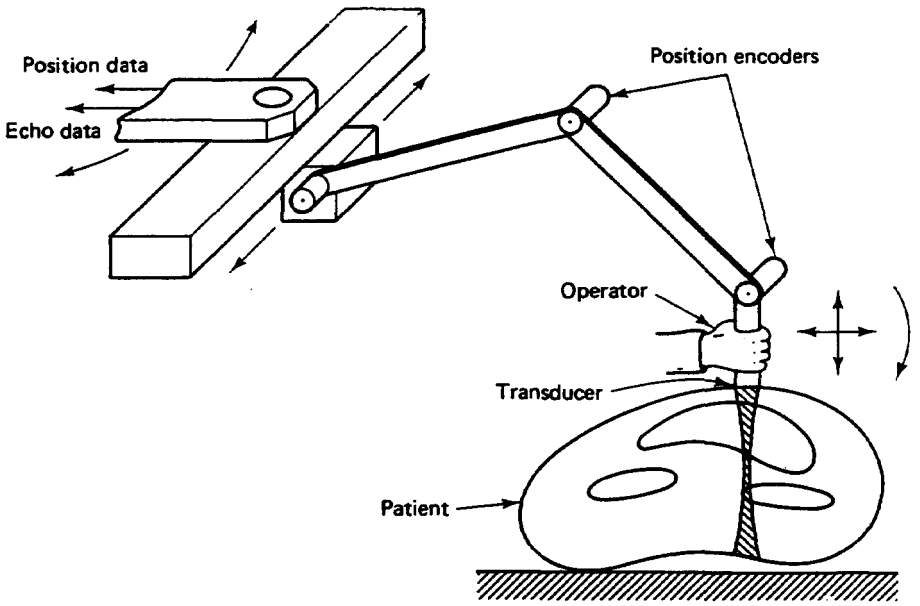

Figure 3.5.2 Scanning arrangement for a static medical B-scan system. (After Maginness [29].)

imaging is not often employed in NDT applications. On the other hand, the technique has been useful in the medical field because a greased transducer can make contact with the body very easily. Because the body itself is flexible, the transducer can be moved around it and tilted to direct the beam in an arbitrary direction.

The B-scan static medical imaging system illustrated in Fig. 3.5.2 employs a single fixed-focus transducer, typically focused to a point in the middle of the view region. The transducer is supported from a mechanical arm and can be moved along the body surface and tilted at will. Position data are encoded by the mechanical arm system, which makes it possible to display the reflected echo as an intensity display; a single point on the body always appears in the same position on the cathode ray tube. An image of a cross section perpendicular to the body surface is obtained. The transverse and range definition of the system are determined in part by the size of the transducer and in part by the play in the mechanical system, which can often be as poor as 1 cm. Although the mechanical system could be improved with enough care in design, the static B-scan system has been replaced by real-time systems in which the image is obtained at frame rates of at least 15 Hz.

C-scan. A third technique, illustrated in Fig. 3.5.3(a), is to employ transmission imaging in the *C-scan* mode to form an image in a plane that is perpendicular to the direction of propagation of the acoustic beam. For example, a focused transducer can be used to transmit an acoustic beam through the object of interest. A thin object is placed at the focus of the acoustic beam, which is received by a second confocal focused receiving transducer. The object is then mechanically scanned across the beam, while the beam itself is moved back and forth, to create a raster scan. The amplitude of the received signal is used to vary the intensity

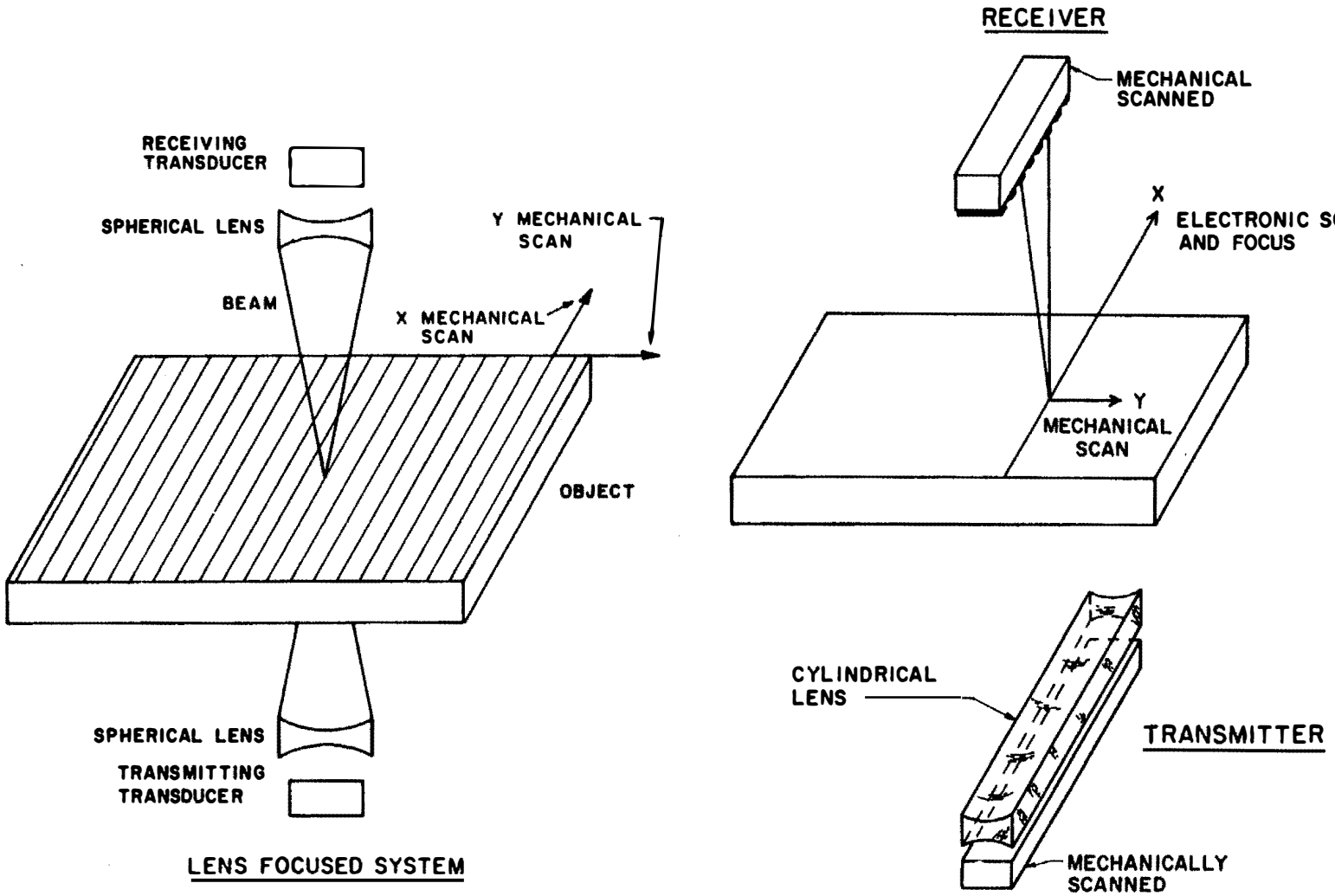

Figure 3.5.3 (a) C-scan transmission system: (a) mechanically scanned system focused with physical lenses; (b) mixed electronically and mechanically scanned system with electronic focusing, with electronic scanning and focusing in one direction and mechanical scanning and focusing with a lens in the other.

of a light spot and is displayed and recorded on either a TV screen or paper. The advantage of this method is that it gives good definition and a high-quality transmission image of sheet metal and other thin objects. An acoustic transmission microscope of the type described in Sec. 3.3.2 is a good example of the use of this technique.

The same C-scan technique is also employed for reflection imaging (as in the acoustic microscope), using a single transducer as transmitter and receiver. Figure 3.5.4 shows an example of such a reflection mode scan taken of an impact damaged fiber epoxy composite by Khuri-Yakub and Reinholdtsen with an F 0.9 transducer operating at 3 MHz [30]. The depth of focus of this transducer is small, so that damage to layers at different depths can be found by moving the transducer up or down to focus on the different layers.

C. Focusing Systems and High-Speed Scanning

By now it is apparent that two improvements in acoustic imaging techniques are needed. First, the process must be speeded up by using high-speed mechanical scanning or electronic scanning. Second, the acoustic beam must be focused so that both good transverse definition and range resolution through the depth of a thick sample can be obtained. The problem with focusing an acoustic beam is that, to do this, a physical lens must be immersed in a medium that can propagate acoustic waves. Typically, this medium is water, which means that for low-frequency imaging systems operating in the megahertz range, where the propagation path may be 10 cm or more, the imaging system tends to be very bulky and heavy when a very tight focus is required. However, a weakly focused lens with a large depth of focus may be made by using a small spherically shaped transducer. On the other hand, for very high frequencies in the gigahertz range, the lenses and water path are very small. Thus physical lenses have been used very successfully to obtain good definition in the acoustic microscope.

Figure 3.5.4 Impact-damaged fiber epoxy composite material. (Courtesy of B. T. Khuri-Yakub.)

A major difficulty with static B-scan imaging is the slow speed at which the image is formed. This requires use of a storage oscilloscope display with a very poor gray scale (the number of shades of contrast between black and white) or the use of an electronic scan-converter and storage system. In either case, slowly scanned B-scan devices are not suitable for observing rapidly moving targets, such as a moving heart valve, and may even have problems observing a patient who is breathing normally rather than holding his or her breath.

Figure 3.5.5 shows a very successful approach to high-speed imaging, which combines B-scan imaging with a high-speed mechanically scanned system that has a radial sector scan format. This technique is now being used by several manufacturers. A small transducer 1 to 2 cm in diameter is mounted in a small liquid bath in a plastic enclosure, one surface of which is placed against the body. The transducer itself is vibrated back and forth over an angular range of the order of $\pm 30°$ or more. This provides an excellent picture with a frame rate of the order of 15 to 30 Hz. By using more than one transducer and switching between them, the effective frame rate and the angle of the scan can be increased. The transverse definition over the region of most interest can be improved by using focused transducers, focused at the center of the range. At the present time, mechanical scan systems of this type are relatively low in cost compared to the highly complex, electronically focused systems that provide good focusing at all ranges but in only one transverse direction.

Elimination of physical lenses. It is desirable to eliminate physical lens systems because of the problem of varying their focal length and because of their size. Two techniques have been employed for this purpose. The first is *holography*, a lensless system that uses optical or computer reconstruction techniques

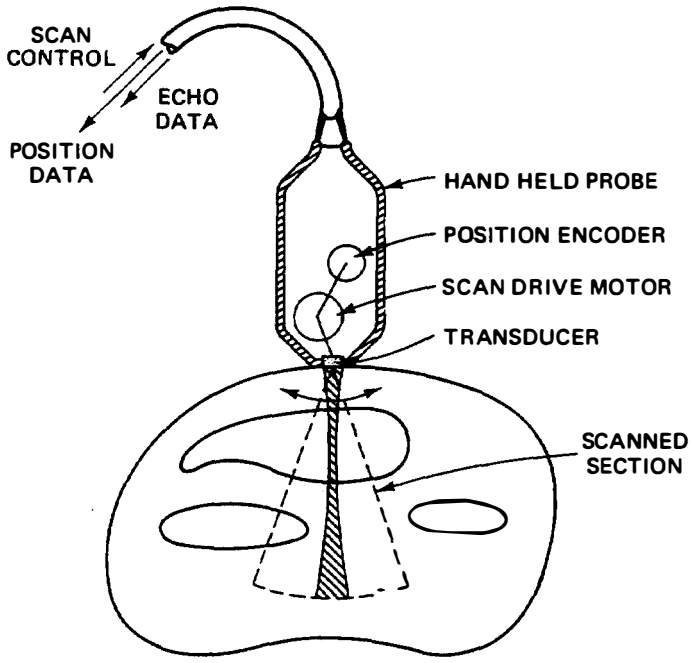

Figure 3.5.5 Mechanically scanned B-scan system with a radial sector scan. (After Maginness [29].)

to synthesize the phase change made by a lens. The second uses an array of transducers and processes the signals arriving at them, to make the array behave like an electronically focused lens.

The holographic system typically provides good transverse definition in both directions, but its range definition is limited to essentially the depth of focus of the equivalent lens. Furthermore, holographic systems tend to be complicated, costly, and inconvenient. The use of a water bath in some versions makes them insensitive and unwieldy. Other mechanically scanned versions are slow and inconvenient because optical photos of the holograms must be exposed and developed.

An electronically scanned system can provide good range resolution as well as good transverse resolution. Its disadvantages, however, are its great complexity and the large number of transducer elements and electronic components it requires; the quantity must often be limited by economic considerations, which means that the system usually gives good definition in only two dimensions: normally, range and one transverse dimension. One advantage, however, of using an array to provide electronic scanning over the face of the object, rather than mechanical scanning, is that it speeds up the process of forming an image, since a single mechanically scanned transducer is now replaced with an array of small transducers in which the signal can be switched electronically from one element to another, with the speed controlled by the electronic switching rather than by a relatively slow mechanical scan.

As an example, consider the transmission system illustrated in Fig. 3.5.3(b), using an N-element array, which transmits a cylindrically focused beam through a thin object to a similarly focused receiver array or the other side of the object. If the system is mechanically scanned at right angles to the electronic scan, we expect the speed of the scan to be increased by a factor N. The electronic scan rate is extremely fast, and mechanical scanning is carried out in only one direction, not two. We shall describe later how such improvements in scan speed have, in fact, been obtained.

Physical lens. To understand which components are needed for an electronically focused and scanned array or for a holographic system, let us first consider the action of a physical lens, which focuses the signal received from one point on an object onto the plane of a single large-area transducer, as shown in Fig. 3.5.6(a). The physical lens delays the rays passing through it so that all rays reaching the transducer from the focal point suffer the same phase and time delays. Thus if an object at this point is illuminated by a short pulse, all signals arrive at the transducer at the same time and with the same phase.

Time-delay focusing. To carry out this process electronically, all the signals received by the individual array elements must be delayed in such a way that they can be added to each other. The simplest way to do this, conceptually, is to connect electrical delay lines to each element of the array so that a pulsed RF signal emitted from a point on the object will arrive at the receiver, with all pulses passing through each element of the array arriving at the same time at a common sum line, as illustrated in Fig. 3.5.6(b). There will therefore be a strong response

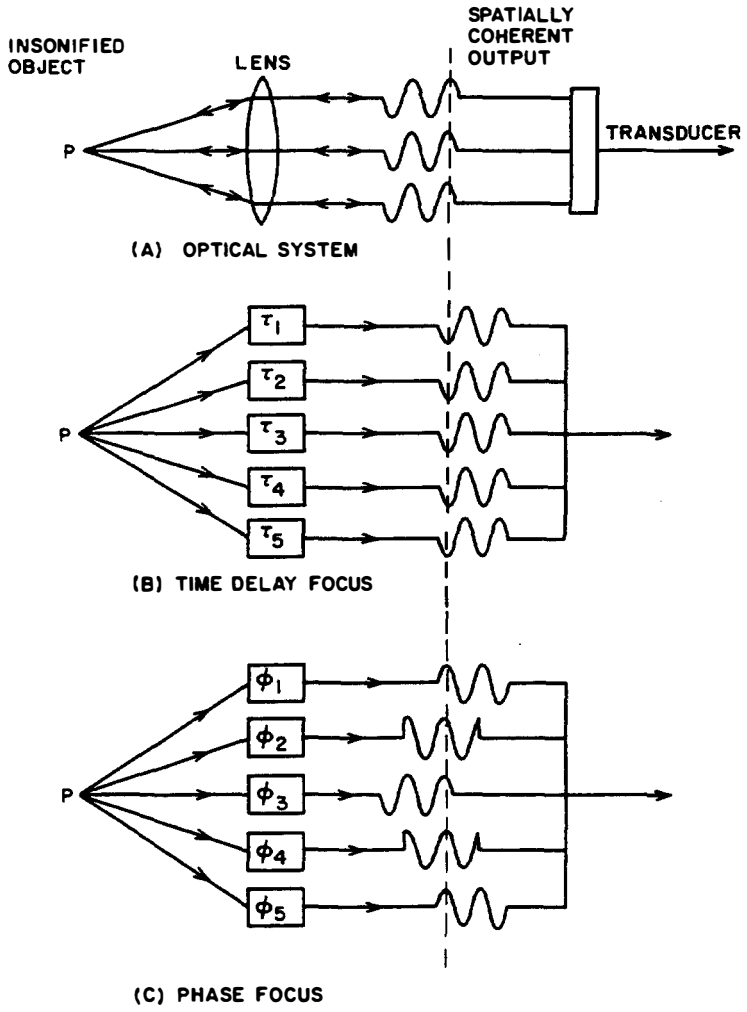

Figure 3.5.6 (a) Rays passing through a physical lens to a plane transducer; (b) time-delay system for focusing; (c) phase-delay system for focusing.

from the point P on the object, but the signals from some other point will arrive at different times and be out of phase. We call this a *time-delay imaging system.*

Phase-delay focusing. The *phase-delay system*, illustrated in Fig. 3.5.6(c), is often simpler to implement. An RF pulse several cycles long, arriving from a point in the object, passes through the individual transducer elements and into a phase-delay instead of a time-delay system. In this case, the nth RF cycle from one element can be added to the $(n + 1)$th RF cycle from another array element. Thus all signals from the array elements can be added to give a strong output corresponding to the point of interest. The rays emitted from any other point will give signals that will arrive out of phase, so the sum of the signals from the receiver elements will be relatively small. The disadvantage of such a phase-delay system is that it requires an RF pulse that is several RF cycles long. The range definition of the system therefore tends to be worse than that for a system in which the time delays of the signals arriving from all elements are equal; in the latter case, the RF pulse can be only one or two cycles long.

The change in phase required in a phase imaging system can be provided by phase changes in the transducer itself, for example, the Fresnel transducer, de-

scribed in Sec. 3.5.3.A, or by mixing a reference signal with the signal arriving at the transducer. These two signals can be multiplied together in a mixer to produce an output at the sum or difference frequencies. The phases of the two input signals are similarly added or subtracted. It follows that if signals with the correct reference phases can be inserted into the mixers, they can compensate for the phase differences of the different signals arriving at the transducers from a point on the object. Therefore, the outputs from the mixers will all be in phase.

Alternatively, in one form of a holographic system, the mixing can be accomplished in two steps. Two signals of the same frequency, one scattered from an object in water and one a reference acoustic beam, are incident on the surface of a water bath. The static sound pressure, which is proportional to the square of the total incident signal amplitude, modulates the height of the surface of the water bath. Thus there is a spatial variation in the height of the water that is proportional to the product signal from the reference and the object and depends on the phase difference between the two waves. To reconstruct an image, a laser beam is reflected from the surface of the water bath and is deflected by the surface ripple. When a point in the water bath is to be observed, the laser beam deflected from the water surface is passed through an optical lens, which focuses it to an equivalent image point. More generally, the object illuminated by an acoustic beam in the water tank is reproduced as an optical image. This system will be described in more detail in Sec. 3.5.6.

3.5.2 Basic Imaging Theory

A. Matched Filter Concepts

The focusing systems discussed in Sec. 3.3, which use physical lenses or spherically shaped transducers, and those in Sec. 3.5.1, which use electronic focusing or holographic imaging, are all examples of matched filters. Here we will discuss how physical, electronic, or holographic lenses can be regarded as spatial matched filters for a spatially varying input signal.

For simplicity, we consider initially a two-dimensional receiver system with a line source of radian frequency ω at the point x, z, as illustrated in Fig. 3.5.7. Ideally, the acoustic imaging system must be able to reconstruct this line source as a δ function (line) in space.

A common way to study a signal processing system is to consider the response of the system to an impulse or mathematical delta function. As we show in Sec. 4.3, if the system has a response $f(t)$, the optimum signal-to-noise ratio or maximum peak signal (i.e., the best approximation to a δ function) can be obtained by passing the output of the system through a *matched filter* with a response $f^*(-t)$.

By analogy, the signal arriving at the plane x', 0 from a line source at x, z is of the form $f(x - x', z)$. The appropriate spatial response to this signal to obtain the maximum output is at matched filter with the response $f^*(x' - x, z)$.

Suppose that a one-dimensional receiving system is composed of continuous array of infinitesimally wide transducers at the plane $z = 0$. Let the coordinates of any point on the transducer array be x', 0. After the signal from the point x,

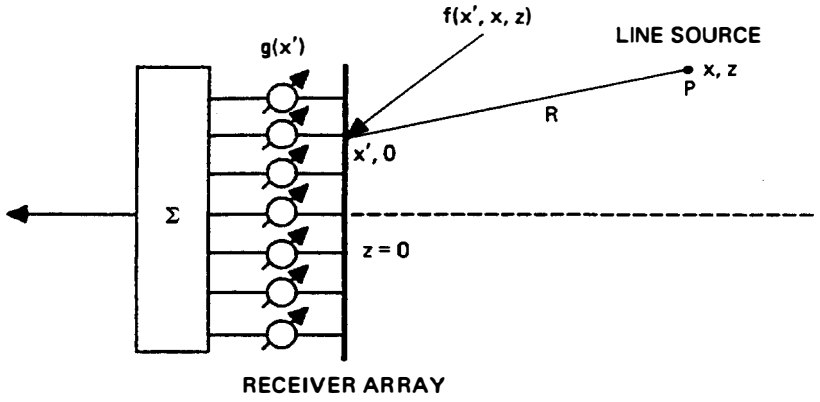

Figure 3.5.7 Two-dimensional receiver system with a line source at x, z.

z has passed through the medium, which in general may be nonuniform, the signal arriving at the plane $z = 0$ is of the form $f(x', x, z)$. We regard the receiving system as a continuous structure with a response $g(x')$. We will show that the maximum output is obtained from the point 0, z_i when we choose $g(x')$ so that it is a matched spatial filter for the spatially varying signal $f(x', 0, z_i)$.

The distance from x', 0 to x, z is

$$R = \sqrt{(x - x')^2 + z^2} \tag{3.5.1}$$

Thus the signal from a line source at x, z, which varies as exp $(j\omega t)$, is of the form†

$$f(t, R) = \frac{e^{j\omega(t - R/V)}}{R^{1/2}} \tag{3.5.2}$$

As the spatial response of the system depends only on R, we can write $f(x', x, z)$ in the form $f(x - x', z)$.

We suppose that the electrical response of the receiver system in the region between x' and $x' + dx'$ of the transducer array is of the form $g(x')\,dx'$, and that all signals from the receiver elements are added and weighed by the response $g(x')$. The output from the receiver will therefore be

$$y(x, z) = \int f(x', z)\, g(x - x')\, dx' \tag{3.5.3}$$

where we assume that all signals vary as exp $(j\omega t)$. The output $y(x, z)$ is the convolution of $f(x', z)$ and $g(x')$. We know from signal processing theory, as shown in Sec. 4.3, that if $g(x')$ is chosen so that $g(x') = \alpha f^*(-x', z)$, then $g(x')$ is the matched filter for $f(x', z)$ (i.e., for the signal emitted from the point 0, z). Here α is a constant and f^* denotes the complex conjugate of f.

It is convenient to write $f(x', z)$ in the form

$$f(x', z) = a(x', z)e^{-j\Phi(x', z)} \tag{3.5.4}$$

†We have used the asymptotic form for the potential from a line source, corresponding to the assumption that $(\omega R/V) >> 1$ [see Probs. 3.1.3 and 3.2.2 and Eq. (3.2.59)].

where the amplitude term $a(x', z)$ is a real function. It follows that the matched filter response becomes

$$g(x', z) = \alpha f^*(-x', z) = \alpha a(-x', z)e^{j\Phi(-x',z)} \tag{3.5.5}$$

With the matched filter, the output $y(0, z)$ from the point 0, z becomes

$$\begin{aligned} h(0, z) &= \alpha \int f(x', z) f^*(-x', z)\, dx' \\ &= \alpha \int [a(x', z)]^2\, dx' \end{aligned} \tag{3.5.6}$$

More generally, $h(x, z)$ is the line spread function (LSF) of the focused system to the point 0, z. We derive the form of $h(x, z)$ in the paraxial approximation in Sec. 3.5.1.B.

We see that with this choice of $g(x')$ as a matched filter, all phase errors are removed by the matched filter and the integrand is always positive. When noise is present, it is implied by signal processing theory (see Sec. 4.3) that by using this matched filter we obtain the maximum possible signal-to-noise ratio when observing the point $(0, z)$ (see Prob. 2).

In the simplest case, the signal emitted from a point source at x, z varies as $\exp(j\omega t)$. It follows from Eq. (3.5.2) that the signal arrives at the receiver in the form

$$f(x' - x, z) = \frac{e^{-j\omega[(x-x')^2 + z^2]^{1/2}/V}}{[(x - x')^2 + (z^2)]^{1/4}} \tag{3.5.7}$$

where we have omitted the $\exp(j\omega t)$ term for simplicity.

B. Paraxial Approximation

To keep the analysis simple, we shall use the paraxial approximation or Fresnel approximation of optics, and assume that $(x - x')^2 \ll z^2$, keeping only up to second-order terms in $(x - x')^2$ in the phase-varying term and zeroth-order terms in the amplitude variation. Thus we find that

$$f(x' - x, z) \approx \frac{1}{\sqrt{z}} e^{-j\omega z/V} e^{-j\omega(x-x')^2/2zV} \tag{3.5.8}$$

The resultant signal arriving at the plane $z = 0$ therefore has a square-law spatial phase variation with the coordinate x'; that is, in signal processing terms it is a spatial frequency-modulated (FM) chirp. The spatial filter response to an object point 0, z should therefore be of the form

$$\begin{aligned} \mathrm{f}^*(\mathrm{x}', \mathrm{z}) &= \mathrm{e}^{j\omega z/V} \mathrm{e}^{j\omega(x')^2/2zV} \\ &= \mathrm{e}^{2j\pi z/\lambda} \mathrm{e}^{j\pi(x')^2/z\lambda} \end{aligned} \tag{3.5.9}$$

where we have taken the matched filter constant (see Sec. 4.3) to be $\alpha = \sqrt{z}$, and where $\lambda = 2\pi V/\omega$ is the wavelength of the acoustic wave. Using $g(x')$ for the matched filter to the point 0, z, we find that the output from a source at x, z, using

a receiver system of finite length D, is

$$h(x, z) = \int_{-D/2}^{D/2} e^{-j\omega(x-x')^2/2zV} e^{j\omega x'^2/2zV}\, dx' \tag{3.5.10}$$

or

$$h(x, z) = e^{-j\omega x^2/2zV} \int_{-D/2}^{D/2} e^{j\omega xx'/zV}\, dx' \tag{3.5.11}$$

Line spread function. Integration of Eq. (3.5.11) yields

$$\begin{aligned} h(x, z) &= De^{-j\omega x^2/2zV} \frac{\sin\,(\omega xD/2zV)}{\omega xD/2zV} \\ &= De^{-j\pi x^2/z\lambda} \operatorname{sinc} \frac{xD}{z\lambda} \end{aligned} \tag{3.5.12}$$

where $\operatorname{sinc} x = (\sin \pi x)/\pi x$, the wavelength $\lambda = 2\pi V/\omega$, and $h(x, z)$ is known as either the *point spread function* (PSF) in the x direction or, more correctly in this two-dimensional system, the *line spread function* (LSF) in the x direction for the point 0, z. More generally, if the matched filter is designed to focus on an image point x_i, z_i, we choose $f(x') = h^*(x_i - x', z_i)$ and find that

$$h(x - x_i, z) = De^{-j\pi(x^2 - x^{2\prime})/z_i\lambda} \operatorname{sinc} \frac{(x_i - x)D}{z_i\lambda} \tag{3.5.13}$$

The response is a sinc function, which, as $D \to \infty$, approaches a δ function at $x = x_i$. Thus, by using a matched filter to compensate for the phase differences of the rays arriving at the receiver, we can construct a system with a spatial response narrowly centered about the point of interest. It follows that the construction of a matched spatial filter for the point x_i, z_i is equivalent to designing a lens focused on this point. Thus *all lenses, whether electronic, physical or holographic, give basically the same transverse definition and spatial response if their apertures or F numbers, z_i/D, are the same.* The analysis we have given is valid only for the paraxial approximation, but it serves to give a very reasonable estimate of the basic results, even with wide-aperture lenses.

3 dB definition of a paraxial rectilinear system. From Eq. (3.5.13), the 3-dB points of the response are where $x - x_i = 0.45\lambda z_i/D$ (the 4-dB points are at $x - x_i = \pm 0.5\lambda z_i/D$). Thus the 3-dB points are a distance $d_x(3\text{ dB})$ apart, where

$$d_x(3\text{ dB}) = \frac{0.89\lambda z_i}{D} \tag{3.5.14}$$

We regard this parameter $d_x(3\text{ dB})$ as the definition of the lens.

C. Radial Sector Scan System

It is also useful to consider the 3-dB definition in a cylindrical coordinate rather than a Cartesian coordinate system. We do this because many medical systems use a relatively small transducer array and carry out an azimuthal scan.

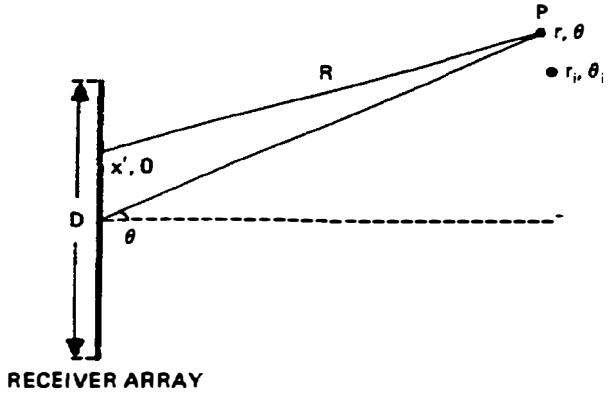

Figure 3.5.8 Imaging system in a cylindrical format.

As illustrated in Fig. 3.5.8, this is a *radial sector scan* in an r, θ coordinate frame, based on an axis normal to the page at the center of the receiver transducer array.

We consider this imaging system to be focused on the point r_i, θ_i with a flat transducer array of length D, with the center of the coordinate system at the center of the array. The distance to the point r, θ from a point x' on the array is

$$R = (r^2 + x'^2 - 2x'r \sin \theta)^{1/2} \tag{3.5.15}$$

We expand Eq. (3.5.15) to second order in x'/r and find that

$$R \approx r - x' \sin \theta + \frac{x'^2}{2r} \cos^2 \theta \tag{3.5.16}$$

Our previous treatment, in Cartesian coordinates, was for the case $x_i = 0$. More generally, if x_i is finite, we reverse the sign of x_i and $f(x' - x_i, z_i)$ to find the matched filter and write $g(x' - x_i) = \alpha f^*[-(x' - x_i), z_i]$. The equivalent operation in cylindrical coordinates is to change the signs of both x' and $\sin \theta_i$. The output obtained, when the system is focused on the point r_i, θ_i, is of the form

$$h(r, \theta, r_i, \theta_i) = Ae^{j\omega(r_i - r)/V} \int_{-D/2}^{D/2} e^{j\omega x'(\sin\theta - \sin\theta_i)/V} \times e^{j\omega x'^2/2V[(\cos^2\theta_i)/r_i - (\cos^2\theta)/r]} dx' \tag{3.5.17}$$

where A is a constant.

The maximum output is obtained when $r = r_i$ and $\theta = \theta_i$; it is

$$h(\theta_i, r_i) = AD \tag{3.5.18}$$

When $\theta \neq \theta_i$, the square-law term in x' is zero, provided that

$$r = \frac{r_i \cos^2 \theta}{\cos^2 \theta_i} \tag{3.5.19}$$

Thus if $\theta_i = 0$, r decreases slightly as θ increases. In this case,

$$|h(r, \theta, r_i, \theta_i)| = AD \left| \operatorname{sinc} \left[\frac{D}{\lambda} (\sin \theta - \sin \theta_i) \right] \right| \tag{3.5.20}$$

Taking $\delta\theta = \theta - \theta_i$ to be small, we see that to first order in $\delta\theta$,

$$|h(r, \theta, r_i, \theta_i)| = AD \left| \operatorname{sinc} \left(\frac{D \cos \theta_i}{\lambda} \delta\theta \right) \right| \tag{3.5.21}$$

Therefore, the effective width of the transducer is $D' = D \cos \theta_i$ (i.e., the definition decreases as the angle θ_i is increased). In this case the 3-dB azimuthal definition is

$$d_\theta(3 \text{ dB}) = r_i \, \Delta\theta(3 \text{ dB}) \tag{3.5.22}$$

where $\Delta\theta$ (3 dB) is the total angular spread between the 3-dB points. Thus

$$d_\theta(3 \text{ dB}) = \frac{0.89 r_i \lambda}{\pi D \cos \theta_i} \tag{3.5.23}$$

It is apparent that the definition deteriorates as θ_i is increased from zero.

An important feature of this kind of focusing is that the phase change required for focusing on the point θ_i may be divided into two parts, a linear term, which varies as x', and a square-law term, which varies as x'^2. The system can be focused on the point 0, r_0 if the square-law term is chosen to vary as $\exp(j\omega x'^2/2Vr_0)$, where r_0 is the focal length at the center of the lens. In this case the focusing term is independent of the azimuthal angle θ_i. We then find that

$$\begin{aligned} h(r, \theta, r_i, \theta_i) = A e^{j\omega(r_i - r)/V} \int_{-D/2}^{D/2} & e^{j\omega x'(\sin\theta - \sin\theta_i)/V} \\ & \times e^{(j\omega x'^2 2V)}(1/r_0 - \cos^2 \theta/r) \, dx' \end{aligned} \tag{3.5.24}$$

We note that such a focusing system focuses on the point r_i, θ_i, where

$$r_i = r_0 \cos^2 \theta_i \tag{3.5.25}$$

and has the transverse definition given by Eq. (3.5.23).

The advantage of this system, in practice, is that it is far easier to construct than other scanning systems. The square-law phase variation can be programmed independently of the azimuthal linear phase variation, and the two phase variations can be added. Only the linear phase variation term must be changed with angle. The two operations are similar to what happens when a parallel beam passes through a lens and the beam is tilted to vary the angular position of the focal spot. We discuss further implications of this principle in Sec. 3.5.5, when we deal with time-delay focusing.

Rayleigh criterion. As we discussed in Sec. 3.3.1, a standard criterion for the transverse definition of an imaging system is to consider when two point sources of equal amplitude can be distinguished from each other. The *Rayleigh criterion* is based on the idea that this can be done when one point is placed at the position where the response to the other point is zero. This criterion yields a definition d_x (Rayleigh) that is equal to that for the 4-dB points, or

$$d_x(\text{Rayleigh}) = \frac{\lambda z_i}{D} \tag{3.5.26}$$

This formula, like the one for d_x (3 dB), can easily be generalized for a radial sector scan system by replacing D with $D' = D \cos \theta_i$, z_i with r, and d_x with d_θ.

Sparrow criterion. The Rayleigh result is inadequate when the signals from two neighboring points are in phase. In general, the total output from two equal amplitude point sources with a phase difference ϕ is of the form

$$|y(x, z)| = \left| \operatorname{sinc} \frac{(x_i - a/2)D}{z_i \lambda} + e^{j\phi} \operatorname{sinc} \frac{(x_i \quad a/2)D}{} \right| \tag{3.5.27}$$

where the points are at $x = \pm a/2$, z_i, respectively, and the system is focused on the point x_i, z_i. For $\phi = 0$, the response at $x_i = 0$, with $a = \lambda z_i/D$, is $4/\pi$. This is larger than the response at $x_i = \pm \lambda z_i/2D$, where it is 1. Thus the two points cannot be distinguished from each other.

A similar problem occurs with signal processing and is discussed in Sec. 4.5.4; the same situation for spherical lenses is covered in Sec. 3.3. When $\phi = 0$, it follows from Eq. (3.5.27) that the signal at the midpoint $x = 0$ is just equal in amplitude to the signals at $x = \pm a/2$, if the points are a distance d_x(Sparrow) apart. Thus, for a coherent system,

$$d_{xi}(\text{Sparrow}) = \frac{1.22\lambda}{D} \tag{3.5.28}$$

This is known as the *Sparrow criterion* (see Sec. 3.3.1).

Range definition. By using a filter based on the point $x_i = 0$, z_i, we can also make a similar estimate for the definition in the z direction. We consider a correlation filter or lens with the characteristic $f^*(-x', z_i)$. We can write $h(x, 0; z, z_i)$ in a normalized form, as follows:

$$h(x, 0; z, z_i) = \frac{1}{} \left(\frac{z_i}{z}\right)^{1/2} e^{j(2\pi/\lambda)(z_i - z)} \int_{-D/2}^{D/2} e^{-j\omega(x-x')^2/2zV} e^{j\omega x'^2/2z_i V} \, dx' \tag{3.5.29}$$

or

$$\begin{aligned} h(x, 0; z, z_i) = \frac{1}{D} \left(\frac{z_i}{z}\right)^{1/2} & e^{j(2\pi/\lambda)(z_i - z)} e^{-j\omega x^2 2zV} \\ & \times \int_{-D/2}^{D/2} e^{jx'^2/\lambda)(1/z_i - 1/z)} e^{2j\pi x x'/\lambda z} \, dx' \end{aligned} \tag{3.5.30}$$

Equation (3.5.30) is, in general, a Fresnel integral. For $4z_i\lambda/D^2 << 1$ and $|z - z_i| << z_i$, we can write the on-axis PSF in the form

$$|h(0, 0; z - z_i)| \approx \frac{1}{D} \left| \int_{-D/2}^{D/2} e^{j\pi x'^2 (z - z_i)/\lambda z_i^2} \, dx' \right| \tag{3.5.31}$$

It is convenient to normalize Eq. (3.5.31) by putting $Z = D^2(z - z_i)/4\lambda z_i$

and $u = x'/D$. Equation (3.5.31) can then be written in the form

$$|h(Z)| = \left| \int_{-1/2}^{1/2} e^{j\pi Z u^2} \, du \right| \tag{3.5.32}$$

This function has a response 3 dB below its maximum value, where the normalized distance $\delta z(3\text{ dB})$ is defined as

$$\delta z(3\text{ dB}) = \frac{D^2}{\lambda} \frac{z - z_i}{z_i^2} = 3.8 \tag{3.5.33}$$

This corresponds to the argument of the exponential (the phase error) being approximately π at its limits. The appropriate 3-dB range definition for a CW signal is therefore

$$d_z(3\text{ dB}) \approx 7.6 \frac{\lambda z_i^2}{D^2} = 1.9 z_i S \tag{3.5.34}$$

where we define the *Fresnel parameter* S as

$$S = \frac{4\lambda z_i}{D^2} \tag{3.5.35}$$

We observe that, in terms of S, the tranverse Rayleigh definition is

$$d_x(\text{Rayleigh}) = \frac{DS}{4} \tag{3.5.36}$$

Thus, just as with a spherical lens, the transverse definition is much smaller than the aperture width D if the parameter S is such that $S \ll 4$.

Typically, for a small aperture system with $z_i/D \gg 1$, the definition in the range direction d_z is far poorer than in the transverse direction. Later we discuss how to avoid this difficulty by using short pulses to obtain good range definition without deteriorating the transverse definition.

More exactly, if we use the more general form of Eq. (3.5.30) for the on-axis ($x = 0$) LSF, then

$$|h(Z)| = \frac{1}{\sqrt{1 + ZS}} \left| \int_{-1/2}^{1/2} e^{j\pi Z u^2/(1+ZS)} \, du \right| \tag{3.5.37}$$

The value of $|h(Z)|$ is plotted in Fig. 3.5.9 for several values of S. The curves are cut off for the region near $z = 0$ ($Z = -1/S$), where the variation of $|h(Z)|$ with Z becomes very rapid and the paraxial theory is no longer valid. The result obtained in Eq. (3.5.36) corresponds to the $S = 0$ solution. In this case, the first sidelobe is reduced in amplitude by 8.4 dB from the main lobe. In practice, with, for instance, $z_i = 10$ cm, $D = 4$ cm, and $\lambda = 0.5$ mm, $S = 0.125$. So, as we can see from Fig. (3.5.9), S may be large enough to make the use of normalized curves, at best, a rough approximation to the truth. However, provided that $S < 0.25$, this result is still adequate for estimating the range definition of a cylindrical lens.

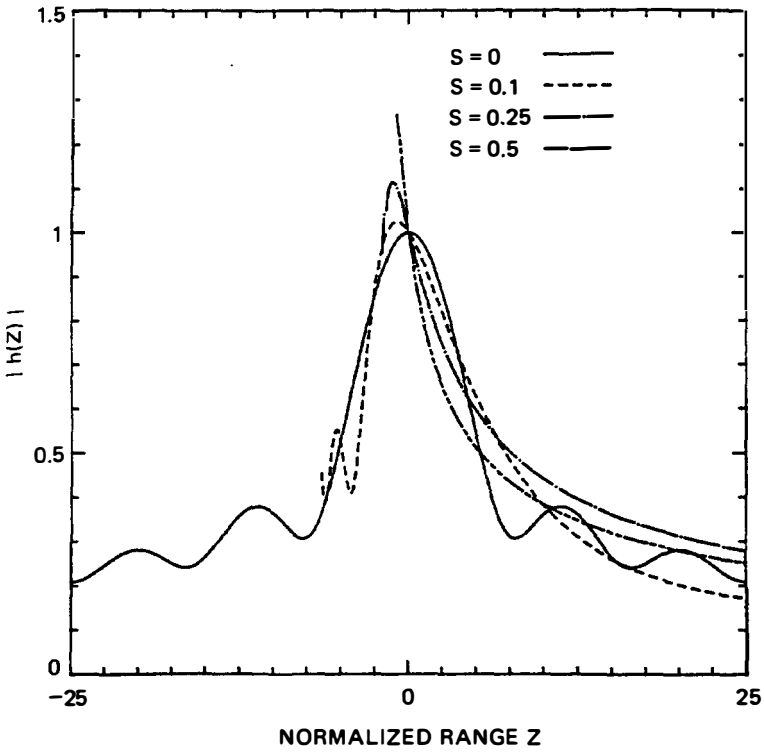

Figure 3.5.9 Normalized line spread function in the z direction. The normalized range Z is defined as $Z = D^2(z - z_i)/\lambda z_i^2$.

D. Generalization of the Matched Filter Theory

The matched filter theory is obviously much more general than the special case given above. Returning to Eq. (3.5.2), we see that if the rays pass through a nonuniform medium, the signals arriving at the receiver will be distorted. However, provided that $f(x - x', z)$ is known, we can still construct a matched filter that will image a point in a nonuniform medium. As with a uniform medium, this matched filter must be changed for each point in the image, but with a far more complicated algorithm. The process is still equivalent to signal processing with matched filters; that is, our focused system essentially operates as a matched filter to compensate for phase differences of the rays arriving at the receiver. If the process is generalized to a two- or three-dimensional system, two- or three-dimensional matched filters must be constructed to give good range definition in the z direction and good transverse definition in the x and y directions.

As an example for a three-dimensional system, we write

$$f(x', y', x, y, z) = \frac{e^{-j\omega R/V}}{R} \tag{3.5.38}$$

where

$$R = [(x - x')^2 + (y - y')^2 + z^2]^{1/2} \tag{3.5.39}$$

The matched filter for the point 0, 0, z_i is $f^*(-x', -y', 0, 0, z_i)$.

When the system is cylindrically symmetric and the transducer is of radius a, we can work in cylindrical coordinates by writing $x = r\cos\phi$, $y = r\sin\phi$, $x' =$

$r' \cos \phi'$, and $y' = r' \sin \phi'$. At the plane $z = z_i$, these substitutions yield $h(x, y, z_i) = h(r, \phi, z_i)$ in the form

$$h(r, \phi, z_i) = \int_0^{2\pi} \int_0^a [f(r' \cos \phi' - r \cos \phi, r' \sin \phi' - r \sin \phi, z_i)] \tag{3.5.40}$$

$$\times [f^*(-r' \cos \phi' - r \cos \phi, -r' \sin \phi' - r \sin \phi, z_i)] r' \, dr' \, d\phi'$$

To the paraxial approximation, this implies that the PSF is

$$h(r, z_i) = C \int_{\phi'=0}^{2\pi} \int_{r'=0}^{a} e^{-j\omega r r' \cos(\phi' - \phi)/z_i V} r' \, dr' \, d\phi' \tag{3.5.41}$$

where C is a constant.

Following the analysis of Sec. 3.3.1, it can be shown that

$$h(r, z_i) = K e^{-j\omega r^2/2z_i V} \operatorname{jinc} \frac{ra}{\lambda z_i} \tag{3.5.42}$$

where $\operatorname{jinc}(X) = J_1(2\pi X)/\pi X$, and the parameter $h(r, z_i)$ is known as the *radial PSF*. Here K is a constant and $J_1(x)$ is a Bessel function of the first kind and first order. This result, of course, is of the same form as the one we obtained in Sec. 3.3.1 for the transverse response in the geometrical focal plane of a spherical lens, which is plotted in Fig. 3.2.6.

E. Sidelobes and Grating Lobes

In the foregoing analysis, if the receiver is a spatial matched filter of infinite width, the response to the line source it is focused on is a delta function. On the other hand, if the receiver system has a finite width D, it is no longer a perfectly matched filter and the transverse LSF is of the form

$$f(x, z) = D \operatorname{sinc} \frac{xD}{z\lambda} \tag{3.5.43}$$

In this case, sidelobes or subsidiary maxima in amplitude occur at the points x_{sn}, where

$$x_{sn} = \frac{(2n + 1)z\lambda}{2D} \tag{3.5.44}$$

The amplitude of the first sidelobe is -13 dB relative to the main lobe at $x = 0$. The second sidelobe is -18 dB relative to the main lobe at $x = 0$ and so on.

As we discussed in Sec. 3.3.1, such effects can be a serious disadvantage for imaging. Suppose that we want to image two points, A and B, where B is located on a sidelobe of A. If the amplitude of B is less than the sidelobe amplitude of A, then B will be essentially undetectable. Thus the lower the sidelobe level of the system, the more easily we can detect a weakly reflecting or emitting object in the presence of another, much larger reflector or more powerful emitter.

Such problems are typical, for instance, in NDT, where the aim is to detect

a small flaw near one surface of a metal object. In medical imaging, the problems are even more severe: there are so many scatterers present in the body that the sidelobes from them may add up to obscure completely the image of a small object of interest. As a result, much effort has been made to reduce the sidelobe levels in imaging systems; this criterion is often the most important in determining the practical quality of an imaging system.

Many of the same kinds of problems arise in signal processing systems when a sharp pulse is needed; for example, for use in a radar system. Sidelobes of a compressed pulse give rise to very similar difficulties. In Sec. 4.3 we show that the solution is to apodize the response of the filter.

The basic reason for sidelobes is because the matched filter is of finite spatial width. Thus, if we consider the amplitude response of an infinite width matched filter to be artificially weighted by a function $w(x')$, it follows from Eq. (3.5.11) that the output of the system at the plane $z = z_i$ is

$$h(x, z_i) = e^{-j\omega x^2/2z_iV} \int_{-\infty}^{\infty} w(x') e^{j\omega x x'/z_iV}\, dx' \tag{3.5.45}$$

The basic response of the system at the focal plane is the Fourier transform of the weighting function $w(x')$. The implications of using this result for apodization of the acoustic beam are discussed in Secs. 4.5.1 and 3.3.3.

It is apparent that if

$$w(x') = \begin{cases} 1 & |x'| < \dfrac{D}{2} \\ 0 & |x'| > \dfrac{D}{2} \end{cases} \tag{3.5.46}$$

the response is the sinc function of Eq. (3.5.12).

Grating lobes. All electronically scanned systems use an array of separate transducers to simulate the effect of the continuous matched filter or artificial lens described earlier in this chapter. Thus the individual transducer elements and the associated electronic circuitry are designed so that the response of the array, at the center point of each array element, matches that of the continuous system. It is therefore as if the array elements sample the received signal at points spaced a distance l apart. If we use a finite number of receiving elements (i.e., sampling), we introduce grating lobes, or aliasing. This is because the phases of signals arriving at the individual elements can change by 2π and still give rise to the same output acoustic beam.

Suppose, for simplicity, that a receiving array is focused on a point at infinity, as illustrated in Fig. 3.5.10. Individual rays entering the array will be in phase when they arrive normal to the surface of the array, as shown in Fig. 3.5.10(a). However, if the rays arrive at an angle θ_{Gp} to the normal to the array surface, as illustrated in Fig. 3.5.10(b), the difference in length of the rays arriving at neighboring elements, spaced a distance l apart, is $l \sin \theta_{Gp}$. If this distance is such that $l \sin \theta_{Gp} = p\lambda$, all the rays will arrive at the individual elements of the array in

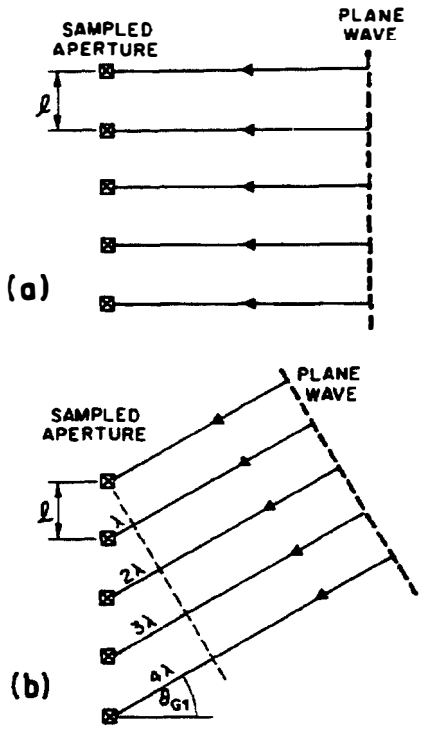

Figure 3.5.10 The $p = 1$ grating lobe for a system focused at infinity: (a) plane wave normally incident on a periodically sampled aperture; (b) plane wave obliquely incident on the same sampled aperture at angle $\theta_{G1} = \sin^{-1}(\lambda/l)$.

phase. Generally, a focused image will repeat itself, that is, aliasing or a repeated lobe will occur at a point that is d_{Gp} distant from the original main lobe, where

$$d_{Gp} = z\theta_{Gp} = \frac{zp\lambda}{l} \tag{3.5.47}$$

We can obtain this result more rigorously using Eq. (3.5.45). For simplicity, we assume that each element of the receiving transducer is infinitesimally thin. We suppose that there are N elements in the array a distance l apart, as illustrated in Fig. 3.5.11; for simplicity, we assume N to be an even number. It follows that the weighting function $w(x')$ becomes

$$w(x') = \sum_{n=-N/2}^{n=N/2-1} w(x_n)\lambda(x' - x_n) \tag{3.5.48}$$

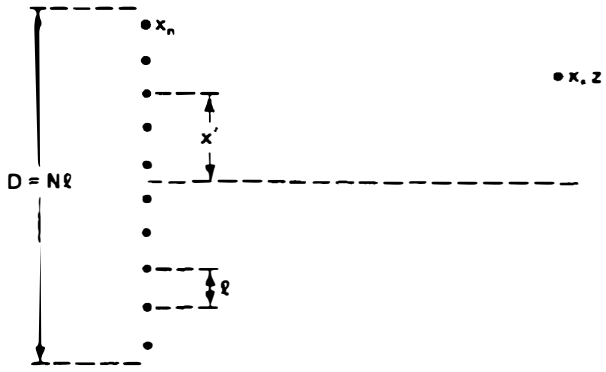

Figure 3.5.11 An N-element array with an even number of elements.

where $x_n = (2n + 1)l/2$ and $\delta(x)$ is the Dirac delta function. Inserting this expression in Eq. (3.5.45) leads to the following result at the focal plane:

$$h(x, z_i) = e^{-j\omega x^2/2z_iV} \sum_{n=-N/2}^{n=N/2-1} w(x_n) e^{j\omega x_n x/z_iV} \tag{3.5.49}$$

where $w(x_n)$ is the weighting of the nth element. Note that this result is valid only for an even number of elements.

Now consider a uniform array $[w(x_n) = 1]$ with N elements a distance l apart, as illustrated in Fig. 3.5.11. Summing Eq. (3.5.49) results in

$$h(x, z_i) = \frac{e^{-j\pi x^2/\lambda z_i} \sin (N\pi lx/\lambda z_i)}{\sin (\pi lx/\lambda z_i)} \tag{3.5.50}$$

Thus the maximum output amplitude is at $x = 0$ and is of amplitude N, or N times the output from a single element. When N is large and $\pi lx/\lambda z_i$ is small, the output is $h(x, z) \rightarrow N \operatorname{sinc} (Dx/\lambda z_i)$, where the length of the array of infinitesimal elements is regarded as being $D = Nl$, just as in the uniform continuous receiving system. For larger values of x, the denominator of Eq. (3.5.50) becomes zero where $\pi lx/\lambda z_i = p\pi$ (i.e., where $x = d_{Gp}$), as given by Eq. (3.5.47).

We note that for the first sidelobe,

$$d_{G1} = Nd_x(\text{Rayleigh}) \tag{3.5.51}$$

Therefore, as the image and sidelobe pattern repeats itself around each grating lobe, the number of resolvable points in the image that are free from aliasing (i.e., free of regions where the image repeats itself) is N, the number of elements in the array.

Examples of apodization and grating lobes. The sampled Fourier transform relation (3.5.49) yields the form of the LSF for any arrangement of tap weighting. The result for a 32-element unapodized system [31] is shown in Fig. 3.5.12(a). The 13-dB sidelobe level and the grating lobes can be seen clearly.

As a second example, we consider the use of Hamming weighting (see Secs. 3.3 and 4.3). In this case, taking $x = 0$ to be at the center of the array, $w(x_n)$ is chosen so that

$$w(x_n) = 0.08 + 0.92 \cos \frac{\pi x_n}{D} \tag{3.5.52}$$

The maximum output or the sum of the signals from N elements is, for $N >> 1$,

$$h(0) \approx 0.54N \tag{3.5.53}$$

An illustration of Hamming weighting for a 32-element system, with the maximum amplitude normalized to unity, is shown in Fig. 3.5.12(b). At the expense of a slight loss in definition, the use of apodization clearly improves the sidelobe level.

We now consider the effect of errors on the sidelobe levels.

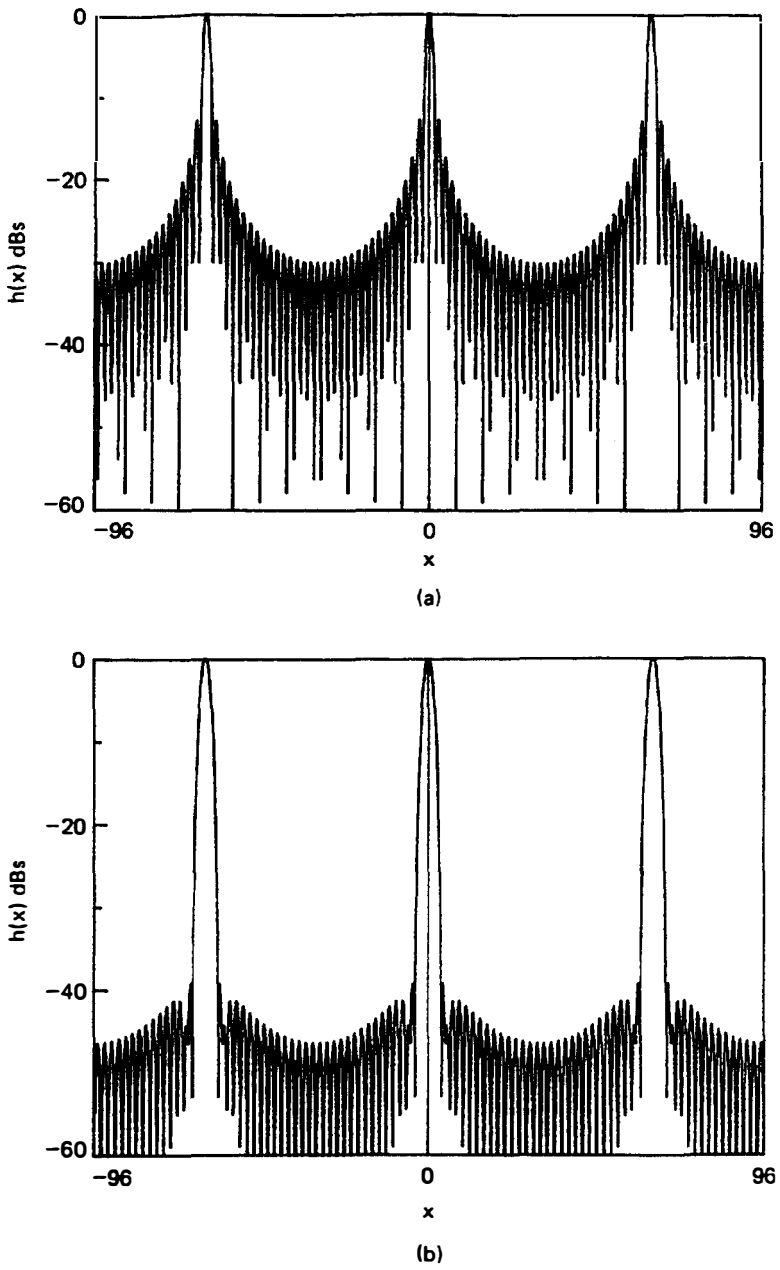

Figure 3.5.12 (a) LSF for a 32-element uniform array. Note the −13-dB sidelobes near the central lobe and the grating sidelobes. (b) LSF for a 32-element Hamming weighted array. Note the −43-dB near-in sidelobes. (c) LSF for a 32-element Hamming weighted array with one central element missing (31 elements present). The absence of this single element raises the sidelobe level from −43 to −23 dB. (d) LSF for a 32-element Hamming weighted array with two elements missing (30 elements present, central element and third from center element missing). The sidelobe level is −18 dB. (Two units of the abscissa correspond to the 4-dB size of one spot.)

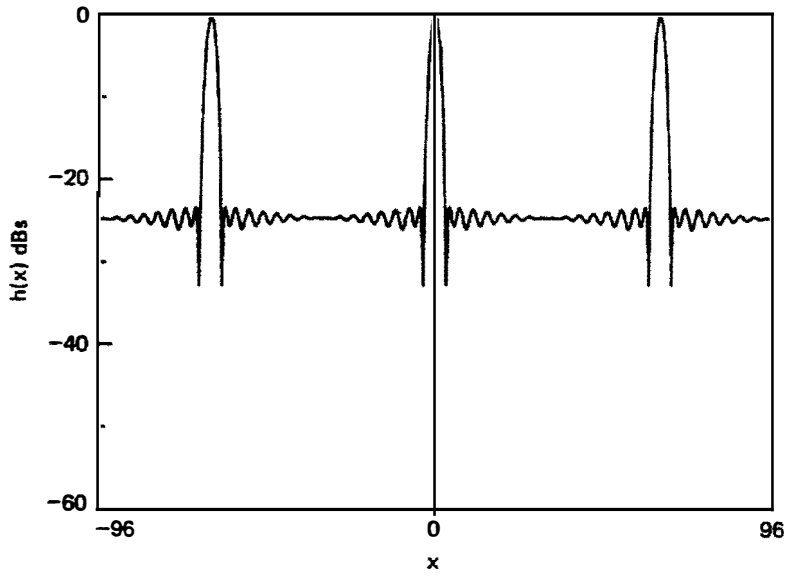

(c)

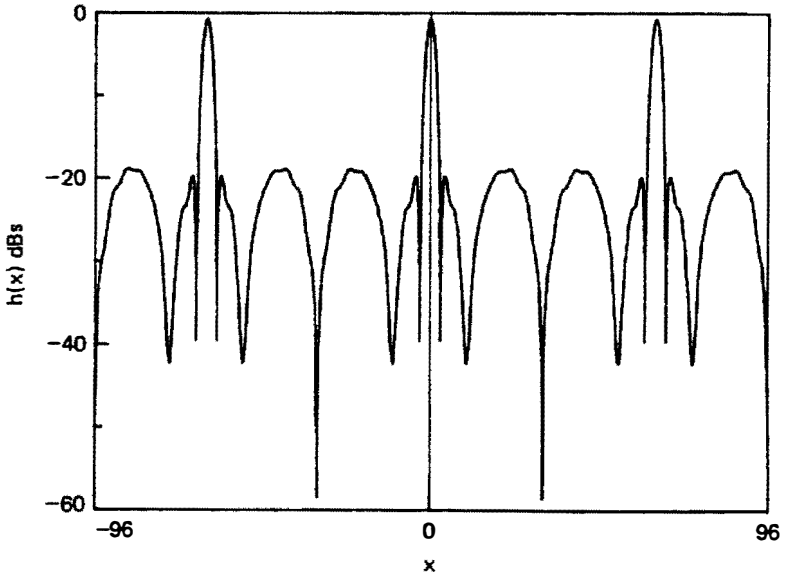

(d)

3.5.12 (cont.)

F. Effect of Missing Elements (Amplitude Errors)

The sidelobe level increases when transducer elements are missing or there are phase errors in the system. In this section, following the work of Fraser et al. [31], we analyze the response of an array to a point source and show how this is affected by missing elements. By using the formulas already given, we can calculate how both amplitude and phase errors affect the output. We can use a computer to do this, but it is helpful to try to obtain an analytic formula first, with which we can estimate errors and find how many elements we can afford to have missing.

Suppose that the qth element is missing. It follows from Eq. (3.5.49) that this is equivalent to subtracting an error term $e(x, x_q)$ from the output that is equal to the contribution of the qth element to the output. The error in the output is

$$e(x, x_q) = w(x_q)e^{2j\pi x x_q/\lambda z} \tag{3.5.54}$$

where $w(x_q)$ is the amplitude of excitation of the correctly excited qth element. Thus the total output is

$$h(x) = h_0(x) - e(x, x_q) \tag{3.5.55}$$

where $h_0(x)$ corresponds to the output when there are no missing elements.

The phase of the function $e(x)$ depends on the position x_q of the error. If it is in the center, $e(x)$ has virtually no phase change with position x. Assuming that the level of $e(x)$ is much larger than the sidelobe level in the error-free array, the magnitude of the ratio of the sidelobe to the main lobe amplitude, due to one missing element, will be $R(x_q)$, where

$$r(x_q) = \frac{w(x_q)}{\Sigma_n w(x_n) - w(x_q)} \tag{3.5.56}$$

In a Hamming weighted system, this corresponds to

$$R(x_q) = \frac{w(x_q)}{0.54N - w(x_q)} \tag{3.5.57}$$

Thus, for a missing element at the center of the array,

$$R(x_q) = \frac{1}{0.54N - 1} \tag{3.5.58}$$

For $N = 32$ elements, this corresponds to $R(x_q) = 0.061$, or -24 dB.

A more exact calculation would take account of the sidelobe level that was present before the errors were introduced (i.e., 0.007 down from the main lobe). The worst possible sidelobe level in the presence of errors would then be 0.061 + 0.007, or -23 dB. This result agrees fairly well with the computer result shown in Fig. 3.5.12(c).

When there are several missing elements, the question is whether their effects are additive or tend to add only randomly; that is, if there are q missing elements, is the amplitude error proportional to q or $q^{1/2}$? Unfortunately, the effects are additive, for if there are several missing elements, the effect on the error signal is like that of an array made up of the missing elements. This array produces a signal with a main lobe in which the effect of all the elements is additive, and if the element spacing is periodic, the main lobe tends to repeat itself in a distance corresponding to that of the grating lobes of the error array. If most of the missing elements are near the center of the array, the main lobe of the error array will be wider than that of the full array. Thus there will be sidelobes near the main lobe of the original array that have the full amplitude of the main lobe of the error array. More than likely, there will also be other sidelobes of similar amplitude farther out from the main lobe, due to the quasi-spatial periodicity of the error

signal. An illustration of what occurs when two elements are missing is shown in Fig. 3.5.12(d).

The results obtained from these simple concepts agree well with the computer results; they indicate that it is critically important to have all elements working correctly in the transducer array. Otherwise, the maximum sidelobe amplitude is of the order of q/N below that of the main lobe, where q is the number of missing elements. Because not all elements are fully excited in an apodized array, the maximum sidelobe level can actually be worse than the results given by this simple formula. This happens when elements are missing near the center of the array. If they are missing from one end of the array, however, the level is better than this estimate.

3.5.3 Fresnel Lenses and Digital Sampling

A. Basic System

As we discussed, a physical acoustic lens is often difficult to construct because it suffers from multiple reflections at each surface, must be immersed in an acoustic medium such as water, and has relatively large aberrations in comparison to optical lenses. These difficulties are caused in large part by the great difference in refractive index and impedance between water and the typical media available. In addition, mode conversion at the surface of the lens from longitudinal to shear waves, and vice versa, can give rise to unwanted signals that are extremely difficult to eliminate.

A reasonably good physical acoustic lens can be made using liquid, RTV rubber, urethane, or some other plastic. The refractive indices of these materials differ from that of water, but their impedances can be chosen to match that of water very closely. Furthermore, they all have high shear wave attenuation. The best alternative to using these materials, if it is convenient, is to construct a properly shaped acoustic transducer.

Another approach is to use the Fresnel lens concept of optics. In this case, the basic principle is to synthesize the spherical or cylindrical phase front produced by a physical lens.

Consider a plane disk transducer at $z = 0$ in a rigid baffle. Suppose that the wave excited at $z = 0$ varies as $\exp [j\Phi(r')]$ and has a displacement $u_z(0)$ of unit negative amplitude. Then the wave excited at $(0, z_i)$ has a potential of the form

$$\phi(0, z_i) = \frac{1}{2\pi} \int \frac{e^{j[\Phi(r') - kR]}}{R} r' \, dr' \tag{3.5.59}$$

where

$$R = \sqrt{z_i^2 + r'^2} \tag{3.5.60}$$

If $\Phi(r') = kR$, all signals arriving at $(0, z_i)$ will be excited in phase, which synthesizes the action of a perfect lens. The Fresnel lens approximates this desired

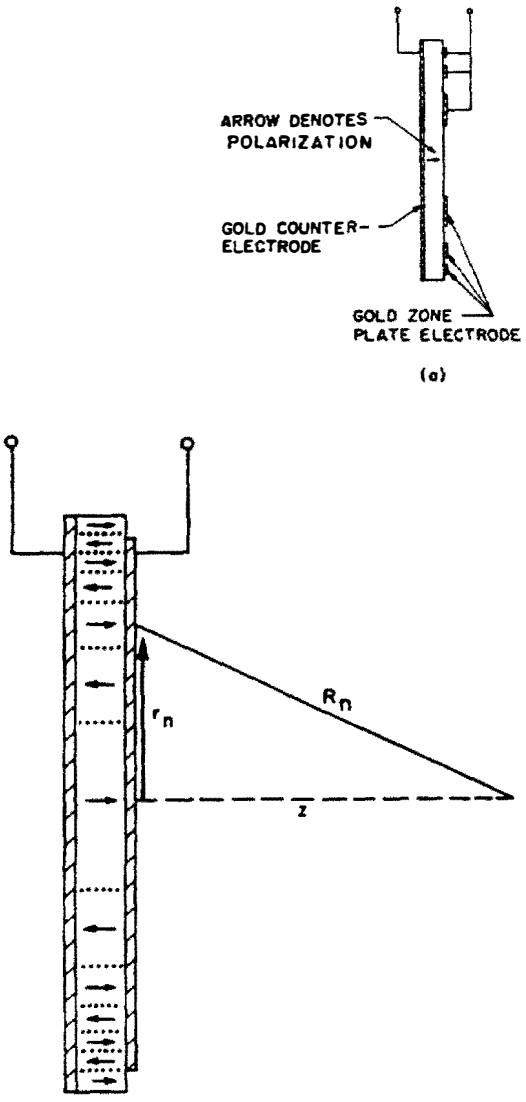

Figure 3.5.13 Fresnel lens imaging system: (a) the PZT polarization is determined by reverse poling an already poled transducer; (b) a simple disk electrode is placed over the phase plate pattern. (After Farnow and Auld [32].)

behavior by sampling the desired response, usually with two samples for every 2π phase change.

Consider the system due to Farnow and Auld [32], illustrated in Fig. 3.5.13(b), in which a disk-shaped PZT transducer is divided into rings of radius r_n. Suppose that a point on the object a distance z along the axis of the lens is a distance $R_n = \sqrt{r_n^2 + z^2}$ from the nth ring. Suppose also that the object is illuminated with a signal of frequency ω and wavelength λ. The phase delay of the ray reaching the nth ring will therefore be $2\pi R_n/\lambda$. If we choose the $n = 0$ element (i.e., the center element) as the reference, we choose the first element, $n = 1$, to have a radius at its center r_1 such that the arriving signal is π out of phase with the signal on the axis. We choose the $n = 2$ element so that the signal arriving at it is in phase, and so on in turn (i.e., all even elements are in phase and all odd elements are out of phase). This means that all the signals arriving at the rings can be added

if an extra π phase shift is introduced into the electronic signals picked up by the odd elements.

Farnow and Auld built their device by using a PZT ceramic transducer with ring radi r_n chosen so that

$$\sqrt{r_n^2 + z^2} - z = \frac{n\lambda}{2} \tag{3.5.61}$$

The poling of the ceramic (see Sec. 1.3.1) was reversed in sign at the appropriate positions, as shown in Fig. 3.5.13(a), to obtain the required π phase shift automatically. Operating this system at 10 MHz, in either reflection or transmission, with two Fresnel lenses placed opposite each other, they were able to mechanically scan the lenses across an object to form an image in the same way as with the acoustic microscope. By this means, they obtained good reflection and transmission pictures. A reflection image of a serrated metal sheet obtained with this system operating at a frequency of 10 MHz is shown in Fig. 3.5.14. The definition is excellent, and comparable to the theoretical prediction.

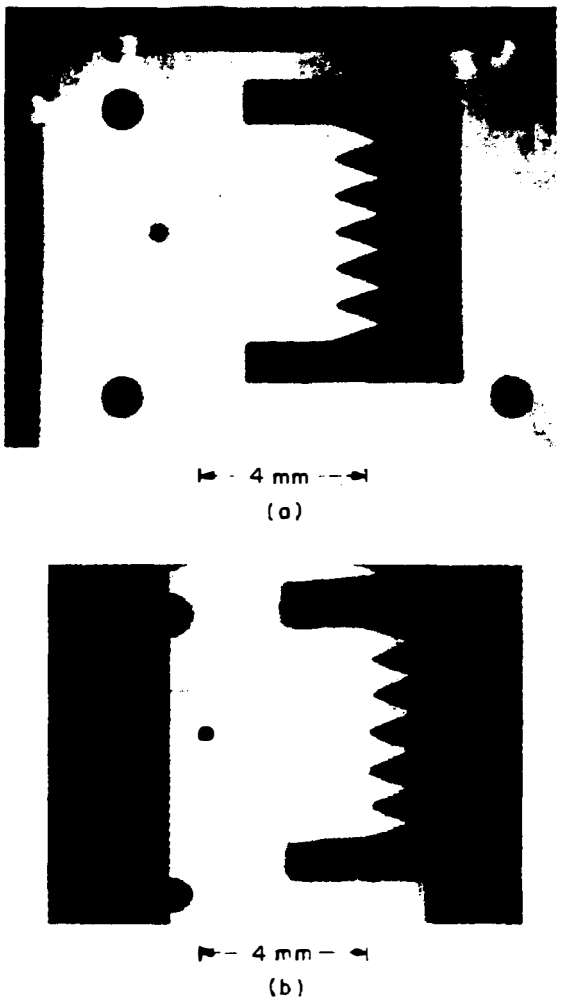

Figure 3.5.14 Comparison of optical (a) and acoustic reflection (b) images of a sawtooth pattern punched in a 3-mil nickel sheet. The results were taken with a Fresnel lens at a frequency of 10 MHz. (After Farnow and Auld [32].)

There are two problems with such a simple Fresnel imaging system. First, the only phases introduced are 0 and π; intermediate phases are required to obtain a perfect image with low sidelobes. As we shall see, because of the errors due to phase sampling, extra subsidiary foci occur, as well as a relatively high sidelobe level at the main focal plane. Second, if there are N rings, the total difference in length to the axial point between the outer and inner rings is $N\lambda/2$. Therefore, if a pulsed RF signal (i.e., a signal M cycles long) is employed, M must be chosen so that $M > N/2$ in order for signals from all the rings to arrive together at the focal point on the lens. This implies, in turn, that the range definition will be dictated mainly by the depth of focus of the lens, and that short pulses cannot be used unless the rings themselves are excited at different times so that all pulses arrive at the focus at the same time.

B. Fresnel Lens Sidelobes and Phase Sampling in Digital Systems

The ideal matched filter response to image the point 0, z_i is $2\pi z_i/\lambda$ $g(r', z_i) = \exp(j\pi r'^2/\lambda z_i)$, where we have omitted the term $\exp(2j\pi z_i/\lambda)$, which may for the present purposes be regarded as a constant. In general, with the development of digital processing and Fresnel lenses, it is important to consider the effect of sampling the phase $\phi = \pi r'^2/\lambda z_i$ at M points (i.e., dividing the possible phases into M steps). Such phase sampling leads to errors in the response of the receiving system, which in turn show up as a decrease in the main lobe amplitude and the production of additional sidelobes and spurious focal points.

To understand the principles involved, let us consider a one-dimensional rectilinear Fresnel lens. Suppose that the response of the transducer array is either $+1$ or -1 at its different elements. If we write $u = x'^2/\lambda z_i$, the optimum spatial response of the two-phase Fresnel transducer array can be written in the form

$$g(u) = \operatorname{sgn}(\sin \pi u) \tag{3.5.62}$$

This expression has the form of a simple square wave in u, where $u = x'^2/\lambda z_i$ is defined only for u positive, with $\operatorname{sgn}(s) = 1$ for $x > 0$ and $\operatorname{sgn}(s) = -1$ for $s < 0$, where $s = \sin(\pi u)$.

We can carry out a Fourier expansion of $g(u)$ to obtain the results, stated as a function of u or x', respectively, in the form

$$g(u) = \frac{2}{\pi} \sum_{m=-\infty}^{\infty} \frac{e^{j(2m+1)\pi u}}{2m+1} \tag{3.5.63}$$

or

$$g(x') = \frac{2}{\pi} \sum_{m=-\infty}^{m=\infty} \frac{e^{j(2m+1)\pi x'^2/\lambda z_i}}{2m+1} \tag{3.5.64}$$

Note that in this case, as the response of the transducer array is $g(u) = \pm 1$, the transducer can consist of individual electrodes with infinitesimal spacing between them, connected to either the positive or negative terminals of an individual amplifier, or it can be made of a piezoelectric material in which individual elements

are poled in the $+z$ or $-z$ directions, as we have already discussed. Each element of the transducer must decrease progressively in width from the one before it, for $x' \propto u^{1/2}$.

We observe that each harmonic term of the expansion in Eq. (3.5.64) corresponds to an individual matched filter or lens with a focal point at

$$z_m = \frac{z_i}{2m + 1} \tag{3.5.65}$$

Thus the $m = 0$ term corresponds to a simple lens with a focal length z_i. In addition, however, there are subsidiary foci at $z_i/3$ ($m = 1$), $z_i/5$ ($m = 2$), and so on, as illustrated in Fig. 3.5.15, with virtual foci at $-z_i$ ($m = -1$), $-z_i/3$ ($m = -2$), and so on. As a receiver, the amplitudes of the transducer response to the individual harmonic terms are reduced by a factor of $2/(2m + 1)\pi$, and that of the main lobe ($m = 0$) by $2/\pi$, in comparison to a system with a continuous analog phase reference of unit amplitude. This result is identical to that for the cylindrical Fresnel lens.

Sidelobe level. It is interesting to consider, for a transmitting array, the sidelobes generated by the subsidiary beams passing through the subsidiary foci. The reciprocity theorem then yields results of the same form for a receiver system. For the mth focus, using Fig. 3.5.15, it follows from simple geometry that the beam passing through the focus at $z_m = z_i/(2m + 1)$ has a width $|2mD|$ at the focal plane $z = z_i$. It therefore produces a uniformly distributed field at the focal plane that is reduced in amplitude by $1/|2m|^{1/2}$ from its value at the array. The strongest subsidiary beams are the $m = -1$ and $m = +1$ beams. The interference between

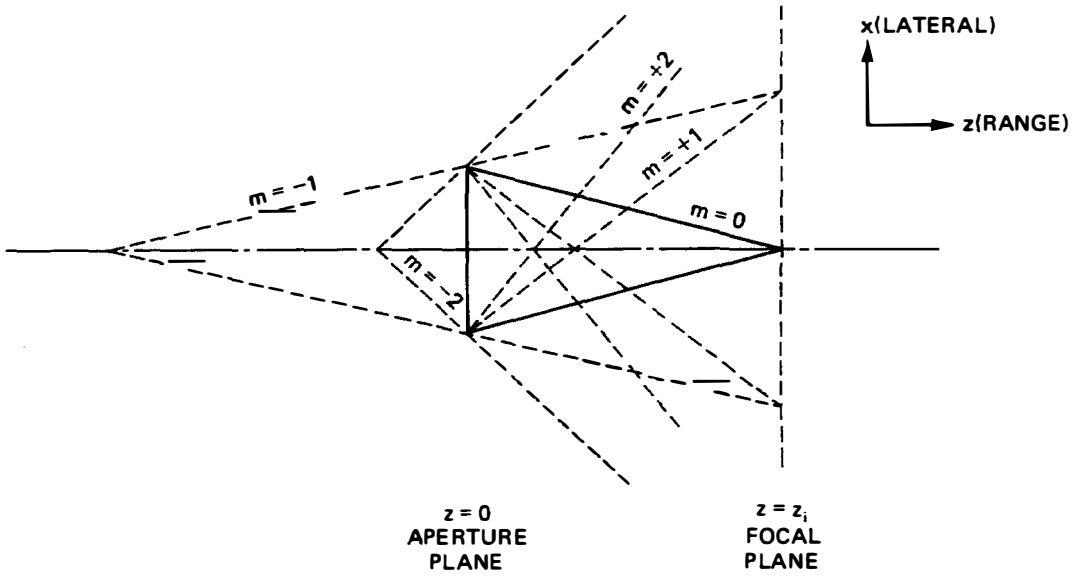

Figure 3.5.15 Subsidiary foci due to a Fresnel lens or to digital sampling of phase.

them gives rise to nonuniformly distributed sidelobes, which can be at a fairly high level in a two-phase system.

To treat this subject more quantitatively, we take the normal displacement at the transducer to be $u_z(x', 0) = Kg(x')$, where K is a constant. It then follows from the Rayleigh–Sommerfeld formula (see Prob. 3.1.3) that for a rectilinear system in the paraxial approximation, the LSF is of the form

$$h(x, z) = \frac{e^{-jkz}}{z^{1/2}} \int g(x')e^{-jk(x-x')^2/2z}\, dx' \tag{3.5.66}$$

where $k = 2\pi/\lambda$. Substituting Eq. (3.5.64) in Eq. (3.5.66), we obtain

$$h(x, z) = \frac{2e^{-jkz}}{\pi z^{1/2}} \int_{-D/2}^{D/2} \sum \frac{e^{j(2m+1)\pi x'^2/\lambda z_i}\, e^{-j\pi(x'-x)^2/\lambda z}}{2m + 1}\, dx' \tag{3.5.67}$$

where D is the length of the array.

As we have already discussed, for the mth harmonic, the quadratic terms in x' cancel out where $z = z_i/(2m + 1)$, and each harmonic term can be treated as if it were associated with a lens of focal length $z_i(2m + 1)$.

At the focal point $(0, z_i)$, we find that the fundamental harmonic gives rise to a term

$$h_0(0, z_i) = \frac{2De^{-jkz_i}}{\pi z_i^{1/2}} \tag{3.5.68}$$

where the mth harmonic is denoted by the subscript m. Thus the strength of the main lobe is reduced by a factor of $2/\pi$, compared to a perfect continuously excited system.

Similarly, the amplitude of the mth harmonic at the focal plane is

$$h_m(x, z_i) = \frac{2e^{-jkz}}{\pi z_i^{1/2}} \int_{-D/2}^{D/2} \frac{e^{j(\pi/\lambda z_i)(2mx'^2 + 2xx' - x^2)}}{2m + 1}\, dx' \tag{3.5.69}$$

The integral can be evaluated by the method of stationary phase (Appendix H) to yield the result

$$h_m(x, z_i) = \frac{2e^{-jkz_i}}{\pi(2m + 1)} \left|\frac{\lambda}{2m}\right|^{1/2} e^{[j\pi \operatorname{sgn}(m)/4]} e^{-[j\pi(2m+1)x^2/2z_i\lambda m]} \tag{3.5.70}$$

It follows that

$$\left|\frac{h_m(x, z_i)}{h_0(0, z_i)}\right| = \left(\frac{\lambda z_i}{D^2}\right)^{1/2} \left|\frac{1}{2m}\right|^{1/2} \left|\frac{1}{2m + 1}\right| \tag{3.5.71}$$

This agrees with our earlier physical derivation, which implied that the fields of the mth harmonic at the focal plane are reduced in amplitude by a factor $1/|2m^{1/2}$. The $1/|2m + 1|$ factor in Eq. (3.5.71) is proportional to the excitation of the mth harmonic.

We observe that the $m = -1$ harmonic is the one most strongly excited. It yields a background level reduced by $(\lambda z_i/2D^2)^{1/2}$ from the main lobe. As an

example, with $z_i = 10$ cm, $\lambda = 0.5$ mm (3 MHz in water), and $D = 2$ cm, the background level is 12 dB below the main lobe level. The $m = +1$ term can add to the $m = -1$ term, bringing the peak sidelobe level to 9.5 dB below the main lobe. So the sidelobe problem of a Fresnel lens can be a serious one.

A similar analysis can be carried out for an M-phase system of the type used in a receiver. When lumped delay lines are employed to synthesize the phase, or when a signal is digitally sampled with a clock rate M times the signal frequency, there are M samples per cycle. In this case a similar analysis yields the result (see problem 4)

$$\left|\frac{h_m(x, z_i)}{h_0(0, z_i)}\right| = \left(\frac{\lambda z_i}{D^2}\right)^{1/2} \left|\frac{1}{mM}\right|^{1/2} \left|\frac{1}{mM + 1}\right| \tag{3.5.72}$$

Note that the sidelobe level falls off with M. A five-phase system (e.g., an analog-to-digital converter operating at a clock frequency of five times the fundamental frequency) will therefore give a sidelobe level that is still by no means adequate for a high-quality medical imaging system. For example, a system with $M = 5$, $m = -1$, $z_0 = 10$ cm, $D = 2$ cm, and $\lambda = 0.5$ mm gives a background level of -28 dB. The inclusion of the $m = 1$ term raises the peak sidelobe level to approximately -22 dB below the main lobe. The reader is referred to more detailed numerical calculations for further information [33]. Note that such sidelobe levels are far higher than the -60-dB level required, which is obtained in some very high quality medical imaging systems.

3.5.4 Chirp-Focused Systems

A. Basic System

In Sec. 3.5.2 we showed that the use of a matched spatial filter makes it possible to obtain good definition of point or line sources. One way to realize such a filter is by employing SAW techniques of the type described in Chapter 4.

Here we will describe principles of the chirp-focused system because the concept is simple, the concepts used are related to holography (see Sec. 3.5.6), and experiments have been carried out, using the technique, that demonstrate many possible forms of electronically focused acoustic imaging.

Chirp-focused imaging systems have been constructed that operate as both receivers and transmitters of focused beams and, at the same time, provide automatic scanning along a line parallel to the acoustic array. The systems have been demonstrated mainly in NDT, rather than medical, applications, because they are basically phase-focused systems and thus suffer from relatively poor range definition and severe sidelobe problems. This tends to make them unsuitable for medical imaging.

Chirp-focused systems employing SAW delay lines are no longer used, because it is difficult and expensive to make the physically large, multiple tap delay lines they require. Since SAW delay lines are analog devices with fixed taps, they tend to be somewhat inflexible in this acoustic imaging application and may not,

in practice, give the necessary accuracy. However, the same concept can also be implemented with more flexible digital systems to provide the required sampled phase references for focusing and scanning [31, 34–36].

Consider the FM chirp-focused receiver system using an array of transducer elements, which is illustrated schematically in Fig. 3.5.16. Suppose that the object is illuminated by a signal of frequency ω_s and wavelength λ in the medium being examined. The signal arriving at each array element is mixed with a signal from a corresponding tap on an SAW line.

The signal propagating along this delay line is chosen to have a parabolic variation of phase on the same magnitude but opposite sign as the signals arriving from the point x, z. When the two signals, one from the tap and one from the array element, are mixed, their frequencies add, as do their phases. Therefore, if the phase delay of the wave propagating along the delay line is chosen correctly, it is possible to cancel out the phase differences between the different rays arriving from the point x, z. Using this technique, we can construct an electronically focused lens focused on the point x, z; this lens is a matched spatial filter for the point x, z, as described in Sec. 3.5.2.

The correct signal to inject into the delay line is a *linear FM chirp*, one whose frequency varies linearly with time as $\omega = \omega_1 + \mu t$. This signal has its frequency at the nth tap given by the relation

$$\omega = \omega_1 + \mu\left(t - \frac{x_n}{V_R}\right) \tag{3.5.73}$$

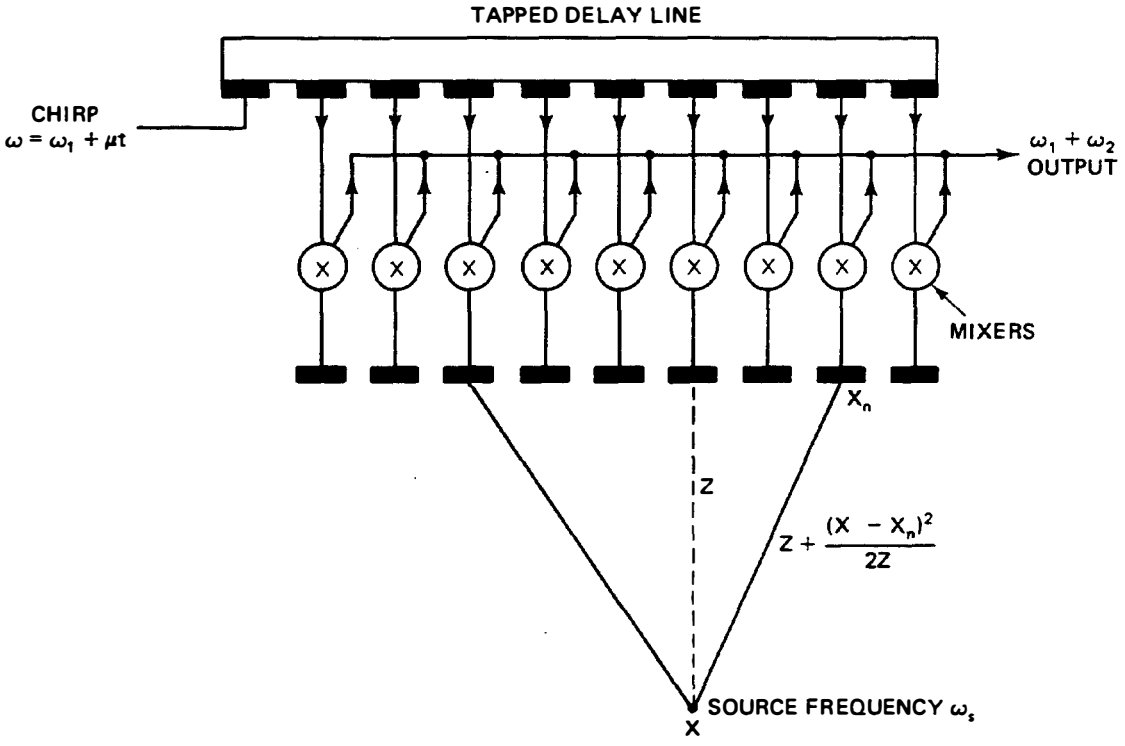

Figure 3.5.16 Arrangement used for mixing the signals from the array elements with a signal from the delay line.

Because the phase is $\phi = \int \omega\, dt$, it follows that the phase at the nth tap is

$$\phi_{Rn} = \omega_1\left(t - \frac{x_n}{V_R}\right) + \frac{\mu}{2}\left(t - \frac{x_n}{V_R}\right)^2 \tag{3.5.74}$$

that is, the filter response is of the form

$$g(x_n, t) = e^{j\omega_1(t - x_n/V_R) + (\mu/2)(t - x_n/V_R)^2} \tag{3.5.75}$$

where $V_R = l/\tau$ is the effective velocity of the surface acoustic wave (or reference wave) along the array, $x_n = nl$, l is the tap spacing, and τ is the time delay of the acoustic wave from tap to tap of the delay line. The FM chirp signal generates a spatial chirp, which moves at a velocity V_R along the delay line. The equivalent matched filter generated by this process therefore moves in the x direction at a velocity V_R, thus providing automatic scanning along one line of the image.

The summed output from the mixers is of the form

$$y(x, t, z) = \sum_{x_n} w(x_n) g(x_n, t)\, f(x_n - x, t) \tag{3.5.76}$$

where $w(x_n)$ is the amplitude response or weighting of the transducers and $f(x_n - x, t)$ is the signal arriving from a line source at the nth transducer.

It follows that for $w(x_n) = 1$, the output from the array is of the form

$$h(x, t, z) = \frac{1}{z^{1/2}} \sum_{x_n} e^{j[\omega_1(t - x_n/V_R) + \mu/2(t - x_n/V_R)^2]} \times e^{j\omega_s[t - z/V - (x_n - x)^2/2zV]cb} \tag{3.5.77}$$

The first exponential term in Eq. (3.5.77) is the filter response $g(x_n, t)$. For $g(x_n, t)$ to be a sampled version of a matched spatial filter for the point x, z [i.e., equivalent to $f^*(-x', z)$ in Eq. (3.5.6), the chirp rate μ must be chosen so that the square-law spatial phase variation terms cancel out, or for $z = z_i$

$$\mu = \frac{\omega_s V_R^2}{V z_i} = \frac{2\pi V_R^2}{\lambda z_i} \tag{3.5.78}$$

It is also convenient, but not necessary, to have $\omega_1 l/V_R = 2m\pi$, where $x_n = (2n + 1)l/2$ and m is an integer. This choice of ω_1 implies that at $t = 0$, all elements are at the same phase and the system is focused on $x = 0$. The choice of μ is equivalent to choosing the focal length of the lens so that it focuses on the plane $z = z_i$.

With these assumptions, Eq. (3.5.77) can be summed to give the result

$$h(x, t, z_i) = \frac{\sin N\pi l(x - V_R t)/\lambda z_i}{\sin \pi l(x - V_R t)/\lambda z_i} e^{j[(\omega_1 + \omega_s)t + \mu(t^2 - x^2/V_R^2)/2]} \tag{3.5.79}$$

Thus the output of the system is in the form of a modulated FM chirp with a frequency $\omega_1 + \omega_s + \mu t$, with the modulation corresponding to the LSF of the system.

The system behaves like a moving lens, focused on the plane $z = z_i$, that moves at a velocity V_R. By displaying the detected output of the system as a

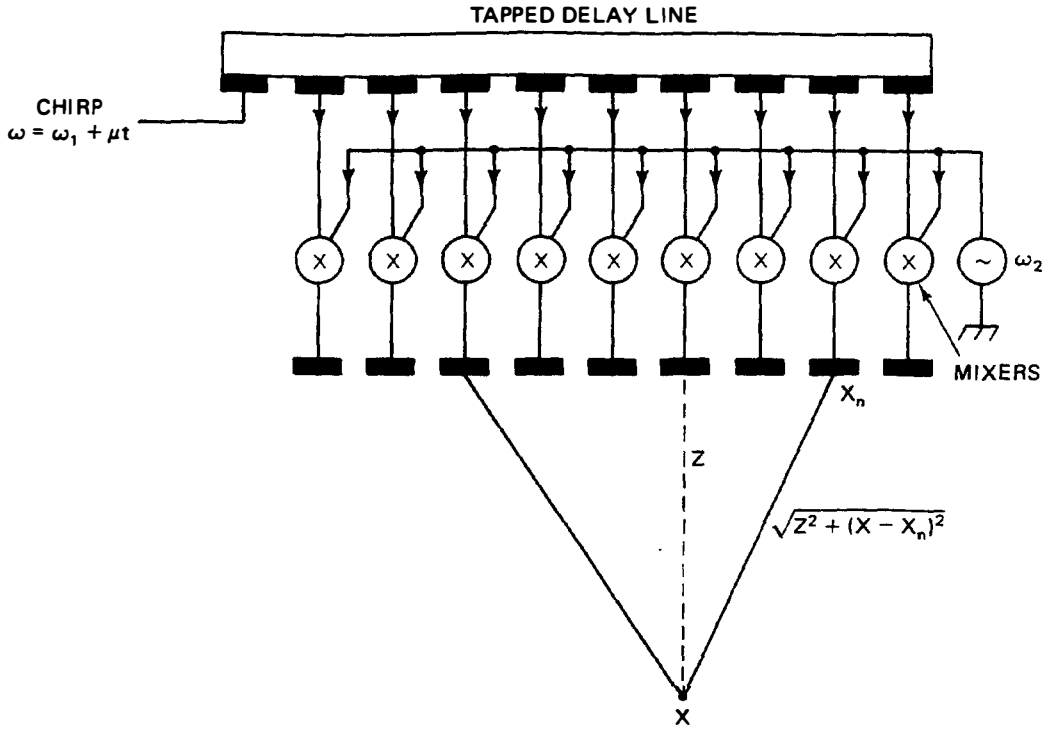

Figure 3.5.17 Chirp-focused transmitter system.

function of time, as an intensity modulated line on a cathode ray tube, we automatically obtain a display of one line of the image. The line x, z_i in the image is displayed at the time $x = V_R t$.

This system behaves in exactly the same way as the matched filter discussed in Sec. 3.5.2. The sidelobe level will be of the same form, and grating lobes will occur in the same relative positions as given by the earlier derivations. The only difference is that the use of the chirp obtains the very useful feature of automatic scanning, with the main lobe focused on the point $x_i = V_R t$, $z_i = \mu V/\omega_s V_R^2$.

This basic system is simple, in principle. In practice, however, it typically requires mixers and amplifiers on each element, and suitable summing networks. It also requires an SAW delay line several inches long, with perhaps as many as 100 taps, and a total delay comparable to a TV line scan (64 μs). It is not easy to construct such delay lines free of defects. This is a serious problem because, as was shown in Sec. 3.5.2.F, if q elements are missing from an N-element array, the maximum sidelobe amplitude due to the missing elements will be approximately q/N lower than the main lobe.

The same system can be used as a transmitter as well as a receiver, by exciting the mixers from the delay line and a separate oscillator, as shown in Fig. 3.5.17, to give an output signal centered about a frequency ω_s, which can be used to excite an element of the array. In this case, of course, separate transmitter amplifiers are needed for each element.

When this device is used in the transmit mode, it behaves like a moving lens traveling at a velocity V_R parallel to the array. The time for which a single spot

in the image is illuminated is approximately

$$\tau_x(4\text{ dB}) = \frac{d_x(4\text{ dB})}{V_R} = \frac{\lambda z_i}{DV_R} \tag{3.5.80}$$

where $d_x(4\text{ dB})$ is the spot size.† The time difference between the ray paths from the center and the outside of the beam is

$$\tau_R = \frac{D^2}{8z_iV} \tag{3.5.81}$$

In order for the spot to be illuminated by all the rays, and hence for optimum definition to be obtained, the requirement $\tau_R < \tau_x$ is apparent. This, in turn, implies that when $\tau_R = \tau_x$, the minimum spot size to the 4-dB points is

$$d_x(4\text{ dB}) \approx \left(\frac{z\lambda^2V_R}{8z_iV}\right)^{1/3} \tag{3.5.82}$$

with

$$D = \left(\frac{(8z_i^2V\lambda}{V_R}\right)^{1/3} \tag{3.5.83}$$

provided that the central axis of the beam is opposite the point of interest.

The differences in transit time from the edge and the center of the array, respectively, to the focal point, give problems with such a phase focused system, but would not in a time-delay focused system. Similar difficulties occur with Fresnel lenses and with holographic imaging systems. In each case, the length of the excitation signal has a minimum value τ_R fixed by the requirement for phase focusing. The minimum range resolution of a phase focusing system in which the scan is very slow is of the order of τ_R. As we shall show below, the fast chirp scan gives better range resolution, albeit with other disadvantages.

B. Various Forms of Chirp-Focused Systems

Chirp-focused systems have been made in several versions, some with as many as 128 elements. Several examples are illustrated in Fig. 3.5.18. The left-hand figure of Fig. 3.5.18(a) shows a system employing transmitting and receiving transducer arrays placed opposite each other with the object placed between them and mechanically scanned up and down in the y direction. Such a system has the advantage, already discussed in Sec. 3.5.1 and illustrated in Fig. 3.5.3(b), of giving the speed and focusing in the x direction of electronic scanning, which speeds up the scan by approximately a factor of N. Also, because the receiver and the transmitter are both focused on the same point, the response of the system will vary as $[\text{sinc}\,(x/d_x)]^2$, giving the same advantages as those we have already discussed for the acoustic microscope in Sec. 3.3.3.

An example of an NDT application is shown in Fig. 3.5.18(a). The system

† It is convenient here to work with the 4-dB resolution, $d_x(4\text{ dB}) = \lambda z/D$, thus omitting the 0.89 factor used in the definition of the 3-dB resolution.

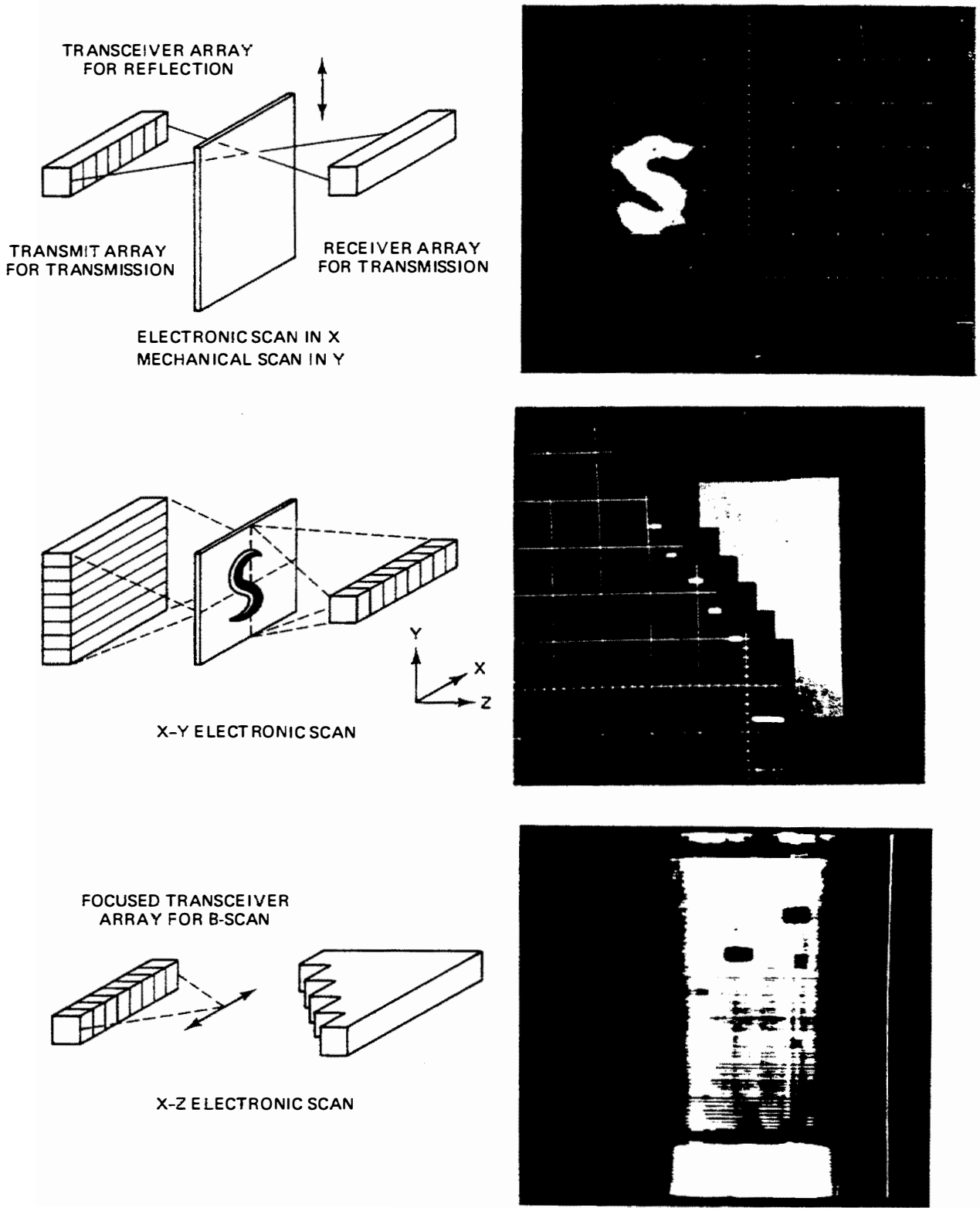

Figure 3.5.18 Chirp-focusing schemes. (a) Transmission image of a boron fiber epoxy laminate carried out with transmitting and receiving arrays placed opposite each other. (After Waugh et al. [36].) (b) Two-dimensional transmission image with the two arrays placed at right angles to each other. (After Fraser et al [31].) (c) Simple B-scan image, using the same array as transmitter and receiver. (After Waugh et al. [36].)

was used to scan a boron fiber–reinforced epoxy laminate laid down on titanium. The sample measured approximately 22 × 7.5 cm and defects were deliberately introduced into it, as can clearly be seen. The total scan took only a few seconds because the mechanical scanning was only in one direction.

A second example of the use of two arrays, illustrated in Fig. 3.5.18(b), is to work in a transmission mode with the transmitting and receiver arrays arranged at right angles to each other. As in the previous example, the transmitter and the receiver are both focused on the same plane, but the transmitter array scans in the x direction and the receiver array scans in the y direction. This makes it possible to obtain N^2 resolvable spots with only $2N$ array elements. The major disadvantage of such a system, though, is the very high sidelobe level. We have to pay for the saving in electronic complexity!

Systems of this type have also been used in a reflection mode. In this case, the same SAW delay line and array are used for both transmission and reception, with appropriate switching to transmit or receive. In this case, the basic transverse definition is comparable to that of the two-lens transmission system shown in Fig. 3.5.18(a) or that of the acoustic microscope; this implies that there is a $(\sin x/x)^2$ response function in the focal plane. The receiver is operated at a time $T_z = 2z/V$ later than the transmitter. By varying the time delay T_z, along with the chirp rate μ, a B-scan in the form of a series of lines or a raster in a plane perpendicular to the array can be scanned, as illustrated in Fig. 3.5.19. In principle, the range definition should be fairly good, because the object point is illuminated for a time $\tau_x = d_x/V_R$, so that the range definition becomes

$$d_z \approx V\tau_x \approx \frac{Vd_x}{V_R} \tag{3.5.84}$$

As the scan velocity V_R in such systems is comparable to the velocity V in the medium, the implication is that the range definition is comparable to the transverse definition. We use the relation that the total frequency excursion of the chirp is

$$\Delta f_c = \frac{\mu T}{2\pi} = \frac{\mu D}{2\pi V_R} \tag{3.5.85}$$

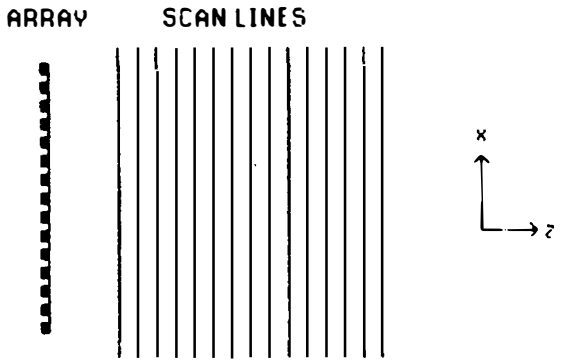

Figure 3.5.19 Scan format for a B-scan FM chirp system.

where D is the length of the array. It then follows from Eqs. (3.5.80) and (3.5.85) that

$$\tau_x \approx \frac{\lambda z}{DV_R} = \frac{2\pi V_R}{\mu D} = \frac{1}{\Delta f_c} \tag{3.5.86}$$

Thus the range definition turns out to be just what we would expect from a pulse with approximately the same bandwidth as the chirp.

The FM chirp-focused system has provided fairly good images in NDT applications; an example is illustrated in Fig. 3.5.18(c). But work on systems of this type was abandoned because of their poor sidelobe response. In this system, a point in the image can be insonified by the main lobe of the transmitter and received on a sidelobe of the receiver, and vice versa. A further difficulty is that the sidelobes can be due to reflectors that are closer to the array than the focal point of, for example, the transmitter. This makes the device particularly difficult to use in medical applications, where the attenuation in body tissue is very high. In such cases, the effective sidelobe level is higher than that caused by a reflection at the focal plane by an amount corresponding to the two-way attenuation between the plane of the unwanted reflector and the required image plane.

These examples serve to point out the difficulties that may occur in the application of practical imaging systems. In principle, we expect the reflection imaging system to give a $\text{sinc}^2\,(x/d_x)$ response and a fairly good range definition. In practice, the system responds just this way for the transverse definition in the focal plane, but sidelobes occur in regions we might not have expected to see them in initially.

Systems of this type are at their best when used in a reflection or transmission mode to look at a thin object for which range resolution is not of great importance. In such cases, the sidelobe level is low. The phase reference of the chirp delay line can be synthesized digitally, and the scan in the x direction can be made at any velocity, from zero to a value larger than that for a typical SAW system.

Focused optical beams can also be used to give the required phase reference. This is the basic principle of holography, which will be described in Sec. 3.5.6.

Reflection mode imaging is best carried out with a system that defines at least two of the dimensions of the focal spot very precisely and has very low sidelobe levels. One example is time-delay focusing, discussed in Secs. 3.5.1 and 3.5.5, in which the region to be imaged is confined by the use of a short pulse to a short range (z direction). A second example is the acoustic microscope, in which both the transverse dimensions (x and y) of the focal spot are well defined, while the range resolution in the z direction can be very good because of the short range definition of a wide aperture confocal imaging system (see Fig. 3.5.4).

3.5.5 Time-Delay and Tomographic Systems

A. Introduction

In Sec. 3.5.1 we discussed the various types of scanned systems that can be employed for imaging. As we saw, time-delay systems are very attractive because their range definition is not necessarily limited by the aperture size, as it is in a

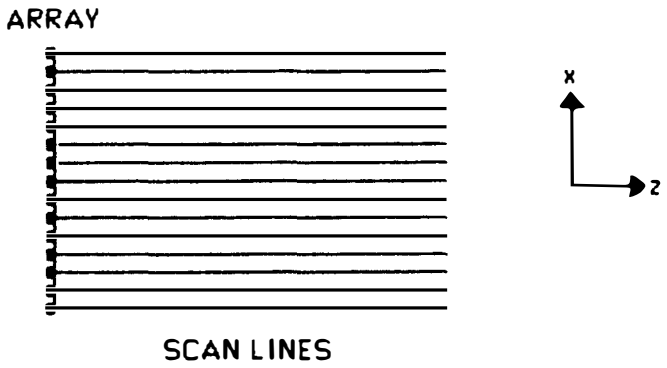

Figure 3.5.20 Standard B-scan pulse array system illustrating scan lines.

phase-focused system. However, a variable time-delay system is more difficult to make than a variable phase-delay system.

Simple implementations of unfocused array systems are commonly employed for medical imaging. As an example, several commercial systems use an array of transducer elements with a total length of the order of 10 cm in the x direction (center frequency 2.25 MHz). Typically, 64 or 128 elements, each 1 cm wide (y direction), are employed.

In one example of a 64-element system, these elements are excited sequentially with a short pulse in groups of four, to emit a parallel beam in the z direction, approximately 1 cm square. The beam is received by the same four elements that emitted it, and displayed in the form of one line of a B-scan image. The device then moves one element on, to the next group of four elements, and the process is repeated. Thus a 64-line image is obtained, with a scan form like that shown in Fig. 3.5.20. This image has accurate range definition, because of the short pulse employed, but relatively poor transverse definition, because the device behaves as if it were a 1-cm-square transducer being moved along the x direction in 2.5-mm steps.

This type of system has been developed by a number of laboratories; it has been applied mainly in medical and, to a limited extent, NDT applications. Because no delay lines are employed, it is possible to use the same technique at relatively high frequencies.

Other alternatives have been considered. One, employed by Becker et al. at Battelle [37], is to use 128 elements in a row, exciting them sequentially in much the same manner already described. However, by exciting the array elements with a programmed time delay between them, it is possible to excite a wave at an arbitrary angle to the array. One application of this technique is to look for faults in nuclear reactor walls. The standards that have been set up for pressure vessels require such observations to be made with several incident beam angles, to pick up specular reflectors. By using time-delay techniques, the system is scanned like the system described earlier, except that the scan is now carried out at several different angles. By mechanically scanning in the other direction, a large volume of material can be tested in a relatively short time. Using sophisticated display techniques, three-dimensional information can be obtained in the form of an isometric projection display that makes the results relatively easy to interpret. A sample of an image obtained with this system is shown in Fig. 3.5.21.

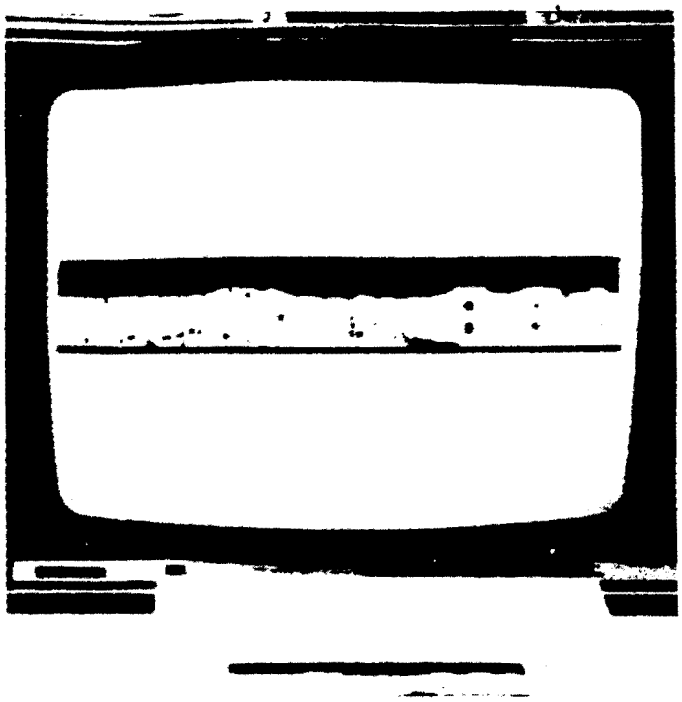

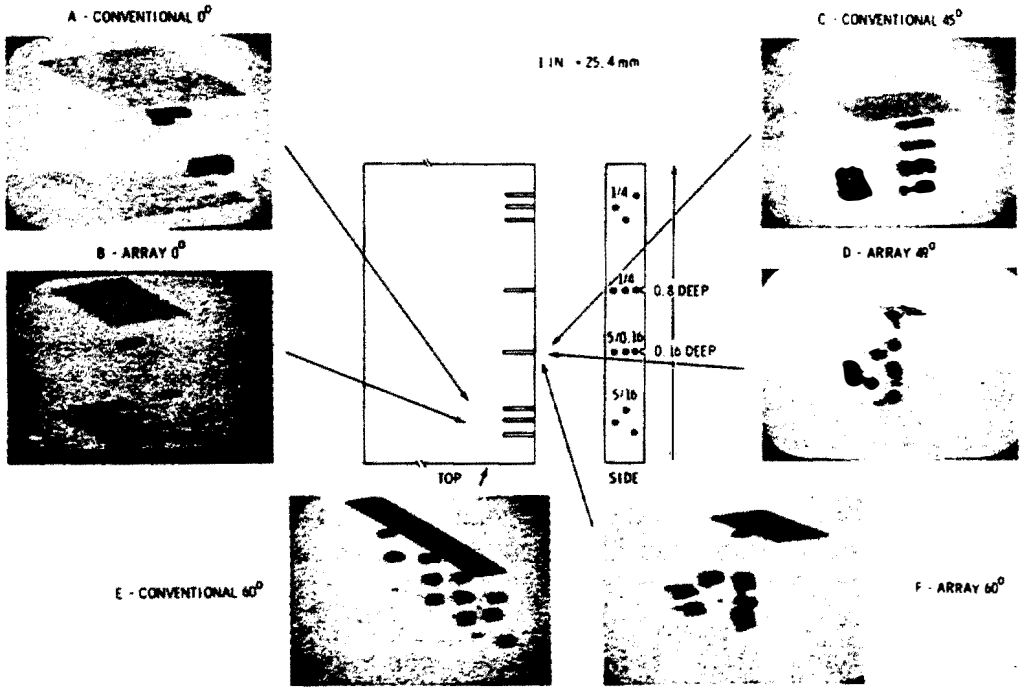

Figure 3.5.21 Isometric images of side-drilled holes taken with the Battelle imaging system. (After Becker et al. [37].)

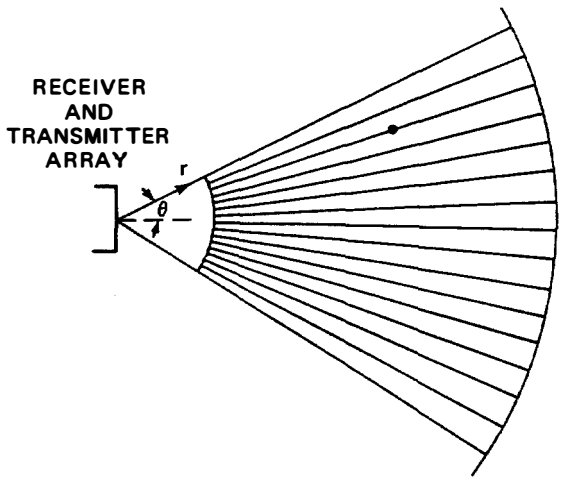

Figure 3.5.22 B-scan radial sector scan format. Scan lines are radial.

The design problem for a full-time-delay system is difficult because adequate delay lines must be provided for the receiver, with delays that can be varied with time to focus on the return echo signal for the transmitted pulse as it travels out from the array.

The simplest solution is to put a fixed-focus physical lens in front of the array to give optimum focusing at the center of the field. However, although a cylindrical lens can help focus a beam in the y direction, a lens to focus a long array in the x direction cannot be made easily.

An alternative technique is to excite four or more elements of the array from the transmitter, with suitable time delays, to provide an optimally focused beam at a fixed distance from the array. With a finite depth of focus, this is equivalent to using a focused transducer for the transmitter, which can be stepped along the array just as it is with the simpler system already described. At other ranges, the focusing will be worse than the optimum value. This stratagem is now employed in several commercial medical imaging systems to provide focusing in the x direction, in combination with a fixed cylindrical lens to provide better definition in the y direction.

In cardiac imaging systems, a dynamically focused receiver array is used with a radial sector scan format, with scans along radial lines extending from the center of the transducer array, as illustrated in Fig. 3.5.22. In this system, a parallel beam is transmitted at an angle θ to the axis by appropriately delaying the signals that excite the elements. The signals received on the elements are passed through delay lines so that the receiver is aimed in the θ direction. As the transmitted pulse travels out from the array, the focusing of the receiver must be changed. To do this, the original system, by Thurstone and Von Ramm [38], changed the delay time from each element to the detector by switching the taps on electromagnetic (EM) delay lines, with this switching controlled from a minicomputer. This system, which changes focusing as signals arrive from different depths, is known as a *dynamically focused system*.

The disadvantage of using lumped EM delay lines is that only a limited number can be used, and they tend to be bulky, which implies that the phase sampling of

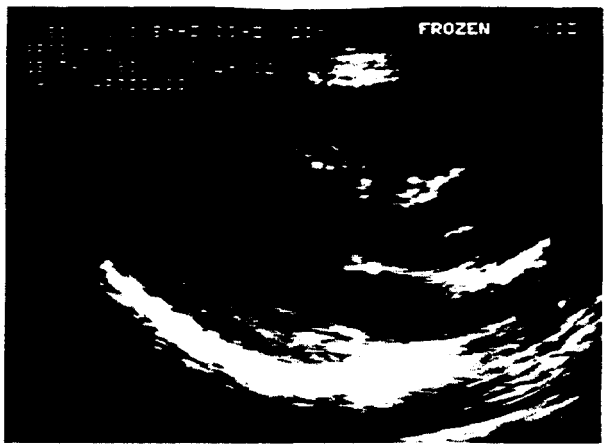

Figure 3.5.23 Image of the heart taken with a Hewlett-Packard radial sector scan real-time ultrasonic imaging device. (Courtesy of J. Larson.)

this system may be coarser than would be ideal. As shown in Sec. 3.5.3.B, this implies that the sidelobe level is higher than acceptable in a high-quality medical imaging system; often in such systems, it is desirable to have a sidelobe level no higher than 60 dB below the main lobe level.

Several stratagems have been adopted to circumvent these difficulties. One, for a relatively narrow aperture system, is to use lumped EM delay lines to provide the basic time-delay increments required for steering. Additional phase adjustments are made by mixing the received signals with phase references in a manner similar to that described in Sec. 3.5.3.B. An image of the heart taken at 3.5 MHz with a 64-element array, 1.5 cm wide, is shown in Fig. 3.5.23. This system has been adopted by Hewlett-Packard for cardiac imaging [39], where the access region to the heart is limited.

Another technique is to use CCD delay lines (see Sec. 4.3) to provide the necessary time delays; these are changed by varying the clock rates of the lines [40]. This approach has proven less simple than it appeared initially, basically because of interference from the clock signals.

Finally, there are several examples of such digital systems that provide the necessary delays. One approach is to use an analog-to-digital (A/D) converter to convert the received analog signal to, for example, an 8-bit digital signal, and then using variable digital delays. The digital signals from the different transducer elements are summed and then reconverted to analog signals with a D/A converter. In some cases, signal detection is carried out before A/D conversion, which makes it possible to design linear detectors that are almost perfect.

Another such system, which has been demonstrated with *synthetic aperture imaging* [28, 33, 41–45], is illustrated in Fig. 3.5.24. This system is based on the idea that the required information does not have to be gathered simultaneously. Since the processing operations required are all linear, we can obtain signals from individual elements at different times, store and delay them, and add them later, or put the delays in later, after storing them; it does not matter.

In one example of this system, a short pulse is emitted from a single transducer and enters the object of interest. Reflected echoes are received on the same transducer, then passed through an amplifier and an A/D converter into an 8 ×

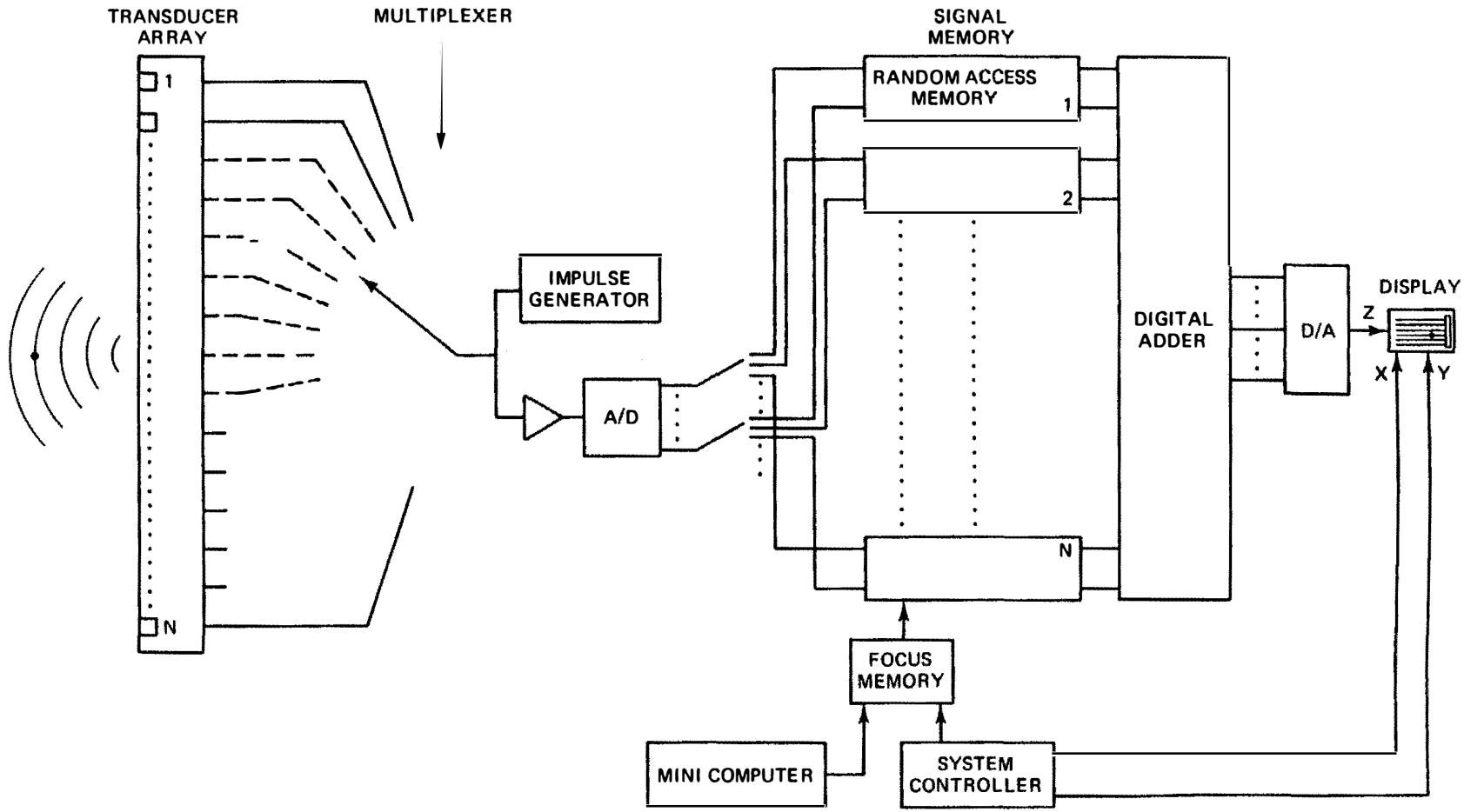

Figure 3.5.24 Schematic of a synthetic aperture digital imaging system. (After Corl et al. [41].)

1000-bit random-access memory (RAM). The process is then repeated for the next element in the array, and the signals from that element are stored in a separate RAM. Using a clock rate several times the signal frequency, several samples per RF cycle are obtained. Thus a relatively high frequency A/D converter must be used. Once the process is completed, information from the entire field of view is stored in the RAM memories and is available for reconstruction of an image. To image a particular point in the field, signals are taken from the appropriate points in the RAM, corresponding to the correct time delays. A basic system of this type was first demonstrated by Johnson et al. [42] at the Mayo Clinic, using a computer for storage and reconstruction of the image.

In the system designed by Corl et al. [41, 45], high-speed RAMs are employed with a separate RAM focus memory, to program the registers in the RAM from which the signals are read out. The digital signals are added in a digital adder, passed to a D/A converter, and then used to intensity modulate the signal on the screen of a cathode ray tube. By carrying out these processes in turn, any line in the image can be scanned in any direction to construct a complete raster image.

The same basic technique can be used to provide time delays in any focusing system. Signals can be emitted from all the elements of the transducer at once. As described above, separate A/D converters can be used on each element of the receiving transducer array, with the signals from all these elements processed simultaneously instead of separately, as in the synthetic aperture system. The advantage of simultaneous reception is that fast motion, like the flutter of a heart valve, can be reproduced in real time. Although a real-time synthetic aperture system takes only of the order of $\frac{1}{60}$ of a second to gather in one frame of information and another $\frac{1}{60}$ of a second to process it, the time delay from transducer to transducer in gathering information is of the order of 100 μs; this is obviously a disadvantage. Another difficulty with synthetic aperture imaging is the small size of an individual transmitting element and the wide area that must be insonified by this element. Consequently, the beam intensity at the object to be examined tends to be low, and hence the signal-to-noise ratio poorer, than with a more conventional time-delay system.

On the other hand, an important advantage of the synthetic aperture system is that it requires only a single front-end amplifier, regardless of the number of elements in the transducer array. This means that a great deal of effort can be put into the design of the front-end amplifier with little regard for its complexity, number of adjustments, expense, and so on, all of which are important considerations in a system where an amplifier is required for each element of the array. Furthermore, as the signal emitted from an array element must travel to a point in the field and back, its effective length of travel is double that of an equivalent receiver system, with a definition d_x, with the object illuminated by an unfocused transmitter. Thus the transverse definition in this system is $d_x/2$ and the sidelobe amplitude near the focal point varies as sinc $(2xD/\lambda z)$. On the other hand, as we have seen in Sec. 3.3, a system with a focused transmitter and receiver has a sinc^2 $(xD/\lambda z)$ response and hence a much lower sidelobe level, but not such good 3-dB definition, as the synthetic aperture system. In comparison to a system with an unfocused transmitter, such as the radial sector scan system described above, the

3-dB definition is better by a factor of 2, but the far-out sidelobes of the radial sector scan system are much weaker.

The range resolution is determined essentially by the pulse length (bandwidth), as it is with other imaging techniques. The system provides the same improvement in transverse resolution as a scanned holographic imaging system (see Sec. 3.5.6.D). But because time-delay rather than pulse-delay techniques are being used to reconstruct the image, excellent range resolution is also obtained.

B. TV Display

A major difficulty with real-time acoustic imaging systems is the format and nature of the display. The format of a radial sector scan, for instance, is quite different from that of a TV display, and the frame rates of each system may also be different. This problem is normally circumvented by using a digital scan converter, which can also provide additional sorts of image processing, such as averaging over several frames, contrast enhancement, artificial color displays, and quantitative measurements on the display. The synthetic aperture system, on the other hand, can use a rectilinear scan format like that of a TV image, which makes it possible, with the correct choice of clock rate, to display the image in real time on a TV screen. In all cases, it helps to use a magnetic deflection cathode ray tube of the type used in normal TV systems to obtain a good gray-scale display.

C. Sidelobes, Grating Lobes, and Sampling Lobes in Time-Delay Systems

We have already discussed how the use of short pulses can improve the range resolution of an acoustic imaging system. Using short pulses or tone bursts, instead of quasi-CW signals, also lowers the far-out sidelobe levels, and decreases the grating lobe and sampling lobe levels. We shall treat these effects here; most of the examples will refer to synthetic aperture imaging, since numerical calculations for this case are easily available to the author. However, the conclusions reached are pertinent to any kind of short-pulse focused imaging system.

We assume that the system is excited by a pulse of the form $f(t)\exp(j\omega t)$, where $\omega = 2\pi f_0$. The system is assumed to be focused on the point x_i, z_i. We shall consider both a synthetic aperture system in which the same transducer is used for transmission and reception, and a conventional pulsed system in which insonification of all points in the field is carried out by an unfocused beam and signals are received on separate transducers. The radial sector scan system is an example of the latter configuration. We will find it convenient, initially, to consider a continuous array system with points on the array located at x', 0. Later we consider a finite number of elements with the array elements located at the points x_n, 0, a distance l apart.

A time-delay focusing system focused on the point x_i, z_i introduces a time delay $T_0 - T_i$, where T_0 is a constant and

$$T_i = \frac{[z_i^2 + (x' - x_i)^2]^{1/2}}{V} \tag{3.5.87}$$

After suitable time delays have been introduced, the sum of the delayed signals returning to the transducers at x', 0 is of the form

$$h(t) = \int f\left(t - \frac{\gamma \Delta R}{V}\right) e^{j\omega(t - \gamma \Delta R/V)} w(x')\, dx' \tag{3.5.88}$$

where $\gamma = 1$ for a standard pulsed imaging system and $\gamma = 2$ for a synthetic aperture system, and where $w(x')\, dx'$ is the amplitude response of the transducer in the receive-only or in the transmit–receive mode in the region between x' and $x' + dx'$. The $1/R^{1/2}$ or $1/R$ amplitude variation has been included in the definition of $f(t)$, and we define ΔR by the relation

$$\Delta R = \sqrt{\qquad\qquad} \qquad \sqrt{z_i^2 + (x' - x_i)^2} \tag{3.5.89}$$

as the difference in range from x', 0 to x, z and x_i, z_i.

Range resolution. By making the paraxial approximation $(x' - x)^2 << z^2$, and taking $x_i = 0$, for simplicity we can write

$$\Delta R \approx \Delta z - \frac{x'\, \Delta x}{z_i} \tag{3.5.90}$$

where, in general, $\Delta z = z - z_i$ and $\Delta x = x - x_i$. It follows that the range resolution (i.e., the result with $\Delta x = 0$) is determined by the function $f(t - \gamma \Delta z/V)$ for all transducers. So the range resolution is determined by the pulse shape and length.

Transverse definition. On the other hand, the transverse definition of a line reflector and sidelobe levels at the focal plane ($\Delta z = 0$) are determined by the integral

$$h(t, \Delta x, z_i) = \int f\left(t + \frac{\gamma x'\, \Delta x}{z_i v} \qquad {}^{\gamma x' \Delta x / z_i V)} w(x')\, dx' \tag{3.5.91}$$

with, if $f(t)$ is a sufficiently long puls

$$d_x(3\ \mathrm{d} \qquad \frac{0.89 \lambda z_i}{\gamma D} \tag{3.5.92}$$

It is important to realize that the 3-dB width of the main lobe in a synthetic aperture imaging system ($\gamma = 2$) is half that of a conventional imaging system.

At $t = 0$, $\Delta x = 0$, and $\Delta z = 0$, the output is

$$h(0, 0, 0) = f(0) \int w(x')\, dx \tag{3.5.93}$$

So the magnitude of $h(0, 0, 0)$ is determined by the maximum amplitude of the pulse and the spatial integral of the transducer response.

Grating lobes. We shall take the signal $f(t)$ to have the form of a Gaussian pulse:†

$$f(t) = e^{-(t/T)^2} \tag{3.5.94}$$

We represent the weighting function of the array by its Fourier series,

$$w(x') = \Pi\left(\frac{x'}{D}\right) \sum A_p e^{-j2\pi p x'/l} \tag{3.5.95}$$

where $\Pi(x'/D) = 1$ when $|x'| \leq D/2$, $\Pi(x'/D) = 0$ when $|x'| > D/2$, and

$$A_p = -\int w(x') e^{j2p\pi x'/l}\, dx' \tag{3.5.96}$$

The pth grating lobe is associated with the pth harmonic of the aperture weighting. It follows from Eqs. (3.5.91) and (3.5.95) that if $f(t)$ is a very long pulse, the response is centered at the point

$$x_p = x_i + \frac{p\lambda z_i}{\gamma l} \tag{3.5.97}$$

By using the pth term of Eq. (3.5.95), $w_p(x') = A_p \exp(-j2p\pi x'/l)$, in Eq. (3.5.91), with $x_p = \Delta x$ ($x_i = 0$), we can determine the effect of the pulse envelope on the pth grating lobe amplitude, by writing

$$h_p(0, x_p, z_i) = A_p \int_{-D/2}^{D/2} f\left(\frac{px'}{f_0 l}\right) dx' \tag{3.5.98}$$

Therefore, when the duration of the pulse envelope is shorter than $D/\gamma f_0 l$ or $N/\gamma f_0$, corresponding to N RF cycles for conventional system ($\gamma = 1$), there will be a significant reduction in the grating lobe amplitude. In a system using Gaussian envelope pulses, the grating lobe will be diminished by the factor

$$\begin{aligned} h_p(0, x_p, z_i) &= \frac{A_p \int_{-D/2}^{D/2} e^{-(px'/f_0 Tl)^2} dx'}{A_0 \int_{-D/2}^{D/2} dx'} \\ &= \frac{A_p}{A_0} \frac{\sqrt{\pi}\, f_0 T}{|p|N} \operatorname{erf}\left(\frac{N}{|p| f_0 T}\right) \approx \frac{A_p}{A_0} \frac{\sqrt{\pi}\, f_0 T}{|p|N} \end{aligned} \tag{3.5.99}$$

where we have assumed in the last term that $pf_0T \ll N$, so that we can use the asymptotic approximation to the error function erf (x).

For a 32-element array of infinitesimally wide transducers ($A_0 = A_p$) trans-

†The shape of a Gaussian pulse can be specified in many different ways. For instance, with $f_0T = 1$, the 3-dB duration of the pulse is $1.2T$, or 1.2 RF cycles, and the 20-dB duration is $3T$, or 3 RF cycles. For the same pulse, the 3-dB bandwidth is 37% and the 20-dB bandwidth is 97%.

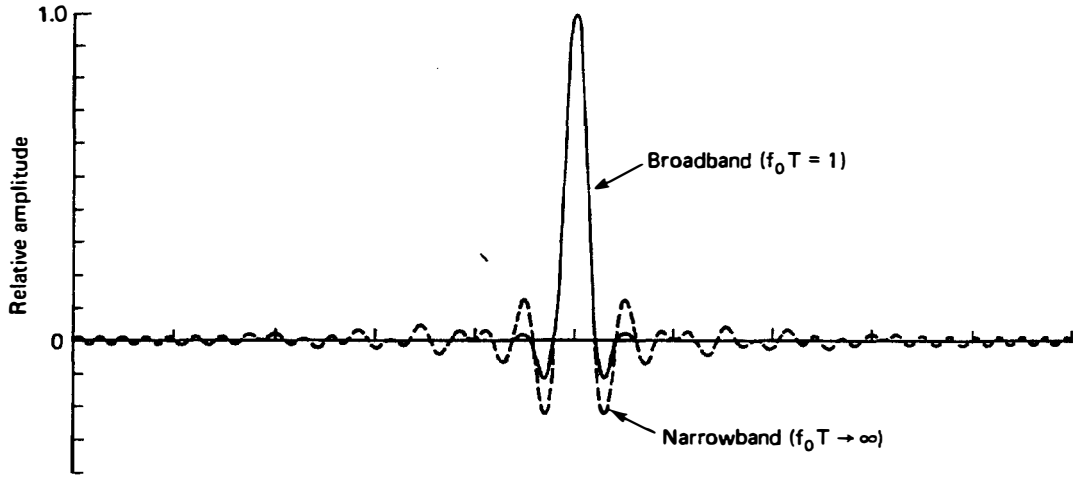

Figure 3.5.25 Comparison of narrowband (dashed line) and broadband (solid line) LSFs of continuous delay imaging system. The sidelobes of the broadband LSF diminish very quickly away from the main lobe. (From Peterson and Kino [33].)

mitting a broadband pulse with $f_0T = 1$, the grating lobe is reduced in amplitude by a factor of $0.06 = -25$ dB.

We conclude that for imaging systems using broadband pulses, the CW and broadband pulse LSFs resemble each other very closely near in to the main lobe. Features that are well removed from the main lobe (e.g., sidelobes and grating lobes) are "washed out," the effect being proportional to the distance from the main lobe.

To illustrate these effects, we first compare, in Fig. 3.5.25, numerical calculations for the LSFs of two imaging systems with continuous delays, one using narrowband CW imaging signals (dashed line) and the other using broadband ($f_0T = 1$) Gaussian-envelope pulses (solid line). Both have the same main lobe shape, but the sidelobes of the broadband LSF diminish very quickly away from the main lobe.

Broadband imaging systems have lower sidelobe levels, because the sidelobe patterns from different frequency components of the imaging signal shift with frequency, but the main lobe remains in the same location regardless of frequency. This means that the various frequency components add constructively at the main lobe but destructively elsewhere. Delay quantization sidelobes are reduced in a broadband system for exactly the same reason [33, 46].

In Fig. 3.5.26, we demonstrate this point by comparing the LSFs of two numerically calculated, synthetic aperture imaging systems, both of which suffer from delay quantization errors ($M = 4$). The narrowband CW LSF ($f_0T \rightarrow \infty$) is plotted with a dashed line and the broadband ($f_0T = 1$) LSF is plotted with a solid line. Again, the CW and broadband LSFs agree near the main lobe, but the sidelobes of the broadband LSF fall off more rapidly.

The analytical theory we have given here is a paraxial one, which we have evaluated only at the focal plane. More generally, suppose that the imaging system is focused on a point P distance R_n from a transducer at the point x_n, 0, as illustrated

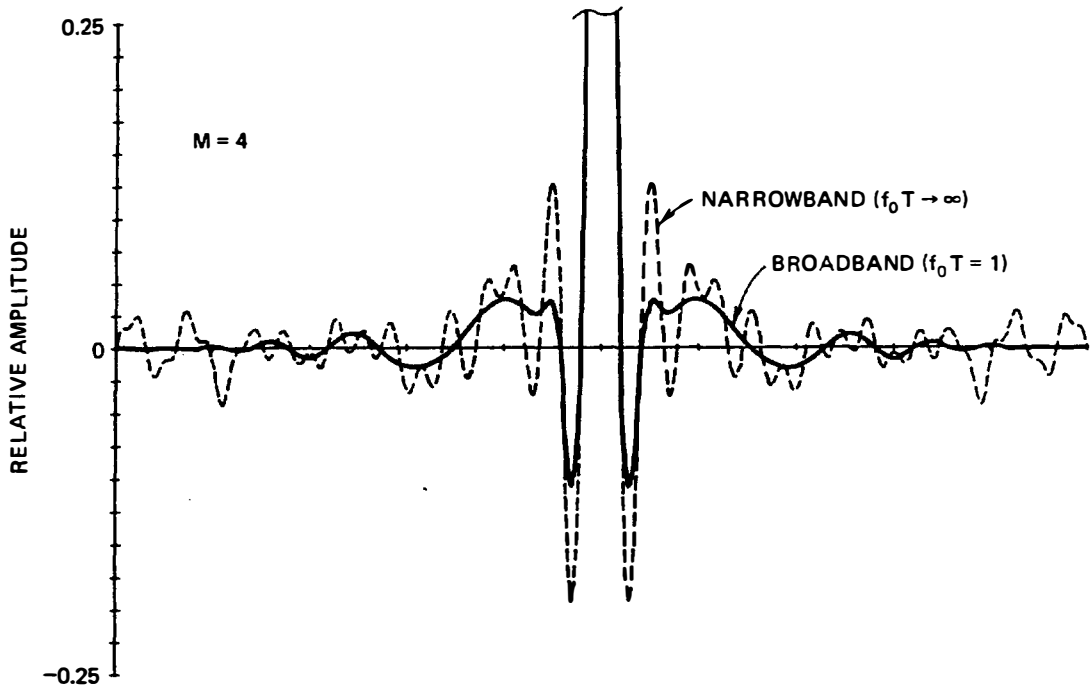

Figure 3.5.26 Comparison of narrowband (dashed line) and broadband (solid line) LSFs of quantized time-delay imaging system. (From Peterson and Kino [33].)

in Fig. 3.5.27. All signals received at the transducers from the point P suffer a total time delay T after processing. The signals from all the transducers are added so that the total amplitude is N times the amplitude of the signal arriving at one transducer. However, it is possible for a point Q, located anywhere on a circle of radius R_n and center x_n, 0, to produce a signal with the same delay time T. Hence sources located anywhere on circles of radius R_n, whose centers are at the transducer elements, can give rise to spurious out-of-focus signals or sidelobes. In

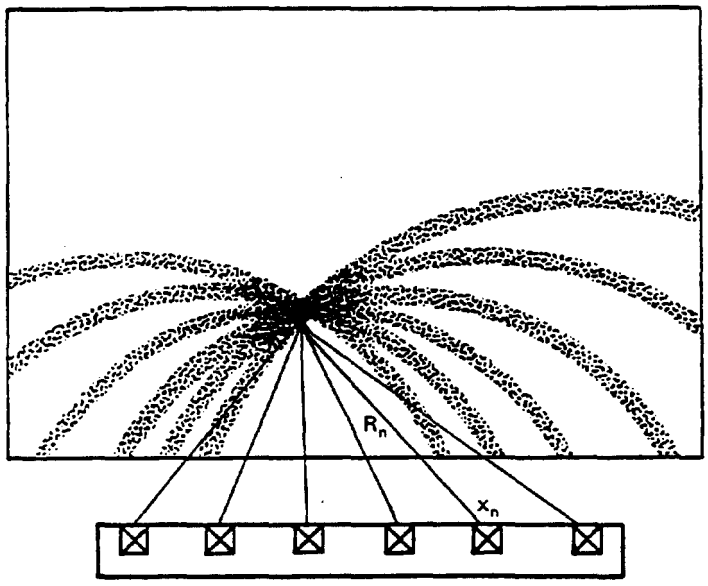

Figure 3.5.27 Causes of near-in and far-out sidelobes.

practice, the pulse length is finite, so that the circles have a finite thickness. Near the main lobe, these "thick" circles overlap and there are phase additions and subtractions, yielding the typical $(\sin x)/x$ response. Farther out from the main lobe, the circles only partially overlap or do not overlap at all. Thus the sidelobe response tends to be washed out, until far out there are only isolated responses along the individual circles, whose amplitudes are reduced by $1/N$ from that of a beam focused on the same point.

D. Examples of Synthetic Aperture Imaging

We now consider some examples of synthetic aperture imaging. These will illustrate some of the theoretical results we have already obtained in Sec. 3.5.5.C, and also demonstrate how synthetic aperture imaging can be applied to NDT. We will draw our examples from work carried out in the author's own laboratory, where the concentration has been mainly on real-time imaging systems. The reader is also referred to work in other laboratories, where computer processing of synthetic aperture imaging has been used to make two- and three-dimensional images of internal features of large structures [43, 44]. In such cases, it is, in principle, possible to work with structures that are not flat, using the signals reflected from the surface as a time reference for the reconstruction process. This procedure makes it possible to correct for the shape of arbitrary structures. In practice, only relatively simple, large radius surfaces have been dealt with, so far, in this manner.

We first illustrate the results for an imaging system with a 32-element array, 1.6 cm long, with transducer element spacing of 0.5 mm, operating at a frequency of 3.5 MHz in water [45]. The acoustic wavelength was 0.42 mm, so we might have expected to see some grating lobes at an angle of the order of 30° to the normal of the array. In this case, however, the array response fell off fairly rapidly in this angular range; thus, due to this effect and because short pulses were used, the grating lobes did not show up very strongly. An image of three wires in front of a metal plate is shown in Fig. 3.5.28. The image in Fig. 3.5.28(a) was taken with an 8-element system that was 1.6 cm long. A similar image, taken with a 32-element system, is shown in Fig. 3.5.28(c). The incoherent sidelobes of the wires and the plate can easily be seen in the 8-element array image, while in the 32-element array image, they are less apparent. Mirror images of the wires in the plate can also be observed. Two additional images using nonlinear processing for the 8- and 32-element systems are shown in Fig. 3.5.28(b) and (d), respectively. Here the image quality was improved by nonlinear processing. But such techniques can often produce artifacts and false images due to the nonlinear interactions; thus their improvement in image quality is not consistent.

Imaging modes. Imaging systems of this type can be used for observing surface and internal features in a solid by either employing an array in water, with water between the array and the solid, or placing the array in direct contact with the solid. In the first case, aberrations occur in the image because angles of the rays entering the solid from water are changed in accordance with Snell's law. Thus we must take account of changes in time delay and phase in the synthetic

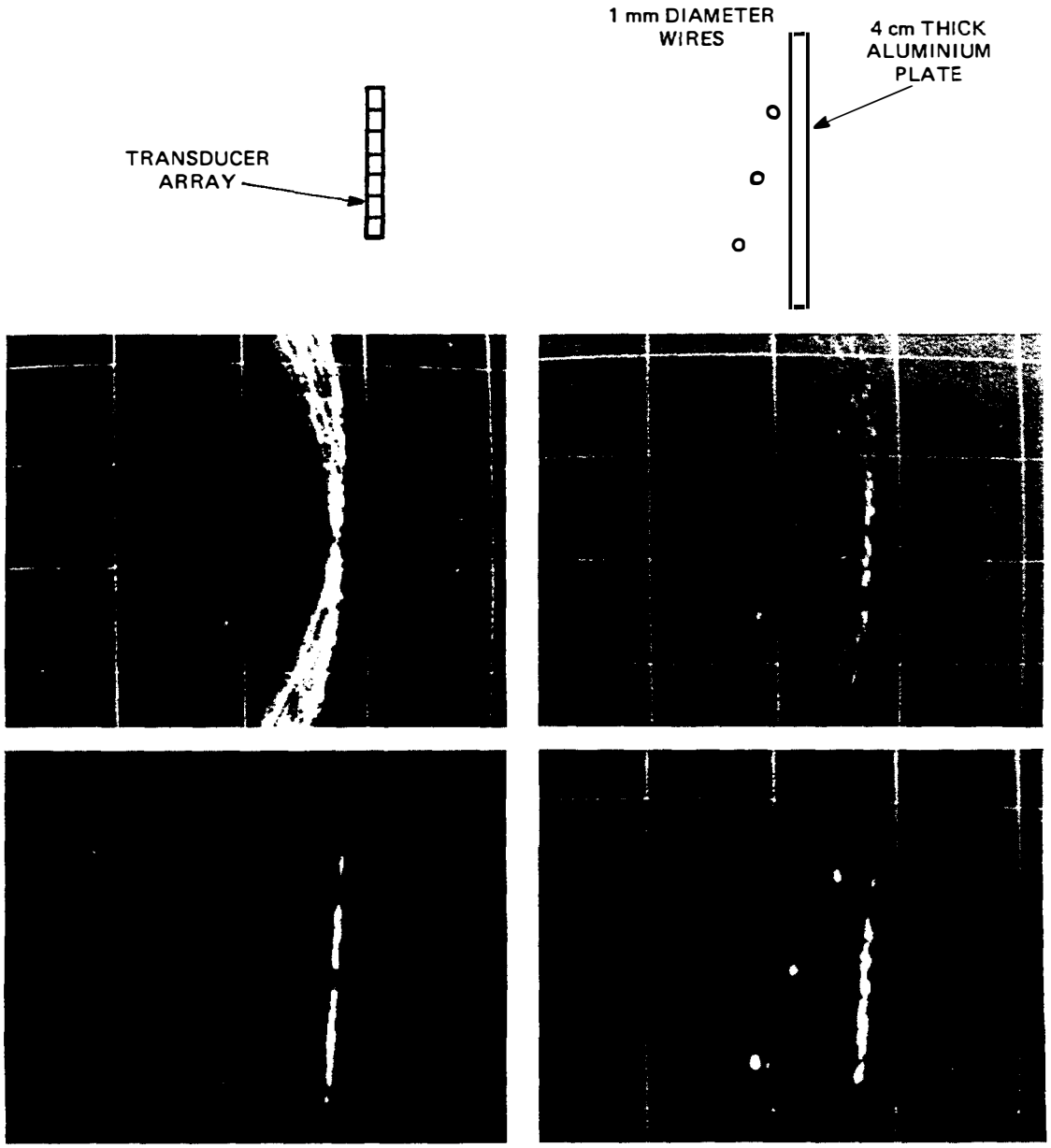

Figure 3.5.28 Schematic and computer-processed images for test targets in water tank with superimposed 1-cm reference grid. Upper photographs show images on left without and right with input gain compression for the 8-channel synthetic focus system. Lower photographs show similar images with 32 active channels. (After Corl and Kino [45].)

aperture reconstruction program and make different corrections every time the array is moved. Therefore, if it is possible, it is far easier to use a contacting array system. If the system is operating in real time (30 frames/s), the array and its contact to the surface can be conveniently adjusted while observing the image; this makes it possible to adjust for the best contact and spot artifacts that may occur in the image.

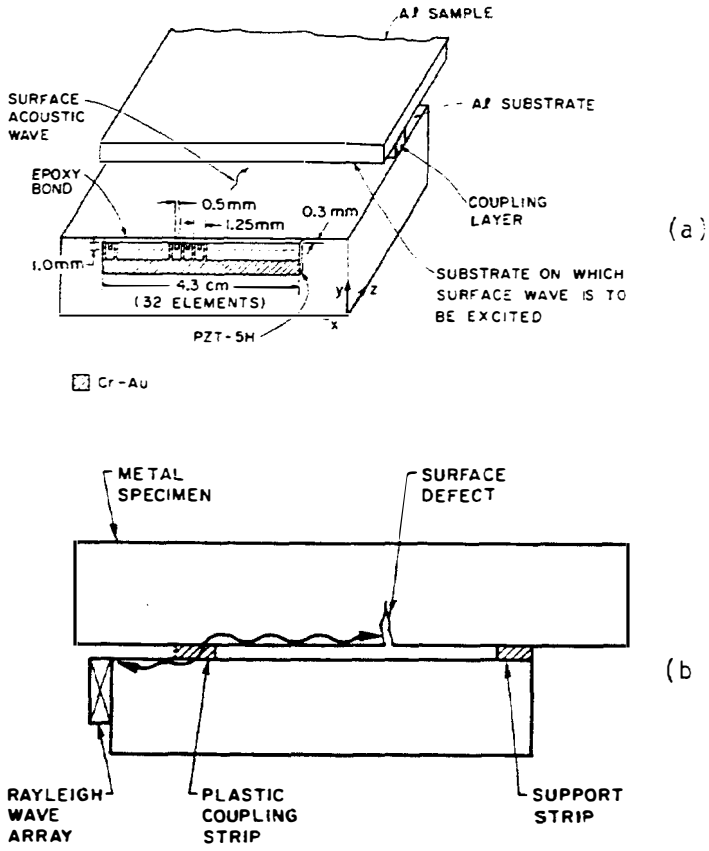

Figure 3.5.29 Edge-bonded transducer (EBT) surface wave array: (a) schematic of array construction; (b) diagram of a sample in contact with the array. (After Tuan et al. [47].)

Surface acoustic wave imaging. As our first example of a contacting array, we consider the Rayleigh wave array using an edge-bonded transducer, illustrated in Fig. 3.5.29. This transducer, which is approximately one wavelength deep, excites surface waves on a substrate of the same material as that being examined. Each element is a point source of surface acoustic waves, which are transferred from the array substrate to the specimens through a plastic strip approximately 10λ long (Sec. 2.5.3). The coupling process is relatively efficient, with a one-way loss of only -2 dB, and introduces no aberrations because the array substrate and specimen are made of the same material and thus have equal surface wave velocities.

Images of an 11-mm spark-machined (EDM) slot taken with this array are shown in Fig. 3.5.30. When the crack is rotated with respect to the array, the image changes. When the crack is parallel to the array, it behaves like a good specular reflector and signals transmitted to the crack are received on the same element of the array. Consequently, the expected bright line image of the crack is obtained. When the crack is rotated through a sufficiently large angle, however, specularly reflected rays are not returned within the array aperture.

Another example utilizes a shear wave array, as illustrated in Fig. 3.5.31, that is constructed on a metal buffer rod, again of the same material as the sample being examined. By using an incident wave at an angle of 45° to the normal, energy is easily transferred between the two substrates by the normal component

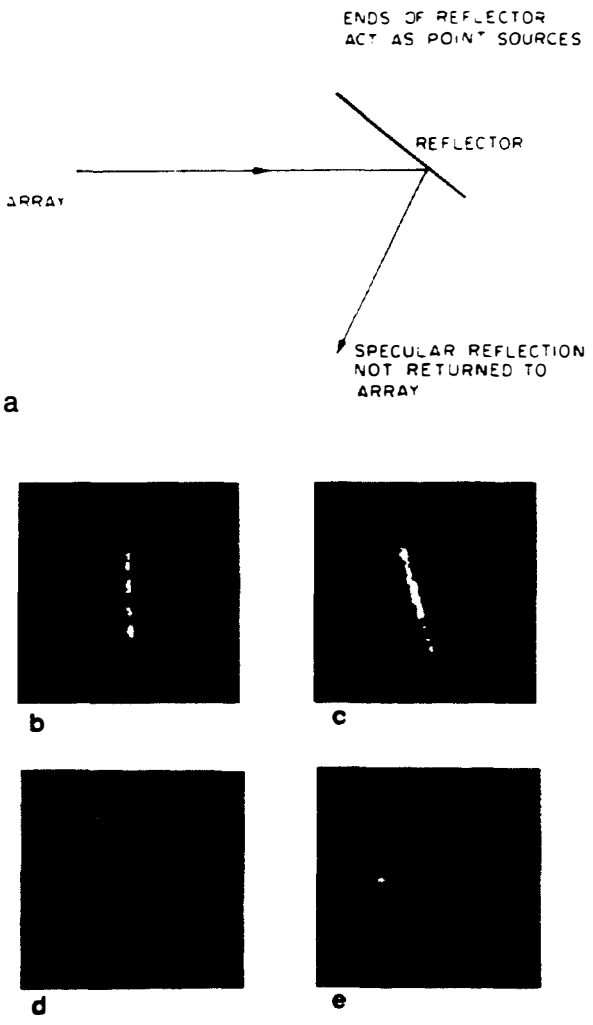

Figure 3.5.30 (a) When imaging specular reflectors at a large angle of incidence, only the two ends are seen. Images of an 11-mm EDM slot at: (b) 0° between normal to reflector and normal ray to array; (c) 15° between normal to reflector and normal ray to array; (d) 45° between normal to reflector and normal ray to array; (e) 90° between normal to reflector and normal ray to array. (After Kino et al. [49].)

of particle velocity at the surface [48, 49]. Typically, a thin layer of grease, whose thickness is kept constant by two Mylar pads, one at each end of the array, is used to keep a uniform contact. With arrays of this kind, contacting is extremely easy and images with a high degree of repeatability can be obtained without effort; good repeatability is most important in a practical system.

A shear wave image of a fatigue crack, approximately 4 mm deep and 10 mm long, obtained with this array is shown in Fig. 3.5.32(d), and compared to a similar image of the same crack taken with a surface wave array on the top surface [part (b)], and with an optical picture of the crack [part (a)]. In both acoustic images, the crack is seen with good resolution; in the shear wave image, a jog in the crack is clearly resolved. Two additional images of this crack are shown, one with a contacting longitudinal wave array [part (c)] and another in a pitch/catch mode [part (e)]. In the pitch/catch mode, the crack was insonified with longitudinal waves from a transducer on the back of the sample, and the image formed with energy scattered by the crack into other modes. The return signals were collected with a Rayleigh wave array.

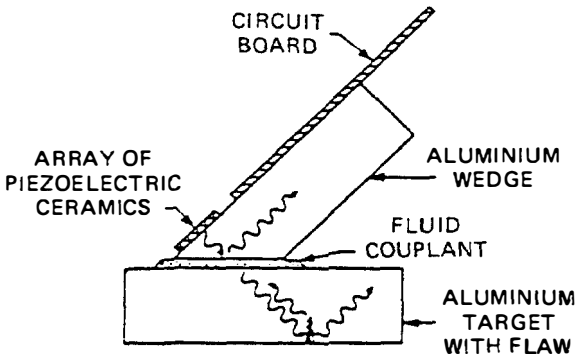

Figure 3.5.31 Shear wave array in contact with an aluminum block. (After Kino et al. [49].)

Figure 3.5.33 illustrates the pitch/catch mode in more detail. The results shown here provide multiple images of a crack corresponding to conversion of the incident longitudinal wave to other modes. The different time delays observed are related to: (1) conversion to a shear wave at the tip of the crack; (2) conversion to a Rayleigh wave at its tip; and (3) conversion to a Rayleigh wave at its root. This technique makes it possible to measure the crack depth accurately.

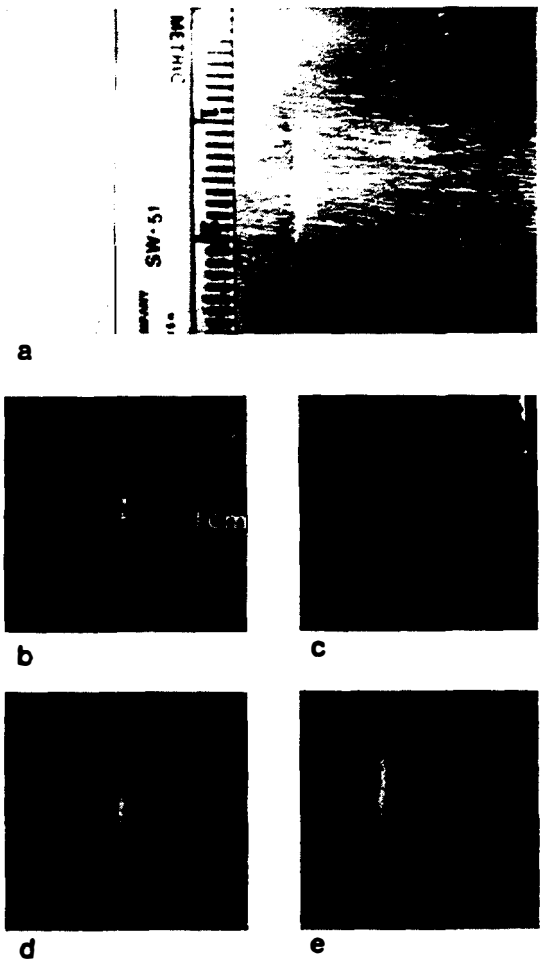

Figure 3.5.32 Imaging a crack with four different wave modes: (a) 10-mm fatigue crack showing the prominent jog about 3 mm from the bottom tip; (b) surface wave image of fatigue crack; (c) longitudinal wave image; (d) shear wave image; (e) Pitch/catch image of waves scattered from an incoming longitudinal wave. (After Kino et al. [49].)

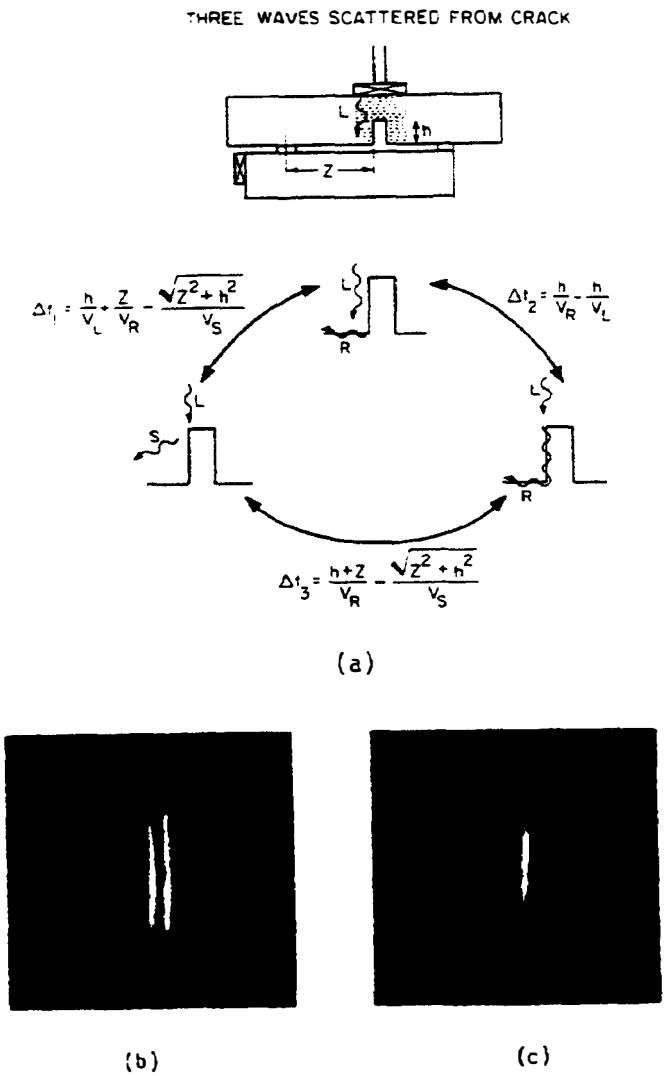

Figure 3.5.33 Pitch/catch imaging: (a) transmitter–receiver geometry and diagram of the three waves scattered from the crack; (b) pitch/catch image of a long 7-mm-deep slot; (c) pitch/catch image of the 10-mm-long fatigue crack. (After Kino et al. [49].)

E. Tomographic Imaging Systems

Synthetic aperture imaging is closely related to tomographic imaging, a type of imaging modality that has become very important since the development of the x-ray *computerized axial tomography scanner* (CAT scanner) [50, 51]. This system is based on the old idea of motion tomography, illustrated in Fig. 3.5.34, in which a film is moved in synchronism with an x-ray source, but in the opposite direction, so that one plane of the object remains in focus while all others are blurred. Since there is no phase information in this image, it can be shown that the PSF of a point in the image plane varies as $1/r$, where r is the distance from the point.

The CAT scanner uses a more complicated scan to construct an image of all points in a thin slice. In one version, illustrated in Fig. 3.5.35, an x-ray source is moved to N points, perhaps 32 along a row, and the collimated x-ray beams emitted are detected at points opposite the source positions. The whole assembly is then

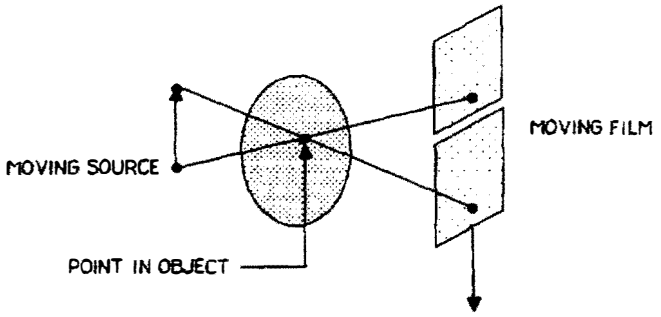

Figure 3.5.34 Motion tomography.

rotated by an angle $\Delta\theta$, perhaps 1°, and this process repeated until the full 360° is covered. Then, by suitable processing, excellent images can be obtained.

Similar techniques have been investigated for acoustic imaging. Either changes in amplitude, associated with the attenuation of the medium, or changes in phase, associated with changes in the refractive index of the medium, are measured. In some respects, acoustic tomography is more complicated than x-ray tomography because, due to diffraction, the beam cannot remain well collimated, and the perturbations in refractive index or attenuation may be so large that a ray path will not be the same as in a uniform medium. Consequently, progress in this field has been slow.

The technique can also be used for reflection-mode, rather than transmission-mode, imaging. For instance, a synthetic aperture quasi-CW system, using a short tone burst, can be constructed as a circular array enclosing the object; each array element is used in turn as a transmitter and receiver before passing on to the next element. It can be shown that the PSF of such a system, anywhere inside the array, with infinitesimally spaced array elements, is $J_0(2kr)$ where $J_0(x)$ is a zeroth order Bessel function of the first kind [52]. A similar analysis can be made for a transmission system in which an element at an angular position θ transmits to a receiver at a position $\pi + \theta$, with θ changed by $\Delta\theta$ until the full 360° circle is completed. Using processing similar to that employed for a synthetic aperture reflection mode system yields an LSF of the form $J_0(kr)$. Such a system can be employed to produce images of small perturbations in refractive index or attenuation. The theoretical definition is excellent because phase information with a full 360° scan is used.

The equivalent x-ray tomographic system uses only intensity information, as if the width of the beam had the form of a Dirac δ function, while in the acoustic

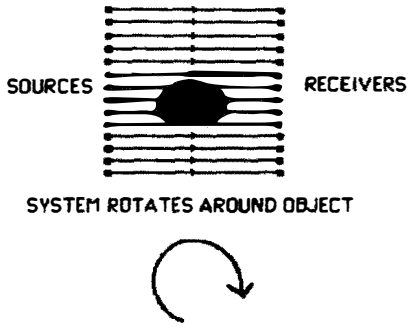

Figure 3.5.35 CAT scan tomographic imaging system.

system, there is phase variation across and along the beam due to the use of short tone bursts. The x-ray tomographic system introduces the phase variation in the computer, rather than in the transmitter, after the signal has been received. The processes are equivalent in a linear system. In a tomographic system, the transmitter is located at one point with the receivers located, ideally, at points around a 180° arc; the system is then rotated until the full 360° circle has been completed. Processing is carried out by convolving the outputs from receiving transducers at different angular coordinates, with a function like a sinc function in angular coordinates. This synthesizes the effect of a spatial phase variation; and also provides more information if a limited number of points are used: if there are N transmitters and M receivers, there will be MN pieces of information available and MN resolvable spots in the image.

A simple N-element synthetic aperture system will tend to have a far-out sidelobe amplitude of the order of $1/N$ below that of the main lobe, while the tomographic system will have much reduced levels of interference from artifacts. Thus the simple synthetic aperture system is not good enough for imaging a continuous medium where there are many equivalent sources present, and the more sophisticated algorithms developed for tomography are required. The reader is referred to the literature on CAT scanners and acoustic tomography for more information [51].

3.5.6 Acoustic Holography

A. Introduction

It was first shown by Gabor that it is possible to construct a system that can form an image without using lenses [53]. His immediate purpose was to eliminate aberrations in electron optical systems, but this basic idea has since been generalized to record and display three-dimensional optical images, and to display acoustical images in visual form. As used in acoustics, the method and its variations are suitable not only for image display, but also for such applications as measuring vibration amplitudes in crystal resonators and aircraft wings. Some closely related alternative techniques are the Schlieren optical system (see Secs. 4.9.4 and 4.9.5) and Bragg scattering of light by acoustic waves. These are suitable for measuring the amplitude distribution over the cross section of an acoustic beam; as a by-product, the latter technique is also important for electronically deflecting and modulating a laser beam.

To understand the basic features of holography, we first discuss the formation of an optical hologram on a photographic film and how images are reconstructed from it. We then discuss general holographic techniques, in particular, the reconstruction of images using waves of a different wavelength from those used to illuminate the original object, and how these techniques are employed in acoustic applications.

We now consider the technique for lensless imaging. A signal arriving from a point x_O, y_O, z_O on an object at the point x, y, 0 on the plane $z = 0$ has a phase variation $\phi_O(x,y) = -k\sqrt{(x - x_O)^2 + (y - y_O)^2 + z_O^2}$. When a lens is employed

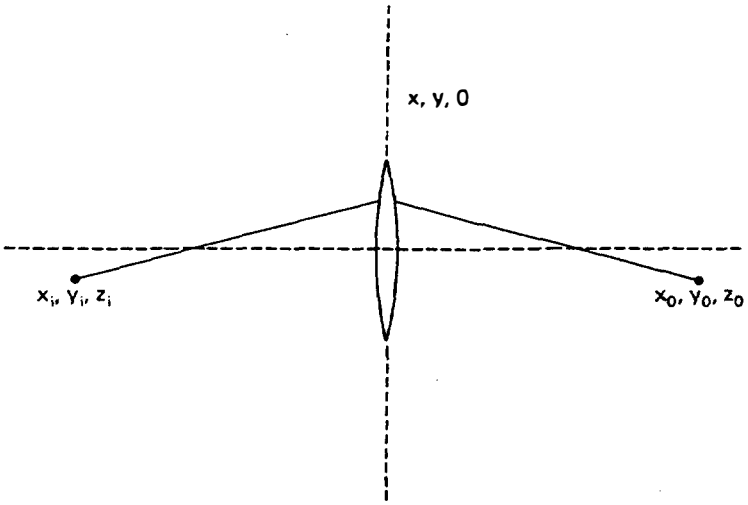

Figure 3.5.36 Imaging with a lens.

to reconstruct the image of this point x_O, y_O, z_O, as shown in Fig. 3.5.36; the lens changes the path lengths of the rays passing through it, and hence their phases, to produce an image at the point x_i, y_i, z_i. Thus the lens introduces a phase change $\Delta\phi$, where

$$\Delta\phi = k[\sqrt{(x - x_O)^2 + (y - y_O)^2 + z_O^2} + \sqrt{(x - x_i)^2 + (y - y_i)^2 + z_i^2} \qquad (3.5.100)$$

The phase change from a point x, y, 0 on a thin lens to the image point x_i, y_i, z_i is $\phi_i = -k\sqrt{(x - x_i)^2 + (y - y_i)^2 + z_i}$. Therefore, the phase of the rays at the image point x_i, y_i, z_i is $\phi_i + \phi_O + \Delta\phi$ and is independent of x and y.

Holography was originally developed as a technique that uses a laser beam for the phase reference and reconstruction needed to form an image. It can be employed for lensless imaging of light or acoustic waves. With light, the phase information is recorded on film in the form of a "hologram" and the necessary reconstruction or imaging is carried out by passing a second light beam through the film. With acoustic waves, the acoustic beam is scattered from the object and a reference acoustic beam ripples the surface of water or of a solid; the image is then reconstructed with a light beam, which introduces the necessary phase change, incident on this surface. In another method, an acoustic transducer is mechanically scanned over the plane $z = 0$ and used to modulate a light source, from which is recorded, on film, an optical hologram. This hologram is reconstructed by the normal optical techniques. A third technique is to synthesize the necessary phase changes in a computer and then reconstruct the image.

The holographic reconstruction of images yields a definition determined by the aperture of the original receiving system. This definition will be entirely equivalent to that obtained by a physical or electronic lens of the same aperture, for the holographic method is essentially an alternative technique for constructing the matched spatial filter described in Sec. 3.5.2.

The use of the direct optical reconstruction technique in acoustic holography has an advantage over electronically scanned systems or computer reconstruction

in that it provides rapid parallel processing and a detector that is essentially continuous. Thus grating lobes do not occur. On the other hand, such systems, which record the hologram on photographic film, are slow in operation because of the time required to develop the film. They also require a laser optical system, which needs a large, stable, mechanical table as a platform on which to reconstruct the optical image. Some types of acoustic holography systems use the ripple of a water surface due to an acoustic wave to reflect a laser beam. Such systems need a high-power argon laser for reconstruction; in addition, they are not very sensitive and are mechanically quite restricted, because the water surface must be kept level. Thus they are unsuitable for medical imaging and have been employed only in NDT testing applications.

As we have already discussed, some of these difficulties can be eliminated by using computer rather than optical reconstruction techniques. Either a movable acoustic transducer, or the deflection of an optical beam reflected from the rippling surface of a solid, is used to detect the acoustic beam. If the number of detection points is limited, however, the problem of grating lobes may then reoccur.

Acoustic holography excited a great deal of interest when it was first introduced, and topical research conferences were devoted to the subject for several years. However, it is now rarely used because in addition to the unwieldy optics required, it employs a phase compensation process to reconstruct the image. This means only a very narrow band of frequencies can be used for insonification (illumination) of the object and, as a result, the problems of speckle and interference fringes that occur with coherent light illumination still occur in holography. Furthermore, using a narrowband signal means that short pulses cannot be used for insonification. Thus the range definition of the system will be the same as the depth of focus of the equivalent lens with the same aperture, and only very poor images of partially transparent acoustic objects, such as inclusions of one solid in another, or of small objects near large reflectors, can be obtained.

With these limitations in mind, it is of interest to study holography as a useful technique for reflection and transmission imaging of isolated flaws, and for its other applications to the measurement of vibrating structures.

B. Holographic Reconstruction with Spherical Reference Waves

We first consider the basic technique for recording an optical or acoustic hologram on film. In principle, the technique requires recording both amplitude and phase information. We shall illustrate some of the basic ideas here by considering optical holography.

A plane wave is incident on a film with an amplitude variation $A \exp(j\omega t)$ along the film surface. The film records only the intensity $I(x)$, where

$$I(x) = AA^* \tag{3.5.101}$$

Thus all phase information is lost.

We consider, initially, the configuration for making a Leith–Upatnieks hologram using a plane wave source and reference [54, 55]. Two plane waves of frequency ω are incident on the film, as illustrated in Fig. 3.5.37. The first one

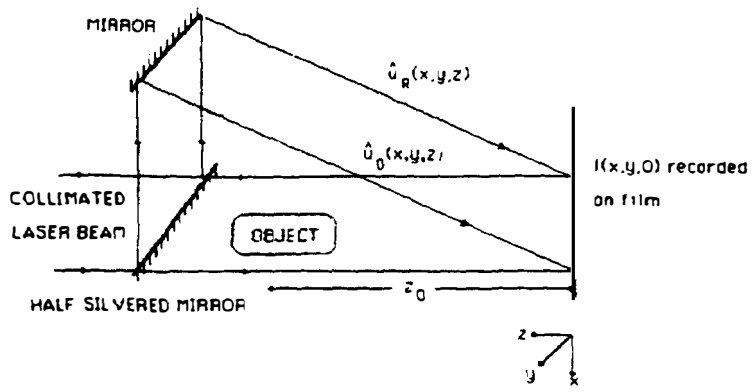

Figure 3.5.37 Recording of a Leith–Upatnieks hologram with a plane wave reference and source.

has the form

$$\hat{u}_O(x, y, 0) = u_O(x, y)e^{j\omega t}e^{-j\phi(x,y)} \tag{3.5.102}$$

The second is a reference plane wave of the same frequency and has fields of the form

$$\hat{u}_R(x, y, 0) = u_R(x, y)e^{j\omega t}e^{-j(k_x x + k_y y)} \tag{3.5.103}$$

along the photographic film.

The intensity of the illumination on the film is therefore

$$I(x, y) = [\hat{u}_O\hat{u}_R^* + \hat{u}_R\hat{u}_O^* + \hat{u}_O\hat{u}_O^* + \hat{u}_R\hat{u}_R^*] \tag{3.5.104}$$

or

$$I(x, y) = 2u_O u_R \cos[k_x x + k_y y - \phi(x, y)] + (u_O u_O^* + u_R u_R^*) \tag{3.5.105}$$

The first term in Eq. (3.5.105) can be written in the form

$$i_{RO}(x, y) = u_O u_R\{e^{j(k_x x + k_y y - \phi(x,y))} + e^{-j[k_x x + k_y y - \phi(x,y)]}\} \tag{3.5.106}$$

We see from Eq. (3.5.105) that the use of a reference wave yields two terms in the intensity variation that retain both the phase and amplitude information in the wave $u_O(x, y)$. This recording of $I(x, y)$ made on the photographic film with plane waves is the Leith–Upatnieks hologram [54, 55]. Note that additional information associated with the incident waves (the $u_O u_O^*$ and $u_R u_R^*$ terms) is also recorded on the film. We shall find it convenient to ignore these terms, as well as one of the exponential terms in Eq. (3.5.106), in our initial treatment of holography. In practice, the terms $(u_O u_O^* + u_R u_R^*)$ can give rise to glare (i.e., a background light corresponding to the sum of the incident wave intensities), and one of the unwanted exponential terms gives rise to an unfocused virtual image in the reconstructed image. These terms can be eliminated by various stratagems, which we discuss later.

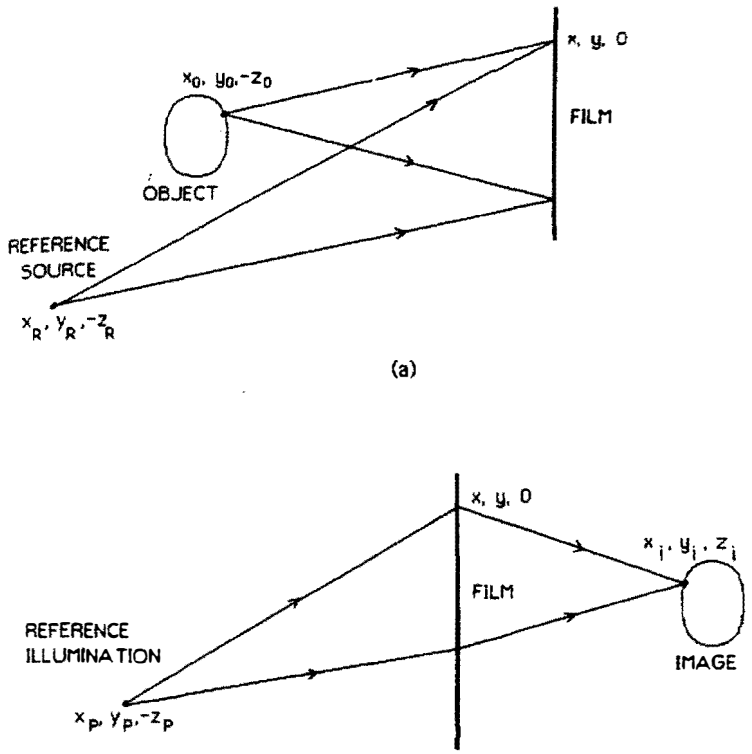

Figure 3.5.38 Spherical reference wave: (a) object and reference source; (b) reconstruction system.

Spherical wave sources. Before we discuss how this hologram is reconstructed, let us consider the more general case, where a spherical reference wave (a point source) is used to illuminate the film originally, and another spherical reference wave of different wavelength is used to form the holographic image.

We illuminate the film with a reference signal from a point source at x_R, y_R, $-z_R$, as shown in Fig. 3.5.38(a). A point on the object illuminated from the same coherent light source is taken to be at x_O, y_O, $-z_O$, and the wavelength to be $\lambda_R = 2\pi/k_R$. We use the paraxial approximation, so that the distances from x_O, y_O, $-z_O$ and x_R, y_R, $-z_R$ to a point x, y, 0 on the film are, respectively.

$$R_O = \sqrt{(x - x_O)^2 + (y - y_O)^2 + z_O^2}$$

$$\approx z_O + \frac{(x - x_O)^2 + (y - y_O)^2}{2z_O} \qquad (3.5.107)$$

and

$$R_R = \sqrt{(x - x_R)^2 + (y - y_R)^2 + z_R^2}$$

$$\approx z_R + \frac{(x - x_R)^2 + (y - y_R)^2}{2z_R} \qquad (3.5.108)$$

It is convenient to write

$$\begin{aligned} \mathbf{r} &= \mathbf{a}_x x + \mathbf{a}_y y \\ \mathbf{r}_O &= \mathbf{a}_x x_O + \mathbf{a}_y y_O \\ \mathbf{r}_R &= \mathbf{a}_x x_R + \mathbf{a}_y y_R \end{aligned} \tag{3.5.109}$$

where $\mathbf{a}_x$ and $\mathbf{a}_y$ are unit vectors in the x and y directions, respectively. Equations (3.5.107) and (3.5.108) can then be written in the simple form

$$R_O = z_O + \frac{(\mathbf{r} - \mathbf{r}_O)^2}{2z_O} \tag{3.5.110}$$

$$R_R = z_R + \frac{(\mathbf{r} - \mathbf{r}_R)^2}{2z_O} \tag{3.5.111}$$

respectively. It follows, from an analysis similar to that used to derive Eqs. (3.5.105) and (3.5.106), that the intensity of the light on the film contains a product term of the form

$$I_{RO} = A \cos k_R \left[\frac{(\mathbf{r} - \mathbf{r}_O)^2}{2z_O} - \frac{(\mathbf{r} - \mathbf{r}_R)^2}{2z_R} + z_O - z_R \right] \tag{3.5.112}$$

where A is a constant.

Reconstruction of the image. Suppose that we now illuminate the exposed film with a wave of wavelength $\lambda_p = 2\pi/k_p$, which is emitted from a point source at x_p, y_p, $-z_p$. This will give rise to a wave with a complex amplitude

$$A_i(x, y) = e^{-jk_p[z_p + (\mathbf{r}_p - \mathbf{r})^2/2z_p]} \tag{3.5.113}$$

along the film surface. This situation is shown in Fig. 3.5.38(b).

When this wave passes through the developed film, which has a density variation proportional to the intensity variation given in Eq. (3.5.112), the amplitude variation of the light beam leaving the film is proportional to $A_i(x, y)I_{RO}$. So we can write that the amplitude of the wave passing through the film is of the form

$$F(x, y) = K \cos k_R \left[\frac{(\mathbf{r} - \mathbf{r}_O)^2}{2z_O} - \frac{(r - r_R)^2}{2z_R} + z_O - z_R \right] e^{-jk_p[z_p + (\mathbf{r}_p - \mathbf{r})^2/2z_p]} \tag{3.5.114}$$

where K is a constant. The phase delay from a point x, y, 0 on the film to a point x'_O, y'_O, z'_O ($\mathbf{r}'_O$, z'_O) is

$$\phi(x'_O, y'_O, z'_O) - \phi(x, y, 0) = k_p \left[z'_O + \frac{(\mathbf{r}'_O - \mathbf{r})^2}{2z'_O} \right] \tag{3.5.115}$$

We now split the cosine term in Eq. (3.5.114) into two exponential components with phases $\pm\phi(x, y, 0)$. It follows that the phase of each signal component

reaching the point x'_O, y'_O, z'_O is $\phi'(x'_O, y'_O, z'_O)$, where

$$\phi(x'_O, y'_O, z'_O) = \phi_O \mp k_R\left[\frac{(\mathbf{r} - \mathbf{r}_O)^2}{2z_O} - \frac{(\mathbf{r} - \mathbf{r}_R)^2}{2z_R}\right] - k_p\left[\frac{(\mathbf{r}_p - \mathbf{r})^2}{2z_p} + \frac{(\mathbf{r}'_O - \mathbf{r})^2}{2z'_O}\right] \tag{3.5.116}$$

where $\phi_0 = \mp k_R(z_O - z_R) - k_p(z_p + z'_O)$ and is independent of $\mathbf{r}$, $\mathbf{r}_O$, $\mathbf{r}_p$ and $\mathbf{r}'_O$. Thus ϕ_O is a constant.

The r^2 terms in the phase cancel out at a plane $z'_O = z_i$, satisfying the relation

$$\pm k_R\left(\frac{1}{z_O} - \frac{1}{z_R}\right) - k_p\left(\frac{1}{z_p} + \frac{1}{z_i}\right) = 0 \tag{3.5.117}$$

It follows that the image lies at the point z_i, where

$$z_i = \left[\mp \frac{\lambda_p}{\lambda_R}\left(\frac{1}{z_O} - \frac{1}{z_R}\right) - \frac{1}{z_p}\right]^{-1} \tag{3.5.118}$$

Two images are formed: the one with z_i positive, on the right side of the hologram film, is real; the one with z_i negative, on the left side, is a virtual one. Thus the two exponential terms forming the cosine in Eq. (3.5.112) give rise to separate images at points determined, respectively, by the + and − signs in Eq. (3.5.118).

The quadratic terms have determined the z location of the image. However, we have not yet determined the x and y locations of the image. We can do this by using the condition that the linear terms in $\mathbf{r}$, like $k_R\mathbf{r} \cdot \mathbf{r}_O/z_O$ in Eq. (3.5.116), cancel out. The condition is

$$\mp k_R\left(\frac{\mathbf{r}_O}{z_O} - \frac{\mathbf{r}_R}{z_R}\right) + k_p\left(\frac{\mathbf{r}_p}{z_O} + \frac{\mathbf{r}_i}{z_i}\right) = 0 \tag{3.5.119}$$

Thus the transverse coordinates x_i and y_i of the reconstructed image are where

$$\frac{x_i}{z_i} = -\frac{x_p}{z_O} \pm \frac{\lambda_p}{\lambda_R}\left(\frac{x_O}{z_O} - \frac{x_R}{z_R}\right)$$
$$\frac{y_i}{z_i} = -\frac{y_p}{z_O} \pm \frac{\lambda_p}{\lambda_R}\left(\frac{y_O}{z_O} - \frac{y_R}{z_R}\right) \tag{3.5.120}$$

respectively. Note that a small change in object coordinates, $\Delta\mathbf{r}_O$, leads to a change in the image coordinates, $\Delta\mathbf{r}_i$, where

$$\Delta\mathbf{r}_i = \pm \frac{\lambda_p}{\lambda_R}\frac{z_i}{z_O}\Delta\mathbf{r}_O \tag{3.5.121}$$

Thus the transverse magnification M_T associated with the wavefront reconstruction

process is defined as

$$M_T = \pm \frac{\lambda_p}{\lambda_R} \frac{z_i}{z_O} \tag{3.5.122}$$

or, equivalently, as

$$M_T = \frac{1}{\left| \frac{z_O}{z_p} \frac{\lambda_R}{\lambda_p} \mp \left(1 - \frac{z_O}{z_R}\right) \right|} \tag{3.5.123}$$

Similarly, the change Δz_i in the z coordinate of the image for a small change in the position of the object Δz_O gives a longitudinal magnification M_L, where

$$M_L = \frac{(\lambda_R/\lambda_p)^2}{\left| \frac{z_O}{z_p} \frac{\lambda_R}{\lambda_p} \pm \left(1 - \frac{z_O}{z_R}\right) \right|^2} = \left(\frac{\lambda_R}{\lambda_p}\right)^2 M_T^2 \tag{3.5.124}$$

If the reference and reconstruction sources have the same wavelength ($\lambda_R = \lambda_p$), then $M_L = M_T^2$. This is identical to the similar magnification formulas for a lens:

$$\begin{aligned} M_T &= \left| \frac{z_i}{z_O} \right| \\ M_L &= \left| \frac{z_i}{z_O} \right|^2 \end{aligned} \tag{3.5.125}$$

where z_o is the position of the object and z_i is that of the image. If a different wavelength is used for reconstruction and illumination in a holographic system (i.e., if $\lambda_R \neq \lambda_p$), the results and the perspective to an observer will be quite different than they are for a normal imaging system.

The definition of the image may be determined directly by carrying out the integral

$$s(x'_O, y'_O, z_i) = \int e^{-j\Phi(x,y,0,x'_o,y'_o,z_i)}\, dx\, dy \tag{3.5.126}$$

over the area of the aperture, where x'_o, y'_o, and z_i are the coordinates in the image plane. This yields exactly the result we would expect; for a square aperture with sides D_x and D_y, for example, the 3-dB definitions in the x and y directions are

$$\begin{aligned} d_x &= \frac{0.89 z_i \lambda_R}{D_x} \\ d_y &= \frac{0.89 z_i \lambda_R}{D_y} \end{aligned} \tag{3.5.127}$$

with a sinc $(x'_O D_x / z_i \lambda_R)$ sinc $(y'_O D_y / z_i \lambda_R)$ variation for the point spread function. With a circular aperture, the point spread function is a jinc function, as we would expect. These definitions correspond, of course, to their scaled versions, using

the magnification factor M_T in the object system. The range definitions also correspond to what we would expect for a lens of the same aperture.

C. Water–Air Surface as an Acoustic Imaging Intensity Detector

When sound waves impinge on the water–air interface in a water bath, there is a static radiation pressure associated with the sound wave of value $p_0 = 2I/V$, where I is the acoustic intensity of the wave approaching the surface; this causes the water surface to lift.† The movement of the water surface at a distance R is proportional to the sound wave intensity and hence, if it can be detected optically, this phenomenon can be used for holographic detection of sound. At the same time, the water is undergoing RF motion due to the presence of the sound waves, with a particle displacement $u = \lambda_a S$, where λ_a is the wavelength of the sound and S is the strain. With typical strains of the order of $S = 10^{-6}$, and wavelengths of the order of 1 mm, the RF displacement of the water is of the order of 10 Å, a very small value. In practice, the water displacement due to radiation pressure is normally comparable to this value and often much larger than it.

We can estimate the water displacement by considering the restoring force due to surface tension, and carrying out a one-dimensional analysis pertaining to displacement of the water surface by a sound wave whose intensity varies in the x direction along the water surface [55]. If σ is the surface tension, the restoring force due to surface tension, after the liquid is displaced a distance h, is $\sigma(d^2h/dx^2)\,dx$ in an elemental length dx. However, the downward force due to gravity is $g\rho_{m0}h\,dx$, and the upward force due to the radiation pressure of the sound wave is $p_0\,dx$. Hence we can write

$$\sigma \frac{d^2h}{dx^2} + g\rho_{m0}h = p_0(x) \tag{3.5.128}$$

If we take a spatial Fourier transform of Eq. (3.5.128), we can write

$$\begin{aligned} H(\nu_x) &= \int_{-\infty}^{\infty} h(x)e^{-j\nu_x x}\,dx \\ P(\nu_x) &= \int_{-\infty}^{\infty} p_0(x)e^{-j\nu_x x}\,dx \end{aligned} \tag{3.5.129}$$

It follows from Eq. (3.5.128) that

$$H(\nu_x) = \frac{P(\nu_x)}{(\nu_x^2\gamma^2 + 1)\rho_{m0}g} \tag{3.5.130}$$

where $\gamma^2 = \sigma/\rho_{m0}g$.

If the second term in the denominator of Eq. (3.5.130) can be neglected

†The easiest way to understand this effect is to use quantum mechanics. We regard the wave as composed of acoustic phonons. If there are N acoustic phonons per unit area per second reaching the surface, the rate of change of momentum due to the phonons reflected at the surface is $p_0 = 2N\hbar k$, where $\hbar$ is Planck's constant and k is the propagation constant. Therefore, $p_0 = 2N\hbar\omega/V$. However, $N\hbar\omega = I$. Thus $p_0 = 2I/V$.

compared to the first term, we find that

$$H(\nu_x) = \frac{P(\nu_x)}{\nu_x^2 \sigma} \tag{3.5.131}$$

or, more generally, in a two-dimensional system,

$$H(\nu_x, \nu_y) = \frac{P(\nu_x, \nu_y)}{\nu^2 \sigma} \tag{3.5.132}$$

where $\nu^2 = \nu_x^2 + \nu_y^2$.

Equations (3.5.131) and (3.5.132) are valid if the spatial period of the hologram has a wavelength $\lambda = 1/\nu$ that is much smaller than the parameter γ, where γ is typically of the order of 2 mm. In this case, the second spatial derivative of the height h is proportional to the acoustic intensity at the surface. In a holographic system, this implies that the cross product term of the wave passing through the object and of the reference wave is the important term, and that d^2h/dx^2 is proportional to the amplitude of the wave passing through the object. More generally,

$$p_0(x, y) \propto \frac{\partial^2 f}{\partial y^2} + \frac{\partial^2 h}{\partial y^2} \tag{3.5.133}$$

Smith and Brenden holographic technique. Many different types of acoustic holographic imaging methods that use the ripple of a water surface for reconstruction of the image have been described in the literature [55]. First we will describe the Holosonics industrial system of Brenden, which has been fairly widely used [56]. If a spherical reference source is employed, the water surface must, in principle, be lifted into a spherical shape, and distortion inevitably occurs. The Brenden system eliminates this problem by using a plane wave acoustic reference beam ($z_R = \infty$), a small separate tank for the region where the reference beam impinges on the water surface, and a lens between the object and the water surface to bring the image plane $z_O' = z_i$ of the optical system to a finite distance. A schematic of the system is shown in Fig. 3.5.39.

As illustrated, a lens is placed in front of the optical reference source to produce a collimated or parallel optical beam ($z_p = \infty$) at the water surface.

It follows from Eq. (3.5.118) that

$$z_i = \pm \frac{\lambda_R}{\lambda_p} z_O = \pm \frac{\lambda_a}{\lambda_L} z_O \tag{3.5.134}$$

where $\lambda_R = \lambda_a$ is the acoustic wavelength and $\lambda_p = \lambda_L$ is the wavelength of light. By using a lens in front of the object, z_O has been made very small. However, it follows from Eq. (3.5.134) that because $\lambda_a >> \lambda_L$, the image plane can be at a finite distance from the water surface.

Note that two images are formed, a virtual one, indicated by the negative sign, and a real one, indicated by the positive sign. An optical lens of focal length f, a distance d from the water surface, will focus the image to a plane a distance

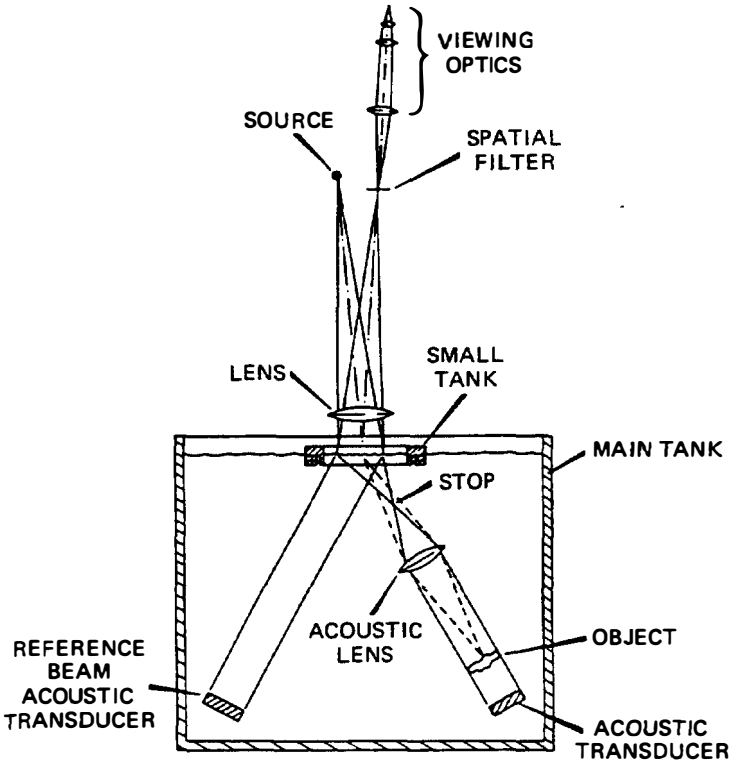

Figure 3.5.39 Liquid surface imaging system due to Brenden. This is the system employed by Holosonics. (After Brenden [56].)

z_i from the lens, where

$$\frac{1}{z_i'} = \frac{1}{f} - \frac{1}{d - z_i} \tag{3.5.135}$$

The true and conjugate images will therefore be focused at different planes.

If the acoustic image is focused on the water surface, then $z_O = z_i = 0$, with the real and virtual images focused at the same plane, although they will be displaced in the x, y plane from each other. If, on the other hand, z_O is chosen to be finite, as above, the lens can be used to focus on one image or the other. Thus, by a combination of transverse and longitudinal displacements, the two images can be separated from each other.

We now consider the magnification of the image. At the plane $z = z_O$, the magnification M_T of the image is

$$M_T = \pm\left(\frac{\lambda_L}{\lambda_a}\right)\frac{z_i}{z_O} = 1 \tag{3.5.136}$$

When light is reflected from the vibrating water surface, there is very little change in amplitude, as there is when light passes through a hologram on photographic film. Instead, the light is phase modulated by the change in the length of the light path. This phase modulation must be converted to amplitude modulation. We will show below how this is done in the Brenden imaging system [55, 56].

When a plane optical wave of amplitude A_0 is reflected from the water surface, the reflected wave is phase modulated by the change in its path, $2h$, and a com-

ponent is obtained with an amplitude variation $a(x, y)$, defined as

$$a(x, y) = A_0 e^{-4j\pi h(x,y)/\lambda_L} \approx A_0\left[1 - \frac{4j\pi h(x, y)}{\lambda_L}\right] \tag{3.5.137}$$

where it has been assumed that $h \ll \lambda_L$.

Suppose that we observe the light at the back focal plane of the optical lens. At this plane, the amplitude of the light can be shown to be proportional to the Fourier spatial transform $A(\nu_x, \nu_y)$ of the function $a(x, y)$. This has the form

$$A(\nu_x, \nu_y) = \delta(\nu_x, \nu_y) - \frac{4j\pi H(\nu_x, \nu_y)}{\lambda_L} \tag{3.5.138}$$

where $H(\nu_x, \nu_y)$ is the two-dimensional Fourier transform of $h(x, y)$. The spatial frequencies ν_x and ν_y are proportional to x'' and y'', respectively, where x'' and y'' are the coordinates at the back focal plane $z = z_i''$ of the lens.

The Dirac δ function represents the bright central spot corresponding to the light reflected directly from the surface of the water. It can be eliminated with a simple opaque dot located on the axis at the back focal plane of the lens. In addition, a neutral density filter with a density variation proportional to r''^2, where r'' is the distance from the axis, can be used along with the small stop. This filter will lower the response to the higher spatial frequencies, yielding an image with a light-amplitude variation of the form $\nu^2 H(\nu_x, \nu_y)$. However, we have shown [Eq. (3.5.133)] that $P(\nu_x, \nu_y) \propto \nu^2 H(\nu_x, \nu_y)$; hence the amplitude of the light passing through the filter is proportional to $P(\nu_x, \nu_y)$. Because the viewing optics can display a Fourier transform of the light amplitude at the back focal plane of the first lens, the image amplitude obtained can be made proportional to $p_0(x, y)$. However, by focusing the viewing optics on the plane $z = z_i$, a focused image whose amplitude is proportional to the acoustic amplitude of the wave passing through the object can be obtained.

An image of a deliberately disbonded aircraft honeycomb structure, taken some years ago with the Holosonics imaging system, is shown in Fig. 3.5.40. In this example, the honeycomb structure was immersed in the water tank; the operating frequency was 2.25 MHz. Note that the definition of the image is fairly good, but there is considerable speckle. This is to be expected with a coherent, phase-imaging, single-frequency system.

D. Scanned Holographic Imaging

There have been many ideas for producing holograms and forming images from them during the last few years. One of them, *scanned holography*, is interesting because of its close relation to synthetic aperture imaging [57, 58]. This system employs a focused transducer mechanically scanned in the x and y directions, as illustrated in Fig. 3.5.41. The transducer is immersed in water to form holograms of either objects in water or objects inside a solid.

In the latter case, the acoustic transducer is focused on the surface of the solid and forms a moving point source or receiver at that plane, which is the plane of the hologram, $z = 0$. The output signal from the receiving transducer is mixed

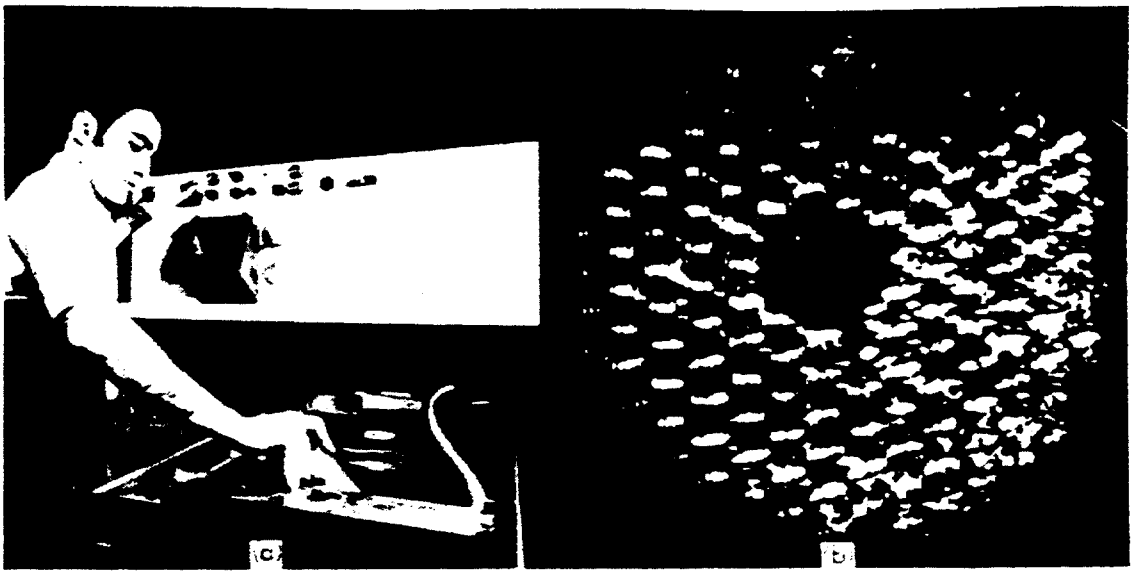

Figure 3.4.40 (a) Holosonics holographic ultrasound imaging system; (b) honeycomb structure ($\frac{1}{2}$-in. period) with intentionally introduced nonbonding areas as imaged by the Holosonics system at 5 MHz. (After Mueller [55].)

with a signal of the same frequency, which is equivalent to using a plane wave reference normal to the surface of the solid. However, as the phase of the reference signal can be changed with an adjustable phase shifter, the phase can be varied linearly with time, while the transducer is scanned in the x direction, to produce the effect of a tilted plane wave reference source.

The dc output from the mixer has an amplitude that varies with time in the same way as the light intensity passing through a hologram. Therefore, if a light source is modulated by this output signal and scanned in synchronism with the

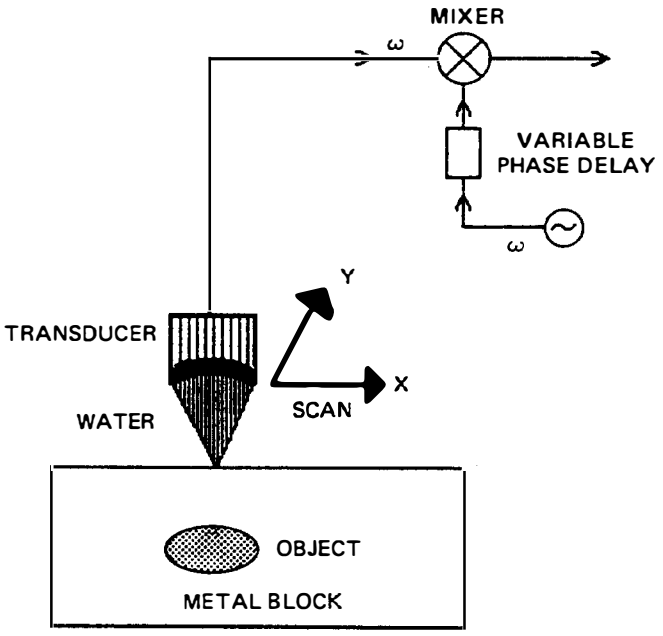

Figure 3.5.41 Simplified scanned holography system.

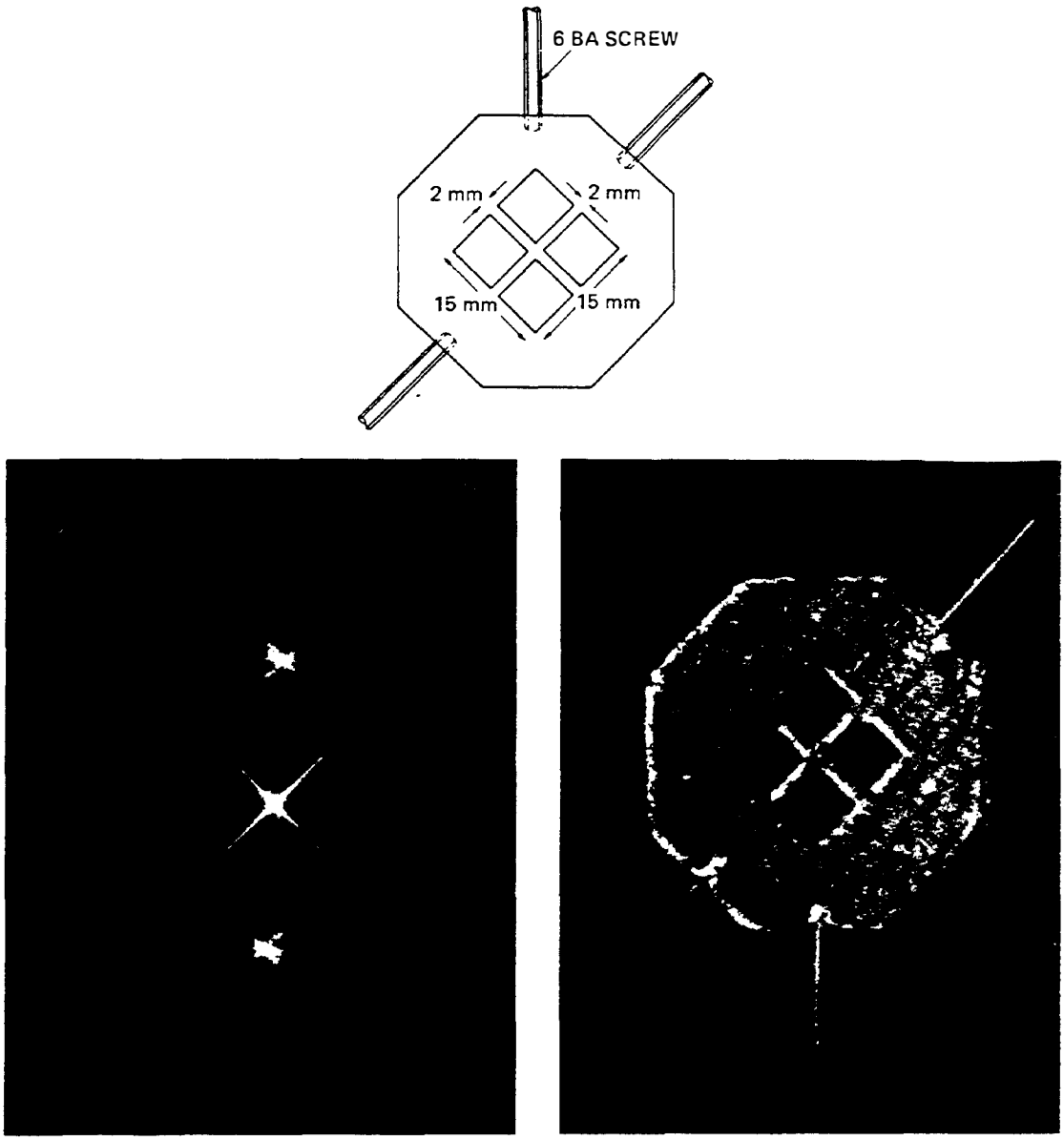

Figure 3.5.42 Reflection mode imaging of a simple object: (a) drawing of the object; (b) space frequency spectrum as seen optically; (c) holographic image. (After Aldridge et al. [57].)

movement of the acoustic transducer, it can be used to expose a photographic film to form a hologram. The hologram can then be reconstructed by the standard techniques already described.

Because of Snell's law, a transducer with a relatively narrow aperture produces a wide angle beam in a metal. Since the transducer can be scanned in the x and y directions over an aperture that is large in comparison to its size, it is possible by holography to synthesize the effect of a lens with a very large aperture.

The system can be used with a plane wave insonifying transducer, either at the top surface or incident on the object from another direction. Alternatively,

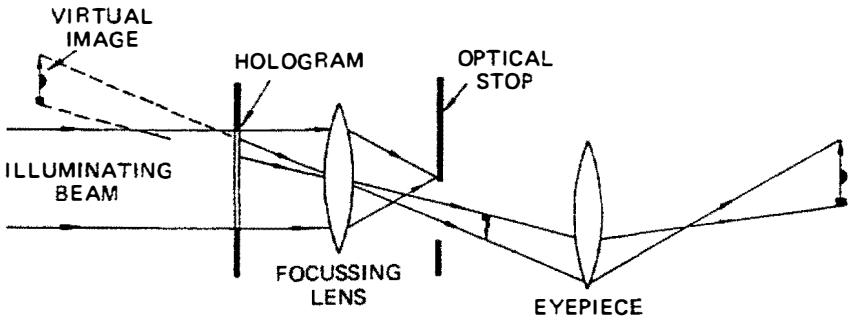

Figure 3.5.43 System used by Aldridge for reconstruction of a scanned holographic image. (After Aldridge et al. [57].)

the same focused transducer can be used as transmitter and receiver. In this case, just as with synthetic aperture imaging, the effective ray lengths are doubled, and the definition of the image is improved by a factor of 2 [57, 58].

A flat structure immersed in water, as illustrated in Fig. 3.5.42(a), was used for a reflection mode imaging experiment by Aldridge et al. [57]. With plane wave illumination at 10 MHz, they obtained the hologram shown in Fig. 3.5.42(b). The hologram was reconstructed with a helium–neon laser source, using the system illustrated in Fig. 3.5.43; the image obtained is shown in Fig. 3.5.42(c). Although there is some evidence of speckle, we see that this early system produced an image of very high quality.

The results obtained for objects inside a solid are less impressive, although they demonstrate that changing the focus of the optical reconstruction system makes it possible to image different planes within the solid. One reason they are less impressive is that there are often interfering signals present, due to reflections from the surface of the solid. Gating the transmitter signal helps, but a minimum pulse length is required to accommodate the time differences between the acoustic ray paths reaching the object at different angles to the axis of the transducer.

A very similar system has been used by a number of authors for short-pulse synthetic aperture imaging. Computers can be used either for holography or for short-pulse synthetic aperture time-delay reconstruction of images. If the phase and amplitude of the acoustic signal are recorded, it can be shown that a fast Fourier transform technique can be used to reconstruct a holographic image (see Prob. 8). But since it does not take much longer to form a true synthetic aperture time-delay image instead, which has the advantage of good range resolution, development of such computer techniques has been centered on synthetic aperture imaging or tomography.

E. The Scanning Laser Acoustic Microscope

Before leaving the subject of holography, we will describe a microscope that uses a laser readout; this is known as the *scanning laser acoustic microscope* (SLAM). We discuss it here because although it is not a strictly holographic system, it can be used in this mode, and it employs very similar techniques to those used in acoustic holography.

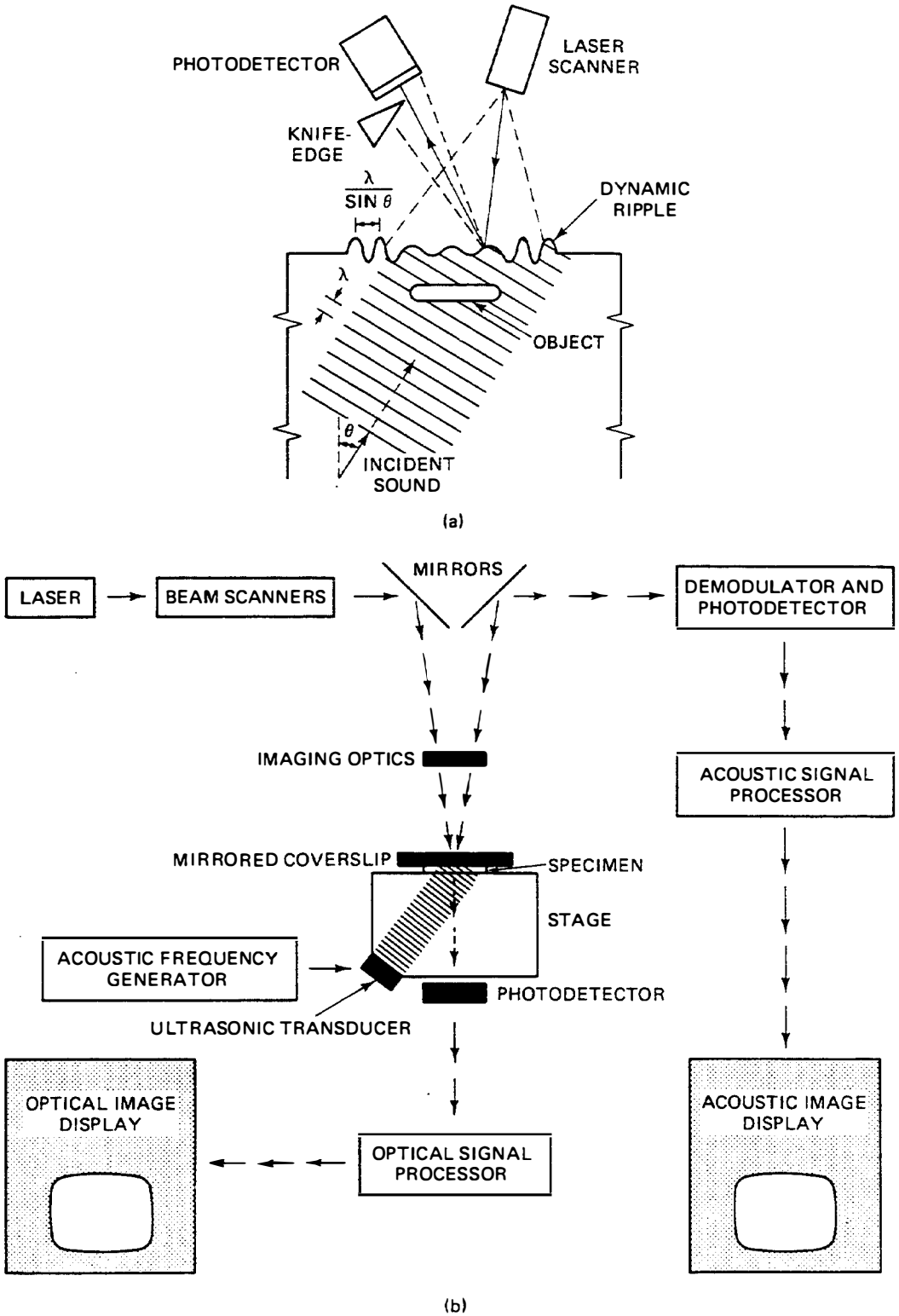

Figure 3.5.44 (a) Laser detection of acoustic energy at an interface. (From Kessler and Yuhas [59], and Korpel et al. [60].) (b) Schematic diagram of the scanning laser acoustic microscope. (After Kessler and Yuhas, as noted in Kessler and Yuhas [59, 61].)

Schematics of the device developed by Kessler and Yuhas are shown in Fig. 3.5.44. The sample to be examined is placed on the microscope stage, which consists of a solid block of quartz or other material, and is insonified by a longitudinal or shear acoustic plane wave directed at an angle to the normal to the surface. If the sample has a polished surface, the surface displacements due to the acoustic wave passing through it can be measured directly with the laser beam; alternatively, a plastic mirror in the form of a coverslip can be placed in contact with the sample and used to relay the sonic information to the laser.

An incident laser beam is reflected to a photodetector from the surface to be examined. When there is a surface ripple present due to an acoustic wave, the laser beam will be tilted by an angle $2\Delta\theta$ when the surface tilts by $\Delta\theta$. This small tilt in the laser beam would not normally affect the output from the photodetector. However, if a knife edge stop is placed in front of the beam, the slight tilt in angle will change the output amplitude. Thus the surface displacement due to the acoustic wave of frequency ω is changed to an amplitude modulation of the same frequency at the photodetector. A Bragg cell (see Sec. 4.9.5) is used to scan the laser beam rapidly over the surface in the x direction. A servo-controlled moving mirror (not shown) is used for the scan in the y direction. A lens (not shown) is placed in front of the knife edge to focus its image on the mirror image of the center of the Bragg cell in the reflecting surface. In this way, the scanned laser beam is always incident on the knife edge.

The operating frequency of the SLAM is usually between 100 and 500 MHz and the frame time is $\frac{1}{30}$ s, identical to the standard TV frame rate. The definition of the SLAM is not controlled, principally, by the acoustic wavelength, since the sample is insonifed by a plane wave. The system is basically a near-field shadow imaging system, with the definition controlled by the size of the laser beam at the reflecting surface. Since the beam must be focused on the image of the knife edge, its size is larger than it is at the focus. The definition for features below the surface rapidly deteriorates at a rate depending on the wavelength of the acoustic waves.

One major advantage of the SLAM, in addition to its real-time imaging capability, is the fact that the object can be viewed optically while the acoustic image is being obtained. An illustration of the configuration used for this purpose is shown in Fig. 3.5.44(b). When the sample is transparent, a half-silvered cover slip can be used and a photodetector placed below the transparent stage to detect the transmitted light. In this way, scanned optical and acoustic images can be obtained simultaneously.

Images of a live mouse embryo heart, taken at 100 MHz, are shown in Fig. 3.5.45. An optical image is shown in Fig. 3.5.45(a), with the acoustic image in Fig. 3.5.45(b). By mixing the output signal with the reference input signal to the insonifying transducer, an interferogram can be generated, as in Fig. 3.5.45(c). If the phase delay through the sample is uniform, the spacing of the fringes in this interferogram is constant and corresponds to $\lambda/\sin\theta$, where θ is the angle between the direction of propagation of the insonifying plane wave and the normal to the surface. When the thickness of the sample is nonuniform, as in the example shown

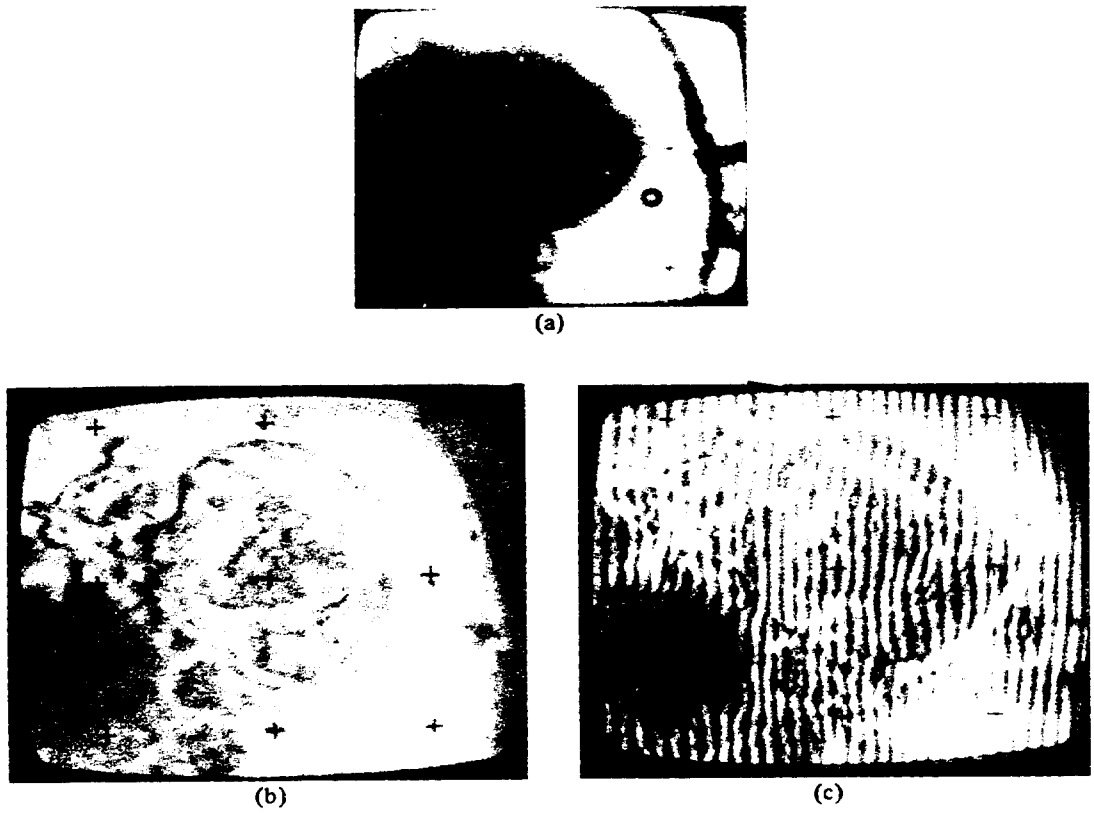

Figure 3.5.45 Live mouse embryo heart: (a) optical image; (b) SLAM acoustic micrograph at 100 MHz (cross-marks are placed 1 mm apart); (c) acoustic interferogram from which variations in elastic properties of the muscles are determined. (After Eggleton and Vinson, as noted in Kessler and Yuhas [59, 62].)

here, the finger spacing varies and can be used to measure the variation in thickness of the sample.

When the sample is far from the surface, the interferogram obtained is, in fact, a hologram. Some theoretical analyses involving digital techniques to reconstruct images from these holograms have been made [63, 64], but at the time of writing, there are few, if any, experimental results.

F. Holographic Imaging of Vibrating Objects

One of the most useful applications of holographic techniques is to the imaging of vibrating objects and the determination of the amplitude of vibration of any point on the object [2].

We suppose that any point x_O, y_O, z_O on the object is vibrating with an amplitude

$$\Delta z = m(m_O, y_O) \sin \Omega t \tag{3.5.139}$$

When a point x_O, y_O, z_O on a stationary object, as illustrated in Fig. 3.5.46, is illuminated by a spherical source with its center at x_p, y_p, z_p, and the reference

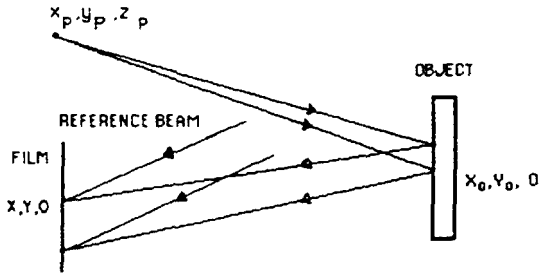

Figure 3.5.46 Holographic system for observing vibrating objects.

wave is a plane wave ($z_R = 0$), the image intensity at a point x, y, 0 on the film is

$$I = A \cos k\left[\frac{(x}{\qquad\qquad}\right.$$

$$\left. \frac{}{2(z_O - z_P)} + 2z_O + \text{constant}\right] \tag{3.5.140}$$

$$= A \cos (\theta_O + \theta_P)$$

where $k = 2\pi/\lambda$ and λ is the optical wavelength.

If the object is vibrating, $I_{RO} = A \cos (\theta_O + \theta_P + \theta_1)$, where $\theta_1 \propto \Delta z$. If the angles of incidence of the reference beam and of the rays from the object at the film are small, it follows from the second-to-last term in Eq. (3.5.140) that $\theta_1 \approx 2k\,\Delta z$. Hence

$$I = A \cos (\theta_O + \theta_P + 2k_P m \sin \Omega t) \tag{3.5.141}$$

We can write I in the form

$$I = \frac{A}{2}\left[e^{-jkA(\theta_O + \theta_P + 2k_P m \sin \Omega t)} + \text{c.c.}\right] \tag{3.5.142}$$

where c.c. stands for complex conjugate. However, we can write

$$e^{-2jkm \sin \Omega t)} = \int_{-\infty}^{\infty} c_n e^{-jn\Omega t}\, dt \tag{3.5.143}$$

with

$$c_n = \frac{1}{2\pi}\int_0^{2\pi} e^{j(n\Omega t - 2km \sin \Omega t}\, dt = J_n(2km) \tag{3.5.144}$$

where $J_n(z)$ is an nth-order Bessel function of the first kind.

It follows that the static value of the intensity varies as

$$I_0(x_O, y_O) = AJ_0[2km(x_O, y_O)] \tag{3.5.145}$$

due to the vibration. Thus the intensity of the holographic image of a plane object varies with $m(x_O, y_O)$ in the manner given by Eq. (3.5.145).

This result for the intensity variation gives us a way to measure the vibration

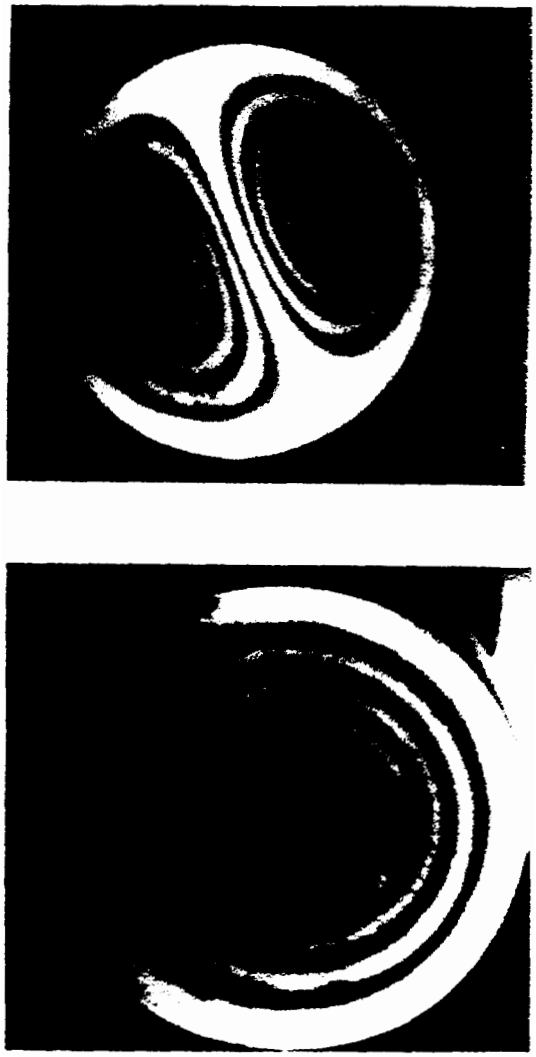

Figure 3.5.47 Holographic images of a diaphragm vibrating in (a) a circularly symmetric mode, and (b) a mode without circular symmetry. (After Powell and Stetson, as noted in Goodman [2, 65].)

amplitude. We see that $I_0(x_O, y_O) = 0$, where $J_o(2km) = 0$ (i.e., at $2km = 2.4$). With illumination from a helium–neon laser, this requires only a vibration amplitude of the order of 1250 Å. With small vibration amplitudes, the intensity I_o varies as

$$I_o \approx A(1 - k^2m^2) \tag{3.5.146}$$

Thus, when m is small, the reduction in intensity is proportional to the square of the amplitude of vibration. A holographic image of a vibrating object is shown in Fig. 3.5.47.

PROBLEM SET 3.5

1. Use diffraction theory to treat the reflection of a finite beam of width w, incident at an angle θ to the normal on a perfect plane reflector (a specular reflector), as illustrated in the figure. Suppose that the incident beam can be regarded as a section of a plane wave

(i.e., to have uniform fields over its width w and a propagation constant k in the θ direction). Find the value of the normal particle displacement u_z^i of the incident wave at the plane $z = 0$ of the reflector.

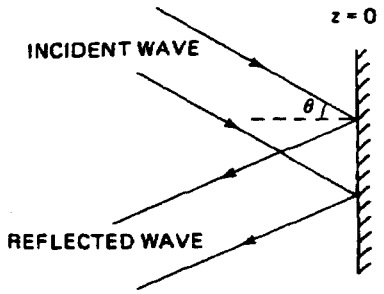

(a) Regard the specular reflector as a rigid object, so that the normal displacement of the reflected wave at the plane $z = 0$ is $u_z^R = -u_z^i$. Use the Rayleigh–Sommerfeld theory to determine the form of the reflected beam in the far field, and work out its 3-dB width and the angular position of its central axis. You will need the Rayleigh–Sommerfeld formula for a strip beam (i.e., a beam that is infinite in length in the y direction). This is given as the solution of Prob. 3.1.3. The result justifies ray optic theory in the limit $w/\lambda \to \infty$.

(b) Now consider sampling the reflected wave source by regarding it as a set of N line sources, with a spacing $w/[(N-1)\cos\theta]$ between them. Work out the form of the far field, regarding each source as a δ function multiplied by the correct phase term. Show that as $N \to \infty$, your result converges to one of the same form as the solution of part (a). Show that when N is finite there are subsidiary maxima associated with the finite number of sampling points. These are called grating lobes. Find a formula for the positions of these grating lobes.

2. Consider an N-element transducer array at the plane $z = 0$. Suppose that the field due to a point source at x, z is $f(x - x_n, z)$ at the nth element of the array, and that the response of each element of the array is $g(x_n)$. If the random noise power at each element of the array is N_0, and the noise powers received at each element add linearly, the total noise power P_N into a 1-Ω load at the receiver will be

$$P_N = N_0 \sum_n |g_n^2(x)|$$

Work out the signal power S into a 1-Ω load at the receiver, and show that the signal-to-noise ratio S/P_N is maximum when $g(x_n) = f^*(x - x_n, z)$. Show also that when $|g(x_n)| = A$, where A is a constant, the signal-to-noise ratio is increased by a factor N by using N transducer elements instead of only one.

Note: You may find it helpful to use Schwarz's inequality in a similar manner to the derivation that leads to Eq. (4.4.31).

3. Prove Eq. (3.5.70) using the method of stationary phase in Appendix G.

4. Consider an M-phase digital imaging system with a continuous linear array. As discussed in Secs. 3.5.2.B and 3.5.3.B, the ideal matched filter response for a continuous array is

$$g(u) = e^{i\pi u}$$

where $u = x'^2/\lambda z$, and the phase is $\phi = \pi u$.

Assume that a digitally sampled system is designed to match this requirement as closely as possible, with M samples per cycle. Take the phase of the digital system to

be ϕ with an error ε, defined as

$$\varepsilon = \frac{2n\pi}{M - \pi u} \qquad \left[\frac{(2n-1)\pi}{M} < u < \frac{(2n+1)\pi}{M}\right]$$

where n is an integer. The phase ϕ and error ε as functions of u are illustrated, respectively, in Figures (a) and (b) below.

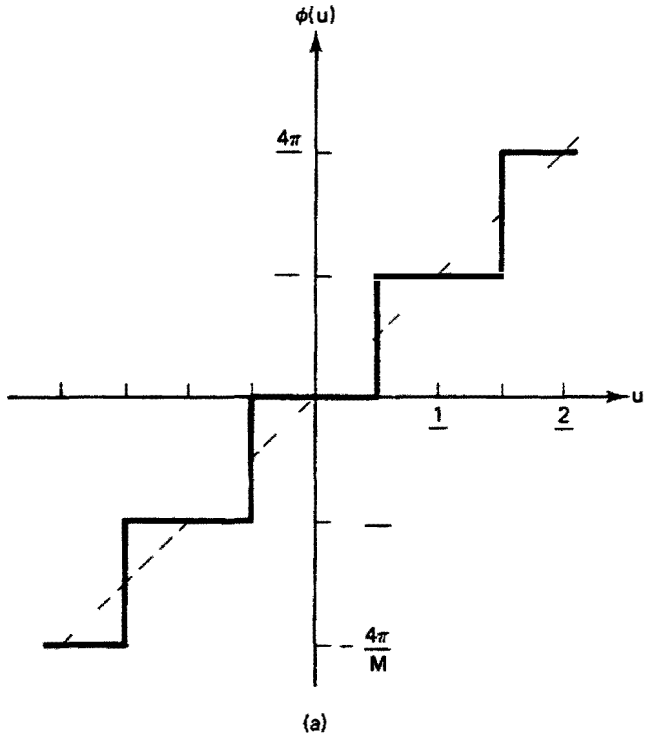

(a)

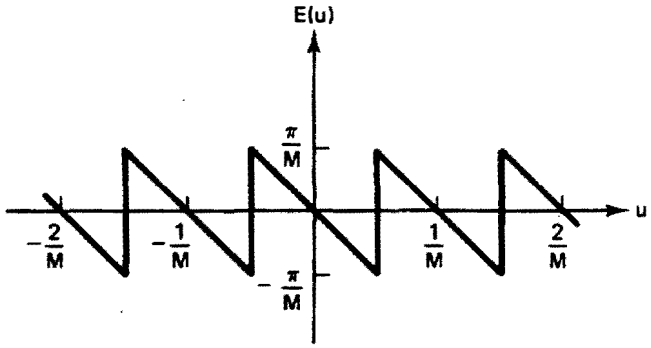

(b)

(a) Expand $\exp(j\varepsilon)$ in the form

$$e^{j\varepsilon} = \sum_m A_m e^{2jm\pi u}$$

and show that

$$A_m = \text{sinc}\left(\ldots + \frac{1}{M}\right) = \frac{\qquad}{\pi(m + 1/M)}$$

to be ϕ with an error $\varepsilon(u)$ defined as:

$$\varepsilon(u) = \frac{2n\pi}{M} - \pi u \quad ; \quad \frac{2n-1}{M} < u < \frac{2n+1}{M} \, .$$

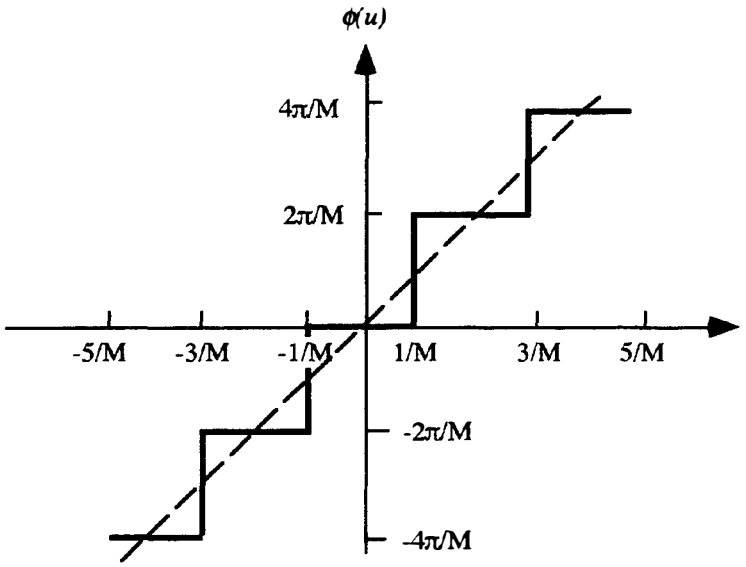

(a)

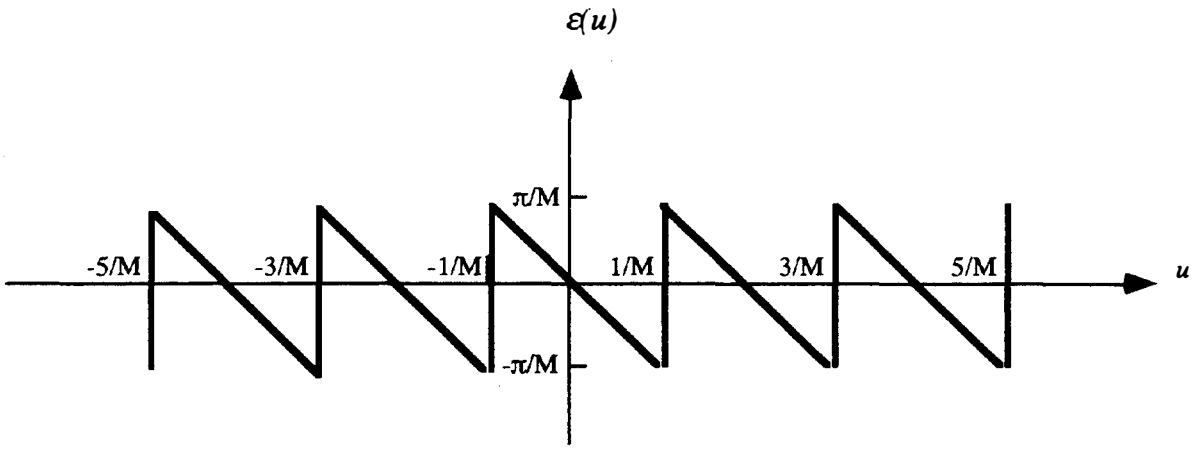

(b)

(a) Expand exp ($j\varepsilon$) as a Fourier series:

$$e^{j\varepsilon(u)} = \sum_s A_s e^{js\pi u}$$

where $\phi(u) = \varepsilon(u) + \pi u$, or

$$\phi(u) = 2\pi n / M \quad ; \quad \frac{2n-1}{M} < u < \frac{2n+1}{M}$$

with

$$e^{j\phi(u)} = \sum_s B_s e^{js\pi u}$$

In one cycle ϕ varies from 0 to 2π , su from 0 to 2s. , and u from 0 to 2. In this case, with M samples per cycle, $\phi(u)$ has sampled values of $2\pi n/M$, where n is an integer. For u varying from $-1/M$ *to* $1/M$, the digitized or approximate value of f(u) is taken to be f$(u) = 0$. For u varying from $1/M$ to $3/M$,$\phi(u) = 2\pi/M$ and so on as shown above.

Work out the Fourier coefficient by integrating for a general value of n and summing terms.

The mathematics required is very similar to that used for the analysis of grating lobes. You may find it convenient to work in terms $exp\, j\varepsilon(u)$ and show that the only finite Fourier coefficients arethose with $s = mM$. If you decide to write $exp\, j\phi(u)$ as a Fourier series, then the only finite terms would be with $s = Mm + 1$. Either approach will work. By expanding over one period of the error from $u = -1/M$ *to* $1/M$, the analysis will be simpler.

(b) Use your result and the method of stationary phase (Appendix G) to prove Eq. (3.5.72).

(c) Determine the positions of the subsidiary foci associated with the mth harmonics.

5. (a) Consider a nonparaxial chirp-focused system, used as a receiver, with transducer elements a distance l apart. Find the form of the chirp required to focus on a point x, z.

   (b) Now consider the system as a transmitter. What is the form of the chirp required for nonparaxial focusing on the point x, z?

   Note: You may find it helpful to consider the signal at each element of the transducer and allowing the phase to change by an extra 2π from element to element.*

6. (a) Consider a radial sector scan imaging system in which focusing and steering are handled separately, as described in Sec. 3.5.2.C. Suppose that we want to limit the number of lumped delay lines required for focusing in the receiver. Examine one strategy: Suppose that the receiver is focused on the point 0, z, and that the maximum phase error allowed is $\pi/4$. Then, if the receiver is focused on $z = z_1 = \infty$, find the value of z for which the maximum phase error is $\pi/4$. Now find the value of $z = z_2$ for which the error is $\pi/2$ and suppose that the receiver is refocused at this point. Repeat the process to find how z_n depends on n, the nth refocusing point.

   (b) Consider a system operating in body tissue (acoustic velocity 1.5 km/s) at a frequency of 3.5 MHz. Suppose that we require the system to have a range of focus from 2 cm to ∞. How many focal points will be needed, and hence how many lumped delay lines per element will be required? Assume, in this case, that the error for an individual element may be less than the maximum error allowed for the outside elements, and that the width of the system is 2 cm.

7. Consider the Leith–Upatnieks hologram, which uses a plane wave reference, shown in Fig. 3.5.37.

   (a) Show that an image may be reconstructed by using a plane wave source of the same wavelength to illuminate the film from the same angle as the original reference. You may regard any image as being composed of plane wave components incident at all angles to the film. If these plane wave components can be reconstructed, so can the original image.

   (b) Consider the situation when reconstruction is attempted with a plane wave source of different wavelength. Will it work or not? Do not use the paraxial approximation.

8. Consider the problem of forming an image from a hologram by using fast Fourier transform (FFT) techniques on the computer. As an example, the hologram of a point x, y, z is formed with a SLAM. For simplicity, assume that a plane wave reference source is directed normal to the surface $z = 0$. This plane wave source insonifies the point x, y, z, so that the total signal arriving at the plane $z = 0$ may be regarded as the sum of a plane wave and a source at the point x, y, z.

   (a) Using the paraxial approximation, work out the intensity of the image at the plane $z = 0$. This is the recorded signal.

   (b) Now, in analogy to the FM chirp imaging method, multiply the recorded signal by a term of the form $\exp(j\{[(x - x')^2 + (y - y')^2]/2z\})$, where x', y', and 0 are the coordinates at the plane $z = 0$ being scanned by the laser beam. Now show how a Fourier transform technique can be used to reconstruct the image of the point x, y,

*Reference: W. H. Chen, F. C. Fu, and W. L. Lu, "Scanning Acoustic Microscope Utilizing SAW-BAW Conversion," *IEEE Trans. Sonics Ultrason.*, SU-32, No. 2 (Mar. 1985), 181–88.

z and, in general, the image of a thin layer at the plane z, whose attenuation varies as $f(x, y, z)$.

(c) Determine from your analysis the 3-dB definitions of the image in the x and y directions, for total laser scan distances of D_x and D_y in the x and y directions, respectively.

3.6 REFLECTION AND SCATTERING BY SMALL AND LARGE OBJECTS

3.6.1 Introduction

There are many applications in nondestructive testing (NDT), medical acoustics, and sonar for which we must be able to determine how different types of objects scatter acoustic waves. An object that is large in cross section compared to the wavelength, and whose surface roughness is small in scale compared to the wavelength, like a bone in the human body or a large hole in a metal or a ceramic, will tend to behave like specular reflectors. On the other hand, objects whose dimensions are small compared to the wavelength, such as grains in a metal, sand in the sea, fatty globules in tissue, or blood cells, will tend to give rise, individually, to weak waves, which are scattered in all directions. Thus a large number of fine particles will tend to behave, collectively, like a diffuse reflector. This scattering regime is known as *Rayleigh scattering*, named for Lord Rayleigh, who first investigated it in connection with the scattering of light by dust particles in the sky. He showed that the intensity of the scattered radiation varies as the fourth power of the frequency, which makes the sky appear blue.

The same law holds true for acoustic waves, so that Rayleigh scattering is one of the principal causes of attenuation in granular materials, although it is not present in a high-quality single crystal. The attenuation occurs because power is scattered from the incident acoustic beam by the grains. When the grain size is small compared to the wavelength, the implication is that the attenuation per unit length varies as the fourth power of the frequency [24, 66, 67].

Recently, considerable advances have been made in NDT by adapting the earlier electromagnetic (EM) theory and the theory used for scattering in liquids to the study of scattering in solids. This makes it possible to predict the frequency and angular variation of amplitude of the signals scattered from various types of objects, such as cracks, inclusions, and bounding surfaces, in terms of their size and material constants. Thus, by carrying out quantitative theory, it is becoming possible to establish the position, nature, and size of flaws in a solid body [1, 66, 67].

The NDT or sonar fields are convenient vehicles for such studies because for the simplest cases, scatterers of simple shape and composition are treated. Simple scatterers, like spheres and cylinders, can be treated theoretically and investigated in the laboratory. In the medical field, the problem is more difficult because of the complicated and less controllable nature of biological materials. A study of

scattering from simple objects, however, is fundamental to understanding scattering from more complicated structures, and leads to very useful insights.

In Sec. 3.6.2 we will examine an easy way to treat specular scattering from spherical objects. Then, in Sec. 3.6.3 we will describe a more sophisticated theory to deal with scattering from different types of scatterers, applying it to scattering from both small and large objects.

3.6.2 Scattering by Large Objects (Physical Concepts)

Acoustic scattering of an incident wave, by objects in the sea, parts of the body, and flaws in materials, tends to be specular. This is because, unlike the case for optical waves, the surface roughness of these objects is typically small compared to the wavelength. The scattering from biological and solid objects at frequencies in the 1-GHz range is not specular, because the acoustic wavelength is of the order of 1.5 μm, comparable to the scale of surface roughness or to the size of biological cells. At low frequencies, as we have seen, the scale of surface roughness is small compared to the wavelength, and most discontinuities in impedance give rise to specular reflections. Thus it is difficult to obtain diffuse reflecting surfaces at low frequencies, even when we want to do so.

We first consider a large, perfectly rigid sphere insonified by a plane wave. We assume, for simplicity, that if the sphere is much larger in diameter than the wavelength, it behaves like an isotropic reflector. The power intercepted by the sphere, of radius a, is $\pi a^2 I_i$, where I_i is the intensity of the wave and πa^2 is the cross-sectional area of the sphere exposed to the incident wave. The reflected power radiated by the sphere will be $P_R = \pi a^2 I_i$. Thus the power per unit area in the reflected wave at a radius r will be the intensity $I_R = P_R/4\pi r^2$. We write

$$I_R = \frac{\pi a^2}{4\pi r^2} I_i = \frac{a^2}{4r^2} I_i \tag{3.6.1}$$

Thus for $a >> \lambda$, the reflected power intensity is proportional to a^2 and inversely proportional to the distance squared from the sphere. We obtain this result another way in Sec. 3.6.3.

We can extend the same general idea to account for reflection at normal incidence from any convex surface where all radii of curvature are large compared to a wavelength. We consider a plane wave normally incident on the convex surface at the point P, as shown in Fig. 3.6.1(c). Let its principal radii be R_1 and R_2. Imagine a series of planes that intersect the surface of the object: The *principal normal sections* are defined as those having a maximum and minimum radius of curvature, called R_1 and R_2, respectively. Suppose that AA' and BB' are lines on the convex surface that lie in the two respective principal normal sections, as shown in Fig. 3.6.1(a) and (b).

Consider the plan view shown in Fig. 3.6.1(c). The two incident rays subtending an angle $2d\theta_1$ at the center of curvature intercept a segment of length dl_1, where

$$dl_1 = R_1\, d\theta_1 \tag{3.6.2}$$

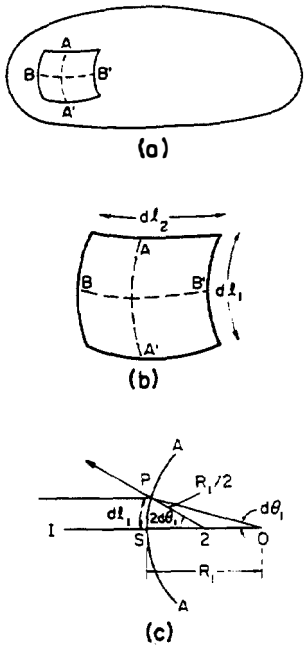

Figure 3.6.1 Reflection from convex surface: (a) cross-section through AA' with radius of curvature R_1; (b) reflection from a small element of area $dl_1\ dl_2$ with AA' and BB' as the principal normal sections; (c) ray incident from O at the point P on the convex surface.

If we consider the element dl_2 at right angles to this segment, we can write

$$dl_2 = R_2\, d\theta_2 \tag{3.6.3}$$

The power incident on this element of area $dl_1\ dl_2$ is

$$dP = I_i\, dl_1\, dl_2 = R_1 R_2\, d\theta_1\, d\theta_2 \tag{3.6.4}$$

The reflected wave in the plane view of Fig. 3.6.1(c) subtends an angle $2d\theta_1$ and appears to be emitted from a point $R_1/2$ from the center of curvature. Thus the area over which the reflected power is distributed at a radius r is

$$ds = r^2(2\, d\theta_1)(2\, d\theta_2) \tag{3.6.5}$$

Hence the reflected intensity I_R is

$$I_R = \frac{dP_R}{ds} = \frac{I_i R_1 R_2}{4r^2} \tag{3.6.6}$$

For a sphere of radius a, Eq. (3.6.6) reduces to the relation

$$\frac{I_R}{I_i} = \frac{a^2}{4r^2} \tag{3.6.7}$$

This result is the same as Eq. (3.6.1).

When the sphere is nonrigid and made of a material with a reflection coefficient Γ, we can write

$$\Gamma = \frac{Z_2 - Z_0}{Z_2 + Z_0} \tag{3.6.8}$$

where Z_2 is the impedance of the sphere and Z_0 is the impedance of the surrounding material. We find, by the same arguments, that

$$\frac{I_R}{I_i} = |\Gamma|^2 \frac{a^2}{4r^2} \tag{3.6.9}$$

In practice, a calculation for Γ in the simple form given in Eq. (3.6.8) is reasonable only for waves at normal incidence. As the main contribution to the backscattered wave is from this region, however, the use of Eq. (3.6.8) is valid. On the other hand, reflection of the incident plane wave to an off-axis transducer requires using a more general formula for Γ.

3.6.3 General Scattering Theory

Here, to acquaint the reader with the concepts used in the theory of scattering from small, arbitrarily shaped objects, we treat a simplified case of scattering by a hydrostatically compressible object in a liquid. We also discuss more general formulas for scattering in solids, and their implications.

Surface integral formulation. We use the Green's function theory given in Sec. 3.1.3 [see Eq. (3.1.27)]. There we showed that if the potential ϕ and its normal gradient $\nabla\phi \cdot \mathbf{n}$ are known on a surface s, the potential at any other point due to excitation at this surface is $\phi_s(x, y, z)$, where

$$\phi_s(x, y, z) = \int_s (\phi \nabla' G - G \nabla' \phi) \cdot \mathbf{n} \, ds' \tag{3.6.10}$$

and the prime denotes source coordinates, in this case on the surface of the sphere. Here, to eliminate negative signs in Eq. (3.6.10), we have defined $\mathbf{n}$ as the *outward normal* from the sphere, and have redefined G as

$$G = \frac{e^{-jkR}}{4\pi R} \tag{3.6.11}$$

with

$$R = \sqrt{(x - x')^2 + (y - y')^2 + (z - z')^2} \tag{3.6.12}$$

Now suppose that we consider an object excited by an incident plane wave, as illustrated in Fig. 3.6.2. Suppose that the incident plane wave has a potential ϕ_i when there is no scattering object present. When a scattering object is present, the total potential is

$$\phi = \phi_i + \phi_s \tag{3.6.13}$$

where ϕ_s is the potential of the scattered wave.

Therefore, in principle, if the total potential is known at the surface of the sphere, we can find $\phi^s(x, y, z)$ by writing the integral equation for ϕ, obtained using Eqs. (3.6.10) and (3.6.13), and solving to determine ϕ at any point. The

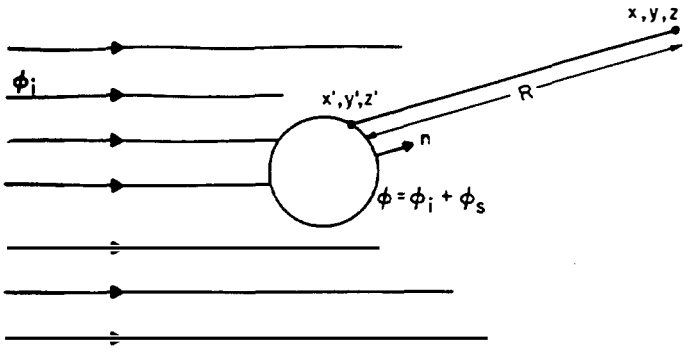

Figure 3.6.2 Object excited by an incident plane wave.

required integral equation is

$$\phi = \phi_i + \int (\phi \nabla' G - G \nabla' \phi) \cdot \mathbf{n}\, ds' \tag{3.6.14}$$

Exact solutions to this problem can be obtained for spheres and cylinders, but not for scatterers of other shapes [66–69].

Volume integral formulation. It is convenient to write Eq. (3.6.10) in the form of a volume integral. Before doing this, however, note that the potentials defined in Eq. (3.6.10) are for a region just outside the perturbed volume V. At the surface of this volume the normal pressure p is continuous, as is the normal component of displacement $u_n = \partial\phi/\partial n$, but the potential is not. Using the relationship $p = \omega^2 \rho_{m0} \phi$ in Eq. (3.6.10), Eq. (3.6.10) can be written in terms of the pressure just inside the volume V in the form

$$p_s(x, y, z) = \int_s \left(p \nabla' G - \frac{\rho_{m0}}{\rho'_{m0}} G \nabla' p \right) \cdot \mathbf{n}\, ds' \tag{3.6.15}$$

where ρ'_{m0} and κ' are the density and compressibility factors, respectively, inside the volume V (see Secs. 2.2 and 3.1). We have dropped the $'$ superscript for all other parameters at this point to keep the notation simple; here the $'$ superscript denotes differentiation with respect to coordinates inside the sphere.

We may now employ Gauss's integral theorem to write Eq. (3.6.15) in the form

$$p_s(x, y, z) = \int_V \left[\nabla' \cdot (p \nabla' G) - \frac{\rho_{m0}}{\rho'_{m0}} \nabla' \cdot (G \nabla' p) \right] dV' \tag{3.6.16}$$

Using the vector relation $\nabla \cdot (\phi \nabla \psi) = \phi \nabla^2 \psi + \nabla \phi \cdot \nabla \psi$, it follows that

$$p_s(x, y, z) = \int_V \left[\left(1 - \frac{\rho_{m0}}{\rho'_{m0}} \right) \nabla' p \cdot \nabla' G + \left(\nabla'^2 G - \frac{\rho_{m0}}{\rho'_{m0}} G \nabla'^2 p \right) \right] dV' \tag{3.6.17}$$

where p and G obey the wave equations

$$\nabla^2 p + \frac{\omega^2 \rho'_{m0}}{3\kappa'} p = 0 \tag{3.6.18}$$

and

$$\nabla^2 G + \frac{\omega^2 \rho_{m0}}{3\kappa} G = 0 \tag{3.6.19}$$

respectively, inside the volume V. Substituting Eqs. (3.6.18) and (3.6.19) in Eq. (3.6.17) and using the relation $k^2 = \omega^2 \rho_{m0}/3\kappa$ finally yields the scattered pressure in the form

$$p_s(x, y, z) = \int_V \left[\left(1 - \frac{\rho_{m0}}{\rho'_{m0}} \right) \nabla' p \cdot \nabla' G - k^2 p G \left(1 - \frac{\kappa}{\kappa'} \right) \right] dV' \tag{3.6.20}$$

We can now use this scattering theorem to determine the scattered power or amplitude resulting from different types of scattering objects.

Born approximation. It is not easy to obtain an exact solution of Eq. (3.6.20) for the scattered pressure, because the total pressure p is not known within the perturbing object. A simple assumption, the *Born approximation*, which is used in many types of perturbation theories, takes the pressure inside the scatterer to be equal to the value of the unperturbed incident wave pressure p_i [1, 66–68] defined as

$$p_i = A_i e^{-jkz'} \tag{3.6.21}$$

where the exciting wave propagates in the z direction. The Born approximation is equivalent to assuming that the perturbations in κ and ρ_{m0} are small. We can find the backscattered wave at the point r, θ, 0, in spherical coordinates, for the simple situation $r \to \infty$ by using the expression for G of Eq. (3.6.11). We write, first,

$$\sqrt{(r\cos\theta - z')^2 + (r\sin\theta - x')^2 + y'^2} \tag{3.6.22}$$

Because $r^2 >>$ $> y'^2$, and $r^2 >> z'^2$, it follows that

$$\begin{aligned} R &\approx r - z'\cos\theta - x'\sin\theta \\ z' &= r'\cos\theta' \\ x' &= r'\sin\theta'\sin\phi' \end{aligned} \tag{3.6.23}$$

We then substitute for G in Eq. (3.6.20) and write

$$\begin{aligned} \frac{p_s(r,\theta)}{A_i} = -\frac{k^2 e^{-jkr}}{r} \int_{\text{object}} \left[\left(\frac{\rho_{m0}}{\rho'_{m0}} - 1 \right) \cos\theta + 1 - \frac{\kappa}{\kappa'} \right] \\ \times \{ e^{-jkr'[1 - \cos\theta)\cos\theta' - \sin\theta\sin\theta'\sin\phi']} \} r'^2 \sin\theta'\, d\theta'\, d\phi' \end{aligned} \tag{3.6.24}$$

In the simplest case, when the diameter of the object is very small compared to the wavelength, the integral becomes merely the volume of the object. Thus the scattered pressure varies with angle as

$$\frac{p_s(r,\theta)}{A_i} = -\frac{k^2 V e^{-jkr}}{r} \left[\left(\frac{\rho_{m0}}{\rho'_{m0}} - 1 \right) \cos\theta + \left(1 - \frac{\kappa}{\kappa'} \right) \right] \tag{3.6.25}$$

Observe that in the *Rayleigh scattering limit*, the scattered pressure varies as the square of the frequency and is proportional to the volume of the scattering object. This result is universal for small scattering objects. In addition, if Eq. (3.6.24) is written in Cartesian coordinates, the integral becomes a Fourier transform of the term in square brackets over the cross-sectional area of the object. Starting from the angular spectrum of the scattered wave, we can go through an inversion process, using Fourier transform techniques to determine the shape of the object. Thus, with only these simple assumptions, a great deal of information is available about the nature of the object.

Quasistatic approximation. Even when the diameter of the scattering object is very small, if there is a large change in its density or elastic constant, the fields inside it will be different from the exciting fields. When the object is very small in dimensions compared to the wavelength, we can assume that in the neighborhood of the object the field variations are quasistatic and can then use static solutions for the fields in this region. To put it another way, in this case the variations of the pressure p in the neighborhood of the object are very large. When the terms $\partial^2 p/\partial x^2$, $\partial^2 p/\partial y^2$, and $\partial^2 p/\partial z^2$ are large compared to $k^2 p$, the solution of the wave equation [Eq. (3.6.18)] will then depend on the solution of Laplace's equation, $\nabla^2 p = 0$.

The exciting pressure wave p_i [Eq. (3.6.21)] in the neighborhood of the object may be written in the approximate form

$$p_i \approx A_i(1 - jkz) = A_i(1 - jkr\cos\theta) \tag{3.6.26}$$

where we assume that the origin of the coordinates is at the center of the scattering object and that $|kz| \ll 1$. This pressure term p_i has associated with it a displacement u_{zi}, defined as

$$u_{zi} = \frac{\partial p_i/\partial z}{\omega^2 \rho_{m0}} = \frac{-jkA_i}{\omega^2 \rho_{m0}} \tag{3.6.27}$$

When an ellipsoid is placed in such an exciting field, the displacement fields within it will also be uniform [67, 68, 70]. The simple case of a sphere is derived in Appendix H, where it is shown that the internal displacement field u_z is

$$u_z = \frac{3u_{zi}}{2 + \rho_{m0}/\rho'_{m0}} \tag{3.6.28}$$

Substituting this result in Eq. (3.6.20) for a sphere of radius a yields the relation

$$\frac{p_s(r, \theta)}{A_i} = -\frac{e^{-jkr}}{r}\frac{k^2 a^3}{3}\left[\frac{3(1 - \rho'_{m0}/\rho_{m0})}{2 + \rho'_{m0}/\rho_{m0}}\cos\theta + \left(1 - \frac{\kappa}{\kappa'}\right)\right] \tag{3.6.29}$$

In the Rayleigh scattering regime, just as with the Born approximation, the scattered pressure varies as the square of the frequency and the cube of the radius of the scattering sphere (i.e., as the volume of the scattering sphere).

We can work out the scattered intensity per unit area at a radius r by taking

the square of Eq. (3.6.29) and integrating over a unit solid angle. We find that as $I_s = (|p_s^2|r^2/2z_0)\, d\Omega$, where $d\Omega = \sin\theta\, d\theta\, d\phi$ is the differential solid angle and $Z_0 = \sqrt{\rho_{m0}c}$ is the impedance of the medium, the ratio of the scattered intensity I_s to the incident intensity I_i is

$$\frac{I_s(\theta)}{I_i} = \frac{k^4a^6}{9r^2}\left[\frac{3(1 - \rho'_{m0}/\rho_{m0})}{1 + 2\rho'_{m0}/\rho_{m0}}\cos\theta + \left(1 - \frac{\kappa}{\kappa'}\right)\right]^2 \tag{3.6.30}$$

We now consider some examples of scattering of acoustic waves in a liquid.

Example: Scattering from a Rigid Sphere in a Liquid

Lord Rayleigh, by carrying out the exact analysis for a rigid sphere, showed that a small rigid sphere acts like a dipole source when illuminated by a plane wave [66, 69]. If θ is the angle between the scattering direction and the incident wave ($\theta = 0$ is forward-scattering and $\theta = \pi$ is backward-scattering), it follows from Eq. (3.6.30) that for a rigid sphere of radius $a << \lambda$, for which $\rho'_{m0}/\rho_{m0} \to \infty$ and $\kappa'/\kappa \to \infty$ (impedance large and velocity finite), the scattered intensity I_s at an angle θ is

$$\frac{I_s}{I_i} = \frac{k^4a^6}{9r^2}\left(1 - \frac{3}{2}\cos\theta\right)^2 \tag{3.6.31}$$

Thus for backward scattering ($\theta = \pi$),

$$\frac{I_s(\text{backward})}{} = \frac{25}{36}\frac{k^4a^6}{r^2} \tag{3.6.32}$$

with

$$\left|\frac{p_s}{a_i}\right| \quad \frac{5}{5}\frac{k^2a^3}{r} \tag{3.6.33}$$

The total scattered power P_s(t

$$P_s(\text{tot} \quad \int_{\phi=0}^{2\pi} \quad r^2 I_s \sin\theta\, d\theta\, d\phi \tag{3.6.34}$$

or

$$P_s(\text{tot}) = \frac{7\pi}{9}k^4a^6I_i \tag{3.6.35}$$

Thus it is as if the incident beam were intercepted by an obstacle of *total cross section* σ (tot), where

$$\sigma(\text{tot}) = \frac{P_s(\text{tot})}{} \quad \frac{7\pi}{} \tag{3.6.36}$$

This parameter $\sigma(\text{tot}) = P_s(\text{tot})/I_i$ is k *ring cross section* of the scatterer. We note that when the scatterer behaves like a specular reflector, then $\sigma(\text{tot}) = 2\pi a^2$. This is twice the physical cross section of a sphere because as much power is radiated in the forward direction as in the backward direction. For a rigid sphere, it follows that

$$\frac{\sigma(\text{tot})}{2\pi a^2} = \frac{7}{18}k^4a^4 \tag{3.6.37}$$

Example: Air Bubbles and Sand Grains in Water

Because air bubbles are easily compressed, I_R/I_i is very large for air bubbles in water. Thus, for air in water, $\kappa/\kappa' = 19{,}000$ and, from Eq. (3.6.30), the backscattering is 77 dB larger than for classical Rayleigh scattering from a rigid sphere. For sand in water, on the other hand, where the sand is regarded as equivalent to a compressible liquid, $\rho'_{m0}/\rho_{m0} = 2.6$, $\kappa/\kappa' = 0.1$, and the scattering from a spherical grain is 4 dB less than it is from a rigid sphere of the same volume.

Kirchoff approximation for scattering from a large sphere ($ka \gg 1$). It is interesting to consider the situation treated in Sec. 3.6.2 by simple specular reflection concepts, by using the field theory techniques developed in this section. When considering scattering from a large sphere, it is convenient to use the surface integral formula of Eq. (3.6.10). We assume that if $ka \gg 1$, any portion of the sphere around the point r, θ, ϕ acts like a planar reflector at an angle θ to the incident wave, and the reflection coefficient from that point is $\Gamma(\theta)$.

The pressure of the incident wave p_i is

$$p_i = A_i e^{-jka\cos\theta} \tag{3.6.38}$$

where we have taken the origin of the coordinates to be at the center of the sphere. The total pressure at the spherical surface, as with a planar reflector, is assumed to be doubled when $\Gamma = 1$. More generally, on the basis of the same types of assumptions,

$$p = -\omega^2 \rho_{m0} \phi = [1 + \Gamma(\theta')] A_i e^{-jka\cos\theta'} \tag{3.6.39}$$

We assume that $p = \phi = 0$ and $0 < \theta < \pi/2$ in the shadow region. For simplicity, we consider only backscattering in the $\theta = \pi$ direction. For $r \gg a$, we write $R \approx r + r' \cos\theta'$, where the coordinates just outside the sphere are r', θ'. Then the Green's function G at $r' = a$ can be written in the form

$$G\Big|_{r'=a} \approx \frac{e^{-jka\cos\theta'}}{4\pi r} e^{-jkr} \tag{3.6.40}$$

with

$$\frac{\partial G}{\partial r'}\Big|_{r'=a} \approx -\frac{jk\, e^{-jka\cos\theta'}}{4\pi r} e^{jkr}\cos\theta' \tag{3.6.41}$$

and

$$\frac{\partial p}{\partial r'}\Big|_{r'=a} = -jk[1 - \Gamma(\theta')] A_i \cos\theta\, e^{-jka\cos\theta'} \tag{3.6.42}$$

It follows from Eq. (3.6.10), taken for a surface just outside the volume V, that

$$\frac{p_s(r, \theta)}{A_i} = \frac{jke^{-jkr}}{\Gamma} \int_{\theta=\pi/2}^{\pi} a^2 \cos\theta' \sin\theta' \, e^{-2jka\cos\theta'} \Gamma(\theta')\, d\theta' \tag{3.6.43}$$

Assuming that Γ = constant, we find that when $ka \gg 1$, Eq. (3.6.43) can be

integrated to yield

$$\frac{p_s(r, 0)}{A_i} \approx \frac{e^{-jk(r-a)}}{2r} \Gamma a \tag{3.6.44}$$

Here we have ignored terms of the order of $1/ka$ down from the main term, because the theory should not be expected to be reliable for terms of this order. The backscattered intensity I_s is defined as

$$I_s = \frac{|p_s|^2}{2Z_0} \tag{3.6.45}$$

Therefore, the ratio of the backscattered intensity to the incident intensity I_i is

$$\frac{I_s}{I_i} = \frac{\Gamma^2 a^2}{4r^2} \tag{3.6.46}$$

As we might expect, this result agrees with Eq. (3.6.1). Note that we can estimate the backscattering cross section σ_{Rs} by assuming that the power is radiated uniformly in all directions, which implies, from the argument in Sec. 3.6.1, that

$$\sigma_{Rs} = \pi a^2 \tag{3.6.47}$$

We note that this is just half the total scattering cross section, for as much power is radiated in the forward direction as in the backward direction.

Comparison with exact results and the concept of creeping waves. The exact results for scattering from a rigid obstacle are plotted by the solid line in Fig. 3.6.3; for comparison, the dashed lines plot Rayleigh scattering theory, which is approximately true for $ka < 0.5$, and the asymptotic specular approximation for reflection for $ka >> 1$. The exact results have an extra periodicity due to the presence of leaky waves, which propagate around the surface of the sphere with approximately the longitudinal wave velocity in the liquid. These leaky waves, known as *creeping waves*, are illustrated in Fig. 3.6.4. For this reason, it is rarely worthwhile to carry out the integral of Eq. (3.6.43) in more detail and keep terms that vary as $1/ka$. Such analyses can be improved to reproduce the theory of scattering from the front surface with accuracy. They cannot, however, reproduce the effect of creeping waves.

The fact that there are waves that can propagate around an obstacle is important. If the sphere of radius a is surrounded by another sphere of very large radius b, and if $ka >> 1$, a series of longitudinal or shear waveguide modes propagates around the inner sphere. If the outer sphere were removed to infinity, a mode propagating around the inner sphere would tend to have infinite energy. Instead, as it radiates power radially, this creeping wave becomes a leaky wave, and its amplitude decreases along the circumference away from the point of excitation [66, 69, 71].

When the plane wave incident on the sphere is longitudinal, as it is in a liquid, it tends to excite a longitudinal creeping wave at the shadow boundary (i.e., where

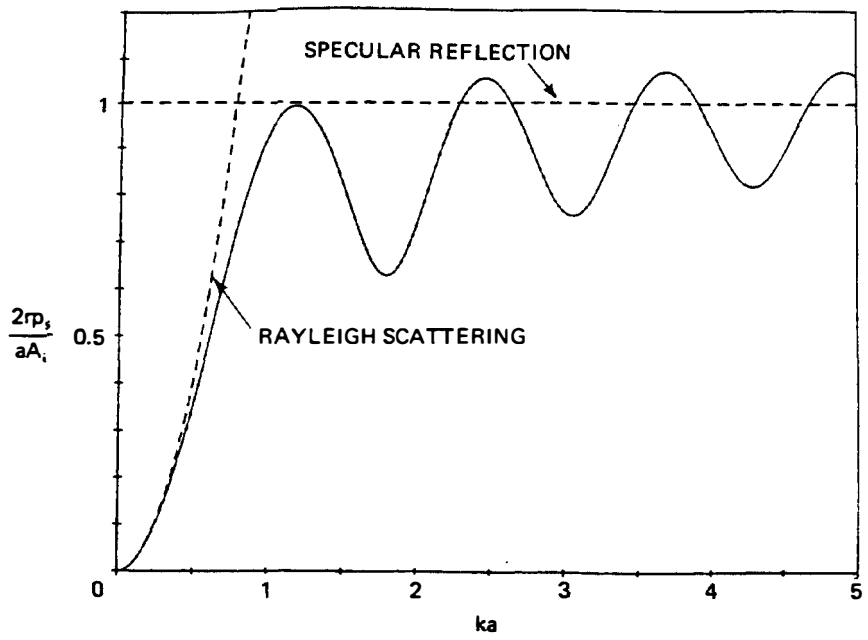

Figure 3.6.3 Solid line, plot of the exact result for backscattering from a rigid sphere in a liquid; Dashed lines, plots of the specular reflection theory [Eq. (3.6.1)] and the quasistatic Rayleigh scattering limit [Eq. (3.6.31)].

the phase velocity of the creeping wave is in the same direction as that of the incident wave). The creeping wave excites a reflected plane wave on the other side of the sphere, as illustrated in Fig. 3.6.4. The results of this concept are clear in Fig. 3.6.5, which shows the time-domain backscatter response to a short pulse. This has been found by taking the Fourier transform of Fig. 3.6.3.

Generalizations of the theory. We see that a pulse is reflected from the front surface of the sphere and that a further weak pulse, corresponding to the creeping wave, arrives at a time $t = a(2 + \pi)/V$ later. The response in the frequency domain thus corresponds to the interference between the specularly reflected wave and the later signal from the creeping wave, which travels around the circumference at a velocity close to that of a longitudinal wave [69].

The creeping wave concept can be generalized further for obstacles on which there are sharp points or corners. In this case, each sharp discontinuity behaves like a source for reflected waves [72]. Sharp discontinuities also generate creeping

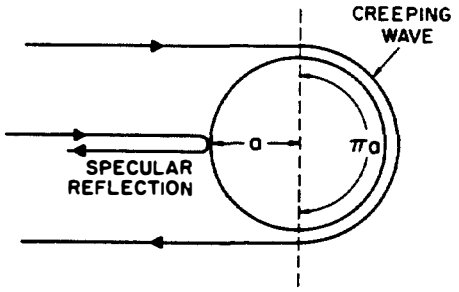

Figure 3.6.4 Specular reflection and creeping wave from a sphere.

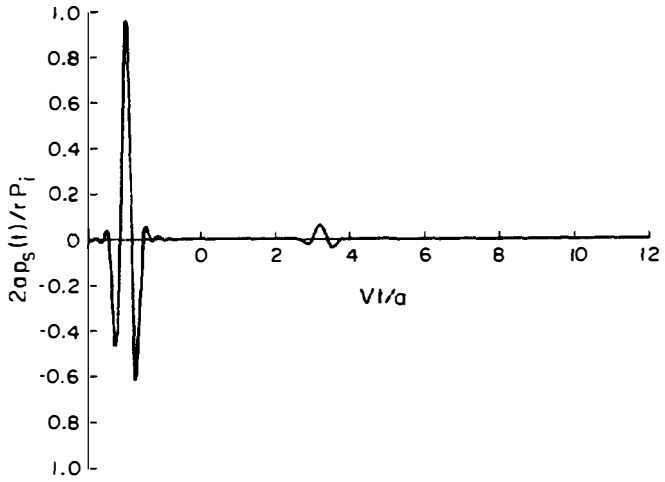

Figure 3.6.5 Plot of the backscatter reflected pressure from a rigid sphere in a liquid as a function of time when the excitation is a short pulse.

waves, which propagate along the surface of the object and are reemitted at another similar discontinuity. A good example is a smooth crack in a solid, which behaves like a specular reflector. The crack may not emit a reflected wave in the direction of the receiving transducer; the ends of the crack, however, scatter waves in all directions, to create a characteristic angular interference pattern between the two waves emitted, one from either end of the crack; this pattern varies with frequency [73, 74]. Creeping waves can also be excited at one end of the crack, propagate along the crack surface, and be emitted from the other end of the crack. The situation becomes even more complicated if the surface is rough. In this case, there may be a number of secondary sources along the surface of the object, as we discussed when considering the phenemonon of speckle in Sec. 3.3.2.

The results can also be generalized in other ways. For instance, the dependence of scattering with angle will change with the shape of the object, even when its size is small, and the intensity of the scattered wave can have a different frequency dependence in the Rayleigh limit. As an example, we consider scattering of a surface wave from a small cylinder of radius a, whose axis is normal to the direction of propagation of the incident wave. For $kR >> 1$, the Green's function will vary as $[\exp(-jkR)]/\sqrt{kR}$, and the scattered wave intensity will vary as f^3a^4 (see Prob. 3.1.3). This compares to scattering of a volume wave from a sphere of radius a, where the scattered intensity varies as f^4a^6 [1, 66–69].

Similarly, if we consider scattering of a longitudinal wave in a solid from a small defect, we can find generalized forms of Eq. (3.6.20) [1, 68, 75]. In general, both shear and longitudinal waves are excited and the angular dependences of these scattered waves will be quite different and complicated, even in the Rayleigh limit, by their dependence on stress type and direction rather than pressure. Thus, even in the Rayleigh limit, we can obtain a great deal of information from the angular dependence of scattering on the elastic properties of the scatterer [1, 68, 70].

At higher frequencies, scattering behavior becomes even more complicated. Consider a void in a solid, which behaves partially like a specular reflector; the reflection coefficient of a short pulse reflected from the front surface is given by Eq. (3.6.1). In addition, as we have seen, creeping waves, which give rise to very weak reradiated signals, will propagate along the surface of the object. When

excited by a pulse, such a void then gives a strong reflection from its front surface, followed by a short pulse corresponding to a creeping wave, as illustrated in Figs. 3.6.4 and 3.6.5 [71].

The behavior of inclusions is still more complicated and is best understood on the basis of ray tracing theory. Once more there will be a reflection from the front surface, but there will also be waves that propagate through the middle of the inclusion and are reflected from its back surface. As mode conversions can take place from longitudinal to shear waves, and vice versa, quite complicated behavior occurs and there may be relatively strong reflections from the back surface of such an inclusion. Furthermore, waves can also propagate around the outside of the inclusion, which can give rise to still other pulses. Hence the behavior in the frequency domain is relatively complicated because of the interference pattern that occurs between these various, multiply reflected waves [71, 75, 76].

As with the simpler theories described in this section, the detailed behavior of scattering from spherical voids and inclusions in solids can be worked out with an exact theory, and approximate techniques, very similar in nature and form to those of Eqs. (3.6.15) and (3.6.20), can be derived. Both Born approximations and quasistatic approximations have been made in the manner described here. The quasistatic approximations are particularly interesting for dealing with scattering from small cracks, because they rest on a foundation of static fracture mechanics theory, which has been developed over the years [68, 70, 77–79]. The theories have been generalized to deal with excitation by Rayleigh surface waves as well as plane longitudinal and shear waves. Variational techniques and other methods have also been developed to deal with these problems. Thus a great deal of theoretical insight into scattering from flaws can be obtained. The inverse problem of determining the shape, size, and nature of a flaw from the scattered signals is also of great interest, and a great deal of theoretical work on the subject is being carried out.

PROBLEM SET 3.6

1. **(a)** Work out the scattering from a disk-shaped crack of radius a excited by a plane wave. Assume that $ka >> 1$ and that the incident plane wave is incident on the disk at an angle θ to its axis. Assume that the reflection coefficient is zero at the crack, so that u_z is doubled at the crack from its incident value. Regarding the crack as a piston transducer surrounded by a rigid baffle, find the amplitude of the backscattered wave in the far field (the Fraunhofer region of the crack) as a function of angle ($\theta > \pi/2$). Thus consider only specular reflection and neglect creeping waves.

   (b) Compare the amplitude of your result for the backscattered signal ($\theta = \pi$) with that for a spherical void of the same radius. Again, ignore creeping waves.

2. Use a quasi-static theory to work out the scattering, as a function of angle, of a normally incident longitudinal plane wave from a penny-shaped (disk-shaped) crack of radius a, when $ka << 1$.

   Hint: Using quasistatic theory, we can show that the crack opening displacement Δu_z (the incremental distance between the two crack faces), when an RF field T_{3i}, or pressure,

is applied, is of the form

$$\Delta u_z = \frac{4}{\pi} \frac{1 - \sigma}{\mu} (a^2 - r^2)^{1/2} T_{3i}$$

Treat the crack like a small piston transducer, or use Eq. (3.6.10) with $\phi = 0$ (i.e., $T_3 = 0$ on the crack). Here σ is Poisson's ratio and μ is the second Lamé constant.

3. The attenuation per unit length of a plane wave is

$$\alpha = \frac{P_L}{2P_T}$$

where P_L is the power lost per unit length and P_T is the incident power transmitted.

(a) Consider the problem of observing objects in turbid water, in which there are N sand particles per unit volume. Suppose that the particles are spherical and 100 μm in diameter. Derive the total scattered power of a light wave from a particle, using the concepts of Sec. 3.6.1 and the discussion after Eq. (3.6.36). Then work out the attenuation per unit length for N sand particles per unit volume.

(b) Work out a formula for the attenuation in turbid water, due to sand, of a 0.5-MHz acoustic wave (V = 1.5 km/s). Suppose that there are 10^4 particles/cm^3. Find the attenuation per meter of light and sound.

Hint: See the example after Eq. (3.6.37).

4. Consider a spherical reflector of iron in a medium such as silicon nitride. In this case, the velocity of a wave inside the sphere is almost exactly half the acoustic wave velocity in the surrounding medium. Show by ray tracing in the paraxial limit that rays entering the sphere will return along a parallel path after being reflected from the back of the sphere. For this reason, reflections from the back of a sphere are often larger than those from the front surface. This phenomenon is known as "the scotchlight effect."

REFERENCES

1. G. S. Kino, "The application of Reciprocity Theory to Scattering of Acoustic Waves by Flaws," *J. Appl. Phys.*, 49, No. 6 (June 1978), 3190–99.
2. J. W. Goodman, *Introduction to Fourier Optics*. New York: McGraw-Hill Book Company, 1968.
3. B. Delannoy, H. Lasota, C. Bruneel, R. Torguet, and E. Bridoux, "The Infinite Planar Baffles Problem in Acoustic Radiation and Its Experimental Verification," *J. Appl. Phys.*, 50, No. 8 (Aug. 1979), 5189–95.
4. H. Seki, A. Granato, and R. Truell, "Diffraction Effects in the Ultrasonic Field of a Piston Source and Their Importance in the Accurate Measurement of Attenuation," *J. Acoust. Soc. Am.*, 28 No. 2 (Mar. 1956), 230–38.
5. R. A. Lemons and C. F. Quate, "Acoustic Microscopy," Chapter 1 in *Physical Acoustics: Principles and Methods*, Vol. XIV, W. P. Mason and R. N. Thurston, eds. New York: Academic Press, Inc., 1979, pp. 1–92.
6. A. Papoulis, *Systems and Transforms with Applications in Optics*. (orig.: New York: McGraw Hill, 1968; rpt.: Melbourne, Fla.: R. E. Krieger Publishing Co., Inc. 1981).

7. K. K. Liang, G. S. Kino, and B. T. Khuri-Yakub, "Material Characterization by the Inversion of $V(z)$," *IEEE Trans. Sonics Ultrason.*, SU-32, No. 2 (Mar. 1985), 213–24.
8. R. N. Bracewell, *The Fourier Transform and Its Applications*, 2nd ed. New York: McGraw-Hill Book Company, 1978.
9. A. Atalar, "An Angular-Spectrum Approach to Contrast in Reflection Acoustic Microscopy," *J. Appl. Phys.*, 49 No. 10 (Oct. 1978), 5130–39.
10. J. Heiserman, D. Rugar, and C. F. Quate, "Cryogenic Acoustic Microscopy," *J. Acoust. Soc. Am.*, 67, No. 5 (May 1980), 1629–37.
11. H. K. Wickramasinghe and C. R. Petts, "Gas Medium Acoustic Microscopy," *Scanned Image Microscopy*, E. A. Ash, ed. London: Academic Press, Inc. (London) Ltd., 1980, pp. 57–70.
12. W. Parmon and H. L. Bertoni, "Ray Interpretation of the Material Signature in the Acoustic Microscope," *Electron. Lett.*, 15, No. 21 (Oct. 11, 1979), 684–86.
13. R. D. Weglein, "Acoustic Microscopy Applied to SAW Dispersion and Film Thickness Measurement," *IEEE Trans. Sonics Ultrason.*, SU-27, No. 2 (Mar. 1980), 82–86.
14. R. C. Bray, C. F. Quate, J. Calhoun, and R. Koch, "Film Adhesion Studies with the Acoustic Microscope," *Thin Solid Films*, 74, No. 2 (Dec. 15, 1980), 295–302.
15. E. A. Ash, ed., *Scanned Image Microscopy*. New York: Academic Press, Inc., 1980.
16. C. F. Quate, "The Acoustic Microscope," *Sci. Am.*, 241, No. 4. (Oct. 1979), 62–70.
17. R. A. Lemons, *Acoustic Microscopy by Mechanical Scanning*, Ph.D. dissertation, Stanford University, Stanford, Calif., 1975.
18. R. A. Lemons and C. F. Quate, "A Scanning Acoustic Microscope," *1973 Ultrason. Symp. Proc.* (IEEE), 73 CHO 807-8 SU, 18–20.
19. B. Hadimioglu and C. F. Quate, "Water Acoustic Microscopy at Suboptical Wavelengths," *Appl. Phys. Lett.*, 43, No. 11 (Dec. 1, 1983), 1006–7.
20. A. Rosencwaig, *Photoacoustics and Photoacoustic Spectroscopy*, Vol. 57 of *Chemical Analysis: A Series of Monographs on Analytical Chemistry and Its Applications*, P. J. Elving and J. D. Winefordner eds., I. M. Kolthoff, ed. emeritus. New York: John Wiley & Sons, Inc., 1980.
21. R. A. Burrier, R. O. Claus, J. W. Gray, and W. T. O'Connor, "Circularly Symmetric Gaussian Field Transducer with Equal Impedance and Equal Voltage Electrode Design," *1983 Ultrason. Symp. Proc.* (IEEE), Vol. 1, 83CH1947-1, 570–72.
22. A. Yariv, *Quantum Electronics*, 2nd ed. New York: John Wiley & Sons, Inc., 1975.
23. H. Kogelnik and T. Li, "Laser Beams and Resonators," *Proc. IEEE*, 54, No. 10 (Oct. 1966), 1312–29.
24. J. P. Weight and A. J. Hayman, "Observations of the Propagation of Very Short Ultrasonic Pulses and Their Reflection by Small Targets," *J. Acoust. Soc. Am.*, 63, No. 2 (Feb. 1978), 396–404.
25. D. E. Robinson, S. Lees, and L. Bess, "Near Field Transient Radiation Patterns for Circular Pistons," *IEEE Trans. Acoust. Speech Signal Process.*, ASSP-22, No. 6 (Dec. 1974), 395–403.
26. W. L. Beaver, "Sonic Nearfields of a Pulsed Piston Radiator," *J. Acoust. Soc. Am.*, 56, No. 4 (Oct. 1974), 1043–48.
27. R. H. Tancrell, J. Callerame, and D. T. Wilson, "Near-Field, Transient Acoustic Beam-Forming with Arrays," *1978 Ultrason. Symp. Proc.* (IEEE), 78CH 1344-1SU, 339–43.

28. G. S. Kino, "Acoustic Imaging for Nondestructive Evaluation," *Proc. IEEE*, 67, No. 4 (Apr. 1979), 510–25.

29. M. G. Maginness, "Methods and Terminology for Diagnostic Ultrasound Imaging Systems," *Proc. IEEE*, 67, No. 4 (Apr. 1979), 641–53.

30. B. T. Khuri-Yakub, private communication.

31. J. Fraser, J. Havlice, G. Kino, W. Leung, H. Shaw, K. Toda, T. Waugh, D. Winslow, and L. Zitelli, "An Electronically Focused Two-Dimensional Acoustic Imaging System," in *Acoustical Holography*, Vol. 6, N. Booth, ed. New York: Plenum Press, 1975, pp. 275–304.

32. S. A. Farnow and B. A. Auld, "An Acoustic Phase Plate Imaging Device," in *Acoustical Holography*, Vol. 6, N. Booth, ed. New York: Plenum Press, 1975, pp. 259–73.

33. D. K. Peterson and G. S. Kino, "Real-Time Digital Image Reconstruction: A Description of Imaging Hardware and an Analysis of Quantization Errors," *IEEE Trans. Sonics Ultrason.*, SU-31, No. 4 (July 1984), 337–51.

34. J. F. Havlice, G. S. Kino, J. S. Kofol, and C. F. Quate, "An Electronically Focused Acoustic Imaging Device," in *Acoustical Holography*, Vol. 5, P. S. Green, ed. New York: Plenum Press, 1974, pp. 317–33.

35. K. N. Bates, E. Carome, K. Fesler, R. Y. Liu, and H. J. Shaw, "Digitally Controlled Electronically Scanned and Focused Ultrasonic Imaging System," *1979 Ultrason. Symp. Proc.* (IEEE), 79CH1482-9, 216–20.

36. T. M. Waugh, G. S. Kino, C. S. DeSilets, and J. D. Fraser, "Acoustic Imaging Techniques for Nondestructive Testing," *IEEE Trans. Sonics Ultrason.*, SU-23, No. 5 (Sept. 1976), 313–17.

37. F. L. Becker, J. C. Crowe, V. L. Crow, T. J. Davis, B. P. Hildebrand, and G. J. Posakony, "Development of an Ultrasonic Imaging System for the Inspection of Nuclear Reactor Pressure Vessels," *Electric Power Research Institute*, EPRI RP 606-1 (Sept. 1977).

38. F. L. Thurstone and O. T. von Ramm, "A New Ultrasound Imaging Technique employing Two-Dimensional Electronic Beam Steering," in *Acoustical Holography*, Vol. 5, P. S. Green, ed. New York: Plenum Press, 1974, pp. 249–59.

39. R. D. Gatzke, J. T. Fearnside, and S. M. Karp, "Electronic Scanner for a Phased-Array Ultrasound Transducer," *Hewlett-Packard J.*, 34, No. 12 (Dec. 1983), 13–20.

40. J. T. Walker and J. D. Meindl, "A Digitally Controlled CCD Dynamically Focussed Phase Array," *1975 Ultrason. Symp. Proc.* (IEEE), 75 CHO 994-4SU, 80–83.

41. P. D. Corl, P. M. Grant, and G. S. Kino, "A Digital Synthetic Focus Acoustic Imaging System for NDE," *1978 Ultrason. Symp. Proc.* (IEEE), 78CH 1344-1SU, 263–68.

42. S. A. Johnson, J. F. Greenleaf, F. A. Duck, A. Chu, W. R. Samayoa, and B. K. Gilbert, "Digital Computer Simulation Study of a Real-Time Collection, Post-Processing Synthetic Focusing Ultrasound Cardiac Camera," in *Acoustical Holography*, Vol. 6, N. Booth, ed. New York: Plenum Press, 1975, pp. 193–211.

43. V. Schmitz and P. Höller, "Reconstruction of Defects by Ultrasonic Testing Using Synthetic Aperture Procedures, in *Quantitative Nondestructive Evaluation*, Vol. 4A, D. O. Thompson and D. E. Chimenti, eds. New York: Plenum Press, 1979, pp. 297–307.

44. J. R. Frederick, C. Vanden Broek, S. Ganapathy, M. Elzinga, W. De Vries, D. Papworth, and N. Hamano, "Improved Ultrasonic Nondestructive Testing of Pressure Vessels," U.S. Nuclear Regulatory Commission Progress Report NUREG/CR-0909 R5

(September 1979), Dept. of Mechanical Engineering, The University of Michigan, Ann Arbor, Mich.

45. P. D. Corl and G. S. Kino, "A Real-Time Synthetic-Aperture Imaging System," in *Acoustical Imaging*, Vol. 9, K. Y. Wang, ed. New York: Plenum Press, 1980, 341-55.

46. A. Papoulis, *Probability, Random Variables, and Stochastic Processes*. New York: McGraw-HIll Book Company, 1965.

47. H. C. Tuan, A. R. Selfridge, J. E. Bowers, B. T. Khuri-Yakub, and G. S. Kino, "An Edge-Bonded Surface Acoustic Wave Transducer Array," *1979 Ultrason. Symp. Proc.* (IEEE), 79CH1482-9, 221–25.

48. R. L. Baer, A. R. Selfridge, B. T. Khuri-Yakub, and G. S. Kino, "Contacting Transducers and Transducer Arrays for NDE," *1981 Ultrason. Symp. Proc.* (IEEE), Vol. 2, 81CH1689-9, 969–73.

49. G. S. Kino, D. K. Peterson, and S. D. Bennett, "Acoustic Imaging," in *New Procedures in Nondestructive Testing*, P. Holler, ed. New York: Springer-Verlag, New York, Inc., pp. 113–25.

50. W. B. Meredith and J. D. Massey, *Fundamental Physics of Radiology*. Bristol, England: John Wight & Sons, Ltd., 1977.

51. A. Macovski, *Medical Imaging Systems*. Englewood Cliffs, N.J.: Prentice-Hall, Inc., 1983.

52. K. Liang, B. T. Khuri-Yakub, C-H. Chou, and G. S. Kino, "A Three-Dimensional Synthetic Focus System," in *Acoustical Imaging*, Vol. 10, P. Alais and A. F. Metherell, eds. New York: Plenum Press, 1981, pp. 643–68.

53. D. Gabor, "A New Microscopic Principle," *Nature*, 161, No. 4098 (May 15, 1948), 777-78.

54. E. N. Leith and J. Upatnieks, "Wavefront Reconstruction with Continuous-Tone Objects," *J. Opt. Soc. Am.*, 53, No. 12 (Dec. 1963), 1377–81.

55. R. K. Mueller, "Acoustic Holography," *Proc. IEEE*, 59, No. 9 (Sept. 1971), 1319–35.

56. B. B. Brenden, "Real Time Acoustical Imaging by Means of Liquid Surface Holography," in *Acoustical Holography*, Vol. 4, G. Wade, ed. New York: Plenum Press, 1972, pp. 1–9.

57. E. E. Aldridge, A. B. Clare, and D. A. Shepherd, "Ultrasonic Hollography in Nondestructive Testing," in *Acoustical Holography*, Vol. 3, A. F. Metherell, ed. New York: Plenum Press, 1971, pp. 129–45.

58. B. P. Hildebrand and H. D. Collins, "Evaluation of Acoustical Holography for the Inspection of Pressure Vessel Sections," *Mat. Res. Stand.*, 12, No. 12 (Dec. 1972), 23-31.

59. L. W. Kessler and D. E. Yuhas, "Acoustic Microscopy—1979," *Proc. IEEE*, 67, No. 4 (Apr. 1979), 526–36.

60. A. Korpel, L. W. Kessler, and P. R. Palermo, "Acoustic Microscope Operating at 100 MHz," *Nature*, 232, No. 5306 (July 9, 1971), 110–11.

61. L. W. Kessler and D. E. Yuhas, "Structural Perspective," *In. Rev.*, 20, ,No. 1 (Jan. 1978), 53–56.

62. R. C. Eggleton and F. S. Vinson, "Heart Model Supported in Organ Culture and Analyzed by Acoustic Microscopy," in *Acoustical Holography*, Vol. 7, L. W. Kessler, ed. New York: Plenum Press, 1977, pp. 21–35.

63. Z. C. Lin, H. Lee, and G. Wade, "Scanning Tomographic Acoustic Microscope: A Review," *IEEE Trans. Sonics Ultrason.*, SU-32, No. 2 (Mar. 1985), 168–80.

64. C. H. Chou, B. T. Khuri-Yakub, and G. S. Kino, "Transmission Imaging: Forward Scattering and Scatter Reconstruction," in *Acoustical Imaging*, Vol. 9, K. Y. Wang, ed. New York: Plenum Press, 1980, pp. 357–77.

65. R. L. Powell and K. A. Stetson, "Interferometric Vibration Analysis by Wavefront Reconstruction," *J. Opt. Soc. Am.*, 55, No. 12 (Dec. 1965), 1593–98.

66. P. M. Morse and H. Feshbach, *Methods of Theoretical Physics*. New York: McGraw-Hill Book Company, 1953, Part II, Chapters 9–13.

67. C. F. Ying and R. Truell, "Scattering of a Plane Longitudinal Wave by a Spherical Obstacle in an Isotropically Elastic Solid," *J. Appl. Phys.*, 27, No. 9 (Sept. 1956), 1086-97.

68. J. E. Gubernatis, E. Domany, and J. A. Krumhansl, "Formal Aspects of the Theory of the Scattering of Ultrasound by Flaws in Elastic Materials," *J. Appl. Phys.*, 48, No. 7 (July 1977), 2804–11.

69. M. C. Junger and D. Feit, *Sound, Structures, and Their Interaction*. Cambridge, Mass.: The MIT Press, 1972.

70. J. D. Eshelby, "The determination of the Elastic Field of an Ellipsoidal Inclusion, and related Problems," *Proc. Roy. Soc.*, A, 241, No. 1226 (Aug. 20, 1957), 376–96.

71. Y. H. Pao and W. Sachse, "Interpretation of Time Records and Power Spectra of Scattered Ultrasonic Pulses in Solids," *J. Acoust. Soc. Am.*, 56, No. 5 (Nov. 1974), 1478–86.

72. A. Freedman, "A Mechanism of Acoustic Echo Formation," *Acustica*, 12, No. 1 (1962), 10–21.

73. J. D. Achenbach, L. Adler, D. K. Lewis, and McMaken, "Diffraction of Ultrasonic Waves by Penny-Shaped Cracks in Metals: Theory and Experiment," *J. Acoust. Soc. Am.*, 66, No. 6 (Dec. 1979), 1848–56.

74. J. D. Achenbach and A. K. Gautesen, "Geometrical Theory of Diffraction for Three-D Elastodynamics," *J. Acoust. Soc. Am.*, 61, No. 2 (Feb. 1977), 413–21.

75. R. Hickling, "Analysis of Echoes from a Solid Elastic Sphere in Water," *J. Acoust. Soc. Am.*, 34, No. 10 (Oct. 1962), 1582–92.

76. C. H. Chou, B. T. Khuri-Yakub, G. S. Kino, and A. G. Evans, "Defect Characterization in the Short-Wavelength Regime," *J. Nondestructive Evaluation*, 1, No. 4 (Dec. 1980), 235–47.

77. B. Budiansky and J. R. Rice, "On the Estimation of a Crack Fracture Parameter by Long-Wavelength Scattering," J. Appl. Mech., 45, No. 2 (June 1978), 453–54.

78. M. T. Resch, B. T. Khuri-Yakub, G. S. Kino, and J. C. Shyne, "The Acoustic Measurement of Stress Intensity Factors," *Appl. Phys. Lett.*, 34, No. 3 (Feb. 1, 1979), 182-84.

79. J. J. Tien, B. T. Khuri-Yakub, and G. S. Kino, "Long Wavelength Measurements of Surface Cracks in Silicon Nitride, in *Review of Progress in Quantitative Nondestructive Evaluation*, Vol. 1, D. O. Thompson and D. E. Chimenti, eds. New York: Plenum Press, 1982, pp. 569–71.